HYPERSONIC CAVITY FLOWS

M.P. Netterfield B.E., MSc

December 1988

A thesis submitted for the degree of
Doctor of Philosophy
of the
University of London
and for the
Diploma of Imperial College

Department of Aeronautics
Imperial College of Science and Technology
London SW7 2BY

Abstract

Axisymmetric cavity flow experiments have been conducted in the Imperial College No.2 Gun Tunnel at Mach 9 and unit Reynolds number of 1.7×10^7/m and 5.5×10^7/m. The oncoming turbulent boundary layer developed over a cone forebody of 5^o semi-angle for a distance of 0.72m, with transition taking place in the first third of the forebody. Pitot measurements were made in the boundary layer to determine the velocity profile just before separation. Surface pressure measurements were made around cavities with length to depth ratios in the range $0.8 < L/D < 2.4$ at both Reynolds numbers, and compared with other two dimensional planar results. Strong Reynolds number effects were noticed in the region of shear layer reattachment on the rear face where the highest pressures were recorded, and where evidence of flow unsteadiness was also found. A frequency analysis of the fluctuating pressures showed that the oscillation could have been due to a transverse acoustic mode in the cavity.

Heat transfer measurements were made at both Reynolds numbers around the surface of cavities with L/D=0.8, 1.6 and 2.4 using a thin film technique. The heat transfer results followed the same basic trends as the pressure results. Strong Reynolds number dependence was noticed again in the region of shear layer reattachment.

A basic semi-empirical analysis was used to try to predict and extrapolate the experimental results. Good predictions of separated shear layer spreading and reattachment were achieved by the use of relatively simple equations, and using this analysis the experimental results were extrapolated to different cavity lengths.

A laminar Navier-Stokes code was developed using a Godunov-type Euler code as a basis. Hypersonic flat plate boundary layer computations gave very accurate results when compared to known solutions. A Mach 8 L/D=2 laminar cavity flow was computed, and surface pressure, heat transfer and skin friction profiles in the cavity produced. These seemed in qualitative agreement with the turbulent experimental results.

Contents

Nomenclature

a (2.6.1)	Critical depth for thin film gauges
a (3.2.3)	Average speed of sound in the cavity
a (6.3.2)	Speed of sound in a cell
A,B	Empirical constants in 3.2.3
B_e	Bandwidth of spectral window in a Fast Fourier Transform
c	Heat capacity
C	Constant in power law temperature-viscosity relation
C_f	Skin friction coefficient
C_p	Specific heat at constant pressure
D	Cavity Depth
e	Internal energy per unit mass
E	Bridge output voltage
f	Frequency
H	Total enthalpy
k	Thermal conductivity
L	Cavity length
L'	Horizontal co-ordinate in 2.6.3
M	Mach number
n	Emperical constant in 5.3.2
p	Static pressure
p_t	Pitot pressure
Pr	Prandtl number
$\dot{q}$	Heat transfer rate
Q	Total heat flux
Q_o	Total heat flux without cavity
R	Gas constant
Re	Reynolds number
S	Reynolds analogy factor
St	Stanton number
Str	Strouhal number
t	Time
T	Temperature
u	Streamwise velocity component
v	Transverse velocity component
x,y	Streamwise and transverse co-ordinates
x_o,y_o	Effective origins for the separtaed shear layer
X_*	Cavity co-ordinate as defined on Fig.33

Greek Symbols

α	Thermal diffusivity = $k/\rho c$
α_R	Temperature coefficient of resistance
γ	Ratio of specific heats
δ	Boundary layer displacement thickness
Δt	Time increment
Δx	Increment in x
Δy	Increment in y
ε_t	Error in Fast Fourier Transform analysis
ϑ	Boundary layer momentum thickness
Θ	Flow deflection angle
λ	Bulk viscosity
μ	Dynamic viscosity
ρ	Density
σ (5.2)	Shear layer spreading parameter
σ (6.3)	Normal stress
τ	Shear stress
φ	Cone angle

Subscripts

aw	Adiabatic wall conditions
c	Cone values; actual surface values (2.6.2)
D	Dividing streamline values
e	Boundary layer edge values before separation
h	Hyperbolic terms
i,j	Finite difference co-ordinates in x and y directions
max	Maximum values in the cavity
min	Minimum values in the cavity
n	Time n
p	Parabolic terms
r	Body radius
s	Measured surface values (2.6.2)
t	Pitot values
w	Wall values

w1,w2	Metal and gauge wall values respectively
x	Streamwise direction
y	Transverse direction
0	Initial values; total values
∞	Free stream conditions

List of Figures

Acknowledgements

I would first of all like to sincerely thank my supervisor, Dr. Richard Hillier, for his guidance during the course of this work. Work of this kind requires motivation, and Richard helped keep me on the rails.

Financial help from the Royal Commisson for the Exhibition of 1851, the Overseas Research Scheme, and the Ministry of Defence is also gratefully acknowledged.

Many other people in the department also deserve mention. Technical support from Mr. Rowland Hutchins, Mr. Earnie Turner, Mr. Dave Clark and Mr. Clive Mott was not only valuable, but took place in a friendly atmosphere. Special thanks also to Mr. Seamus Mularky for his help with the FFT work, and Dr. John Harvey and Prof. Peter Bradshaw for their advice.

Finally, thanks to my fiancee , Monika, and my parents for bearing with me and helping me out these past 3 (and a bit) years.

CHAPTER 1

INTRODUCTION

1.1 General

A cavity, or surface cutout, is a fundamentally important aerodynamic geometry. Apart from being of interest in many practical problems, a cavity flow exhibits some of the most complicated and important aerodynamic phenomena such as separation, reattachment and flow unsteadiness, and therefore has proved ideal as a test problem for studying these flow features. Cavity flows occur practically for a wide range of free stream flow conditions, from subsonic and low supersonic Mach numbers where drag and flow oscillation are of primary importance, to high supersonic and hypersonic Mach numbers where heat transfer is also of considerable importance, and where, generally, bulk unsteadiness of the flow is low.

Cavity flows may be of direct practical interest under a variety of circumstances. At low Mach numbers flow oscillation in bomb bays and wheel wells can lead to noise, buffeting and cyclic stresses on the structure (see Plumbee et.al.(1962)). Gaps between lifting and control surfaces, and surface cutouts, can increase drag and alter the heat transfer characteristics of the surface of vehicles flying at high Mach number (see Larson(1959)) .

Low speed cavity flows have been the subject of considerable experimental effort in the past, but information about such flows in the hypersonic regime is sparse . At a time when several countries are contemplating reusable launch vehicles, a more extended knowledge of such a basic hypersonic flow phenomena is essential. The aim of this work is then to collect pressure and heat transfer data for such a flow, and thereby get a better physical understanding of the important mechanisms involved. Parallel with this is the development of a Navier-Stokes code, with the results of the computations

hopefully enhancing the physical understanding of the flow. The time spent on the experiments and analysis, and on the computations, is in part determined by support from the sponsor of this work.

1.2 Background-Experimental

1.2.1 Mean Flow Characteristics

Most data available in the literature for supersonic cavity flows are for two dimensional flows. A schematic of such a flowfield is shown on Fig.1. A comprehensive series of experiments was performed by Charwat et.al.(1961). These included pressure and heat transfer measurements for cavity length to depth ratios $0.5 < L/D < 30$ for Mach 1.9-3.5 turbulent flows over a range of Reynolds numbers. They, and other investigators, found that there is a critical value of L/D of around 10, and that at this value a fundamental restructuring of the flow occurs. Above this value the separated shear layer from the upstream face attaches to the floor of the cavity, and separates again as the flow approaches the downstream (recompression) face. This is shown in Fig.2a, and is called a closed cavity flow. Below L/D=10, the shear layer effectively jumps the cavity, reattaching at the recompression face. This is shown in Fig.2b, and is called an open cavity flow. Strong stagnation pressure recovery is noticed at the downstream face while the floor pressure is relatively constant.

Other two dimensional flows were investigated by Zhang(1987) at Mach 1.5 to 3, McDearmon(1960) at Mach 3.55, Stallings and Wilcox(1987) at Mach 1.5 to 2.86, Clark et.al .(1980) at Mach 0.6 to 3.0, and an axisymmetric cavity by Johanneson(1955)at Mach 1.97. Nicoll(1964), Ginoux et.al .(1968), and Hahn(1969) all studied axisymmetric laminar cavities at hypersonic Mach numbers. Larson(1959) investigated laminar and turbulent axisymmetric cavities at Mach 0.3-4.0 and found turbulent heat transfer rates (normalized by the value on the forebody) quite similar to laminar ones and relatively Mach number independent, which contradicts the theoretical results of Chapman(1956) for turbulent flows, although agreement with Chapman's theory for the laminar results was good. Fig.3 shows Larson's heat transfer results for both laminar and turbulent flows in terms of average cavity heat transfer coefficient normalised by the heat transfer

coefficient for the attached boundary layer. It can be seen that for his relatively long cavities, the average heat transfer coefficient is about half the attached value. Johanneson showed that the results for axisymmetric cavities are not very different from two dimensional cavities, except that axisymmetric cavities exhibit a slightly larger drop in pressure moving from the front to the rear of the cavity floor. This is illustrated on Fig.4. The "two dimensional" cavity investigations all report strong 3 dimensional effects due to the presence of the cavity side walls, which is one of the features which prompted our interest in axisymmetric configurations.

A hypersonic two dimensional cavity at Mach 6.3 and 8.5 was studied by Nestler et.al. (1968) for values of $5 < L/D < 30$. Heat transfer and pressure measurements were made on the cavity floor. Other heat transfer data were taken by Gortyshov et.al .(1982) for M=3.5-4.5, White(1971) at subsonic and low supersonic Mach numbers, and Wieting(1970) at Mach 7 for deep cavities ($L/D<0.524$). Lamb(1981) attempted a correlation of all the cavity flow parameters to predict heat transfer rates. He found heat transfer rates in the cavity to be primarily dependent on the rate of spreading of the separated shear layer into the cavity flowfield and therefore strongly dependent on initial boundary layer thickness and cavity length. Cavity depth was found to be of secondary importance in determining both peak and average heat transfer rates in open cavity flows.

It is expected that peak heat transfer rates in the cavity will occur in the region of shear layer impingement on the back face. In that sense the reattachment of turbulent separated flows in general are of interest, and a summary of correlated data in this field is given by Merzkirch(1988) et.al., who looked at available experimental data on the influence of Reynolds number, upstream boundary thickness, Mach number, and body geometry on heat transfer rates to cavities, rearward facing steps and base flows. Various attempts have been made, notably by Korst(1956) and Chapman(1956), Nestler(1973) Gerhart and Thomas(1974), Keyes(1977), and Tanner(1976) to analyse the

reattachment process to predict the heat transfer rates. Pressures and heat transfer rates are loosely linked, and some authors have found power laws linking pressure and heat transfer to fit quite well.

Little detail is available on the structure of the captured vortex in open cavity flow. Gortyshov et.al. found the captured vortex to split into a primary and secondary vortex for approximately L/D>2. This is illustrated on Fig.5. In addition to these two main vortices, there is also a sequence of smaller vortices at corners. Roshko(1955) made some measurements in the primary vortex in subsonic flow, and found that recirculation velocities were as high as 40% of the free stream velocity.

The boundary layer in the present experimental study separates at a five degree angle with respect to the cavity alignment (see Fig.32). In this respect the separated shear layer resembles that of a base flow, at least initially, and so it is instructive to look at the wave systems observed in some base flows at the point of separation. Martellucci et.al.(1966) at Mach 6 and Marcillat(1974) at Mach 7 illustrate the shock-expansion system at the point of separation on cone base flows, which is shown on Fig.6a. Pressure is essentially uniform in the base region (that pressure being dependent on the cone angle). The lip shock in the shock-expansion system seems to be due to an initial overexpansion of the inner part of the boundary layer to maintain pressure continuity across the separated shear layer, and then a subsequent compression. This effect later proves important in calculating the separated shear layer of the cavity configuration in this study. Martellucci et.al. measured total temperatures in the base region and found them on average to be about 0.65 times the free stream total temperature. This compares well the experiments of Emery et.al.(1965), who found total temperatures in the separated region of a cavity flow to be 0.66 times the free stream total temperature. In addition to the lip shock in the base flow problem, there is also a trailing shock (as identified on Fig.6) which aligns the flow with the

body axis downstream of separation. The trailing shock is stronger than the lip shock, and pressures immediately downstream of it rise above the free stream pressure before falling gradually further downstream to the free stream value.

Another type of supersonic separated flow that bears similarities to open cavity flows is that induced by shock waves, such as at a compression corner as studied by Lowder(1984) and Holden(1972). A schematic of such a flow is shown on Fig.6b. Similarities with hypersonic open cavity flows include the fact that bulk unsteadiness of the flow is low, and that peak heating and pressures occur near the shear layer reattachment point. However separations at compression corners differ in that full shear layer reattachment occurs (as opposed to partial reattachment for open cavities), and this is reflected in the much higher reattachment heat transfer rates recorded. The mechanism of separation is also different, with pressure induced separation occuring at compression corners rather than "fly away" separation in cavity flows. Lowder conducted his experiments at Mach 9 for two different Reynolds numbers and a number of different axisymmetric and asymmetric compression steps. He found surface pressures at reattachment up to a factor of 100 greater than the surface pressure before separation for compression steps of 40^{o}. Coleman(1973) found reattachment heat transfer rates for such compression steps to rise by a factor of up to 50 over the surface heat transfer rate before separation. Lowder also noticed a Reynolds number dependence for the reattachment process, with higher Reynolds numbers leading to higher normalized reattachment pressures. Holden's experiments were conducted for $6.5<M<13$, and included attempts to identify the onset of separation with increasing wedge angle. This was attempted by the use of skin friction gauges to record at which wedge angle the skin friction reduced to zero.

1.2.2 Fluctuating Flow Characteristics

The flow inside a cavity can oscillate under a wide range of conditions, the nature of the oscillation depending on the free stream Mach number, the cavity geometry, and the thickness of the separated shear layer.

Krishnamurty (1955) found short cavities (L/D=1-2) at transonic speeds emitted high frequency radiation which was strong and directional (out of the cavity) . This frequency was found to be inversely proportional to cavity length in both laminar and turbulent flow. No simple relationship between free stream Mach number and cavity length was noticed.

Rossiter(1966) , also at transonic Mach numbers, found that the unsteady pressures contain both random and periodic components. The random component dominated in shallow cavities (L/D>4) and was most intense near the rear face, while the periodic component dominated in deeper cavities (L/D<4). With the aid of flow visualization he noticed discrete vortices in the shear layer being shed from the cavity leading edge. He constructed a model based on these vortices impacting on the rear face of the cavity and, in doing so, emitting acoustic waves which travel upstream to the leading edge and initiate the shedding of another vortex, thus forming a feedback loop. This theory was found to predict cavity oscillation frequencies quite well. The theory was modified slightly by Heller et.al.(1971) to account for the cavity speed of sound being different from the free stream value , thus improving the accuracy at higher Mach numbers. The discrete vortices noticed by Rossiter look similar to the large scale structures found, for example, in a subsonic free mixing layer by Brown and Roshko(1974). Their study, originally to investigate the effect of density ratio on a mixing layer, identified optically these apparently two dimensional vortical structures being shed from the point of separation of a low speed free mixing layer. Rockwell and Knisely(1979) made a low Reynolds number experimental study of a separated shear layer over a rearward facing step in incompressible flow, and a cavity for the same flow conditions and step size (ie., the same

step Reynolds number). The results for fluctuating pressures in the shear layer, shown on Fig.7, indicate that the effect of the rear face of the cavity was to enhance the organization of the large scale structure of the shear layer, which for the rearward facing step case exhibited vortices of the "Brown and Roshko" type. However Ikawa and Kubota(1975) at Mach 2.47 and Wagner(1973) at Mach 5 found no evidence of these large scale structures in supersonic shear layers.

MacGregor and White investigated flow over short cavities (L/D=0.5-3) over a large Mach number range (0.3-3) to obtain estimates of cavity drag. They claim pressure oscillations can increase cavity drag by up to 250%, and found such oscillations over the entire Mach number range. This increase in drag is presumably due to the large scale unsteadiness in the flow tending to produce a larger vertical exchange of, amongst other flow properties, axial momentum, and hence higher time averaged pressures on the rear face of the cavity and so higher drag. They observed the discrete vortex shedding similar to that of Rossiter at subsonic Mach numbers and found that his theory fitted their data well.

Although the shedding of discrete vortices from the cavity leading edge has been observed at subsonic Mach numbers, it has not been observed over the complete Mach number range where oscillations are found to occur. Bilanin and Covert(1973) constructed a mathamatical model whereby oscillations are caused by shear layer instabilities (ie., disturbances in the shear layer which have grown, rather than being damped out) interacting with the trailing edge of the cavity. As in Rossiter's model, the trailing edge interaction leads to acoustic waves propagating upstream and completing the feedback loop. The empirical constants of Rossiter's formula are found analytically. Bilanin and Covert modelled the shear layer as an zero thickness vortex sheet, which according to Miles(1958) should be stable for free stream Mach numbers greater than $2\sqrt{2}$. Tam and Block(1978) improved upon this by taking shear layer thickness into account and analysing more rigorously the acoustic

radiation from the rear face. A summary of these theories is provided by Rockwell(1983). The Tam and Block theory was extended to supersonic flow by Zhang(1987) , whose flow visualization seemed to confirm the theory that the separated shear layer becomes stable for Mach numbers above about 2.7. However although these theories predict accurately the frequencies at which longitudinal modes can occur, they do not predict which of these modes in practice will dominate, nor the amplitude of the oscillations. However a clue to this may come from the work of Rockwell and Knisely. It seems from their work that the separated shear layer for the cavity flow chose as its dominant frequency, out of the possible resonant frequencies for that cavity, the one closest to the natural vortex shedding frequency (of the "Brown and Roshko" type). In other words, the cavity feedback mechanism seemed to effectively enhance the frequency which already existed in the shear layer. This is backed up by the results of Zhang(1987) who found the dominant frequency in his cavity flows remained effectively constant with cavity length (ie., out of possible resonant frequencies for each cavity, it seemed to "home in" on a particular preferred absolute frequency). These results are illustrated on Fig.8. These pressure fluctuations were noticed throughout the entire cavity, and were most intense on the rear face.

Heller and Bliss(1975) point out that the discrete vortices observed by Rossiter and the shear layer instabilities observed at higher Mach numbers are not necessarily different mechanisms. They contend that the discrete vortices are actually a manifestation of the shear layer instabilities, which at subsonic speeds are far more rapidly amplified and roll up into these vorticies.

Clark et.al.(1980) conducted a comprehensive series of experiments looking at fluctuating pressures over the entire cavity for a Mach number of 0.6 to 3.0 and L/D ranging from 5 to 10. They found at all positions a broad band frequency spectrum upon which was superimposed one or more peaks. Highest fluctuating pressures were found on the rear face of the

cavity. Although peaks were noticed over the entire Mach number range, the contribution of the peaks decreased with increasing Mach number.

Although the longitudinal oscillation mode (shear layer instability, longitudinal acoustic feedback) seems to dominate for most flow conditions, a different mode has been noticed for deep cavities. Plumbee et.al.(1962), East(1966) and Tam(1976) found evidence of a transverse mode in these flow conditions. A schematic of this mode is shown on Fig.9, and compared with the longitudonal mode. This transverse mode is a vertical acoustic mode in the cavity, where the air mass in the cavity acts in some way like a Helmholtz resonator. It is not clear whether natural shear layer instability is required to excite this mode, and if not it seems that quite high Mach numbers would be required to excite this mode in shallow cavities if the energy for the oscillations was to come from turbulent fluctuations within the shear layer. The reduced frequencies (fD/a), where f is the frequency and a the average speed of sound in the cavity, measured by East were in the range 0.15-0.20.

In summary, it is not clear from the literature whether cavity pressure oscillations are to be expected at Mach 9, the Mach number of the present study. The well documented longitudinal mode of shear layer instability and acoustic feedback should cease to exist above about Mach 2.7. However other investigators have found evidence of unsteadiness above this Mach number (eg., the Schlieren photographs of Ginoux et.al.(1968) at Mach 5.3). It seems that if oscillations do occur, they would be most severe on the rearward face. It also seems possible that transverse modes could be excited at the high Mach number of the present study. It is important to recognize any unsteadiness in the cavity flowfield as White(1971) showed that such pressure oscillations can substantially alter the heat transfer rate in the shear layer reattachment zone.

1.3 Background-Computational

Numerical modelling of cavity flows can yield enormous amounts of information about such flows that is difficult to obtain experimentally, and so is becoming increasingly popular. The main literature review for this field can be found in Chapter 6, but at this stage it is instructive to look at the status of such Navier-Stokes computations and the main problems in carrying them out.

Solution of the time dependent Navier-Stokes equations is essential for almost all cavity flowfields. At subsonic and low supersonic speeds, large scale unsteadiness of the flowfield is usual and time marching is obviously required. At higher supersonic Mach numbers time marching is also highly desirable in order to calculate subsonic and supersonic portions of the flowfield simultaneously, as the time dependent equations are always hyperbolic regardless of the flow velocity. Unfortunately solution of the time dependent equations tends to lead to large computational times before a steady or stationary state is established, and the finer the mesh, the smaller the time step that is allowed. Recent work by Baysal et.al.(1988) and Zhang(1987) demonstrate the capabilities of such methods in calculating supersonic cavity flows in two dimensions.

Baysal et.al. used a computational grid of 9000 cells for their Mach 1.5 computations and were able to capture the fluctuating flow characteristics and time mean pressures reasonably accurately (within about 15% of experiment). However shock waves did not seem to be accurately captured. Zhang used a slightly more coarse grid of about 6500 cells, and although his computations seemed to reproduce the basic flow physics correctly (in terms of bulk unsteadiness of the flowfield), his computations could not accurately predict the time mean pressures or the wave structures. These methods have numerical diffusion (due to the finite difference formulation) and artifical dissipation to damp oscillations near shock waves. It is important to ensure that these mechanisms do not swamp the

real viscous dissipation in the flow, and inaccurate capture of wave structures is an indication that this has not been achieved. In both of the above cases a simple turbulence model was used to relate the Reynolds stresses to the mean flow field, which was probably inadequate for a cavity flow situation.

Three dimensional cavity computations were attempted by Rizzetta(1988). These computations seemed to predict essentially the correct pressure field, and highlighted the highly 3 dimensional nature of planar cavity flows.

None of the above studies attempted to predict the cavity heat transfer rates. These are more difficult to predict than the cavity pressures because it is necessary to resolve accurately the boundary layers on the cavity walls. This then requires small numerical diffusion, a more elaborate turbulence model, and a finer mesh, and so much larger computational times. However laminar hypersonic separated flows can be modelled quite accurately, as shown by Power and Barber(1988) in their computations of flow over a compression step, where skin friction and surface heat transfer were found to agree quite well with experiment.

The approach of this study is then to start with a very high resolution Euler scheme, and to minimise numerical diffusion, so that the viscous features can be captured with fewer cells than would be otherwise necessary. Then a Navier-Stokes option will be added, and tested extensively for laminar flows where the viscous equations are exactly known. The next stage would be the addition and assessment of a turbulence model, but this is not regarded as an objective here.

CHAPTER 2

FACILITIES AND INSTRUMENTATION

2.1 The Imperial College No.2 Gun Tunnel

The No.2 Gun Tunnel is located on the ground floor of the Aeronautics Department of Imperial College, and a full description is given by Needham et.al.(1970) . The tunnel was last run 5 years previous to the beginning of this work, and so initially required considerable effort to restore it to an operational state, which was actually in itself one of the aims of the current work. This entailed not only replacing or repairing major parts of the equipment (eg., a new vacuum pump), but also "rediscovering" experimental techniques where expertise has been lost in the department in recent years (eg., the production of thin film heat transfer gauges). The important stages of this work are described in the following sections.

The schematic of the tunnel is shown in Fig.10 and its operational conditions in Table1. The low pressure condition is achieved using aluminium diaphrams and the high pressure condition using mild steel diaphrams. The nozzle produces a nominal Mach number of 9 which is slightly higher at high pressure due to decreased boundary layer thickness on the nozzle walls.

The steady run period is approximately 5 ms, and a typical tunnel total pressure trace is shown on Fig.11[a]. These data are taken for each run by a Kistler piezoelectric transducer mounted adjacent to the nozzle throat. A real gas correction factor was estimated for the total pressure values in the test section using the results of Cullotta and Richards(1970) . Thermodynamic equilibrium was assumed to have been achieved at the nozzle exit. Reynolds numbers are of the order of 0.5 million/cm. Since model lengths of the order of 1m will be used, this permits natural transition of the boundary layer, if desired, and

a. Due to the transducer mounting arrangement, high frequency components of the total pressure record are attenuated.

turbulent separation to be studied. The stream total temperature is 1070K, whereas the model will be at room temperature, so that highly cooled wall conditions will be simulated. This leads to a high transition Reynolds number, which Edwards(1981) found to be about 6 million on a flat plate.

The tunnel always requires two operators and strict safety procedures are maintained. The minimum turn around time is about 45 minutes.

2.2 Data Acquistion

Analogue signals from the test section were passed into the control room, the tunnel total pressure being fed straight into the digital recording system and model instrumentation signals through bridge-amplifier systems into the digital recorder. The previous digital sampling system was found to be inoperational and so a new system was purchased and installed. The new digital recorder is an expandable *Microlink* system which for this project recorded 6 channels of data simultaneously, each channel containing 4k samples, at a maximum sampling rate of 125kHz. This gives about 625 samples during the steady run time of the tunnel. The whole system is software controlled, and is triggered by the tunnel total pressure transducer. The digital recording system is connected through an IEEE interface to a BBC microcomputer which controls the system. Software in BBC basic was written to set up the data system and to unload the data after a run, and finally a graphics package written to display any part of the data on the screen. Numerical integration of the heat transfer data also took place on the BBC, and this is described in more detail in Section 2.6.2. A hard copy of graphical output was obtained by means of a screen dump to an EPSON printer.

2.3 Model Design

2.3.1 Axisymmetric or 2-Dimensional

Considering the wealth of data available on two dimensional cavities, it may seem at first that this would be the best geometry to study to allow a more direct comparison with the results in the literature. However several investigators, notably McDearmon and Zhang , found that supposedly two dimensional cavity flows in fact showed very strong three dimensional effects due to the presence of the side walls from subsonic right through to hypersonic Mach numbers. The boundary layers on the side walls were found to roll up into vortices which moved into the main flow. The results of McDearmon show clearly how cavity width could substantially change the mean pressure distrubution, thus casting considerable doubt on the validity of comparisons between different sets of "two dimensional" data. Considering that Johanneson and Charwat et.al. found no great differences between their axisymmetric and two dimensional results, it is probable that comparisons between axisymmetric and two dimensional studies are as valid as between two different sets of two dimensional data. Of course a disadvantage of an axisymmetric model is the reduced quality of the Schlieren flow visualization, but it was felt that this was far outweighed by the desire not to include "end effects", and so an axisymmetric model was chosen.

2.3.2 Forebody

A cone forebody was chosen mainly from the point of view of obtaining reliable boundary layer data (avoiding serious external effects, such as streamwise pressure gradient, which are difficult to document) at the point of separation into the cavity. A previous study by Lin and Harvey (1987) gives boundary layer data on a cone of 5^{o} semi angle at positions 620, 720, and 820 mm from the tip. Thus a 5^{o} semi angle cone forebody was chosen with the cavity positioned 720 mm from the tip. Following the cavity was a cylindrical afterbody, and a schematic of the entire model is shown on Fig.12.

At first glance it would seem simplest to have the approach flow parallel with the top of the cavity (ie., a cone cylinder forebody, with the cavity positioned some distance downstream of the junction). However, at this high Mach number, the Mach angle is very low and the recovery zone quite long, and so expansion waves from a cone cylinder junction on the forebody would inevitably interfere with the flow at the cavity. This would be highly undesirable in terms of limiting the usefullness of the study as a reference flow, and in terms of documenting an upstream boundary layer influenced by a strong pressure gradient, and so it was decided to make the expansion an integral part of the cavity configuration. Other advantages of the model to be used are ease of manufacture, and the fact that the conically developed boundary is already documented for this flow condition and geometry. Computations were carried out to obtain a rough assessment of the effect of the approach flow being angled at 5^{o} to the cavity, and it was found to reduce cavity pressures by a factor of about 2 compared with the parallel approach flow situation for the same free stream pressure. This dispelled worries that cavity pressures might be too low to measure experimentally. In fact, the effect of an expansion at the point of separation on a cavity flowfield is worth studying in itself in terms of simulating gaps between lifting and control surfaces on hypersonic vehicles.

The material for the cone forebody, except the tip, was aluminium. The screw on tip was machined from mild steel to give it greater hardness.

2.3.3 Cavity Dimensions

It appears from the literature that a fundamentally important parameter in determining cavity flows is the length to depth ratio, L/D, and so it was decided to vary this parameter over a reasonably large range ($0.8 < L/D < 2.4$), although only open cavity flows are expected for these values. This range of L/D was achieved with a 25mm deep cavity, and cavity lengths of 20, 30, 40, 50, and 60mm. The L/D=2.4 case was also achieved using a 12.5mm deep and 30mm long cavity. The cavity section of

the model, shown in Fig.13, was made of mild steel and was able to slide along a central member and lock into the cone forebody (which was also screwed into the central member). The rear bulkhead could slide backwards and fowards to change the cavity length. The cylindrical aluminium afterbody was fastened to the cavity section by four screws. The whole assembly was located rotationally by a locking pin through the afterbody and axially by two lock nuts behind the afterbody.

2.3.4 Model Support

In the test section of the Gun Tunnel, there exists a sting into which models can be inserted. The central member of the model was designed in such a way that it could be inserted through the sting and locked into position by two locking rings from the rear. Stress calculations were carried out to make sure that the model could withstand starting loads. The design load used was that of a badly asymmetric starting condition, with zero pressure across one side of the model, and pressure corresponding to conditions behind a normal shock on the other side.

The model was aligned by the equalisation of static pressure at three different circumferential positions on the model surface. An error of 2% was achieved for these readings. The final alignment was very close to the geometric alignment of the model with the bed on the floor of the test section.

2.4 Static Pressure Instrumentation

Pressure readings were taken using ENDEVCO absolute pressure transducers. Six were used rated at either 15 or 50 psi. Brass caps were machined to screw onto the transducers, which enabled them to be connected by a small length of plastic tubing to equally small lengths of copper tubing (ID 1.0mm) soldered to the model pressure tappings (also of 1.0 mm diameter). The set-up is shown on Fig.14. Care had to be taken not to "crimp" the plastic tube. The dead volume in the transducer/brass cap arrangement was about $22mm^3$. Tappings

at the same radius from the model centreline were placed at several different circumferential positions in the cavity to assess any non axisymmetric effects that might occur (as opposed to model alignment). The closest tapping to the top of the cavity was centred 2mm from the rear lip.

The entire cavity was instrumented, as well as the area immediately downstream of the cavity and the cone surface 30mm upstream of the cavity. Particular interest was payed to the top of leading and trailing faces of the cavity, as the top of the trailing face is where strong shear layer impingement can be expected, and the top of the front face is a possible region where any longitudinal cavity feedback mechanisms could be noticed (see Zhang(1987)).

The transducers were calibrated in position by sucking the test section down to a near vacuum, and then letting small amounts of air back in, with the transducer output and test section pressure being read about one minute after each closing of the exhaust valve to the test section. This was done prior to the start of the pressure measurements. The calibrations were found to be linear, with correlation coefficients greater than 0.999.

As will be discussed later, fluctuating pressures were found to occur on the rear face of the cavity. In order to study this phenomenon accurately, it was necessary to reduce the "dead" volume between the pressure tapping and the transducer, as it transpired that the Helmholtz resonance frequency of this volume (roughly 5kHz) was of the same order as the frequency of the fluctuations to be measured. It was decided not to flush mount a transducer directly because of fears for its safety under the starting conditions and also because of a loss of spatial resolution if this were done (the diaphram diameter of the transducer is 3.8mm), but instead to recess it 1mm from the surface behind a 1.5mm diameter pressure tapping. This setup gives a calculated Helmholtz resonance frequency of about 60kHz, which is still smaller than the basic transducer resonant frequency of 120kHz , but an order of magnitude above the likely frequencies to be measured.

2.5 Pitot Pressure Instrumentation

Pitot pressure measurements were required to check the upstream boundary layer documentation as measured by Lin and Harvey (1987). A pitot tube was manufactured in the department and is shown in Fig.15. This was clamped in the cavity section by the device shown in Fig.16, and the nose of the pitot tube protruded approximately 20mm upstream from the point of separation. Schlieren photographs taken earlier showed no discernible influence from the cavity on the upstream boundary layer. Although this is not a really sensitive measure of upstream influence, the literature does not indicate that any is to be expected, and in any case it was desired to measure the boundary layer in an "as is" condition. The position of the pitot tube could be moved about 10mm in the vertical direction, which was easily enough to measure a boundary layer about 6mm thick. The pitot tube itself was made of stainless steel with an initial inside diameter of about 1.13mm. The nose was flared out and squashed to give a vertical resolution of 0.4mm and the same cross sectional area as the tubing (2.8mm wide nose). It was considered that this vertical resolution would be adequate across a boundary layer which should be about 6mm thick at separation. The total height of the nose was 0.8mm.

As discussed later, the initial boundary layer study yielded results slightly different to those of Lin and Harvey. A second pitot tube was then constructed, twice as long as the first one to remove the clamp as far as possible from the point of measurement, and with a thinner nose (0.2mm internal height and 0.5mm total height) in an attempt to reduce blockage effects (if any significant blockage effects existed) and give better vertical resolution. The total width of the nose of this probe was 5.3mm, which gave a difference in height between its centre and edges of 0.05mm from the surface of the model.

The accuracy of the pressure measurements (static and pitot) is estimated as follows:

Gauge Calibration	± 1%
Amplifier Calibration	± 1%
Tunnel Running Conditions	± 3%
Spatial Errors	± 1%
TOTAL	± 6%

2.6 Heat Transfer Instrumentation

2.6.1 Gauge Design

The theory and operation of heat transfer gauges is given by Schultz and Jones(1973). For this study thin film gauges were chosen, as used previously in this department by Edwards(1981) and Lowder(1984) amongst others.

The substrate material chosen was quartz because of the uniformity of its thermal properties over a relatively wide temperature range. The Gun Tunnel has quite a short run time (total run time about 20ms), and the surface temperature of the gauge should not rise by more than about 15^{o}, which Edwards(1981) concluded would result in an error of no more than 4% if $\sqrt{\rho ck}$ for quartz was taken as constant at its room temperature value of 0.151 J cm^{-1} K^{-1} $s^{-1/2}$. The film material chosen was platinum because of previous experience in dealing with this material in the department. Silver paint was used to connect the platinum film to copper strips at the base of the gauge, onto which the connecting leads were soldered, as shown on Fig.17.

Schultz and Jones give an approximate analysis for the required substrate depth to be considered semi-infinite. This is defined as the depth at which the temperature and heat transfer should be less than 1% of their surface values, and their one dimensional analysis for constant heat flux yields

$$a > 40\sqrt{\alpha t} \text{ mm}$$

which gives the minimum depth of a=0.6mm in this case.

The quartz was ground and polished by the Optics Section of the Physics Department at Imperial College. Two different shaped gauges were used. For the front and rear faces of the cavity and on the cone surface, single cylindrical button gauges

were used as shown in Fig.17 . The measuring face was 3mm diameter and the length of the gauge 10mm, much longer than the 0.6mm required to be considered semi infinite. On the cavity floor a strip gauge was used 2mm thick, 3mm wide and 70mm long, as shown in Fig.18. Limitations of space underneath the cavity floor of the model (the metal wall thickness is only 5mm) meant that this gauge depth could not be more than 2mm thick, but this is still comfortably above the 0.6mm required. Thin platinum films were deposited at 5mm intervals on this gauge. All platinum films were deposited by a sputtering process in the Thin Films section of the Electrical Engineering Department at Imperial College.

Because the thermal properties of platinum films can vary from gauge to gauge, each gauge had to be calibrated separately. This was done in a heated oil bath, using a multimeter to measure gauge resistances at different temperatures over the expected operating range. A least squares method was then used to deduce the temperature coefficient of resistance, α_R, for each gauge. These least squares calculations gave a correlation coefficient of more than 0.999 for all gauges used, indicating little scatter in the calibration.

Each gauge is connected into one arm of a Wheatstone bridge curcuit, with output voltage proportional to resistance change. This resistance change can be converted directly to temperature rise, and then integrated to find the heat transfer rate.

Once in place, the gauges seemed to be quite robust. During the time they were used for measurements, which for each gauge was about 10 tunnel runs, the gauge resistances were found to increase by less than 1%. Repeatability was good, with run to run variations for the same gauge within the range of tunnel run to run variations. No dynamic or direct heat flux calibration of the gauges was carried out.

2.6.2 Digital Reduction of Data

The bridge output voltage (proportional to temperature rise) was digitized at a sampling rate of 125kHz, which was then integrated to find the surface heat transfer rate $\dot{q}$ using every

32nd sample point to reduce the computational time involved. Tests were made to prove the accuracy of this procedure, which showed that in terms of average heat flux over the steady run time of the tunnel there was a difference of less than 0.5% between integrating every data point and every 32nd data point.

A one dimensional analysis of heat flowing into a homogeneous solid yields

$$\dot{q}_s(t) = \frac{(\rho ck)^{1/2}}{\sqrt{\pi}\alpha_R E_o}\left[\frac{E(t)}{\sqrt{t}} + \frac{1}{2}\int_o^t \frac{E(t)-E(\tau)}{(t-\tau)^{3/2}}\,d\tau\right] \qquad 1.$$

where E(t) is the bridge output voltage at time t and E_o is the initial bridge voltage.

A numerical evaluation of the integral is possible but leads to problems at the singularity where $t=\tau$. There are various methods available for dealing with this singularity. Cook and Felderman(1966) approximate $E(\tau)$ in the region $t=\tau$ by a piecewise linear relation such that

$$E(\tau) = E(t_{i-1}) + \frac{E(t_i)-E(t_{i-1})}{\Delta t}(\tau - t_{i-1}) \qquad 2.$$

The finite difference formulation of Eqn.1 then becomes

$$\dot{q}(t_n) = \frac{(\rho ck)^{1/2}}{\sqrt{\pi}\,\alpha_R E_o}\left[\frac{E(t_n)}{\sqrt{t}} + \sum_{i=1}^{n-1}\left(\frac{E(t_n)-E(t_i)}{(t_n-t_i)^{1/2}} - \frac{E(t_n)-E(t_{i-1})}{(t_n-t_{i-1})^{1/2}}\right.\right.$$

$$\left.\left. + \frac{2\,E(t_i)-E(t_{i-1})}{(t_n-t_i)^{1/2}+(t_n-t_{i-1})^{1/2}}\right) + \frac{E(t_n)-E(t_{n-1})}{\Delta t}\right] \qquad 3.$$

We also know that at $t=0$, $E(t_o)=0$, so Eqn.3 simplifies to

$$\dot{q}(t_n) = \frac{2(\rho ck)^{1/2}}{\sqrt{\pi}\,\alpha_R E_o}\sum_{i=1}^{n}\frac{E(t_i)-E(t_{i-1})}{(t_n-t_i)^{1/2}+(t_n-t_{i-1})^{1/2}} \qquad 4.$$

A program, in BBC basic, was written to implement this. A constant heat flux of the form

$$T_s = \frac{2\dot{q}\sqrt{t}}{\sqrt{\pi\rho ck}}$$

was entered in the form of the surface temperature T_s and the program output was seen to give the correct value of $\dot{q}$.

A typical surface temperature trace and corresponding heat transfer trace are shown in Fig.19.

2.6.3 Errors in Heat Transfer Measurement

2.6.3.1 Variations in Thermal Properties of Quartz

As mentioned previously, the thermal properties of quartz have been assumed constant over the range of temperatures measured, and this is expected to give an error of no more than ± 4%.

2.6.3.2 Surface Temperature Discontinuities

The thermal properties of quartz are such that the heat transfer gauge will assume a temperature higher than that of the surrounding material under flow conditions. This surface temperature discontinuity can effect the thermal boundary layer by reducing the wall temperature gradient and thus the heat transfer at the wall. This is illustrated on Fig.20.

Kays(1966) investigated this effect for both incompressible laminar and turbulent boundary layers over a two dimensional flat plate. Winter(1976) extended this analysis to compressible flows, which yielded the following results

$$\frac{\dot{q}_s}{\dot{q}_c} = 1 + \frac{T_{w1} - T_{w2}}{T_r - T_{w1}} \left[1 + \left(\frac{L'}{x} \right)^{3/4} \right]^{-1/3} \quad \text{for laminar flows}$$

$$\frac{\dot{q}_s}{\dot{q}_c} = 1 + \frac{T_{w1} - T_{w2}}{T_r - T_{w1}} \left[1 + \left(\frac{L'}{x} \right)^{9/10} \right]^{-1/9} \quad \text{for turbulent flows}$$

where the variables are defined on Fig.21.

It can be seen that the error is worst in areas of high heat transfer (where $T_{w2}-T_{w1}$ is large) and for small gauges (where x is only just greater than L).

Assuming the model remains at room temperature, and ignoring axisymmetric effects, this analysis yields a 4% error for the button gauges for a 15^{o} rise in surface temperature. This error is in the negative sense (ie., underestimating the heat transfer rate), and is less applicable to the strip gauges on the cavity floor.

Lowder(1984) measured relatively high heat transfer rates (over 100 W/cm^2) in flare induced separated flows, and concluded that the above formula may have been an underestimate of the likely error in that situation. However the heat transfer rates expected in this study are much more modest, and so this analysis deemed to be adequate.

2.6.3.3 Heat Leakage from Gauge Edge

Another result of the gauge being at a higher temperature than the surrounding metal is that heat will leak from the edge of the gauge into the surrounding material, so that a transient one dimensional heat transfer analysis does not exactly model the true situation. To get an estimate of the error involved, the problem was broken up into two one dimensional heat transfer problems- heat transfer into the surface of the gauge, and heat transfer out of the sides of the gauge and into the surrounding metal. A full two dimensional analysis was not deemed necessary to obtain an estimate of the likely errors involved in neglecting heat loss from the gauge to the surrounding metal. A small program was written to solve these two one dimensional heat flow problems simultaneously. The gauge is exposed to a constant heat flux and the surrounding model is assumed to remain at room temperature. The two problems are time marched simultaneously, and the result, illustrated on Fig.22 in terms of gauge surface temperature after 15ms of run time, shows a less than 2% error (again in the negative sense) in the average temperature and hence heat flux across the gauge. In fact, the error will probably have been slightly overestimated as small

chamfers on the gauge surface mean that the thin film does not quite reach the metal interface, although these chamfers may lead to other errors.

2.6.3.4 Presence of the Surface Sensor Film

The equations for calculating heat transfer rate from surface temperature were derived assuming the surface temperature was not affected by the presence of the thin film. Even though the sensor is quite thin (vacuum deposited films such as these have thicknesses down to 0.1μm), the effect is a finite one. Edwards used the results of Schultz and Jones to conclude that the error for this type of gauge would fall within the generally accepted limit of 2% (again in the negative sense).

An estimate of the likely accuracy of the experiment can now be made, as is given below

Systematic Errors

Variation in thermal properties of quartz	± 4%
Due to surface temperature discontinuities	+ 4%
Due to heat leakage from gauge	+ 2%
Due to presence of surface sensor	+ 2%
	+ 12%
	- 4%

Random Errors

Gauge Calibration	± 1%
Tunnel Running Conditions	± 3%
Amplifier Calibration	± 1%
	± 5%

TOTAL	+ 17%
	- 9%

A plus sign indicates a correction that should be added to the experimental value. However all data presented subsequently are UNCORRECTED. Errors due to gauges not being mounted completely flush with the surface of the model are not included here as they are very difficult to quantify. This is discussed in more detail in Chapter 4.

2.7 Flow Visualization

A single pass Schlieren system is included in the test facility. A schematic is shown in Fig.10. The argon spark light source has a duration of 1μs, and is triggered by the tunnel p_o transducer located adjacent to the nozzle throat. A delay between trigger and spark is incorporated such that the photograph is taken during the steady run time of the tunnel. Horizontal cut off is used and the optical path is approximately 50 metres.

CHAPTER 3

PRESSURE MEASUREMENTS

3.1 Boundary Layer at Separation

It was decided to investigate the boundary layer just before separation with two objectives in mind. The boundary layer obviously can be expected to control the separation so knowledge of it is needed both for physical interpretation of the cavity flow, and also as a starting point in any numerical prediction. Transition takes place in the first third of the cone forebody so that the boundary layer at the point of separation is fully turbulent. As discussed in section 2.5, Lin and Harvey(1987) made boundary layer measurements on an essentially identical 5^{o} cone in the same test facility. The idea was to make enough independent boundary layer measurements to confirm their data.

3.1.1 Pitot Pressure

The raw data of pitot pressure against distance normal to the cone surface for the high Reynolds number running condition is shown in Fig.23 , and compared with the results of Lin and Harvey(1987) which were taken in the same tunnel for the same running conditions. There is a small but noticeable difference between the two sets of results, with the boundary layer measured by Lin and Harvey being slightly thicker, which is why a more comprehensive set of tests was carried out than originally planned. It was at first thought that this difference could be due to pitot blockage effects, or the proximity of the pitot clamp, and so a second longer, more slender nosed pitot tube, as described in section 2.5, was built. It was also hoped that this would alleviate the unusual "kink" in the data at about y=1.75mm, which was also noticed by Bartlett(1981) for a flat plate boundary layer, and seemed to be eliminated by probe redesign. However Fig.23 shows that apart from partially eliminating this "kink", the second pitot head gave virtually the

same results as the first. No measurements were possible immediately adjacent to the wall with the second pitot tube as its long unsupported length gave rise to vibrational problems in that area, as evidenced by low frequency oscillations in the pitot measurements. The mechanism for this vibration is not well understood, but would seem to be a wall interference effect.

As mentioned before, upstream influence from the cavity was not expected at the position where the boundary layer measurements were taken. The subsonic portion of the boundary layer at this Mach number and Reynolds number is very thin (less than 0.1mm thick) and is extremely unlikely to carry disturbances far upstream in a turbulent flow. Charwat et.al.(1961a) also found no evidence of upstream influence on the boundary layer just before separation even for Mach 4 cavity flows. In any case, the differences between the results of Lin and Harvey and those of the present study were also noticed in the outer part of the boundary layer, whose domain of influence lies well upstream.

Schlieren photographs, such as that shown on Fig.24, were taken of the flow around the original pitot tube in an attempt to see if it, or the probe support, was severely interfering with the boundary layer. It is difficult to tell from the photograph if there is any interference occuring, but none is obvious.

Misalignment of the model can also be ruled out as the cause of the discrepancy as the measurements were taken at several different circumferential positions. Indeed this is further proof of the accuracy of the original model alignment, as misalignment would have caused a thicker boundary layer on one side model than the other.

Although the pitot tube protrudes about 20mm upstream from the point of separation (in order to remove any upstream influence from the cavity), this shortening of the boundary layer development length is not sufficient, over a total development length of 720mm, to produce the differences observed between the two sets of results. In fact, as shown in Fig.25, the results of the present study are much closer to those

of Lin and Harvey at x=620mm. Pitot displacement errors are also unlikely to be the cause of the differences noticed. The results of Lin and Harvey were also uncorrected for displacement errors, which in any case could not explain the magnitude of the discrepancy noticed. Also, in the outer part of the boundary layer where displacement errors would be smallest, the differences in the two sets of results are still seen.

Bearing these facts in mind , and that the second pitot tube with a smaller inlet and the probe support twice as far away as the first gave virtually the same results as the first pitot, it is safe to assume that the discrepancy is not due to an upstream influence from the probe support or the cavity.

It was concluded that the difference in the two sets of results was most probably due to a difference in the position of transition in the two experiments. The physical position of the model in the tunnel can significantly affect the position of transition, due to disturbances emanating from the nozzle boundary layer. Thus if the model of Lin and Harvey was placed further upstream than that of the present study, transition would have occured earlier and thus the turbulent boundary layer would have had a different effective origin. The model position was kept fixed for the present study (with the cone tip 20cm upstream of the nozzle exit plane), but no information is available about the position used by Lin and Harvey.

3.1.2 Mach Number and Velocity Distributions

Pitot pressure was converted to Mach number through the Rayleigh supersonic pitot formula

$$\frac{p_t}{p_e} = \left[\frac{(\gamma+1)M^2}{2} \right]^{\gamma/\gamma-1} \left[\frac{\gamma+1}{2\gamma M^2 - (\gamma-1)} \right]^{1/\gamma-1}$$

with γ=1.4 for nitrogen.

The average cone static pressure p_c was measured to be 5290N/m^2 (0.77psi), and the static pressure was assumed constant across the boundary layer (ie., p_e=p_c).

The Mach number profile is shown in Fig.26. Taking account of differences in local static pressure (ie., run to run variations), the conversion to Mach number has reduced the difference between the two sets of data considerably.

To convert the Mach number profiles to velocity profiles, information about the temperature distrubution in the boundary layer is required. Usually, in the absence of measurements, an approximate relation linking temperature, velocity and Mach number based on the similarity between heat and momentum transfer is used. However, fortunately in this case the total temperature profile for the boundary layer at X=720mm has been measured and is given by Wang(1987) , and is used in this case. The difference in the pitot pressure profiles as discussed in 3.1.1 does not significantly affect the validity of the use of the total temperature profile to calculate the velocity, as the total temperature profiles seem to change quite slowly in the streamwise direction at this distance from the nose.

The velocity profiles can then be calculated from

$$\frac{u}{u_e} = \frac{M}{M_e} \left[\frac{T_o \left[1 + 1/2(\gamma-1)M^2 \right]}{T_{o_e} \left[1 + 1/2(\gamma-1)M^2 \right]} \right]^{1/2}$$

and the result is shown in Fig.27. It can be seen that, in terms of velocity, there is almost no difference between the results of this study and that of Lin and Harvey.

A few data points were also taken for the low Reynolds number boundary layer. These points, shown on Fig.28, indicate that, as expected, this boundary layer is slightly thicker than the high Reynolds number case.

3.2 Cavity Flows

3.2.1 Cavity Flow Structure

Using the results of flow visualization, pressure measurements, and information from the literature, an initial picture of the cavity flow structure can be built up.

Fig.29 to Fig.31 show Schlieren photographs of the cavity flow at the high Reynolds number condition for L/D= 0.8, 1.6, and 2.4. Obvious in all of these photographs is the reattachment shock at the trailing lip of the cavity. The pressure measurements to be shown later indicate that this shock is followed by an expansion fan, so that what exists at the trailing edge is a shock-expansion system. Also clearly visible for L/D=2.4, and less so for L/D=1.6 and 0.8, is a Prandtl-Meyer expansion which appears to emanate from the leading lip of the cavity. Thus the boundary layer at separation is rapidly expanded as it turns from its initial direction parallel to the cone surface to a direction approximately parallel to the cavity.

Unfortunately, due to the axisymmetric nature of the flow, the Schlieren flow visualization does not provide a clear picture of the flow inside the cavity. However it is known from the literature that cavity flows with these values of L/D will definitely be of the open type (ie., the shear layer reattaches to the rear face of the cavity and not to the cavity floor) which is consistent with the reattachment shock, and from the pressure measurements it will be seen that the shear layer reattaches somewhere in the region $y/D<0.25$ on the rear face for all the cavity lengths studied, where y is the distance down the rear face of the cavity with its origin at the rear lip.

The shape of the captured vortex within the cavity depends upon L/D. The results of other investigators (eg., Stallings and Wilcox (1987) and Zhang(1987)) show that for supersonic flows with L/D less than 1 the captured vortex is a single vortex, whereas for L/D greater than 2 two vortices are present. Of these two, the trailing edge vortex has by far the greater rotational strength. Between L/D=1 and L/D=2 the vortex structure is in a state of transition.

Using all this information, a schematic of the anticipated flowfield can be constructed and is shown on Fig.32.

3.2.2 Mean Static Pressures

Static pressure measurements around the cavity and on the afterbody were made for a 25mm deep cavity with L/D of 0.8, 1.2, 1.6, 2.0 and 2.4 at both the high and low Reynolds number running conditions. Measurements were also made for a 12.5mm deep cavity with L/D=2.4 at both Reynolds numbers.

The mean static pressure at a position was taken to be the time averaged pressure during the steady run time of the tunnel. These pressures are initially normalized by the static pressure on the cone just before separation, p_c, which was measured to be on average 0.77psi (5290N/m^2). The horizontal coordinate X_* is the total distance from the point of separation down the front face of the cavity, along the cavity floor, up the back face of the cavity, and along the afterbody (ie., the distance around the cavity periphery). This is illustrated on Fig.33 . A typical pressure-time trace is shown on Fig.34[a], and compared with the tunnel total pressure trace. The pressure-time traces indicate that the cavity pressures have reached a stationary state during the steady run time of the tunnel, which is in agreement with our expectations of physical response times. To assess this response time, we can consider a viscous disturbance in the boundary layer propagating upstream at, on average, say 1/2 the free stream velocity (~700m/s), would take about 1ms to travel from the tip of the cone to the cavity. Now the steady run time (where the measurements are taken) does not begin until about 15ms after the tunnel fires, so there is plenty of time for the flow on the forebody to reach a steady state. It is more difficult to estimate the time needed for the cavity flow to reach a steady state, but if an average cavity velocity of 10% of the free stream velocity is assumed (Krisnamurty(1955) measured cavity velocities up to 40% of the free stream), then a disturbance would take 0.8ms to travel around the cavity periphery, which is still only a small fraction of the total running time. In fact, this is really an estimate of the time

a. Due to the transducer mounting arrangement, high frequency components of the total pressure record are attenuated.

required for the cavity flow to reach equilibrium in terms of its viscous nature. Pressure equilibrium in the cavity is actually achieved by the propagation of acoustic waves at the local speed of sound (which is probably somewhat greater than the typical viscous convection velocity in the cavity), so that the time required to reach pressure equilibrium is even less than this.

The static pressure tappings were placed in a spiral around the circumference of the cone as a further check on the alignment of the model. Tapping locations can be seen in Appendix 1.

3.2.2.1 General Observations

Fig.35. to Fig.39. show the results for L/D=0.8 to 2.4 at both the high and low Reynolds numbers, with pressure normalized by the cone pressure p_c. The most noticable feature is the impact recovery pressure on the top of the rear face (ie., in the area of shear layer reattachment), which has been noticed by all other investigators and which is seen for this experiment to generally increase with increasing cavity length. Fig.40 plots peak recorded reattachment pressure (at the top of the back lip, y/D=0.08) against L/D. The rapid drop in pressure moving downwards along the rear face implies considerable cavity velocities in this region. Partial pressure recovery then occurs at the bottom of the back face. Along the cavity floor the direction of the pressure gradient is such that the flow once again seems to accelerate (in the reverse flow direction), the pressure reaching a minimum near the middle of the cavity floor and partially recovering again near the bottom of the front face. This minimum in floor pressure most probably lies under the primary vortex core. Pressures along the front face are relatively constant.

Apart from the area of shear layer reattachment, cavity pressures are generally below those recorded on the cone forebody before separation, with pressures on the floor and the front face on average 0.62 times the cone pressure. Investigators of two dimensional planar flows and axisymmetric flows with the cavity floor parallel to the forebody, have found these floor

and front face pressures approximately equal to the static pressure on the forebody, and hence also approximately equal to static pressure in the shear layer since the expansion at separation is quite weak for such flows. The present results are compared on Fig.41 with the two dimensional planar results of McDearmon(1960) at M=3.55 and L/D=2.19, where p_c for McDearmon's results is the forebody pressure. A comparison with results at lower Mach numbers seems reasonable as cavity pressures show only a weak Mach number dependence (see Lamb(1981)), with reattachment pressures generally increasing with increasing Mach number. It can be seen from this comparison that the floor pressures in McDearmon's results are slightly greater than the forebody pressure, whereas in the current experiment they are on average 0.62 times the forebody pressure. The effect of the shear layer expansion at separation in the current experiment is then, by comparing the floor pressures, to reduce the static pressure in the shear layer, and cavity pressures in general, by about 40%. In the external Mach 8 flow, a 5^o expansion (to align the flow with the cavity geometry) would reduce the static pressure by about 65%. In reality this full effect is not felt at the cavity because the Mach number values and the boundary layer thickness mean that the flow has a "relaxation" length several times the cavity length, and the static pressure will only reach this theoretical value far downstream. These effects are analysed in more detail in Chapter 5.

Peak reattachment pressure in the present work can be compared with the results of other studies if it expressed as a ratio of peak recovered pressure to minimum floor pressure, as this minimum floor pressure has been seen by many authors (eg., Stallings et.al. (1987)) to be approximately equal to the static pressure in the shear layer. This normalization procedure then makes an allowance for the 5^o expansion at separation in the present study. For the L/D=2.4 case, we have $(p_{max}/p_{min})=3.65$, which can be compared with the results of McDearmon where $(p_{max}/p_{min})=2.13$ at L/D=2.19 and M=3.55. p_{max} was taken in the

same position in both cases (y/D=0.08 on the rear face). It is not surprising that p_{max}/p_{min} should be greater for the present study than for the results of McDearmon as Charwat et.al. (1961a) showed that this ratio rises with increasing Mach number. The effect of the expansion at separation is discussed in more detail in Chapter 5.

3.2.2.2 Dimensional Analysis

A dimensional analysis can be carried out on the cavity flow to illustrate the parameters governing the flowfield. Fig.42 shows the fundamental layout. Assuming that 3 dimensional effects can be neglected, the pressure at any point in the cavity can then be described by

$$p(x,y,t) = fn(x,\ y,\ t,\ L,\ D,\ \varphi,\ \delta,\ \vartheta,\ p_e,\ \rho_e,\ T_e,\ u_e,\ \mu_e,\ T_w,\ \gamma,\ k_e,\ r)$$

where δ and ϑ denote the displacement and momentum thicknesses of the upstream boundary layer respectively.

Buckingham's theorem states that the number of independent dimensionless groups is equal to the number of independent variables minus the number of fundamental dimensions (here length, mass, temperature and time). Typically the thirteen dimensionless groups in this case could be

$$(x/L),\ (y/D),\ (tu_e/L),\ (\rho_e u_e \delta/\mu_e),\ (\delta/D),\ \delta/\vartheta,\ (u_e/(\gamma p_e/\rho_e)^{1/2}),$$
$$(T_e/T_w),\ (L/D),\ \varphi,\ \gamma,\ \frac{\gamma p_e \mu_e}{(\gamma-1)\rho_e T_e k_e},\ D/r$$

From past experiments it is clear that L/D is a fundamentally important parameter in determining the cavity flow. $(\rho_e u_e \delta/\mu_e)$ is a Reynolds number (several could have been chosen), $u_e/(\gamma p_e/\rho_e)^{1/2}$ is the Mach number, $\gamma p_e \mu_e/((\gamma-1)\rho_e T_e k_e)$ is the Prandtl number (which can be regarded as constant during this experiment), and tu_e/L is a non-dimensional time or inverse frequency that characterises any unsteadiness in the flow. Heat transfer is obviously dependent on T_e/T_w, which again is nearly constant for the experiment. Other researchers have found that the upstream boundary layer thickness, characterised by δ/D or

δ/L, is important in determining conditions in the area of shear layer reattachment. The parameter δ/ϑ is a type of shape factor for the boundary layer just before separation, and is determined by the growth of the boundary layer along the forebody. Strictly, there are several other thicknesses (eg., energy) needed to describe the boundary layer. In reality, however, this are not all important and can probably be described as unique functions of δ and ϑ given the near zero pressure gradient development of the boundary layer. Axisymmetric effects are characterized by D/r, where r is the body radius.

3.2.2.3 Effect of L/D

Fig.40 shows pressure at y/D=0.08 (ie., near the top of the back face) plotted against L/D. At both high and low Reynolds numbers these pressures rise steadily, and then at high Reynolds number appear to level out between L/D=2.0 and L/D=2.4. Stallings et.al.(1987) also commented on this rise of peak pressure with L/D at relatively low values of L/D. They speculated that this rise and subsequent levelling out of peak pressure was due to the flow structure changing from a single vortex to a double vortex system, as illustrated on Fig.5, with rising L/D. According to their argument, the levelling out of peak pressure at around L/D=2.0 would then correspond to the stabilization of the two vortex system. Although the flow structure does undoubtedly change from a one vortex to a two vortex system with increasing L/D, it seems unlikely that this is the cause of the rise and subsequent levelling out of peak pressure with increasing L/D.

An alternative explanation is found by looking at the physics of the shear layer as it grows into the cavity, as illustrated on Fig.43 and discussed in connection with the effect of Reynolds number (and analysed later in section 5.2). We will now briefly digress to discuss the physics of the development of a free shear layer from an initial boundary layer, which is essential to understand the following discussion. As a boundary layer separates, a new shear layer grows into the bottom of the original boundary layer velocity profile. Moving downstream,

this shear layer gradually "consumes" the original boundary layer profile until, at some distance after separation, the detail of the original boundary layer profile is lost, and the shear layer spreads thereafter at an essentially constant rate. This asymptotic spreading rate is dependent on many parameters, most notably the Mach number and Reynolds number of the free stream. The initial spreading rate of the shear layer (before the asymptotic state is reached) is much greater than the asymptotic rate, as shown on Fig.43.

This knowledge of free shear layer development can now be applied to the cavity flow situation. At low values of L/D the bottom edge of the shear layer just impinges on the top edge of the rear face of the cavity. Increasing cavity length allows rapid growth of the shear layer towards its similarity velocity profile, and so streamlines from further outboard in the shear layer carrying higher momentum fluid impact upon the rear face, raising the reattachment pressure. However once the shear layer has reached its similarity mean velocity profile (in terms of mean velocity, this is approximately an error function profile), or approaches it, the shear layer spreads thereafter quite slowly at an essentially constant rate, and so peak pressure levels out with further increasing of cavity length.

Apart from peak pressures, changing L/D does not seem to significantly affect pressures in the remainder of the cavity. This is consistent with the results of other investigators.

3.2.2.4 Effect of Reynolds Number

The results for the two different Reynolds numbers are not greatly different except that the peak impact recovery pressure is slightly lower for the low Reynolds number case for the shorter cavities, as shown on Fig.40, and slightly higher for the longest cavity. This reversal in trend with increasing cavity length on Fig.40 is not unambiguous, as it is evident only for the L/D=2.4 measurements, and the difference between these points is almost within the accuracy of the measurements. However it is believed that this trend reversal is real, as peak

heat transfer measurements to be presented in Chapter 4 (and shown on Fig.57) illustrate this effect more clearly. The fact that peak p/p_c for the low Reynolds number case is slightly lower than for the high Reynolds number case for the shorter cavities suggests a faster shear layer spreading rate at high Reynolds number for the shorter cavities. This is because a faster spreading rate implies higher velocities on the dividing streamline (ie., the streamline which reattaches near the top of the rear face) and hence larger recovery pressures near the top of the rear face. The trend observed for p/p_c for the longest cavity is the opposite to that of the shorter cavities, and implies a larger spreading rate for the low Reynolds number flow. This is the trend observed by Charwat et.al.(1961b) for longer cavities.

One possible explanation for the apparent change in Reynolds number dependence with increasing cavity length is that the low Reynolds number flow could still be showing the effects of transition, which takes place significantly later than for the high Reynolds number flow. The separated low Reynolds number shear layer might then initially be spreading slower because of this effect, but at the same losing its history effects from transition as it develops, such that by the time of reattachment for the longest cavity it has actually spread further than the high Reynolds number shear layer.

Another possible explanation is the effect of the initial boundary layer thickness at separation. The high Reynolds number boundary layer is thinner, and so the separated shear layer can more quickly "swallow" the initial boundary layer profile to reach its self-similar velocity profile and spreading rate (an error function velocity profile, as will be discussed in more detail in section 5.2). This is illustrated on Fig.43. The evidence is that the shear layer will adjust to this velocity profile quite quickly (see Mach 5 free shear layer measurements by Wagner(1973)). Hence the low Reynolds number shear layer will initially have a smaller spreading rate because of the thicker initial boundary layer. However the low Reynolds number

shear layer will probably have a higher asymptotic spreading rate (see Charwat et.al.(1961b)), and so further downstream will start to spread faster as it approaches the self similar velocity profile, thus explaining the change in Reynolds number dependence with increasing cavity length. The measurements of Charwat et.al. were taken well downstream after the shear layer probably had reached its self-similar profile.

Although both of the above explanations seem reasonable, it is considered that the second is more likely to have the greatest effect as the boundary layer measurements pointed to a thickness change from high to low Reynolds number while not showing any definite evidence of transitional effects on the velocity profile of the low Reynolds number boundary layer.

3.2.2.5 Effect of δ/D

As will be discussed in Chapter 5, reattachment pressures are mainly governed by boundary layer thickness δ and cavity length L (Lamb(1981) used δ/L as a correlating parameter), and so should be relatively independent of cavity depth D. However a second cavity of smaller depth 12.5mm (ie., half the initial value) was studied at L/D=2.4 to see whether cavity pressures away from reattachment are affected by the parameter δ/D. This also changes the axisymmetric parameter D/r, but this effect should be minimal. Results for the shallow cavity are given on Fig.44, and compared with the D=25mm cavity on Fig.45, together with the results of McDearmon. The shallower cavity exhibits slightly higher pressures away from reattachment, but this is probably due to the fact that this cavity is shorter (L=3cm, as opposed to L=6cm for the deeper cavity), and so the geometry of the expansion fan at separation and associated shear layer "relaxation" has meant that the separated shear layer for the shorter cavity has not experienced the same pressure drop as has the shear layer for the longer cavity. In other words, in the case of the short cavity the "relaxation" length of the expansion is relatively longer. This is confirmed by looking at the results for the L=3cm, D=2.5cm cavity (Fig.37), which shows nearly the same pressures away from reattachment (eg., on the cavity floor) as the L=3cm, D=1.25cm cavity (Fig.44).

3.2.3 Fluctuating Pressures

As discussed in Chapter 1, fluctuating pressures in the cavity caused by shear layer instabilities will theoretically not occur for free stream Mach numbers above $2\sqrt{2}$ (Miles(1958)) . However in the present study strong pressure fluctuations in the region of shear layer reattachment on the top of the back face were noticed. A typical trace is shown on Fig.46. Model vibration tests were performed, using accelerometers attached to the model surface, to find the natural frequencies of vibration. These frequencies (0.29kHz in the vertical direction and 0.25kHz in the horizontal direction) were found to be much lower than the pressure fluctuation frequencies recorded, so that model vibration could be ruled out as a possible cause.

The transducer frequency response is modified by the mounting system used. In the data of Fig.46, the transducer was connected to the tapping by a cap-tubing arrangement which would provide a low pass filter frequency of a few kHz at best. To overcome this, the data were repeated using the nearly flush mounted arrangement described in section 2.4. The centre of the flush mounted transducer was positioned at y/D=0.20 below the top lip on the rear face of a cavity with L=6cm and D=2.5cm, and a typical pressure trace over the steady run time is shown on Fig.47. A non dimensional time tu_∞/L is used, as discussed in the dimensional analysis. To determine the extent of vertical shear layer movement required to produce the observed peak to peak pressure fluctuations on the rear face, the experimental time averaged pressure gradient along the rear face can be used. Fig.39 indicates this pressure gradient to be about - $0.4p_c$/mm in the reattachment region. The maximum peak to peak fluctuation on Fig.47 is about $0.8p_c$, indicating that the shear layer oscillating 1mm about its mean position could produce the observed fluctuations. This is quite a small magnitute, and would indicate that no large scale unsteadiness of the flow is occuring.

The pressure-time trace on Fig.47 indicates a low frequency oscillation to be dominating, and to gain a better insight into

this phenomenon it was decided to perform a Fast Fourier Transform on the data. This presented a considerable problem in that the steady run time of the tunnel was far too short for the results of one run to yield any useful answers. A Fast Fourier Transform program, written in BBC basic, was thus modified in such a way that blocks of data, taken from different runs, could be processed separately and the results averaged, thus effectively increasing the total sample time. Sixteen sets of data were recorded and processed in this way. The error in processing data over a total run time of Δt is given by Zhang(1987) as

$$\varepsilon_t = \frac{1}{\sqrt{B_e \, \Delta t}}$$

where B_e is the bandwidth of the spectral window used, limited in this case to 244Hz by the length of each individual data trace. The total run time Δt is the data length of each individual run times the number of runs averaged. Thus if 16 runs are averaged, then the maximum error at each frequency is 17.9%.

The resulting plot of spectral power (energy per bandwidth) against frequency is shown on Fig.48. It is obvious that most of the energy is at relatively low frequencies and there seems to be a broad band feature centered on about 2.8kHz. This also corresponds approximately to the frequency below which half of the total energy lies. The vertical scale is spectral power per bandwidth normalized by the maximum of this value. Although the feature at 2.8kHz is not much greater in magnitude than the accuracy of the analysis, it is possible by looking closely at the pressure time trace of Fig.47 to see the low frequency peaks that correspond to this frequency. This frequency can be non-dimensionalised, either by using a streamwise length scale (normalizing by streamwise convective properties) to give

$$\frac{f \, L}{u_e} = 0.12$$

or in the transverse direction (normalizing by transverse acoustic properties), if the temperature in the cavity is assumed

to be 700K for the purposes of calculating the local speed of sound (which was indicated by preliminary computations),

$$\frac{f\ D}{a} = 0.12$$

The fact that these values are equal is purely coincidental. The first of these non-dimensional frequencies would characterize any longitudinal oscillation mechanism, where disturbances are convected downstream. The second would characterize any transverse acoustic mechanism in the cavity.

Zhang(1987) also noted a broad band low frequency oscillation experimentally and computationally for his experiments at Mach 1.5 and 2.5 which corresponded to a transverse Strouhal number of Str=0.20. East(1966) recorded transverse Strouhal numbers smaller than this in subsonic flow, and found these Strouhal numbers to be dependent on L/D. However the more dominant higher frequency modes caused by shear layer instabilities coupled with longitudinal acoustic feedback which were also noted by Zhang amongst others , and characterized by longitudonal Strouhal numbers in excess of 0.5, are not noticed in the present experiments. This is not surprising since, as discussed earlier, the shear layer should be free of large scale instabilities for free stream Mach numbers above $2\sqrt{2}$ according to Miles(1958), and this also fits in with the magnitude of the fluctuations.

As discussed in the Chapter 1 , there are considered to be basically two different mechanisms which can produce periodic pressure fluctuations in an open cavity flow, and these mechanisms often interact with each other. Firstly, the longitudinal mechanism consists of the separated shear layer rolling up into vortices which convect downstream at roughly 60% of the free stream velocity and interact with the downstream edge of the cavity. This interaction results in the propagation of acoustic waves upstream in the cavity which reach the front face an initiate the shedding of another vortex, thus closing the feedback loop. This mechanism tends to dominate for long cavities (L/D>1 or 2) and low speed flows

($M<2\sqrt{2}$), as shear layers are theoretically stable above this Mach number, and so will not roll up into vortices. Secondly, the transverse acoustic mechanism consists of a normal acoustic resonance in the cavity, where the mass of gas in the cavity behaves like a Helmholtz resonator. This mode tends to dominate in deep cavities, and may be possible in high speed flows.

It seems that the low frequency flow oscillation observed experimentally in the present study cannot be caused by a longitudinal feedback of the type proposed by Rossiter(1966) amoungst others, as the frequency is too low (longitudinal Strouhal numbers for these modes are greater than 0.5). The magnitude of the oscillations is also to small for such large scale unsteadiness to be present, and there is no other experimental evidence of this oscillation mode occuring at high supersonic or hypersonic Mach numbers. Turbulent fluctuations within the shear layer will contribute to some low frequency unsteadiness (see Wagner(1973)), but these fluctuations will presumably be unstructured, and Wagner's results show no evidence to refute this. Although the unsteadiness in the present study is of a broadband nature, there does seem to be some structure present. The magnitude of the pressure fluctuations also seems to be too large to have been caused entirely by turbulent fluctuations, given that it is the low velocity part of the shear layer that is reattaching (see again Wagner(1973)).

Zhang(1987) attributed the low frequency broad band oscillation in his experiments to the captured vortices moving around by a small amount. This would also move the shear a small amount, and given the small amount of shear layer movement needed to produce the observed pressure fluctuations, this must be a possible cause of the oscillations in the reattachment region of the current experiment.

Another possibility is a transverse (normal) acoustic oscillation, and there is other theoretical and experimental evidence to support this. East(1966) measured transverse

acoustic modes at subsonic Mach numbers in a two dimensional cavity. Then, adapting the solution for acoustic resonance in an open ended pipe, he concluded that a formula of the form

$$\left(\frac{f\,D}{a}\right)\left[1 + A\left(\frac{L}{D}\right)^{B}\right] = 0.25$$

would give an accurate prediction of acoustic modes in cavities. Using A=0.65 and B=0.75, he found extremely good agreement between the experimental and theoretical results over a surprisingly large range of L/D. If this formula is used here, it yields a result of (fD/a)=0.11, which is quite close to the experimental result of 0.12.

Tam(1976) solves the acoustic equations for the normal acoustic mode of a two dimensional cavity. His results show that the normal acoustic modes are damped, with the damping increasing with L/D. This means that continuous energy input is required to excite these modes, which he assumes comes from a fluctuating shear layer or turbulent fluctuations within the shear layer. In any case this implies that normal acoustic modes, especially for L/D>1, are more likely to be excited at high Mach numbers. At Mach 8 the shear layer should be stable, so it is assumed that the energy comes from turbulent fluctuations. However once the normal acoustic mode has been excited, it seems likely that it would force the shear layer to oscillate slightly (although these oscillations would not grow naturally). This then could give rise to the large pressure oscillations noticed in the reattachment region on the back face of the cavity.

In summary, the observed pressure fluctuations in the cavity seem to be the result of a complex interaction of different phenomena. Central to this is the behaviour of the separated shear layer, but whether this involves any "resonant" phenomenon is not certain. The shear layer only needs to oscillate by a small amount about its mean position to produce the pressure fluctuations noted in the reattachment region. This

shear layer oscillation could be due to movement of the captured vortices, or possibly a transverse acoustic oscillation. The existence of these oscillations may be important in terms of peak reattachment heat transfer rate as White(1971) showed how broad band unsteadiness could increase this heat transfer.

CHAPTER 4
HEAT TRANSFER MEASUREMENTS

4.1 Cone Forebody

The button gauges described in section 2.4 were not actually designed specifically for measuring heat transfer on the cone surface as the gauge measuring surface was not contoured to the curved shape of the cone surface. However other investigators (eg., Lin and Harvey(1987)) have used similar flat gauges on surfaces with roughly the same curvature as this model without incurring large errors, as can be seen by comparing their data with that of Hopkins et.al.(1969). Thus, bearing this in mind, it was decided to insert two gauges on the cone surface at a position 20mm upstream from the cavity in order to check the data recorded by Lin and Harvey for the same angle cone and the same running conditions.

Both gauges were fixed into the model with araldite, and returned values of heat transfer rate for the high Reynolds number running condition in good agreement with each other with the average being 5.56 W/cm^2. This can be normalized by conditions at the edge of the boundary layer to produce the local Stanton number given by

$$St_e = \frac{\dot{q}}{\rho_e u_e C_p (T_{aw} - T_w)}$$

where T_{aw} is the adiabatic wall temperature.

Assuming the model remains at room temperature, this returns a value of $St_e = 2.34 \times 10^{-4}$. This does not agree well with the average value recorded by Lin and Harvey of 9.7 W/cm^2 which corresponds to $St_e = 4.10 \times 10^{-4}$. Upstream influence from the point of separation is discounted as a possible cause of this discrepancy as the two dimensional results of Nestler et.al.(1968), who made several measurements upstream of separation, showed no evidence of such an influence. The results of Lin and Harvey seem to agree quite well with those of other investigators (eg., Hopkins et.al.), so this pointed to an error in

the mounting of the gauges in the current experiment. In fact, the midpoints of the two gauges used were found to be recessed from the surface by a small amount of 0.1mm. Another gauge was then inserted into the model at a distance 50mm upstream from the point of separation, with great care being taken during the mounting process to ensure that the gauge was not recessed from the surface.

This gauge gave a heat transfer rate for the high pressure condition of 9.18W/cm^2, St_e= 3.86x10^{-4}, which is within 6% of the average result of Lin and Harvey. The conclusion of this experiment is that gauge mounting is very critical to the accuracy of the experiment, especially if gauges are recessed from the surface, and that great care must be taken during the mounting procedure. By implication, heat transfer measurements made on curved surfaces should, if possible, be made with gauges contoured to the surface shape. Edwards(1981) also noticed large sensitivity to the location of button gauges in his experiments on a turbulent boundary layer on a flat plate. He found that a gauge location error of ±0.15mm gave a factor of up to 3 scatter in the data.

The results for the low pressure running condition gave a cone heat transfer rate of 3.10 W/cm^2 , St_e=4.86x10^{-4}. The Reynolds number dependence for an attached turbulent flat plate boundary layer gives $St_e \sim R_e^{-1/5}$. Assuming this Reynolds number dependence is similar for cone boundary layers (see Hopkins et.al.), one would then expect the Stanton number on the cone surface for the low Reynolds number case to be a factor of 1.28 above that of the high Reynolds number case. In fact it is 1.26 times the Stanton number for the high Reynolds number case.

4.2 In the Cavity

Fixing the button gauges into the flat surfaces of the cavity was a considerably easier task than for the curved surface of the cone forebody. The front and rear face modules of the cavity are detachable and so placing each module face down on a flat surface allowed the gauges to be inserted to a considerable degree of accuracy. It was necessary to positively force the gauges in position throughout the whole time the araldite was drying otherwise the drying process pulled the gauges into a slightly recessed position.

The pressure distribution inside the cavity showed a relatively smooth variation as L/D was varied between 0.8 and 2.4, so that it was decided to make heat transfer measurements at L/D=0.8, 1.6 and 2.4 only. Peak heat transfer measurements were also made at L/D=1.2 and 2.0. Limitations of space on the cavity floor meant that unfortunately only 3 gauges could be connected on the quartz strip on the floor.

4.2.1 General Observations

An example of a temperature and corresponding heat transfer trace was shown on Fig.19. The heat transfer rate seems to have reached a stationary state by the steady run time, which was also in agreement with our expectations of physical response times as discussed in relation to the pressure measurements in section 3.2.2. Although there was some evidence of unsteadiness in the heat transfer results in the reattachment region, the procedure used to integrate only every 32nd point to find the heat transfer rate, effectively reducing the sampling frequency to 3.9kHz, meant that a frequency analysis of the data was not possible.

Fig.49 to Fig.51 show the heat transfer rates inside the cavity normalized by the cone heat transfer rate. The variable X_* is the same as that used in the presentation of the pressure measurements. The form of the results bears a strong resemblance to the pressure measurements (see Figs 35-39), indicating a correlation between pressure recovery and heat

transfer rate. This will be discussed in more detail in Chapter 5. As with the pressure measurements, the highest heat transfer rates were recorded in the region of shear layer impingement (ie., the top of the rear face of the cavity). The highest heat transfer rate recorded was 23.24 W/cm^2 (St_e=1.02x10^{-3}) at the point closest to the back lip for L/D=2.0. This is 2.53 times the value on the cone forebody. Also in accordance with the pressure measurements, peak heat transfer rates rise from low values of L/D and seem to level out at higher values, as shown on Fig.52, and there is a strong Reynolds number dependence evident.

Figs 49 to 51 show heat transfer rates falling with distance down the back face and out of the reattachment region, and then rise slightly approaching the floor, which is also what the pressure measurements shown on Figs 35 to 39 indicated. For the short cavity (L/D=0.8), the heat transfer rate on the cavity floor is approximately equal to that near the intersection of the back face and the floor, while the longer cavities show the heat transfer dropping continuously along the floor to quite a low value at the intersection with the front face. The reason for this could be that in the case of the longer cavities, the flowfield has settled to a two vortex system, with the second vortex of much lower rotational strength sitting in the front half of the cavity. This change from a one vortex to a two vortex system was discussed in Chapter 3, and is illustrated on Fig.5. The second upstream vortex in the longer cavities would induce lower velocities in the upstream corner and hence lower heat transfer rates.

A "bump" is noticed in the heat transfer distribution on the front face of the cavity. This was also evident in the results of White(1971), but he offered no explanation. However if the secondary vortex is relatively small compared with the primary vortex, and if it is positioned as illustrated on Fig.53, a secondary stagnation region could occur on the front face and cause the bump noticed in the heat transfer distribution, with the heat transfer rate reducing to nearly zero where the flow

separates at the top and bottom of the front face. This also raises the question as to whether the heat transfer rate should be nearly zero at the downstream corner. The computations in Chapter 6 indicate this to be the case, and presumably the reason the experimental results did not positively indicate this was that there were no gauges close enough to the corner, although the results on Fig.50 and Fig.51 show the start of the trend on closer inspection.

The relatively low heat transfer rates on the cavity floor and front face agree with the conclusion of Lowder(1984) that a region of separated flow effectively insulates the wall from the higher heat fluxes in an attached flow. However where the flow reattaches the heat transfer can be considerably greater than the attached value (here the peak recorded value is about 2.5 times greater than the attached value for the longest cavity).

4.2.2 Effect of Reynolds Number

Figs 54 to 56 show the heat transfer results converted to Stanton number. This indicates quite good Stanton number correlation between the high and low Reynolds number running conditions, with the exception of peak heating rates in the shear layer reattachment region. Fig.57 records peak recorded Stanton number (occuring on the rear face at y/D=0.08, ie., the gauge closest to the rear lip) against L/D for the high and low Reynolds number cases. Peak Stanton number is higher for the low Reynolds number case at larger values of L/D, and the opposite for smaller values of L/D. Larson(1959), and Charwat et.al.(1961) found peak Stanton numbers for longer cavities to vary roughly as $Re^{-2/5}$ (where Re is the unit Reynolds number) for turbulent flows , which agrees with the present results in the reattachment region for the longest cavity (cf. the attached boundary layer on the cone forebody where $St_e \sim Re^{-1/5}$). However at lower values of L/D the high Reynolds number case returns the larger peak Stanton number. This is the same trend as was observed for the peak pressures, as was discussed in Chapter 3. It seems likely that there will be some simple relationship between pressure and heat transfer rates in the

reattachment region, as both should be strongly dependent on dividing streamline values (ie., the streamline which reattaches to the very top of the rear face). As will be illustrated by the computational work in Chapter 6, reattachment pressure is nearly equal to stagnation pressure on the dividing streamline. This is also an assumption behind theories such as proposed by Nash(1963) and Tanner(1978). In the case of heat transfer, Nestler(1972) adapted the solution of Lees(1956) for stagnation point heat transfer, to find that peak reattachment heat transfer rates varied as

$$\dot{q} \sim \left[\rho_D \mu_{DO} \left(\frac{du}{dy}\right)_D\right]^{1/2} (H_D - H_w)$$

where the subscript D indicates values on the dividing streamline, O indicates stagnation values, and W wall values. H denotes total enthalpy, and du/dy denotes the velocity gradient.

Thus, as was the case with peak pressure, the reattachment heat transfer rate should rise as the separated shear layer spreads further into the cavity increasing the dividing streamline velocity and total enthalpy. The other parameters (ie., ρ_D, μ_{DO} and $(du/dy)_D$) will also change individually, but should be of secondary importance as ρ_D and μ_{DO} change in the opposite sense. The value of $(du/dy)_D$ is less easy to predict, but if, as seems likely, only the inner part of the shear layer reattaches to the rear face, then $(du/dy)_D$ should increase with increased shear layer spreading (as the velocity profile of the separated shear layer is approximately an error function profile).

The explanation for the changing Reynolds number dependence of reattachment heat transfer rates with cavity length is then the same as given in Chapter 3 in relation to peak pressures, and illustrated in terms of shear layer spreading on Fig.43. The high Reynolds number flow has a thinner initial boundary layer at separation and so the separated shear layer spreads more quickly towards its self similar profile (ie., "swallows" the detail of the original boundary layer profile). Thus, for shorter cavities where the shear layer has not reached

a self similar profile at reattachment, the high Reynolds number shear layer would have spread further and so would have higher reattachment Stanton numbers. However the low Reynolds number shear layer will spread faster as the self similar profile is approached further downstream in accordance with the turbulent shear layer measurements of Charwat et.al.(1961b). Thus for longer cavities the low Reynolds number shear layer will have spread further into the cavity, and so show the higher reattachment Stanton numbers.

4.2.3 Comparison With Other Results

The heat transfer results, normalized by the attached value before separation, are shown on Fig.58 for L/D=2.4 and compared with the results of Nestler et.al.(1968) at M=6.8 and L/D=5. The L/D=0.8 results are compared on Fig.59 with the results of Wieting(1970) at M=7 and L/D=0.524. These results for comparison are obviously for different test conditions than the present study, and both were two dimensional planar experiments as opposed to axisymmetric, but they were the closest that could be found. However, given the rather different test conditions, there seems to be broad agreement between the results of the present study and those of other investigators. The results of Nestler et.al. show higher heat transfer rates on the cavity floor than in the present study, but it should be remembered that those results were for a L/D=5 cavity (with similar δ/D to the present study), and since heat transfer rate on the floor has been found generally to rise with cavity length for a given δ (see Charwat et.al.), this explains much of the difference. In fact Gortyshov et.al.(1982) at M=3.5 found maximum floor heat transfer to rise by a factor of 2 between L/D=1.8 and L/D=4.8 in their experiments, and this appears to be the trend observed comparing the results of the present study with those of Nestler et.al.

The effect of the Prandtl-Meyer expansion of the upstream boundary layer at the front lip of the cavity on peak recorded reattachment heat transfer rates seems to be less pronounced than for the pressure measurements. The probable reasons for

this are discussed in Chapter 5, including the general relationship between pressures and heat transfer rates in the cavity.

4.2.4 Total Heat Flux

The heat transfer rate distributions in the cavity can be integrated to find the total heat flux through the walls (ie., floor plus front and back faces) of the cavity. This is shown on Fig.60, normalized by Q_O, which is the heat flux that would have existed had there been no cavity (ie., if the outside radius of the cavity is r, then $Q_O=2\pi rL\dot{q}_c$, where $\dot{q}_c$ is the cone forebody heat transfer rate). The results are obviously strongly Reynolds number dependent. At the lowest value of L/D, Q/Q_O is large primarily because the wetted area in the cavity is considerably greater than if there were no cavity. However it is significant that Q/Q_O is less than unity for all cases, indicating that the cavity has reduced the overall heat loading to the model.

Another useful way of presenting the data is in terms of an average cavity Stanton number, $\bar{St}$, which is spatially averaged over the wetted surface of the cavity, and plotted on Fig.61. Here it is evident again that, as for peak reattachment Stanton numbers, the Reynolds number dependence of average cavity Stanton number changes sign between L/D=1.6 and 2.0. For shorter cavities, higher Reynolds numbers lead to higher average Stanton numbers, while the opposite is true for cavity lengths above about 4.5cm (L/D=1.8, or δ/L=0.13). Other researchers (eg., Larson(1959) and Gortyshov et.al.(1982)) have found $\bar{St}\sim Re^{-2/5}$ (unit Reynolds number) , but only studied relatively long cavities (although Gortyshov et.al. studied a L/D=1.0 cavity, the physical cavity length was a constant 14cm). For the longest cavity of the present study, L=6cm, the Reynolds number dependence of $\bar{St}$ would seem to be approaching that found by other investigators.

In his axisymmetric experiments, Larson found $\bar{St}/St_e$ relatively constant over a wide range of Mach numbers and equal to about 0.5 for $Re_L=3x10^6$. The results of the present study for L/D=2.4 show $\bar{St}/St_e=0.4$ for the high Reynolds number running

condition (Re_L=3.3x10^6). However the cavity Larson studied had rounded corners at both ends of the cavity floor, which might eliminate secondary separated regions and thus tend to increase $\overline{St}$.

In terms of hypersonic vehicle design, average Stanton number is a useful parameter as it gives an estimate of total heat loading to the structure which is important for "heat sink" type structures. These results indicate that care must be taken with the use of such a parameter because of strong Reynolds number effects.

CHAPTER 5
THEORETICAL ANALYSIS

It is possible to undertake a limited theoretical analysis of the cavity flowfield to obtain a better physical understanding of the processes involved and flow properties that are important. This has been attempted for separated flows by other investigators such as Korst(1956) and Tanner(1978), but these theories were developed to be more applicable to base flow problems than cavity flows. However there are obvious similarities between base and cavity flows, and certain elements of the base flow analysis of Nash(1963a) will be applied in the subsequent work.

The flowfield will be broken up into 3 main component parts, and each section analysed separately. These component parts are - (1) the rapid turning and expansion of the approaching boundary layer as it separates from the cone forebody- (2) the growth of the separated shear layer from the boundary layer after turning and (3) the partial reattachment of the shear layer on the rear face of the cavity.

5.1 Rapid Expansion of the Cone Boundary Layer

The Schlieren photographs of Fig.29 to 32 indicated that the cone boundary layer encounters a Prandtl-Meyer expansion at the point of separation, as shown on Fig.32. It is thus necessary to analyse how this expansion changes the original boundary layer profile.

It should be remembered that parts 1 and 2 of the analysis, the expansion of the boundary layer and the spreading of the shear layer, are to some extent taking place simultaneously. However the inner part of the boundary layer, which is the most important in terms of reattachment conditions, is expanded quite rapidly before viscous effects can change this part of the profile to a significant extent, and so it seems reasonable to analyse the expansion separately.

If there was no boundary layer profile at separation (ie., uniform inviscid flow), the Prandtl-Meyer expansion at that point would turn all streamtubes in the flow through a constant angle and uniform pressure corresponding to that isentropic expansion angle would exist immediately downstream of the separation. However a Mach number gradient exists close to the surface because of the presence of the boundary layer. Thus if the initial turning angle was indeed constant, the low Mach number layers in the initial boundary layer profile would experience a much smaller pressure drop than the high Mach number layers. In practice, the expanding boundary layer tries to maintain pressure continuity in the normal direction, and this is achieved by a series of wave reflections which modify the shape of the shear layer profile immediately downstream of the expansion. The pressure across the shear layer immediately after the expansion is then somewhat greater than that corresponding to the external flow turning through the same angle as the inner part of the boundary layer. More wave interactions then occur as the shear layer "relaxes" to a condition far downstream where all streamlines are parallel and the pressure asymptotes to the value given by the isentropic turning of the external flow.

It is possible to use several different methods to analyse the expansion, all of varying degrees of complexity and accuracy. The simplest of these is the so called isentropic streamtube method, the accuracy of which was demonstrated by Small et.al.(1973). This method assumes constant turning angle at all levels (ie., x=const) in the shear layer, and hence large normal pressure gradients, through the boundary layer downstream of the expansion. The boundary layer is divided up into streamtubes whose widths after the expansion are calculated from continuity. However the results of this analysis tend to reflect the crudeness of the model in taking no account of the effect of the Mach number gradient on the expansion process.

Inviscid modelling, in particular characteristics calculations, have been found to give good results as the inertial forces dominate viscous forces for a rapid expansion, but are time

consuming. However there is another inviscid method, outlined by Weinbaum(1966), which seems to give results quite close to a characteristics analysis for small turning angles ($\Theta<10^{o}$), and so is applicable here. It will be used in a two dimensional planar analysis, as the axisymmetric correction should be quite small. It is a linearised analysis which takes into account first order wave reflections during the expansion process, and so gives results which approximate conditions immediately downstream of the expansion. If an expansion wave in a fluid of Mach number M (where $M<\sqrt{2}$) meets an interface of Mach number M+dM, then a proportion of the expansion

$$da = \frac{(M^2-2).dM}{2M(M^2-1)}$$

is reflected, and the transmitted wave has strength (1-da). If $M<\sqrt{2}$, the reflected wave is compressive and the transmitted wave has strength (1+da). Following the analysis of Weinbaum, it is possible to sum the effects of these reflected and transmitted waves to yield

$$\frac{(M^2-1)^{1/4}}{M\Theta} = \text{const}$$

which gives flow deflection angle in degrees as a function of Mach number. If the value of the constant is appropriately chosen (based on characteristics results, to give the desired flow angle at the bottom of the boundary layer, or sonic line if desired), then the turning angle can be found anywhere from the pre-expansion Mach number profile, and so the post-expansion Mach number pofile and other flow properties found.

The boundary layer was split into 12 equal vertical segments, and this analysis performed. Based on data presented by Weinbaum for a characteristics analysis, the value of the constant was set to 0.122. Implicit in the setting of this constant is the assumption that the sonic line in the boundary layer turns parallel to the cavity floor, which was the case studied by Weinbaum, and so this is effectively the boundary condition on the shear layer just after expansion. This boundary condition implies a slight over expansion of the subsonic

portion of the boundary layer into the cavity, which is similar to what has been observed in base flows. The calculated Mach number and pressure profiles immediately after expansion are shown on Fig.62 and Fig.63, where y is measured from the inner edge of the layer outwards towards the free stream. These profiles are also compared with the boundary layer profiles before expansion.

The static pressure in the shear layer generally determines cavity floor and front face pressures, and a spacial average of the results of the expanded boundary layer in the transverse direction gives a result of $0.60p_c$, which is quite close to the experimental cavity floor pressure result of $0.62p_c$.

5.2 Growth of the Shear Layer

Growth of the shear layer into the cavity is important in determining peak pressures and heat transfer rates at reattachment. Many authors have found that the error function velocity profile,

$$\frac{u}{u_e} = \frac{1}{2}\left[1 + \text{erf}\left\{\frac{\sigma y}{x}\right\}\right]$$

where the co-ordinates are defined on Fig.64, gives a good estimate of turbulent shear layer velocities for small steamwise pressure gradients. This holds even at high Mach numbers (see Mach 5 free shear layer measurements by Wagner(1973)), providing the appropriate value of spreading rate parameter σ is chosen, and the self-similar state has been reached, or nearly reached. Zero velocity is assumed on one side of the shear layer and free stream velocity on the other. Spreading rate generally decreases with Mach number, but for Mach numbers greater than 3 the data presented by Bradshaw(1980) indicates that spreading rate seems to level out. Based on this information and the data of Wagner, a value of σ=35 is chosen here (cf., σ=12 for incompressible flow as given by Bradshaw).

The error function velocity profile only gives a good approximation to shear layer velocities after the layer has reached a self-similar state in terms of mean velocity. However the initial spreading of the shear layer is dominated by the boundary layer just before separation. After separation a new shear layer begins growing into the bottom of the original boundary layer profile. Some distance downstream the original boundary layer profile is consumed by the shear layer growth and the self-similar state is reached.

Following the analysis of Nash(1963b), the effect of the initial boundary layer thickness on the asymptotic shear layer can be viewed as shifting the effective origin of the shear layer upstream by an amount x_0 so that

$$\frac{u}{u_e} = \frac{1}{2}\left[1 + \text{erf}\left\{\frac{\sigma y}{(x-x_0)}\right\}\right]$$

The value of x_o can be found, following the analysis of Nash, by equating the momentum thickness of the boundary layer after expansion to the momentum thickness of a shear layer at that position but with its origin at x_o. The momentum thickness is given by

$$\vartheta = \int_o^y \frac{\rho u}{\rho_e u_e}\left[1 - \frac{u}{u_e}\right] dy$$

which has a value ϑ=0.45mm for the calculated boundary layer profile after expansion (compared with 0.3mm before expansion). The error function calculation can then be performed to return a value of x_o=-260mm. If there had been no expansion at separation (ϑ=0.3mm), the value of x_o at separation would have been -165mm, so the effect of the expansion is to move the effective origin of the shear layer upstream, as well as, of course, to reduce the static pressure in the shear layer. These calculations were done iteratively, varying x_o until the correct value of ϑ resulted. The total temperature was assumed to vary linearly with shear layer velocity, in a Crocco type relationship, with free stream total temperature on one side of the shear layer, and $0.66T_{oe}$ on the low velocity side (ie., in the cavity). Thus

$$\frac{T_o}{T_{oe}} = 0.66 + 0.44\frac{u}{u_e}$$

This value of total temperature in the cavity was based on the experimental results of Emery et.al.(1965) for cavity flows , and the almost identical result of Martellucci et.al.(1966) for base flows.

There is a question, of course, as to whether the velocity profile has adjusted itself to the error function profile by the time of reattachment. However there is evidence (Nash(1963b)) that the mean velocity profile adjusts remarkably quickly to that of the error function velocity profile. Even at Mach 5, the results of Wagner(1973) seem to indicate that the self-similar profile is approached about 10 initial boundary layer thicknesses from separation, and that, at least for the longer cavities of the present study (L=5 and 6cm), the error function velocity profile

will be a good approximation at reattachment. The results of Wagner were for a unit Reynolds number of 1.6×10^7/m, which is close to the low Reynolds number condition in the current experiment.

Wagner's results show that, despite the velocity profile being roughly symmetric about the $u/u_e=0.5$ line, this line is slightly inclined to the x axis, implying the need to use a small y_o correction similar to x_o such that

$$\frac{u}{u_e} = \frac{1}{2}\left[1 + \mathrm{erf}\left\{\frac{\sigma(y-y_o)}{(x-x_o)}\right\}\right]$$

The results of Wagner show y_o to be quite small. In the absence of experimental shear layer measurements in the current study, the experimental pressure at the point closest to the rear lip can be used to set the value of y_o. This is achieved by calculating the velocity and Mach number distributions at reattachment for different values of y_o, and then assuming that reattachment pressure is equal to the stagnation pressure of the oncoming streamline, "pegging" the calculated reattachment pressure at the $y/D=0.08$ position to the experimental value by chosing the appropriate value of y_o. Using this procedure, a value of $y_o=0.028x$ is chosen. The results of the calculation are then shown in terms of Mach number just before reattachment for the L=6cm cavity on Fig.65., and compared with the results for an unexpanded boundary layer at separation. The implications of these results on reattachment conditions are now analysed.

5.3 Partial Shear Layer Reattachment

5.3.1 Pressures at Reattachment

It is reasonable to assume that the pressure at reattachment is approximately the stagnation pressure of the approaching streamline (Korst(1956)), as the results show Mach numbers on these streamlines to be not much greater than 1, and viscous effects should be generally neglectable during reattachment. Laminar computations described in Chapter 6 also indicate this to be the case. This assumption does, of course, become less valid further away from the dividing streamline, as no divergence of the reattaching streamline is allowed for. Assuming then constant pressure across the shear layer (as calculated earlier), an estimate of reattachment pressures can be made from the calculated Mach number (and hence stagnation pressure) distribution, and the results are shown of Fig.66 for the L=6cm cavity. It is apparent that the experiments agree quite well with the calculated results, given that one of the calculated points was "pegged" to the corresponding experimental point. In addition, the calculations give an idea of what happens right up to the reattachment lip where experimental results could not be obtained because of the spatial resolution of the static pressure instrumentation. It seems that the absolute peak reattachment pressure may be about 4.5 times the cone surface pressure for this cavity length, whereas the maximum measured value was $1.72p_c$. It is also apparent that the initial boundary layer expansion has a considerable effect on peak cavity pressures, tending to lower them. The effect becomes more pronounced very close to the lip, where the calculations predict that the peak pressure is reduced by a factor of slightly more than 2 by the expansion.

It would appear that the experimentally observed rise of peak pressure with L/D from low values of L/D corresponds to the shear layer rapidly adjusting to the self similar velocity profile. Levelling out of the peak pressure at L/D=2.0 and 2.4 then corresponds to the shear layer (or at least the low velocity

portion of it) having reached this profile. It seems that the low Reynolds number case may take longer to reach similarity. Calculations for longer cavities than studied experimentally show peak pressure rising quite slowly with cavity length.

5.3.2 Reattachment Heat Transfer

The relationship between shear layer properties and reattachment heat transfer rate is even more difficult than the case of reattachment pressure. Adapting the solution of Lees(1956) for stagnation point heat transfer, Nestler(1972) found that peak reattachment heat transfer rates varied as

$$\dot{q} \sim \left[\rho_D \mu_{DO} \left(\frac{du}{dy}\right)_D\right]^{1/2} (H_D - H_w) \qquad (1)$$

where the subscript D indicates values on the dividing streamline, O indicates stagnation values, and w wall values. H denotes total enthalpy, and $(du/dy)_D$ is the velocity gradient on the dividing streamline.

The constant of proportionality in the above equation is, however, very uncertain. Nestler found that peak reattachment heat transfer rates could best be predicted in a semi-empirical manner from the pressure measurements in the form

$$\frac{\dot{q}}{\dot{q}_c} = \left(\frac{p}{p_c}\right)^n \qquad (2)$$

where c denotes the cone or forebody values, and he found n=0.8 fitted the data quite well for a two dimensional cavity of L/D=5 and M=6.8. In the current experiment, a value of n=1.6 is found to fit the data at reattachment quite well, as shown on Fig.67. Away from reattachment the power law cannot be expected to be give good results, and the correlation falls away particularly on the front face. This difference in the value of n implies that the effect of the expansion at separation does not reduce the reattachment heat transfer rates as much as the reattachment pressures. This was seen earlier to be the case when comparing pressures and heat transfer rates of the current experiment with those of other investigators.

An estimate of absolute maximum heat transfer rate on the very top of the rear face of the cavity is difficult to obtain. It may seem that equation (2) could be applied to get an estimate based on the theoretical pressure predictions, but Gerhart and Thomas(1974) note that maximum heat transfer occurs slightly away from reattachment, so that equation (2) is unlikely to be valid right up to the rear lip.

A qualitative estimate of the effect of the separation expansion on absolute maximum heat transfer rate can be made using equation (1), with the results of the shear layer calculation being used to give the values on the dividing streamline. Inserting the appropriate values, it can be seen from the result on Fig.68 that for the longest cavity the effect of the expansion is to reduce peak heat transfer by about 40%. In comparison, the effect of the expansion was to reduce peak pressure by over 60%, which is consistent with the earlier conclusion that peak heat transfer rate is reduced less than peak pressure.

Calculations were also made for cavities longer than studied experimentally, and the results showed peak heat transfer rate rising slowly with cavity length, as was the case for peak pressure.

5.4 Reynolds Number and Geometry Dependence

5.4.1 Reattachment

It is apparent from this line of analysis that reattachment conditions are governed generally by spreading of the separated shear layer , so that the important geometric parameters are L and δ. This is in agreement with the conclusion of Lamb(1981), who tried to correlate different sets of experimental data for cavity flows. To a certain extent peak heat transfer rates are affected by the pressure gradient along the rear face, which is determined by the structure of the captured vortex, and that in turn infuenced by L/D, but Lamb found this effect relatively weak such that $St_e \sim (\delta/H)^{-0.25}$ for constant L/δ. He also found a weak Mach number dependence.

The effect of Reynolds number on reattachment conditions seems to be quite complex. The evidence is that reducing Reynolds number will increase the asymptotic spreading rate of the separated shear layer (see Charwat et.al.(1961b). Thus for cavity lengths where the self-similar velocity profile has been reached at reattachment, the low Reynolds number flow should record higher reattachment pressures and heat transfer rates. However reducing Reynolds number also results in a thicker upstream boundary layer. A thicker upstream boundary layer means that the separated shear layer will take longer to reach its asymptotic spreading rate (ie., it will not approach the self-similar velocity profile until further downstream). Thus for short cavities where the self-similar state in the shear layer has not been reached at reattachment, the low Reynolds number flow may have not spread as far as a high Reynolds number flow, and so record smaller reattachment pressures and heat transfer rates. These, in fact, were the trends recorded experimentally. It must, however, be noted that this explanation of Reynolds number dependence changing with cavity length is just a hypothesis, and that experiments on hypersonic separated shear layers need to be performed to find the exact nature of the Reynolds number dependence of shear layer spreading.

5.4.2 Away From Reattachment

Away from the reattachment region cavity pressures are determined mainly by the static pressure in the shear layer, and recirculation velocities in the captured vortex. Heat transfer rates are determined by the new boundary layers growing on the cavity walls. It can be seen that higher reattachment heat transfer rates seem to lead to slightly lower heat transfer rates deeper in the cavity. Lamb(1981) also noticed this, and attributed it to larger impingement heat transfer producing thicker boundary layers deeper in the cavity.

Larson(1959) found total heat flux to an axisymmetric cavity approximately 1/2 the heat flux to the surface if no cavity had existed. Interestingly, on integrating the heat transfer distrubution around the cavity surface for the L=6cm and

D=2.5cm cavity (as described in Chapter 4), an almost identical result is found for the current experiment. The expansion at separation would seem to have had little effect on the total heat flux to the surface, although it seems to have reduced peak heat transfer rates.

CHAPTER 6

COMPUTATIONS

6.1 Background

In recent years, attempts at the numerical solution of the Navier-Stokes equations have become common. The literature is vast, with numerous combinations of methods used. MacCormack(1985) reviewed the current status of such computations at that time. He describes two widely used numerical procedures of his own, one implicit and one explicit. Although the implicit procedure is very efficient, having theoretically an unrestricted time step size, it involves much more complex coding. More complete descriptions of these methods are given by MacCormack(1969) and (1982).

A major problem with methods such as described above is that of artifical and numerical dissipation. Numerical dissipation is caused by truncation errors in the finite difference formulation (higher order terms in the Taylor series expansion are ignored), while artifical dissipation or diffusion is caused by diffusive terms which are intentionally added to the finite difference formulation to counteract truncation errors which cause instabilities in the solution. Kuruvila et.al.(1985) studied the effect of this artifical dissipation in terms of flow over a rearward facing step using MacCormack's standard explicit method. Their results indicated that for a cold wall heat transfer case artifical dissipation has a major effect on the results, particularly in the separated region. However for an adiabatic wall case, artifical dissipation was found to have virtually no effect on the results. They did not put a reason foward as to why the cold wall heat transfer case should be more sensitive to artifical dissipation. For the purposes of comparing experimental and computational results in the current study, highly cooled wall conditions must be simulated and so these results suggest that artifical and numerical dissipation should be minimised as much as possible.

Applications of MacCormack's method to solving the Navier-Stokes equations are abundant. Berman et.al.(1982) deals with flow over a rearward facing step with transverse non-reacting hydrogen injection, in the context of a *scramjet* engine. Sullins(1982) et.al . deals with supersonic base flow with parallel injection, while White et.al.(1982) use the implicit variation for nozzle flows. More complicated applications can be found in Weidner et.al.(1981) , with staged fuel injection for supersonic combustion, and Schetz et.al.(1981) where the complete flowfield of a scramjet combustor with fuel injection is analysed.

Ben-Artzi and Falcovitz(1984) describe a second order "Godunov-type" inviscid scheme which has been under development in the department for the past few years (see Hillier(1987,1988)). It shows excellent ability to capture and resolve flow discontinuities (ie., shock waves, contact surfaces, and vortex sheets) . The method is an explicit time marching scheme, able therefore to compute both steady and unsteady flows, the former being achieved by a time stepping iteration from an impulsive start. The time stepping ability is important, firstly to be able to deal simultaneously with supersonic and subsonic portions of the flow (as the time dependent equations are always hyperbolic), and secondly to be able to deal with any genuine unsteadiness that might be present in the recirculating region. Typical computations were made by Hillier et.al.(1985) using this method. Similar Godunov-type schemes have dealt successfully with a range of aeronautical problems from transonic to supersonic/hypersonic . The Godunov scheme seems to be an ideal Euler code upon which to build the Navier-Stokes option for the current work because of the small amount of numerical diffusion it seems to give.

It is possible to introduce a Navier-Stokes option to convert the code from an inviscid to a viscous one. It can be implemented by an operator splitting technique whereby the computation is advanced one increment in time by two separate coupled stages, firstly an inviscid step, and then a second

viscous solution. MacCormack(1976) shows how an operator splitting technique has been used successfully to split the parabolic (viscous) terms and hyperbolic (inviscid) operators in a Navier-Stokes code.

Navier-Stokes computations have been carried out by Zhang(1987) for cavity flows at supersonic Mach numbers. He used a Brailovskaya finite difference scheme with a two layer eddy viscosity turbulence model. This technique was second order accurate in space and first order accurate in time, and seemed to reproduce the basic physics of the unsteady flowfield, athough an artifical viscosity was used to stabilize the scheme and so the results suffered badly from artifical diffusion.

The aim of the computational work was then the development, testing and use of a shock capturing Euler code, plus the initial development and testing of a Navier-Stokes option for the code. This was to be tested rigourously for laminar boundary layers, and separated cavity flows. In the time available it was not considered possible to develop a turbulent version of the code. Such a turbulence model would be necessarily quite crude, and there is not yet agreement in hypersonic flow as to which modelling strategy to follow. It is thus probable that a fully tested laminar version of the code would yield as much useful information about the cavity flowfield as a code with a simple turbulence model. The computations will build upon an already existing "Godunov" type inviscid code which has been under development in the department. It was hoped that the computational work would shed some light upon the flow structure in the cavity, as well as serve to estimate the accuracy of such a Navier-Stokes scheme in predicting hypersonic separated flowfields. In this respect comparisons with the cavity flow computations of Zhang(1987) and Baysal et.al.(1988) are pertinent.

6.2 Inviscid Computations

6.2.1 The Godunov Code

The Godunov-type code used here is an explicit time marching Euler code, of the type described by Ben-Artzi and Falcovitz(1984) for one dimensional computations, that is second order accurate in both time and space (but has an option to run as a first order accurate scheme). A Godunov scheme is a method whereby the Riemann problem is solved between adjacent cells in the flowfield after an imaginary diaphram between cells is removed at the start of a time step. The resulting fluxes of flow properties into and out of cells can then be calculated as an analytical solution to this initial value problem and so the new values of flow properties within cells found at the end of a time step.

Time marching is important for the calculation of supersonic flows as the time dependent Euler and Navier-Stokes equations are hyperbolic for both subsonic and supersonic flows, allowing convenient calculation of regions of subsonic flow embedded in the supersonic flow. Time marching also allows the calculation of any genuine unsteadiness that might exist in the flowfield (eg., in a separated region), so that it is regarded as essential here. Steady flows are calculated by a time stepping iteration to a steady state.

6.2.2 Finite Differencing

The two dimensional Euler equations are given by

$$\frac{\partial Q}{\partial t} + \frac{\partial E}{\partial x} + \frac{\partial F}{\partial y} = 0 \qquad (3)$$

where Q, E and F are vectors given by

$$Q=\begin{bmatrix}\rho\\ \rho u\\ \rho v\\ \rho e\end{bmatrix} \quad E=\begin{bmatrix}\rho u\\ p+\rho u^2\\ \rho uv\\ u(p+\rho e)\end{bmatrix} \quad F=\begin{bmatrix}\rho v\\ \rho uv\\ p+\rho v^2\\ v(p+\rho e)\end{bmatrix}$$

where u and v are the x and y components of velocity, ρ is the density, p is the pressure, and e is the internal energy per unit volume. Thermodynamic closure is achieved by the perfect gas assumption (ie., $p=\rho RT$)

The Godunov method is a cell based method, as shown on Fig.69. Letting co-ordinates i,j identify a cell and $i\pm1/2,j$ and $i,j\pm1/2$ identify the interfaces, then to advance the solution by Δt, from time level n to n+1, the above Euler equations are represented by

$$\frac{Q_{i,j}^{n+1} - Q_{i,j}^{n}}{\Delta t} + \frac{E_{i+1/2,j}^{n+1/2} - E_{i-1/2,j}^{n+1/2}}{\Delta x} + \frac{F_{i,j+1/2}^{n+1/2} - F_{i,j-1/2}^{n+1/2}}{\Delta y} = 0 \quad (4)$$

where the flux vectors E and F are calculated from the solution of the Riemann problem. The scheme will be second order in space if the fluxes are evaluated to second order accuracy in space, and second order in time if they are temporally evaluated at $n+1/2$ (ie., mid time step).

There are many second order space averagings for the flux, perhaps the most simple and well known being the Jameson finite volume algorithm where

$$E_{i+1/2,j} = \frac{1}{2} (E_{i,j} + E_{i+1,j})$$

Formally this is second order accurate in space (central difference) but as a consequence produces oscillatory behaviour near shock waves which must be stabilised by an artifical damping term which is added to each flux. The Godunov method avoids this particular difficulty by incorporating a shock wave solution (if necessary) as part of the flux function, so that more or less correct dissipation is achieved. This solution is represented by a Riemann solver which is described below.

The Riemann problem itself can be considered (firstly in one dimension) by studying the interface $i+1/2$ between cells i and i+1, as shown on Fig.70, across which there is an initial discontinuity in properties between regions 1 and 4 (where conditions are assumed initially constant, ie., piecewise linear).

The resultant flow generates left and right running waves L and R, separated by a contact surface across which the pressure and velocity must be continuous but all other variables may be discontinuous. Regions 2 and 3 are uniform property regions. In turn, each wave L and R may be either a shock wave or a rarefaction wave, depending on the initial conditions, so that there are 4 possible wave configurations. For piecewise constant initial conditions the wave field is self-similar with time (ie., expands linearly with time). Calculation of the wave field requires an iterative solution which has been described in several references (eg., Godunov(1959)). Once the wave field is known, the flux $E_{i+1/2}^{n+1/2}$ at the cell interface is taken as the value from whatever part of the wave zone is coincident with the interface, so the scheme has an "upwind" nature. Although this wave zone was illustrated as region 3, it could in fact have been region 1 for example, so the ability exists to simulate a slip discontinuity.

The basic Godunov scheme is strictly first order accurate when flow properties across cells are taken as constant across each cell as described above. However various schemes have been used to provide second order accuracy. Ben-Artzi and Falcovitz(1984) allow piecewise linear distributions across cells, and solve the appropriate Riemann problem at the cell interface discontinuity, and the solution of this "generalized Riemann problem" is used here to achieve second order accuracy in space. This results in a non self-similar wave development, and fluxes are evaluated at mid time step. The initial gradient in a cell is found from a central difference of the cell centred values of the cells on either side of it. If fitting a gradient through a cell produces a new extreme at one of the boundaries of the cell, then this boundary value is changed such that the new extreme is eliminated. This monotone constraint appears to be the only condition required to provide a stable scheme.

In two dimensions, there are two versions of the code available. The so-called unsplit version solves for the x and y terms of the Euler equations simultaneously for each cell, while

the split version solves firstly in one direction for all cells and then in other direction. The split version was used for the current computations because it allows the use of a symmetrical operator (as described in 6.3.1) in the x and y directions and so formally maintains second order accuracy, and allows a slightly larger time step to be used. The coding is also less complicated than for the unsplit version.

6.2.3 Inviscid Cavity Flows

The program geometry routine was modified such that boundary conditions for a blunt nosed body with a cavity, as shown on Fig.71a, could be computed. It was decided to perform some inviscid flow computations initially to check the geometry routines and boundary conditions (discussed in 6.3.1), show the importance or otherwise of numerical diffusion, and to act as a rough guide to the experimental pressure levels for the purchase of pressure transducers. The computations were found to reach a steady state for the Mach 3 and Mach 9 cases, the results showing a clockwise circulation inside the cavity.

The geometry routine was modified again to study flow over a flat plate and cavity, as shown on Fig.71b . However even with a non-zero starting velocity in the cavity, the solution converged to a situation of zero velocity in the cavity, indicating the ability of the code to sustain a "shear" or "slip" discontinuity precisely, provided it is aligned with the mesh and stationary relative to it (ie., for these special cases the code provides no numerical diffusion). Presumably the reason the previous geometry of blunt nose followed by cavity showed some circulation in the cavity was that a pressure gradient was present after the flow passed the blunt nose providing a non zero y component of velocity which was sufficient to cause some numerical diffusion and cavity rotation.

The computations were therefore generally tending to the inviscid free streamline solution. To provide circulation therefore requires a proper viscous stress model, but as a final inviscid test a simple "mixing" model was introduced, generating an effective shear stress proportional to shear velocity. If the vertical velocity gradient exceeds a certain limit, x momentum

from the low speed flow is transferred to the high speed flow and vice versa, the amount of momentum transfer being proportional to the streamwise velocity differential. The results approach a steady state, and a typical cavity pressure profile for such a computation is shown on Fig.72. Results from these computations were used as a rough guide to the expected cavity pressure levels and hence for the purchase of pressure transducers.

6.3 Viscous Computations

6.3.1 Addition of the Viscous Terms

The basic inviscid code incorporates the sophisticated wave interaction model or Riemann solver previously described to calculate inviscid fluxes at interfaces between cells. The logic for Navier-Stokes developments gives the option either of adapting this Riemann solver to include viscous effects or separating inviscid (hyperbolic) and viscous (parabolic) calculations into separate "operator-split" routines, as done successfully by MacCormack(1976).

It was decided to follow the latter course of action and therefore to create an entirely separate routine to deal with the viscous terms. Development of a new routine is convenient and also preserves the simplicity of the original Riemann solver, and would seem to be a novel development of Godunov methods. The operator splitting routine is thus alternate inviscid and viscous steps. If $L_h(\Delta t)$ and $L_p(\Delta t)$ are operators which advance the hyperbolic and parabolic parts of the Navier-Stokes equations by a time step Δt, with second order accurate solutions in time and space, then the sequential operator

$$L(2\Delta t)=L_h(\Delta t).L_p(\Delta t).L_p(\Delta t).L_h(\Delta t)$$

or any other symmetric combination, gives a second order accurate operator which advances the solution by $2\Delta t$. Such an operator is no more expensive than a combined solution of the hyperbolic/parabolic terms; indeed ,as will be seen there are some positive advantages to splitting the procedure up into separate operators.

The operator split routine used here is dependent on the stable time steps for the viscous and inviscid parts of the code, which are calculated at regular intervals.

The full two dimensional Navier-Stokes equations are given by

$$\frac{\partial Q}{\partial t} + \frac{\partial E}{\partial x} + \frac{\partial F}{\partial y} = 0$$

where the vectors Q, E, and F are given by

$$Q=\begin{bmatrix}\rho\\ \rho u\\ \rho v\\ \rho e\end{bmatrix} \quad E=\begin{bmatrix}\rho u\\ p+\rho u^2+\sigma_x\\ \rho uv+\tau_{xy}\\ u(p+\rho e+\sigma_x)+v\tau_{yx}+q_x\end{bmatrix} \quad F=\begin{bmatrix}\rho v\\ \rho uv+\tau_{yx}\\ p+\rho v^2+\sigma_y\\ v(p+\rho e+\sigma_y)+u\tau_{xy}+q_y\end{bmatrix} \tag{5}$$

and for laminar flow

$$\sigma_x= -\lambda\left[\frac{\partial u}{\partial x}+\frac{\partial v}{\partial y}\right]-2\mu\frac{\partial u}{\partial x}$$

$$\tau_{xy}=\tau_{yx}=-\mu\left[\frac{\partial u}{\partial y}+\frac{\partial v}{\partial x}\right]$$

$$\sigma_y= -\lambda\left[\frac{\partial u}{\partial x}+\frac{\partial v}{\partial y}\right]-2\mu\frac{\partial v}{\partial y}$$

$$q_x= -k\frac{\partial T}{\partial x} \quad ; \quad q_y= -k\frac{\partial T}{\partial y}$$

where the Stokes approximation is usually made that

$$3\lambda + 2\mu = 0$$

For turbulent flows a model equation is required to relate turbulent stresses (σ_x, σ_y, τ_{xy}, τ_{yx}) to the mean flow field. There is no unique formula, but a simple two layer mixing length model of the type described by Baldwin and Lomax(1978) is commonly used.

After the inviscid terms in the Navier-Stokes equations (5) are solved using the Godunov method and the flow variables updated from that solution, the remaining viscous equations to be solved are

$$\frac{\partial \rho}{\partial t}= 0 \quad \text{(continuity)} \tag{6}$$

$$\frac{\partial(\rho u)}{\partial t}+\frac{\partial \sigma_x}{\partial x}+\frac{\partial \tau_{yx}}{\partial y}= 0 \quad \text{(x-momentum)} \tag{7}$$

$$\frac{\partial(\rho v)}{\partial t}+\frac{\partial \tau_{xy}}{\partial x}+\frac{\partial \sigma_y}{\partial y}= 0 \quad \text{(y-momentum)} \tag{8}$$

$$\frac{\partial(\rho e)}{\partial t}+\frac{\partial(u\sigma_x+v\tau_{yx}+q_x)}{\partial x}+\frac{\partial(v\sigma_y+u\tau_{xy}+q_y)}{\partial y}= 0 \quad \text{(energy)} \tag{9}$$

Central differencing was used for all terms, including the cross derivatives, to maintain second order accuracy. For example, the x momentum equation for a uniform grid reduces to

$$\frac{\Delta(\rho u)}{\Delta t} = \frac{\sigma_{xL} - \sigma_{xR}}{\Delta x} + \frac{\tau_B - \tau_T}{\Delta y}$$

where the subscripts L, R, T, and B denote values at the left, right, top, and bottom interfaces of a cell respectively. Thus, for example

$$\tau_T = \frac{-(\mu_{i,j} + \mu_{i,j+1})}{2} \left[\frac{u_{i,j+1} - u_{i,j}}{\Delta y} + \frac{v_{T,i+1} - v_{T,i-1}}{2\Delta x} \right]$$

where $v_{T,i+1} = \frac{v_{i+1,j} + v_{i+1,j+1}}{2}$ etc.

This differencing is only second order accurate for a uniform mesh. The code actually takes a proper weighting between cells to maintain second order spatial accuracy for stretched meshes.

A predictor-corrector method of time marching was used to retain second order accuracy in time. This involves calculating time derivatives of values at an intermediate time $\Delta t/2$, and then assuming this time derivative constant across the full time step.

The Sutherland temperature-viscosity law given below was used.

$$\frac{\mu}{\mu_\infty} = \left(\frac{T}{T_\infty} \right)^{1/2} \frac{1.505}{1 + 0.505(T_\infty/T)}$$

Continuative boundary conditions at the top and downstream boundaries were used. This means that flow values immediately outside the boundaries are set equal to the values in the corresponding cell immediately inside the boundary, so that gradients at these boundaries are set to zero. On solid boundaries a zero slip condition was used. Adiabatic wall boundary conditions were simulated by setting the temperature in the cell inside the body and adjacent to the wall equal to the adjacent cell in the flowfield, thus producing zero normal temperature gradient at the wall. Isothermal wall boundary conditions were achieved by setting the temperature of the cell in the body such that interpolation between it and corresponding flowfield cell would give the desired temperature at the wall.

Careful checking on the consistency of coding and accuracy of the model was carried out. This included a hand calculation over a time step, and computing boundary layers on identical horizontal and vertical flat plates.

A mesh stretching routine was also added to allow better resolution near solid surfaces or where flow gradients are large.

6.3.2 Laminar Boundary Layer Computations

It was decided to test the viscous version of the code by computing some laminar flat plate boundary layers and comparing the results with the theoretical profiles of van Driest(1952). Although the van Driest results are for the thin shear layer approximation to the Navier-Stokes equations (compared to the full Navier-Stokes computations of the present study), this should have negligible effect in comparing boundary layer profiles. Two Mach 8 boundary layers were chosen, one with an adiabatic wall boundary condition, and the other with an isothermal wall $T_w/T_\infty = 6$ boundary condition. Both cases were computed for several different meshes to assess the effect of mesh refinement on the results.

All computations were time marched to a steady state using a CFL number of 0.8. The stable time step for the inviscid part of the code was set as the maximum time allowed before an acoustic disturbance could travel from one side of a cell to the other in either the horizontal or vertical direction (in other words $\Delta t_{max} = \min(\Delta x/(u+a); \Delta y/(v+a))$). A similar constraint was set for the viscous part of the code based on the diffusion of viscous and thermal disturbances, where the stable time step used was given by Peyret and Taylor(1983) as

$$\Delta t \leq \Delta x^2 \left[\frac{2\mu}{Re\rho} \left(\frac{2\gamma}{Pr} + \sqrt{\frac{2}{3}} \right) \right]^{-1}$$

which seemed to work quite well.

A steady state was assumed to have been reached when flow variables remained constant to 3 decimal places throughout the flowfield. The mesh was designed such that the shock wave from the leading edge of the plate (arising from the leading edge interaction) passed across the downstream boundary of the

flowfield, and not through the top boundary. This allowed a further check on convergence to a steady state by integrating mass and total enthalpy fluxes across the flowfield at several different stations on the plate and checking that the results were equal to the values of the integrated quantities upstream of the plate (less the heat loss to the wall). These values were found to differ by no more than 0.2%.

Fig.73 and Fig.74 show the velocity and temperature profiles for the Mach 8 adiabatic wall boundary layer at Re_x= 587 000, where the pressure in the boundary layer has fallen from the leading edge value interaction value to 15% greater than the free stream value. These profiles show excellent agreement with the van Driest thin shear layer, zero pressure gradient solutions. The recovery temperature for the computational results does not quite reach the Mach 8 van Driest adiabatic solution. This seems to be the result of "contamination" of the flow due to the relative coarseness of the mesh near the leading edge of the plate where the initial boundary layer growth generates a strong leading edge shock which attenuates with distance along the plate. The effect of this shock is raise the surface pressure near the leading edge and exert a pressure gradient on the flow downstream as the pressure slowly reduces to the free stream value. This also introduces a "false origin" effect. As the mesh is refined, the wall temperature moves very slowly towards its van Driest value.

Mesh independence is established for meshes with greater than 14 points across the boundary layer at this Reynolds number, and even the mesh with 7 points across the boundary layer gives a reasonable estimate of the profiles. However Fig.75 to Fig.77, which show density contours for the adiabatic wall for the different meshes, show that the 7 point mesh cannot resolve the leading edge shock properly. These contour plots also show how the density changes most rapidly near the boundary layer edge. Fig.78 shows the pressure contours for the finest mesh. The pressure is almost constant across the boundary layer (ie., vertically), and the streamwise pressure

gradient at the downstream end of the plate (where the profiles were taken) is quite small.

Fig.79 and Fig.80 show the velocity and temperature profiles for the Mach 8 isothermal wall (T_w/T_∞=6) case at Re_x=587 000 for different meshes. For this case the boundary layer pressure has fallen to $1.10p_\infty$ at the position where the profile data is taken. Again excellent agreement with the van Driest solution is seen, although slightly more points across the boundary layer were needed to resolve it accurately. This is presumably the result of a more complex temperature profile. Fig.81 to Fig.83 show the corresponding density contours for this boundary layer and different mesh sizes. The boundary layer thickness is about 25% less than the adiabatic wall case because of the wall cooling.

If a cell adjacent to the wall is of height Δy, the gradients at the wall can be calculated from the cell centered values from $(\partial u/\partial y)_w = 2u/\Delta y$ and $(\partial T/\partial y)_w = 2(T - T_w)/\Delta y$. Using the adiabatic wall temperature from the adiabatic wall computations, the heat transfer and skin friction can then be calculated for the isothermal wall case (at Re_x=587 000) from

$$St_\infty = \frac{k_w(\partial T/\partial y)_w}{\rho_\infty u_\infty C_p(T_{aw} - T_\infty)} = 3.88\times10^{-4}$$

(cf., van Driest $St_\infty = 4.04\times10^{-4}$)

$$C_{f\infty} = \frac{\mu_w(\partial u/\partial y)_w}{1/2\ \rho_\infty u_\infty^2} = 6.46\times10^{-4}$$

(cf., van Driest $C_{f\infty}=6.65\times10^{-4}$)

This yields a Reynolds analogy factor

$$S = \frac{2St_\infty}{C_{f\infty}} = 1.20 \text{ (cf., van Driest S=1.21)}$$

The skin friction coefficient can also be calculated for the adiabatic wall case, which gives $C_{f\infty}=6.14\times10^{-4}$, compared with the van Driest value of 6.07×10^{-4}.

It is also possible to compare the leading edge shock wave/boundary layer interaction predicted computationally with experimental measurements. Fig.84 shows the surface pressure

p_s/p_∞ plotted against an interaction parameter

$$\frac{M^3\sqrt{C}}{\sqrt{Re_x}}$$

where C is a constant from an equivalent temperature-viscosity relationship ($\mu/\mu_\infty=(T/T_\infty)^C$). The value of C is often taken as unity, and that is assumed here. This is also compared with the experimental results of Kendall(1957). Although there is some difference between the computational and experimental results, a few points should be noted. Firstly, Kendall's results were at Mach 5.8 and not Mach 8, and $M^3\sqrt{C}/\sqrt{Re_x}$ may not be a universal correlating parameter. Secondly, experimental results taken by different investigators of this problem show a reasonable amount of scatter between their results, and thirdly, the computational mesh near the leading edge is by necessity relatively coarse in the vertical direction. The effect of this near the leading edge can be seen quite dramatically by looking at the results of two different meshes such as Fig.75 and Fig.77. The mesh with 22 points across the boundary layer at the downstream end of the plate is twice as fine as the mesh labelled 14 points across the boundary layer. However, bearing these points in mind, the agreement with experimental results looks reasonable.

The overall agreement of the boundary layer calculations made with the laminar version of the Navier-Stokes code with known results looks very good. This then allows laminar cavity flow computations to be made with some confidence.

6.3.3 Laminar Cavity Computations

It was decided to embark upon a set of laminar cavity flow computations not from the point of view of trying to produce results that could be directly compared with the experimental data, but rather with the view of producing definitive laminar data whose flow structure may lead to a better understanding of the experimental results. It is obviously incorrect to compare the numerical values of laminar computations with turbulent experimental results, but flow features and trends in such flows may well be qualitatively the same, and much easier to identify

computationally. Indeed turbulent computations would have had to have been treated in much the same qualitative spirit for such a separated flow, as none of the turbulence models available have really been validated for complex hypersonic flows.

The computations will be planar two dimensional and have the upstream flow parallel to the cavity floor. This again differs from the experiments in that the experimental model was axisymmetric (although Charwat et.al.(1961a) found little difference between axisymmetric and two dimensional flows), and that the approach flow to the experimental cavity was angled at 5^{o} to the cavity. However, bearing in mind that direct numerical comparison with the experiments will not be possible anyway, it was decided to incorporate neither of these features, and produce two dimensional calculations that could at some future time be used as a reference flow.

A cavity length to depth ratio of 2 was chosen, which was one of the L/D values studied experimentally and where qualitatively the flow structure should be similar to the experiments. The results of other experiments also indicate that a two vortex flow structure is to be expected for this geometry. The Reynolds number based on cavity length is 3.3×10^{6} (the same as the experiments) and free stream Mach number 8.0 (also the same as the experimental value). An isothermal wall boundary condition with $T_w/T_\infty=6.0$ was used, which was the boundary condition used for one of the boundary layer computations and so allowed the correct upstream boundary layer profiles to be used. This boundary condition is also reasonably close to the experimental situation, which is approximately an isothermal wall boundary with $T_w/T_\infty=5.0$. The upstream boundary layer velocity thickness was set at 0.24 times the cavity depth which is the same as the experimental value.

A stretched mesh in both the x and y directions was used to allow better resolution of the flow where gradients are large (eg., near the cavity walls and in the separated shear layer). Stretching was limited to a 15% change in mesh size between adjacent cells, and the overall mesh size was 70x60. This

allowed approximately a factor of 10 change between the smallest and largest values of Δx and Δy. The mesh can be seen on Fig.85. The computations took place on a CDC *Cyber* 855 at Imperial College.

The calculation reached a steady state after about 40000 sec. on the *Cyber*, with no evidence of bulk unsteadiness of the flow. The physical (flowfield) time required to reach a steady state was about 1.2ms, with the pressure reaching equilibrium a factor of 4 faster than this. This is because pressure equalizes through pressure waves (travelling at the speed of sound), whereas heat transfer depends on boundary layer convection velocities which are quite low in the cavity. However this time to reach a steady state is considerably less than the typical running time for the Gun Tunnel in the experiments (15ms total run time, 5ms steady run time). This implies again that the experimental cavity flow probably did reach a steady state, since it was a turbulent flow which should reach viscous equilibrium quicker than the laminar flow of the computations. The computational result, in terms of velocity vectors, is shown on Fig.85 . On this plot vector length is proportional to velocity. The maximum velocity in the cavity is 12% of the free stream velocity, so vectors are only plotted from one cell above the cavity down, such that cavity velocities are more visible. Fig.86 shows the cavity velocities plotted in a different way. Here vector length is proportional to velocity to the power of 0.25. This enables the entire flowfield up to the free stream to be plotted, and much greater detail to be shown in the recirculating flow inside the cavity. However it must be remembered when looking at Fig.86 that small vectors indicate very small velocities.

The velocity vector plots indicate the two main vortices lying in the cavity. The primary vortex, with greater rotational strength, lies near the rear face of the cavity. The second major vortex lies near the front face of the cavity and rotates in the opposite direction to the primary vortex. Smaller vortices in the bottom corners of the cavity can also be seen. The wave structure in the cavity can be seen from the pressure, density,

and temperature contours which are shown on Fig.87, Fig.88 , and Fig.89 respectively. The pressure contours show a Prandtl-Meyer expansion emanating from the leading edge of the cavity which turns the oncoming boundary slightly into the cavity, and in doing so reduces the pressure in the shear layer by about 6%. At the trailing edge the flow is compressed as the separated shear layer reattaches to the rear lip, with the maximum reattachment pressure being about 15% above the free stream pressure. The computations indicate the dividing streamline Mach number to be approximately 0.455 before the reattachment process begins, which fits well with the assumption in Chapter 5 that reattachment pressure is approximately equal to the stagnation pressure of the oncoming streamline (a Mach 0.455 flow has a stagnation pressure 1.152 times greater than the static pressure).

Further out from the rear lip a reattachment shock forms, and behind this lies another Prandtl-Meyer expansion. Thus the wave system predicted computationally agrees well with that observed experimentally, although, as expected, the reattachment pressures are smaller than observed experimentally because the turbulent shear layer in the experiments grows faster than the laminar shear layer in the computations.

Surface pressure is plotted on Fig.90 for the entire cavity. The variable X_* is the same as that defined in Chapter 3 and on Fig.33 (ie., the total distance around the cavity starting from the leading edge). Fig.91 shows this pressure plot on an expanded scale, and it seems to agree quite well with the experimental pressure distrubutions on a qualitative basis. The pressure drops from the reattachment value with distance down the rear face under the influence of the primary vortex. A small amount of pressure recovery occurs in the bottom corner of the rear face as the flow separates before the corner. The minimum in floor pressure corresponds to, as expected, the position under the core of the primary vortex. As with the experimental results, the pressure along the front face of the cavity is relatively constant.

The boundary layers growing on the cavity walls seem to have been captured quite well, with up to 6 points across these layers. This enables the calculation of other important parameters such as heat transfer and skin friction. Fig.92 shows local Stanton number, normalized by free stream values, for the entire cavity and the afterbody, and Fig.93 shows local skin friction coefficient, also normalized by free stream values. Surprisingly, heat transfer is larger on the front face of the cavity than on the rear face. The reason for this could be that the boundary layer growing on the rear face of the cavity has retained some of the profile of the reattaching shear layer, and so is thicker because it does not grow from a definite origin. On the other hand, the boundary layer on the front face grows from virtually zero thickness near the leading lip, and so is thinner than that on the rear face, and has larger gradients and hence larger heat transfer rates. Because the separated laminar shear layer has spread more slowly than the turbulent shear layer in the experiments, the reattachment heat transfer rates are much lower than recorded experimentally. The dip in the heat transfer distribution near the middle of the cavity floor corresponds to the point of separation between the two main vortices in the cavity. The spatially averaged cavity heat transfer rate is about 80% that of the oncoming boundary layer, which is almost the same as that measured by Ginoux et.al.(1968) for a L/D=2 laminar cavity flow, although their peak reattachment heat transfer rates were somewhat higher. This, however, can be attributed to transition to turbulence of the shear layer near reattachment, which was noticed by Hahn(1969).

An interesting feature of the heat transfer results is that the heat transfer appears to go negative on the afterbody. There must, however, be a question as to whether the vertical mesh resolution of the boundary layer on the afterbody was fine enough to calculate a reversal of temperature gradient near the surface if one occured. To test this, a boundary layer calculation was made using the vertical profiles from the cavity computation two cells along the afterbody as a starting

condition for the new computation. The new mesh used was five times finer near the wall than the mesh used for the cavity computations, in order to capture any reversal of temperature gradient that might occur near the wall. These compuations took a long time to reach a steady state (about 20000 seconds on the Cyber 855) because of the fine mesh. However the results, plotted as Stanton number on Fig.94 and Skin Friction Coefficient on Fig.95 (where x is the distance downstream on the afterbody from the start of the computation), show basically the same trends as the original cavity computations. Skin friction reduces with downstream distance, levelling out at a value close to that on the forebody.

There is other experimental evidence of the heat transfer reducing on the afterbody of a cavity configuration in laminar flow. The experiments of Ginoux et.al.(1968) included a few points on the afterbody and showed heat transfer rate dropping steeply on the afterbody. However the cavity configuration for their experiments had a radius on the rear lip (with the radius equal to the step height), and so is not directly comparable. The physical reason for the heat transfer rate going negative seems to be that the inner part of the original boundary layer which carries the reversal of temperature gradient (and hence produces the heat transfer to the surface), is swallowed by the shear layer growing into the bottom of it. The inner part of the new shear layer is then also swallowed by the cavity as the shear layer reattaches, and so the flow on the afterbody shows the profile characteristics of a shear layer with the low velocity part "chopped off". A sketch of this is shown on Fig.96 . Then before viscous forces can change the inner part of the temperature profile on the afterbody, a rapid expansion occurs (as part of the shock-expansion system at reattachment) which reduces the temperature near the wall, and hence surface heat transfer rate, even further. The relatively high value of T_w/T_∞ is also a contributing factor. Subsequently, as viscous forces begin to take effect, the heat transfer rate levels out at a negative value, and will presumably climb to a positive value further downstream.

In terms of hypersonic vehicle design, this is clearly an effect that deserves further experimental investigation. It is not clear whether the same trends would be noticed for turbulent flow, where viscous forces can take effect much more quickly.

CHAPTER 7

CONCLUSIONS

7.1 Cavity Flow Structure

The flow structure for Mach 8 axisymmetric turbulent cavity flows with dimensions $0.8<L/D<2.4$ was determined at $Re=1.7x10^7/m$ and $5.5x10^7/m$ by means of Schlieren flow visualization, pressure and heat transfer measurements, and by consulting the literature. This revealed a Prandtl-Meyer expansion of the upstream boundary layer at the leading edge of the cavity, and a shock-expansion system as the separated shear layer reattaches at the downstream face of the cavity. The flow structure in the cavity seemed to change from a one recirculation vortex system, to a two vortex system for $L/D\geq2$. The primary vortex, with its centre close to the rear face, induces higher cavity velocities than the secondary vortex situated in the front half of the cavity, as evidenced by the surface pressure measurements.

7.2 Mean Cavity Pressures

Surface pressure vs time traces (and later heat transfer measurements) indicate that the cavity flow has reached a steady state by the steady run time of the tunnel. This is in accordance with expectations of physical response times, and confirmed later in the computational work. Surface pressure measurements were made in the cavity and on the afterbody of cavities with L/D=0.8, 1.2, 1.6, 2.0 and 2.4 at both the high and low Reynolds number running conditions. A large pressure rise was recorded in the area of shear layer reattachment on the rear face of the cavity (maximum pressure closest to the rear lip was 70% greater than the free stream pressure). Pressures in the remainder of the cavity were about 0.62 times the cone pressure, with this reduction relative to the cone pressure being due to

the expansion of the cone boundary layer at the leading edge of the cavity. Apart from the strength of this expansion (which was due mainly to angle of the oncoming flow relative to the cavity), the trends in the data agreed well with two dimensional planar data taken by other investigators at lower Mach numbers.

A strong Reynolds number effect was evident for the reattachment pressures. For shorter cavities, the high Reynolds number flow gave higher reattachment pressures, while for longer cavities the low Reynolds number flow gave the higher reattachment pressures. This Reynolds number dependence was explained in terms of spreading of the separated shear layer, and the effect of upstream boundary layer thickness. Pressures away from reattachment showed little Reynolds number dependence.

7.3 Fluctuating Cavity Pressures

Pressures on the cavity surface were generally steady, except for the area of shear layer reattachment on the top of the rear face of the cavity where large fluctuations were noticed (up to 60% of the mean pressure). Close inspection of the traces revealed some low frequency structure in the oscillations, and a frequency analysis showed a broad band feature at about 2.8kHz. It was hypothesised that these oscillations could have been caused by a transverse (vertical) acoustic mode in the cavity, which may have "bumped" the otherwise stable separated shear layer up and down to produce the unsteadiness in the reattachment region. Comparison with data at subsonic Mach numbers confirmed that the recorded oscillation frequency was approximately correct for a transverse acoustic mode.

7.4 Heat Transfer Measurements

Heat transfer measurements were made at both Reynolds numbers for cavities with L/D=0.8, 1.6 and 2.4. The heat transfer results followed basically the same trends as the pressure

results. Large heat transfer rates were recorded in the reattachment region (up to 2.34 times the cone forebody value), but heat transfer fell well below the cone value in the remainder of the cavity. Total heat flux to the model through the cavity walls was less than if there had been no cavity and the upstream boundary layer had passed over the cone surface. For the longest cavity studied (L/D=2.4), this total heat flux was about 1/2 the no cavity value for both Reynolds numbers.

As for the pressure measurements, strong Reynolds number effects on heat transfer rate were noticed at reattachment. The Reynolds number trends for heat transfer were basically the same as for the pressure results. Reynolds number dependence was also reflected in the values of total heat flux.

Heat transfer measurements on the cone forebody indicated a large sensitivity to gauge location in the surface. A gauge recessed 0.1mm from the surface was found to give a heat transfer rate a factor of 2 lower than a gauge flush with the surface.

7.5 Theoretical Analysis

A simple theoretical analyisis was undertaken in an attempt to gain a better understanding of the flow physics, and to extrapolate the experimental results. The flowfield was broken into 3 component parts and each analysed separately. These 3 parts were the initial turning and expansion of the cone boundary layer, the spreading of the separated shear layer, and the reattachment process at the top of the rear face.

It was found that relatively simple equations, with some empirical constants, could be used to model quite accurately the separation, spreading, and reattachment of the shear layer, and that the experimental results could, by using these analytical tools, be extrapolated to different cavity lengths. It was also possible to get a quantitative estimate of the effect of the expansion of the cone boundary layer on conditions at reattachment, which was found to reduce peak pressures more

than peak heat transfer rates. By assuming that reattachment pressure was equal to the stagnation pressure of the approaching streamline, it was possible to get an estimate of reattachment pressure right up to the rear lip of the cavity. It was found that this could be 4.5 times the cone pressure for L/D=2.4 cavity.

The limitations of the analysis were that it could only predict reattachment conditions for cavity lengths where the separated shear layer had reached a self-similar mean velocity profile at reattachment. At best, this was only valid for the L/D=2.0 and 2.4 cavities. No attempt was made to predict conditions away from reattachment.

It was found that a simple emperical relation such as

$$\frac{\dot{q}}{\dot{q}_c} = \left(\frac{p}{p_c}\right)^{1.6}$$

could be used to express the relationship between surface pressure and heat transfer rate in the reattachment region. The value of 1.6 is somewhat higher than other investigators have found for cavities with no expansion of the upstream boundary layer at the point of separation, and reflects again the fact that reattachment heat transfer rates are affected less than reattachment pressures by this expansion.

7.6 Computational Results

A Godunov-type Euler code was used as the basis for producing a laminar, operator split Navier-Stokes code. This was tested initially against known laminar boundary layer cases. The results were very accurate, and enabled hypersonic laminar cavity flow computations to be tackled with some confidence.

In a qualitative sense, the laminar cavity computations showed basically the same flow trends as the turbulent experimental results. The aim was not to compare the results quantitatively with the experiments, but to try to get a better understanding of the flow structure. A stretched mesh was used near the cavity walls to enable better resolution of the boundary

layers on these walls. Surface pressure, skin friction, heat transfer, and average cavity Stanton number seemed to be consistant with experimental laminar cavity flows. Results in the reattachment region seemed to justify the earlier assumption in the theoretical analysis that reattachment pressure is approximately equal to the stagnation pressure of the oncoming streamline.

An interesting feature of the computational result was that heat transfer on the afterbody was negative. A boundary layer calculation of the afterbody using a much finer mesh was made, and seemed to confirm the result. The reason for the negative heat transfer seemed to lie in the reattachment process, where the innner part of the shear layer is "swallowed" by the cavity, and the profile reattaching to the afterbody is rapidly expanded to produce negative heat transfer rates before viscous forces have time to act and reverse the situation. The relatively high value of $T_w/T_\infty=6$ was probably also a contributing factor.

This Godunov-type code showed little numerical diffusion, and being able to capture shocks and large flow gradients accurately, seems an ideal tool for computing separated hypersonic flows.

7.7 Proposals for Future Work

7.7.1 Experimental

Due to the uncertain nature of the spreading of the separated shear layer, especially for short cavities, experimental data on the spreading of the shear layer, including the effect of Reynolds number and initial boundary layer thickness, would be very valuable in understanding more clearly the process of reattachment. This would also allow a more accurate prediction of reattachment conditions using the simple analytical tools outlined in this work.

The laminar computational prediction of negative heat transfer on the cavity afterbody indicates that this might be a promising area for experimental study. Although a turbulent

cavity flow might not show negative heat transfer, it is possible that the heat transfer rate on the afterbody might be significantly reduced for some distance downstream.

7.7.2 Computational

The next computational task is to introduce a turbulence model into the code. These turbulent computations must then be validated against experimental results such as those produced in this study.

REFERENCES

Baldwin, B.S., Lomax, H.(1978) "Thin layer approximations and algebraic model for separated turbulent flows" AIAA Paper 78-257

Bartlett, R.P.(1981) "A study of mean and fluctuating properties of a turbulent hypersonic boundary layer" PhD Thesis, Aeronautics Department, Imperial College, 1981

Baysal, O., Stallings, R.L.(1988) "Computational and experimental investigation of cavity flowfields" AIAA J. Vol.26 No.1 Jan.1988

Ben-Artzi, M., Falcovitz, J.(1983) "A high resolution scheme for quasi 1-D flows" Proc. of the Euler Workshop, F. Angrand and R. Glowinski (Eds), India 1983. SIAM Publ.

Ben-Artzi, M. Falcovitz, J.(1984) "A second order Godunov-type scheme for compessible fluid mechanics" J. Comp. Phys. Jan. 1984 p1.

Berman, H.A., Anderson, J.D. (1982) "A numerical solution of the supersonic flow over a rearward facing step with transverse non-reacting hydrogen injection" AIAA paper 82-1002, 1982.

Bilanin, A.J., Covert, E.E. (1973) "Estimation of possible exitation frequencies for shallow rectangular cavities" AIAA J. Vol.11 No.3 March 1973 p347.

Bradshaw, P.(1980) "Compressibility effects of free shear layers" 1980-81 Stanford Conference on Complex Turbulent Flows p364.

Brown, G.L., Roshko, A.(1974) "On the density effects and large structures in the 2-D mixing layer" J. Fluid Mech. Vol.64 1974 p775

Butler, T.D.(1967) "Numerical solutions of sharp leading edge flows" Physics of Fluids 1967 p1205

Chapman, D.R.(1956) "A theoretical analysis of heat transfer in regions of separated flow" NACA TN 3792, Oct. 1956

Charwat, A.F., Roos, J.N., Dewrey, F.C., Hitz, J.A.(1961a) "An investigation of separated flows-Part 1: The pressure field" J. Aero. Sci. Vol.28 No.6 June 1961 p457.

Charwat, A.F., Roos, J.N., Dewrey, F.C., Hitz, J.A.(1961b) "An investigation of separated flows-Part 2: Flow in the cavity and heat transfer" J. Aero. Sci. Vol.28 No.7 July 1961 p513.

Clark, R.L., Kaufman, L.G.(1980) "Aeroacoustic measurements for Mach 0.6 to 3 flows past rectangular cavities" AIAA paper 80-0036, 1980.

Coleman, G.T.(1973) "Hypersonic turbulent boundary layer studies" Ph.D. Thesis, Aeronautics Dept., Imperial College, 1973.

Cook, W.J., Felderman, E.J.(1966) "Reduction of data from thin film heat transfer gauges" AIAA J. Vol.4 No.2 March 1966 p561 .

Cullotta, S., Richards, B.E.(1970) "Methods for determining conditions in real nitrogen expanding flows" VKI TN 58, Feb. 1970.

East, L.F.(1966) "Aerodynamically induced resonance in rectangular cavities" J. Sound and Vib. Vol.3 1966 p277.

Edwards, A.J.(1981) "Boundary layer studies at hypersonic speeds" Ph.D Thesis, Aeronautics Dept., Imperial College, Feb. 1981.

Eidelman, S., Colella, P., Shreeve, R.P.(1984) "Application of the Godunov method and its second order extension to cascade flow modelling" AIAA J. 1984 p1609

Emery, A.F., Loll, M., Sadunas, A.A.(1965) "Heat transfer and pressure distrubution in open cavity flow" ASME paper 65-WA/HT-37, 1965.

Gerhart, P.M., Thomas, L.C.(1974) "A model of turbulent momentum and heat transfer at points of separation and reattachment" Proc. of the Heat Transfer and Fluid Mechanics Institute, Stanford University Press, June 1974 p122.

Ginoux, J.J, Thiry, F.(1968) "Cone cavity flow at M=5.3 with injection of light, medium, and heavy gases" VKI TN 35, Nov. 1968

Godunov, S.K.(1959) "Finite difference methods for the numerical computation of discontinuous solutions of the equations of fluid dynamics" Mat. Sbornik Vol.47 p271. Also as U.S. Joint Publications Research Service 7226.

Gortyshov, Y.F., Varfolomero, I.M., Schchutan, V.K.(1982) "Study of heat transfer in separated zones formed by rectangular cavities" Soviet Aeronautics Vol.25 No.1 1982 p33 (English translation by Allerton Press, New York)

Hahn, M.(1969) "Experimental investigation of separated flows over a cavity at hypersonic speed" AIAA J. Vol.7 No.6 June 1969 p1092

Heller, H.H., Bliss D.B.(1975) "The physical mechanism of flow induced pressure fluctuations in cavities and concepts for their suppression" AIAA Paper 75-491, March 1975.

Heller, H.H., Holmes, D.G., Covert, E.E.(1971) "Flow induced pressure oscillations in shallow cavities" J. Sound and Vib. Vol.18 No.4 1971 p545.

Hillier, R.(1987) "Computation of flow past conical hypersonic wings using a second order Godunov method" 1987 AGARD Conf. Proc. 428-Aerodynamics of Hypersonic Lifting Vehicles.

Hillier, R.(1988) "Computation of diffracting shock wave flows" Numerical Methods for Fluid Dynamics 3, Ed. R.W. Morton, M.J. Baines, Clarendon Press, Oxford 1988.

Hillier, R., Graham, J.M.R.(1985) "Numerical prediction of shock wave diffraction" 15th Int. Symp. on Shock Tubes and Waves, Berkley USA 1985.

Holden, M.S.(1972) "Shock wave - turbulent boundary layer interaction in hypersonic flow" AIAA Paper 72-74, 1972.

Hopkins, E.J., Rubesin, M.W., Inouye, M., Keener, E.R., Mateer, G.C., Polek, T.E.(1969) "Summary and correlation of skin friction and heat transfer data for a hypersonic turbulent boundary layer on simple shapes" NASA TN D-5089, June 1969.

Ikawa, H., Kubota, T.(1975) "Investigation of supersonic turbulent mixing layer with zero pressure gradient" AIAA J. Vol.13 No.5 May 1975 p566

Inoue, Y., Page, R.H.(1978) "Aerothermodynamic base heating" AIAA Progress in Aeronautics and Astronautics : Aerodynamic Heating and Thermal Protection Systems, Ed. L.S. Fletcher, Vol.59 1978 p49

Johannesen, N.H.(1955) "Experiments in supersonic flow past bodies of revolution with annular gaps of rectangular section" Phil. Mag. Jan. 1955 p31.

Kays, W.M.(1966) "Convective heat and mass transfer" McGraw Hill Book Co., 1966

Keyes, J.W.(1977) "Correlation of turbulent shear layer attachment peak heating near Mach 6" AIAA J. Vol.15 Dec. 1977 p1821.

Kendall, J.M.(1957) "Experimental investigation of leading edge shock wave - boundary layer interaction at hypersonic speeds" J. Aero. Sci. Vol.24 p48.

Korst, H.H.(1956) "A theory for base pressures in transonic and supersonic flow" J. Applied Mech. Vol.23 1956 p593.

Krishnamurty, K.(1955) "Acoustic radiation from 2-D rectangular cutouts in aerodynamic surfaces" NACA TN 3487 August 1955.

Kuruvila, G., Anderson, J.D.(1985) "A study of the effects of numerical dissipation on the calculation of supersonic separated flows" AIAA Paper 85-0301, 1985.

Lamb, J.P.(1981) "Correlation of convective heat transfer for open cavities in supersonic flow" AIAA Progress in Aeronautics and Astronautics : Aerothermodynamics and Planetary Entry, Vol.77 1981 p36.

Larson, H.K.(1959) "Heat transfer in separated flows" J. Aero. Sci. Nov. 1959 p732.

Lees, L.(1956) "Laminar heat transfer over blunt nosed bodies at hypersonic flight speeds" Jet Propulsion April 1956 p259.

Lin Zhen Bin, Harvey, J.K.(1987) "An experimental study of the hypersonic turbulent boundary layer on a cold slender cone" AIAA Paper 87-1513, June 1987, also IC Aero Report 82-01.

Lowder, J.R.A.(1983) "Hypersonic turbulent separation induced by flares" Ph.D Thesis, Aeronautics Dept., Imperial College, June 1983.

Marcillat, J.(1974) "An experimental study of the near wake of a slender cone at varying incidence at M=7" J. Fluid Mech. Vol.63 1974 p195.

Martellucci, A., Trucco, H., Agnone, A.(1966) "Measurements of the turbulent wake of a cone at Mach 6" AIAA J. Vol.4 No.3 March 1966 p385.

MacCormack, R.W.(1985) "Current status of the numerical solution of the Navier-Stokes equations" AIAA 23rd Aerospace Sciences Meeting, 1985.

MacCormack, R.W.(1969) "The effect of viscosity in hypervelocity impact cratering" AIAA Paper 69-354, 1969.

MacCormack, R.W.(1982) "A numerical method for solving the equations of compressible viscous flow" AIAA J. Sep. 1982 p1275.

MacCormack, R.W.(1976) "A rapid solver for hyperbolic systems of equations" ARC Report 36 946, Oct. 1976.

McDearmon, R.W.(1960) "Investigation of the flow in a rectangular cavity in a flat plate at a Mach number of 3.55" NASA TN D-523, Sep. 1960.

McGregor, O.W., White, R.A.(1970) "Drag of rectangular cavities in supersonic and transonic flow including the effects of cavity resonance" AIAA J. Nov. 1970 p1959.

Merzkirch, W., Page, R.H., Fletcher, L.S.(1988) "A survey of heat transfer in compressible separated and attached flows" AIAA J. Vol.26 No.2 Feb. 1988 p145.

Miles, J.W.(1958) "On the disturbed motion of a plane vortex sheet" J. Fluid Mech. Vol.4 Sep.1958 p538.

Nash, J.F.(1963a) "An analysis of two dimensional turbulent base flow including the effect of the approaching boundary layer" ARC R&M 3344, 1963.

Nash, J.F.(1963b) "The effect of an initial boundary layer on the development of a turbulent free shear layer" ARC CP 682, 1963.

Needham, D.A., Elfstrom, G., Stollery, J.L.(1970) "Design and operation of the Imperial College No.2 Gun Tunnel" Imperial College Aero. Report 70-04.

Nestler, D.E.(1972) "An engineering analysis of reattaching shear layer heat transfer" AIAA Paper 72-717, June 1972.

Nestler, D.E.(1973) "Engineering analysis of reattaching shear layer heat transfer" AIAA J. Vol.11 1973 p390.

Nestler, D.E., Saydah, A.R., Auxer, W.L.(1968) "Heat transfer to steps and cavities in hypersonic turbulent flow" AIAA Paper 68-673, June 1968.

Nicoll, K.M.(1964) "A study of laminar hypersonic cavity flows" AIAA J. Vol.2 No.9. Sep. 1964 p1535.

Peyret, R., Taylor, T.D.(1983) "Computational methods for fluid flow" Springer-Verlag, 1983.

Plumbee, H.E., Gibson, J.S., Lassiter, L.W.(1962) "A theoretical and experimental investigation of the acoustic response of cavities in an aerodynamic flow" U.S. Air Force WADD-TR-61-75, 1962.

Power, G.D., Barber, T.J.(1988) "Analysis of complex hypersonic flows with strong viscous/inviscid interaction" AIAA J. Vol.26 No.7 July 1988.

Rizzetta, D.P.(1988) "Numerical simulation of supersonic flow over a two dimensional cavity" AIAA J. Vol.26 No.7 July 1988.

Rockwell, D.(1983) "Oscillation of impinging shear layers" AIAA J. Vol.21 No.5 p645.

Rockwell, D., Knisely, C.(1979) "The organized nature of flow impingement upon a corner" J. Fluid Mech. Vol.93 p413.

Roshko, A.(1955) "Some measurements of flow in a rectangular cutout" NACA TN 3488, August 1955.

Rossiter, J.E.(1966) "Wind tunnel experiments on the flow over rectangular cavities at subsonic and transonic speeds" ARC R&M 3438, 1966.

Schetz, J.A., Billig, F.S., Favin, S.(1981) "Flowfield analysis of a scramjet combuster with a conical fuel jet" AIAA J. 1981 p1268.

Schultz, D.L., Jones, T.V.(1973) "Heat transfer measurements in short duration hypersonic facilities" AGARD AG-165, 1973.

Sims, J.L.(1964) "Tables for supersonic flow about right circular cones at zero angle of attack" NASA SP-3004, 1964.

Small, R.D., Page, R.H.(1973) "Turbulent boundary shape after a corner expansion" Aeronautical J. March 1973 p146.

Stallings, R.L., Wilcox, F.J.(1987) "Experimental cavity pressure distrubutions at supersonic speeds" NASA TP 2683, June 1987.

Sullins, G.A., Anderson, J.D.(1982) "Numerical investigation of supersonic base flow with parallel fuel injection" AIAA Paper 82-1001.

Tam, C.K.W.(1976) "The acoustic modes of a two dimensional rectangular cavity" J. Sound and Vib. Vol.3 Pt.3 1966 p277.

Tam, C.K.W., Block, P.J.W.(1978) "On the tones and pressure oscillations induced by flow over rectangular cavities" J. Fluid Mech. Vol.18 Pt.2 1978 p373.

Tanner, M.(1978) "Two different theoretical approaches to the base pressure problem in two dimensional supersonic flow" Aeronautical Quarterly May 1978 p114.

Tanner, M.(1976) "Einfluß der Grenzschichtdicke auf dem Basisdruck bei zweidimensionaler und rotationssymmetrischer Überschallströmung" DFVLR Forschungbericht 76-43, 1976.

van Driest, E.R.(1952) "Investigation of laminar boundary layer in compressible fluids using the Crocco method" NACA TN 2597, Jan.1952

Wagner, R.D.(1973) "Mean flow and turbulence measurements in a Mach 5 free shear layer" NASA TN D-7366, Dec. 1973.

Wang, Z.K., Hillier, R.(1982) "The measurement of total temperature profiles in a hypersonic turbulent boundary layer on a cone in a M=9.26 flow" IC Aero TN 82-102.

Weidner, E.H., Drummond, J.P.(1981) "Numerical study of staged fuel injection for a supersonic combustor" AIAA J. 1981 p1426.

Weinbaum, S.W.(1966) "Rapid expansion of a supersonic boundary layer and its application to the near wake" AIAA J. Vol.4 No.2 Feb. 1966 p217.

White, M.E., Anderson, J.D.(1982) "Application of MacCormack's implicit method to quasi one dimensional nozzle flows" AIAA Paper 82-0992, 1982.

White, R.A.(1971) "Some results on heat transfer within resonant cavities at subsonic and supersonic Mach numbers" J. Basic Engineering Vol.93 Dec. 1971 p536.

Wieting, A.R.(1970) "Experimental investigation of heat transfer distributions in deep cavities in hypersonic separated flow" NASA TN D-5908, Sep.1970.

Wilcox, F.J. Jn(1988) "Passive venting for modifying cavity flowfields at supersonic speeds" AIAA J. Vol.23 No.2 Mar. 1988

Winter, K.G.(1976) "Notes on the measurement of aerodynamic heat transfer in model test facilities" VKI Lecture Series 86, 1976.

Woodward, P., Colella,P.(1984) "The numerical simulation of two dimensional fluid with strong shocks" J. Comp. Physics 1984 p115.

Zhang, X.(1987) "An experimental and computational investigation into supersonic shear layer driven single and multiple cavity flowfields" PhD Thesis, Engineering Dept., University of Cambridge, Oct. 1987.

HIGH REYNOLDS NUMBER	LOW REYNOLDS NUMBER
M_∞=9.26	M_∞=9.02
$T_{0\infty}$=1070K	$T_{0\infty}$=1011K
Re_∞=5.5x10^7/m	Re_∞=1.7x10^7/m
p_∞=2473N/m^2(0.36psi)	p_∞=706N/m^2(0.103psi)
T_∞=58.6K	T_∞=58.5K
p_c=5290N/m^2(0.77psi)	p_c=1511N/m^2(0.22psi)

Table 1. Free Stream Values

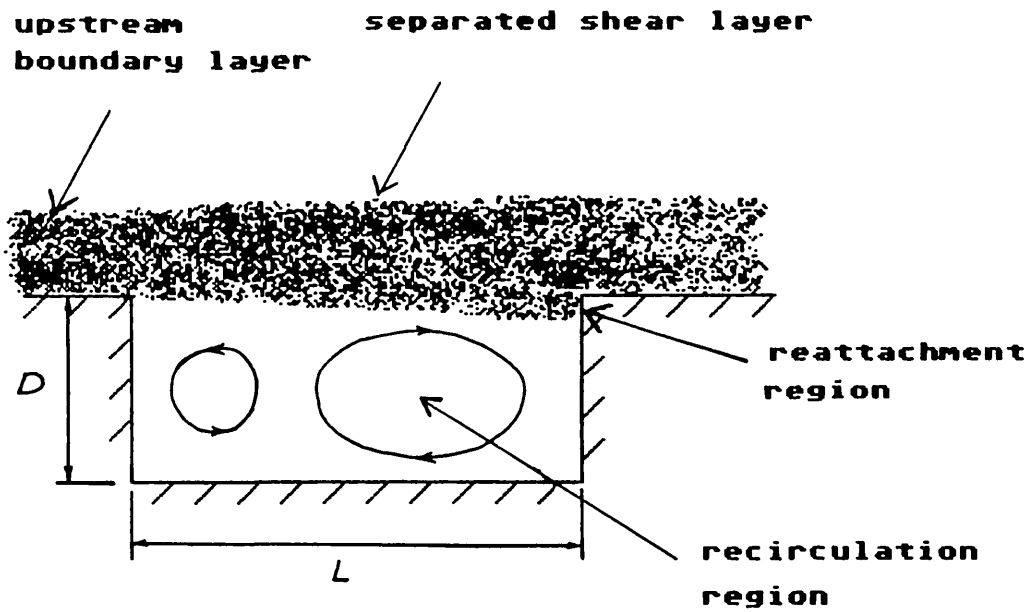

Fig.1 Cavity flow schematic

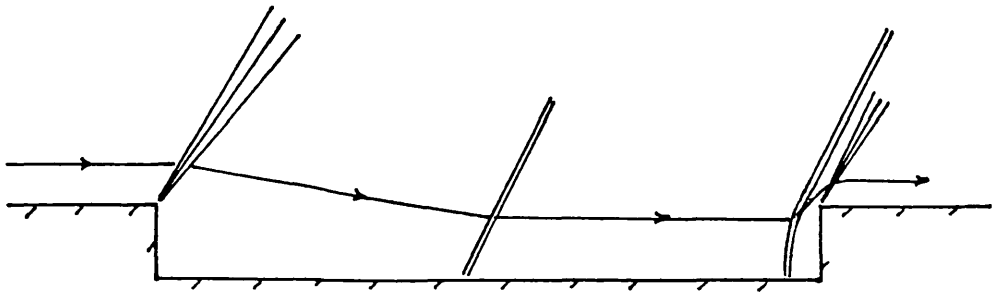

Fig.2a Closed cavity flow

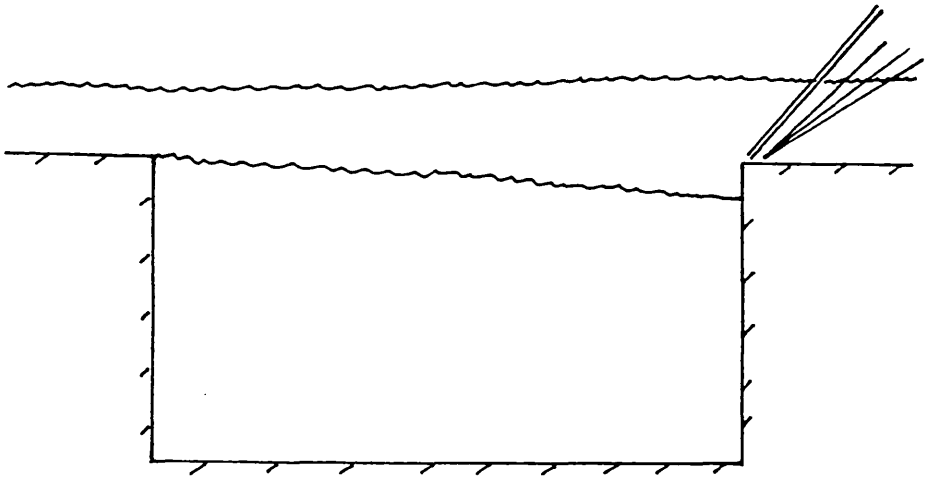

Fig.2b Open cavity flow

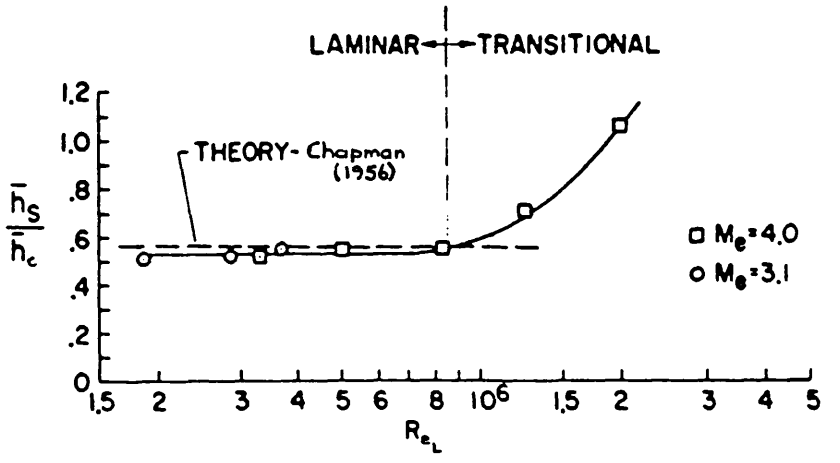

Laminar heat transfer, axially-symmetric flow.

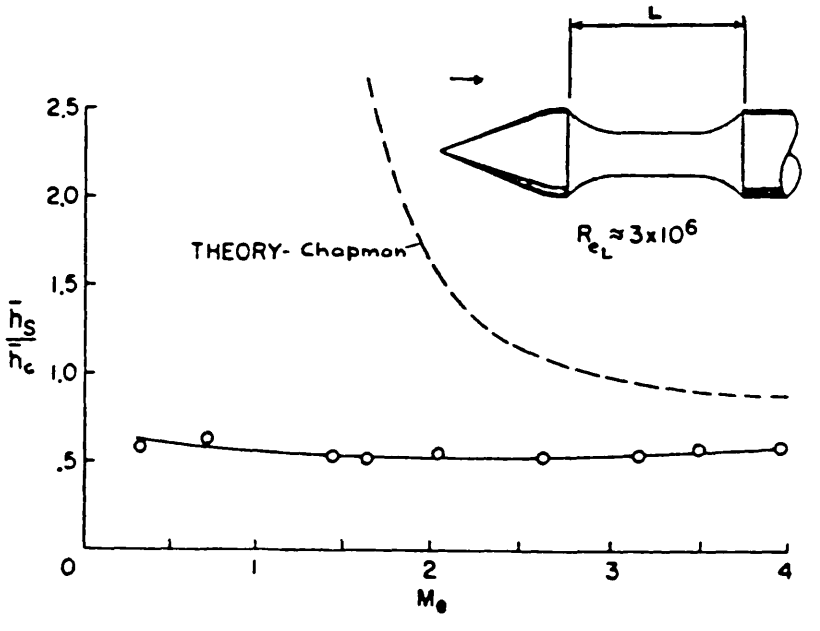

Turbulent heat transfer.

Fig.3 Average cavity heat transfer coefficient (normalized by the value on the forebody), from Larson(1959)

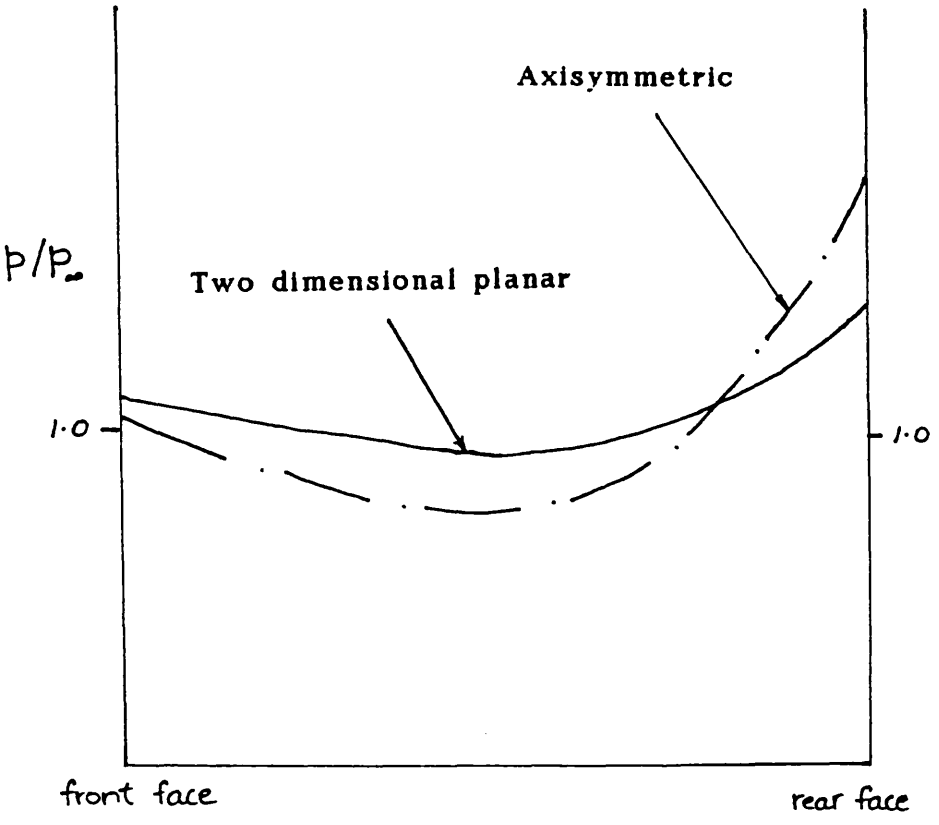

Fig.4 Typical cavity floor pressures for axisymmetric and planar cavities

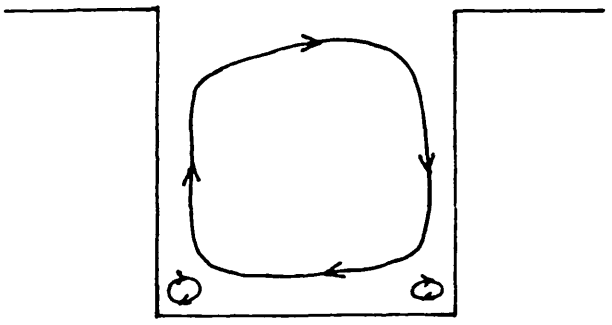

L/D < 2

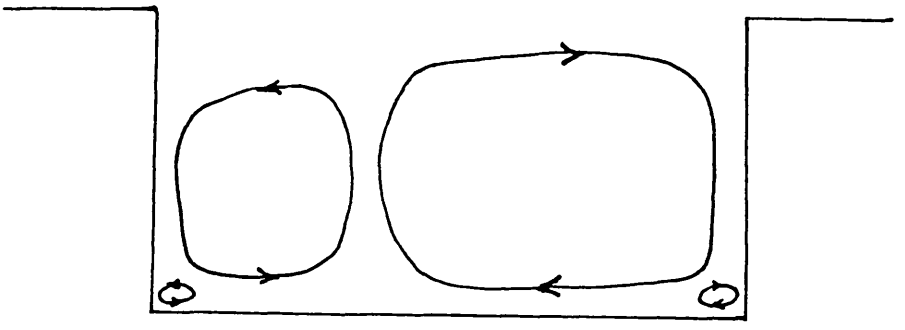

L/D > 2

Fig.5 Schematic of single and double vortex systems

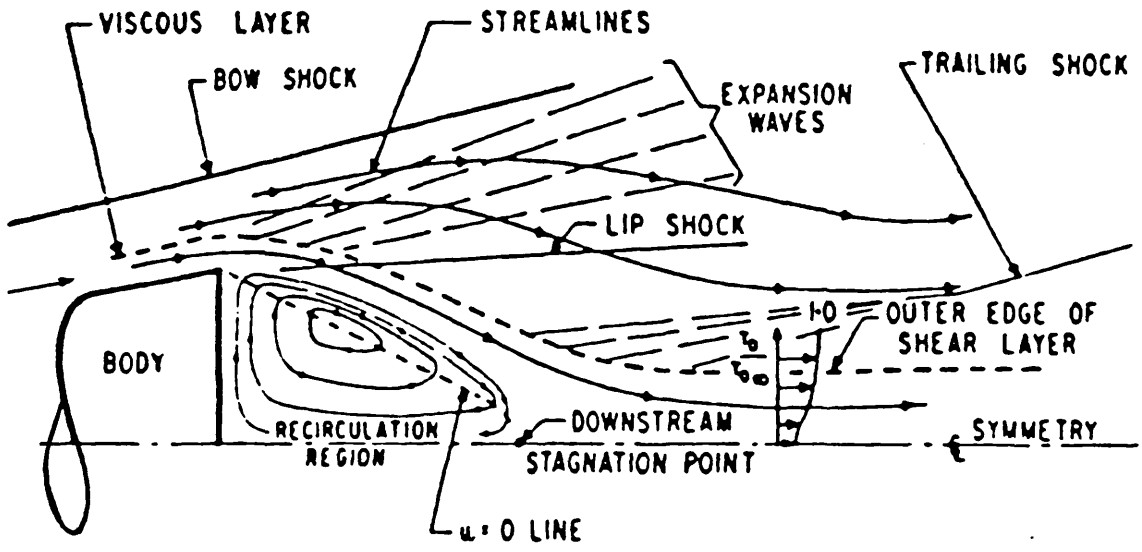

Fig.6a Base flow schematic

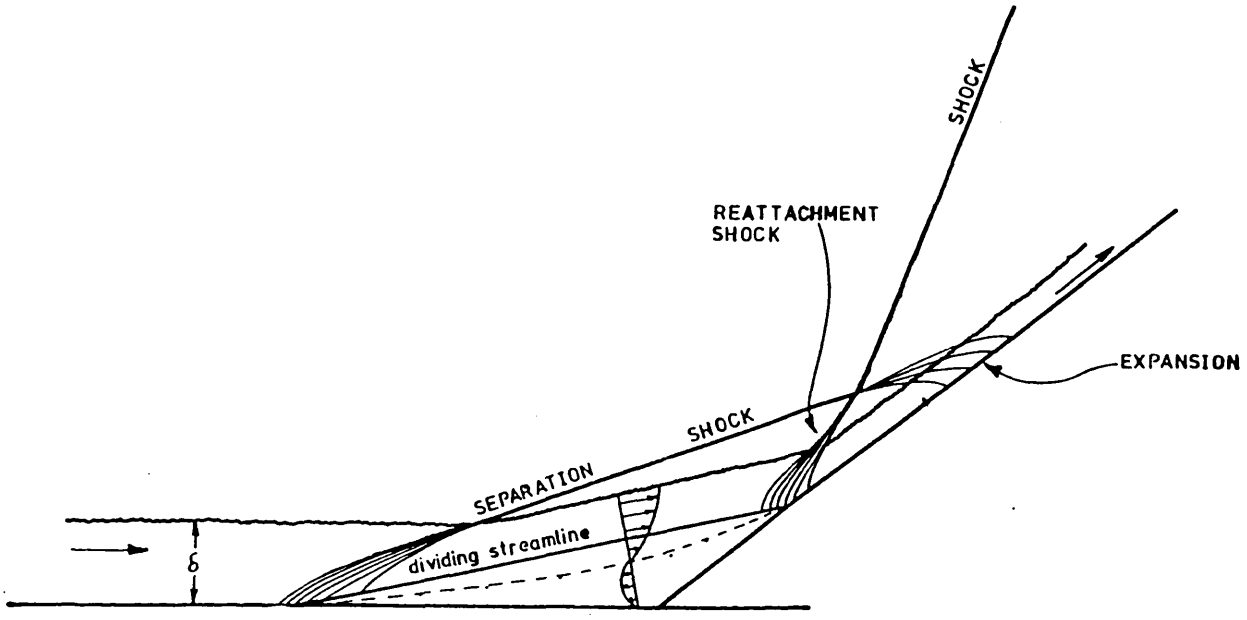

Fig.6b Schematic of supersonic flow at a compression corner

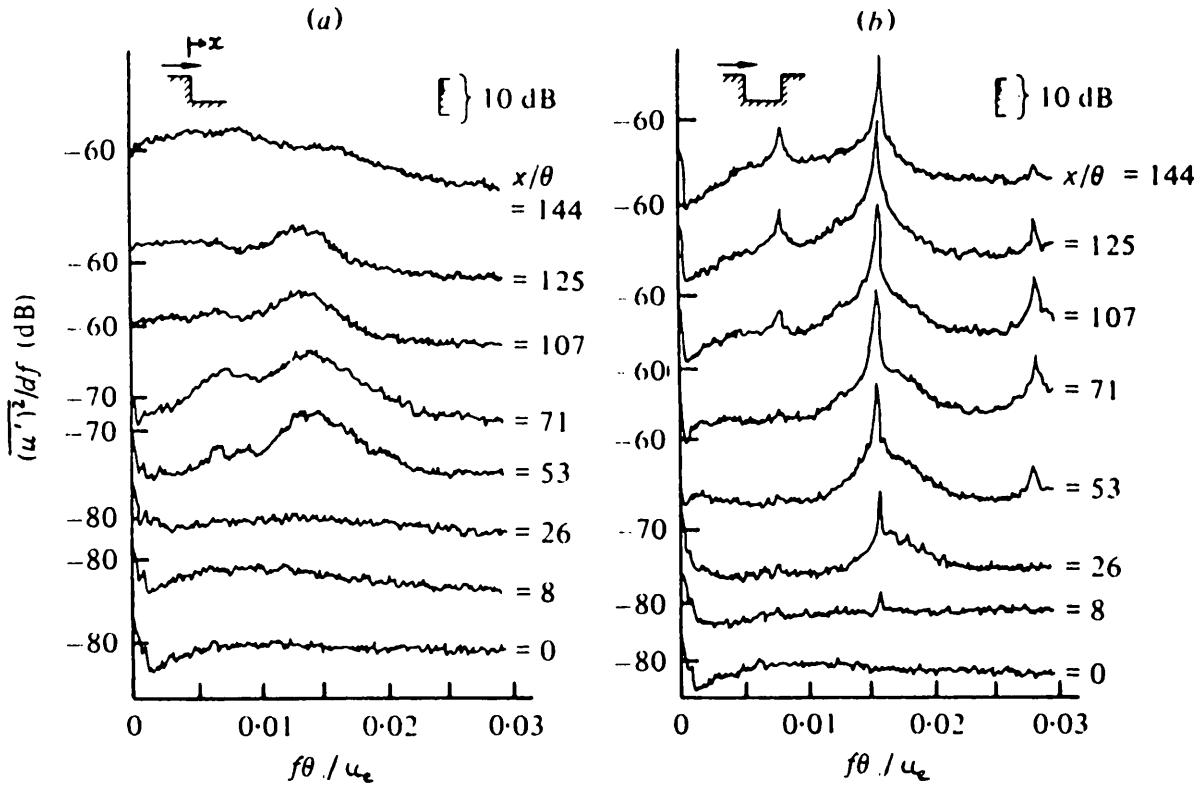

Comparison of streamwise evolution of velocity spectra with and without the cavity impingement edge at corresponding locations in the cavity shear layer ($u/u_e = 0{\cdot}95$).

Fig.7 Shear layer velocity fluctuations for a cavity and rearward facing step from Rockwell and Knisely(1979)

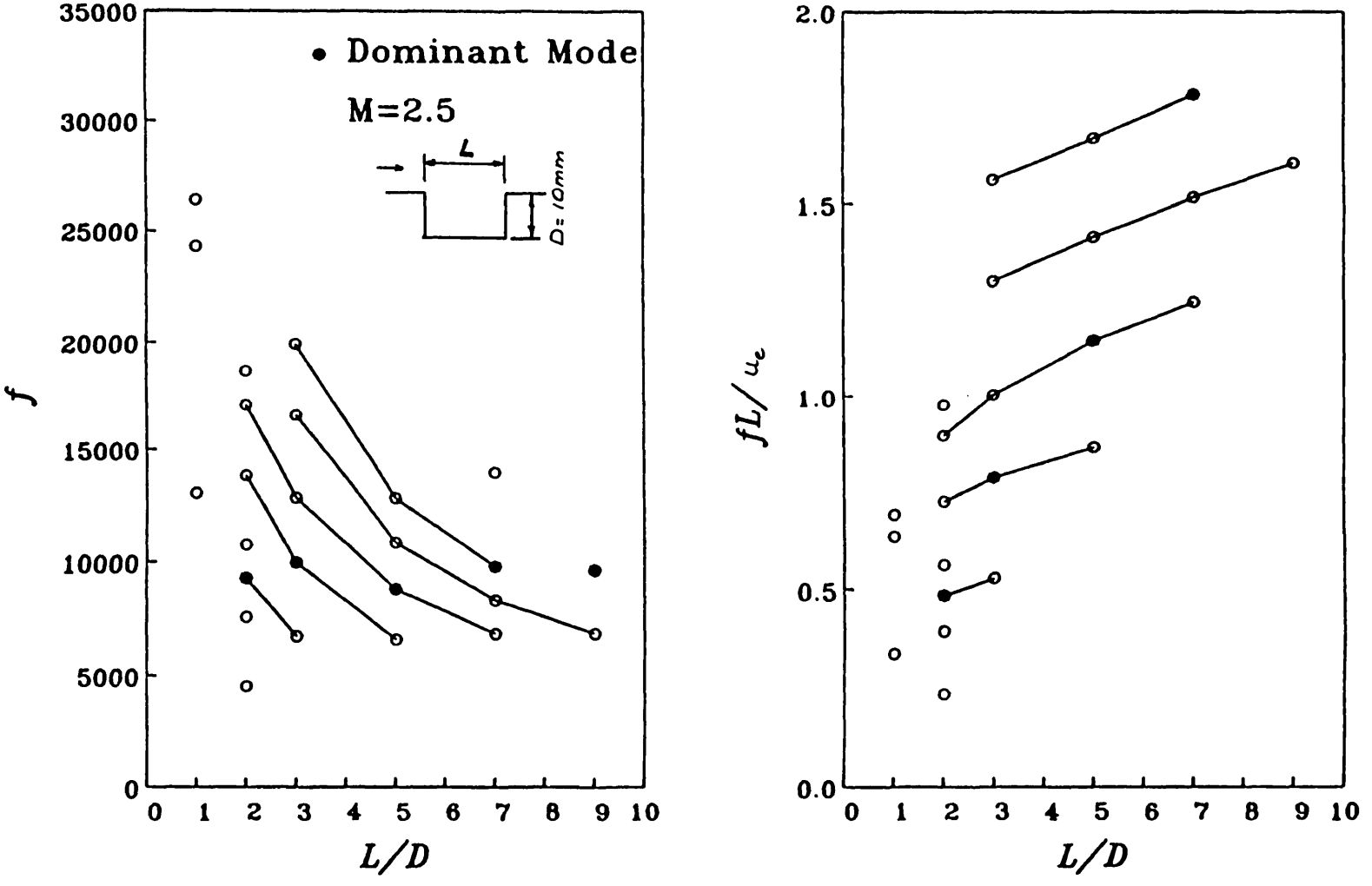

Fig.8 Cavity oscillation frequencies from Zhang(1987)

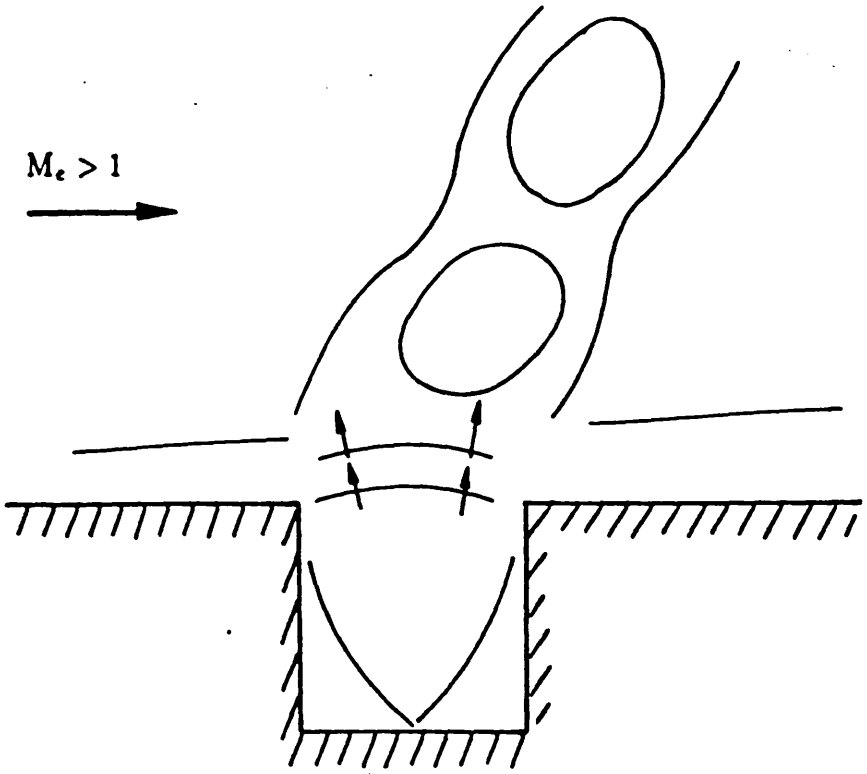

A schematic of the transverse oscillation.

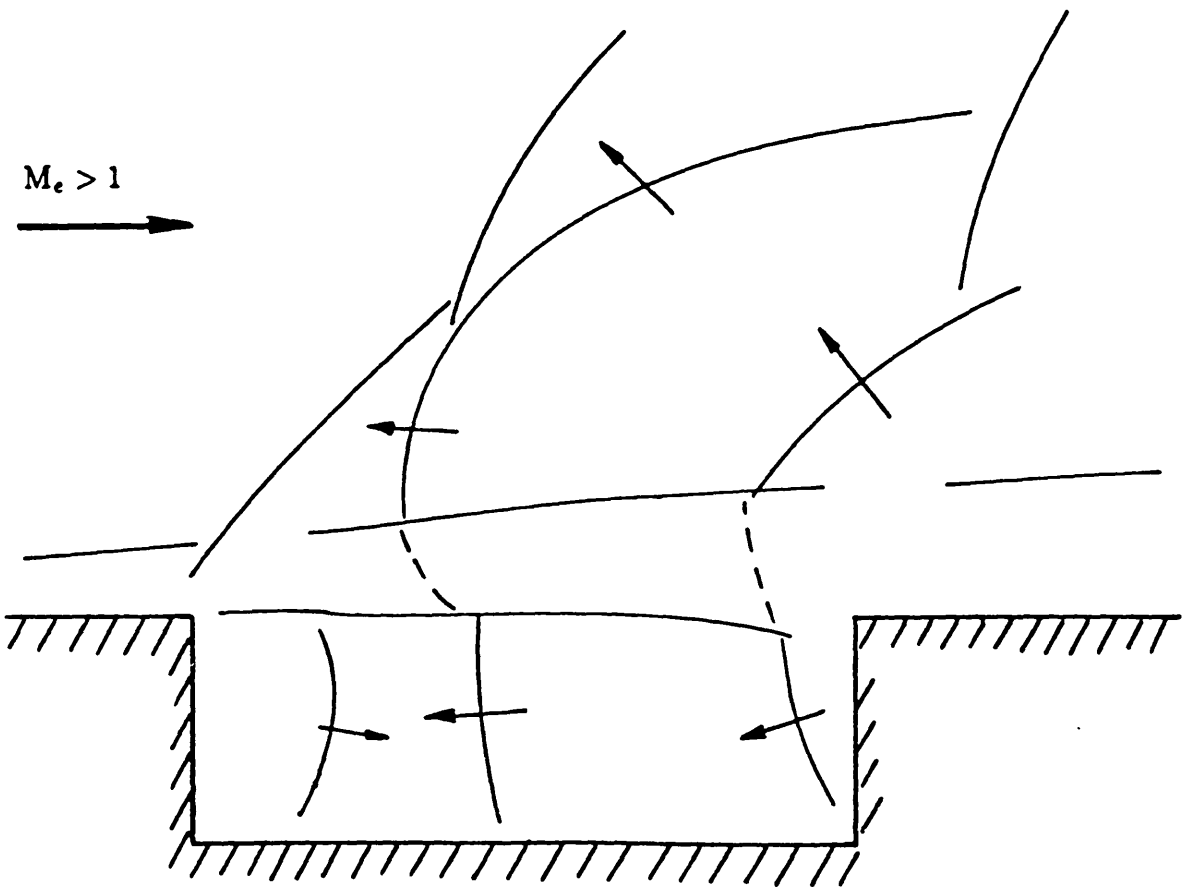

A schematic of the longitudinal oscillation.

Fig.9 Schematic of oscillation modes from Zhang(1987)

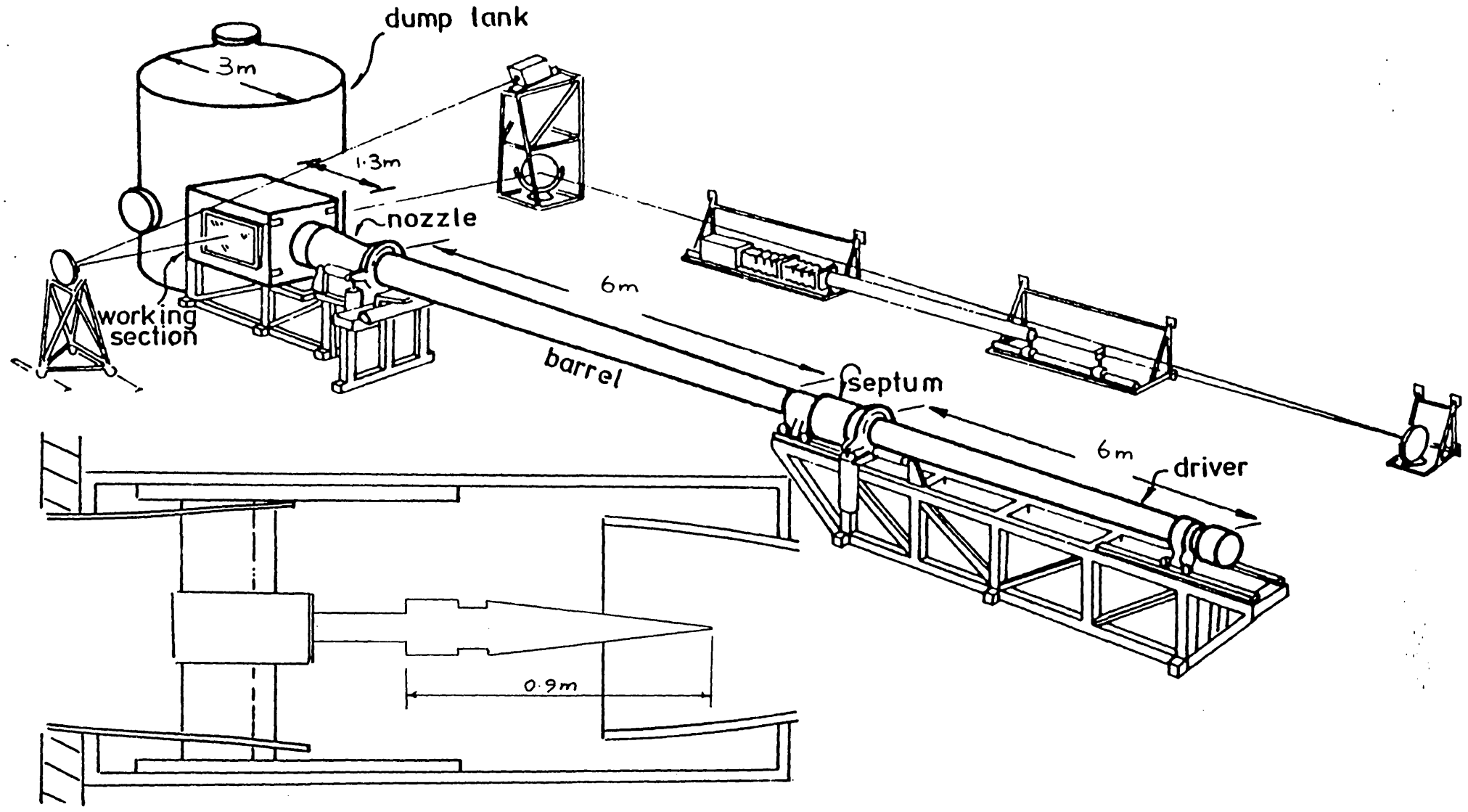

Fig.10 Experimental facility

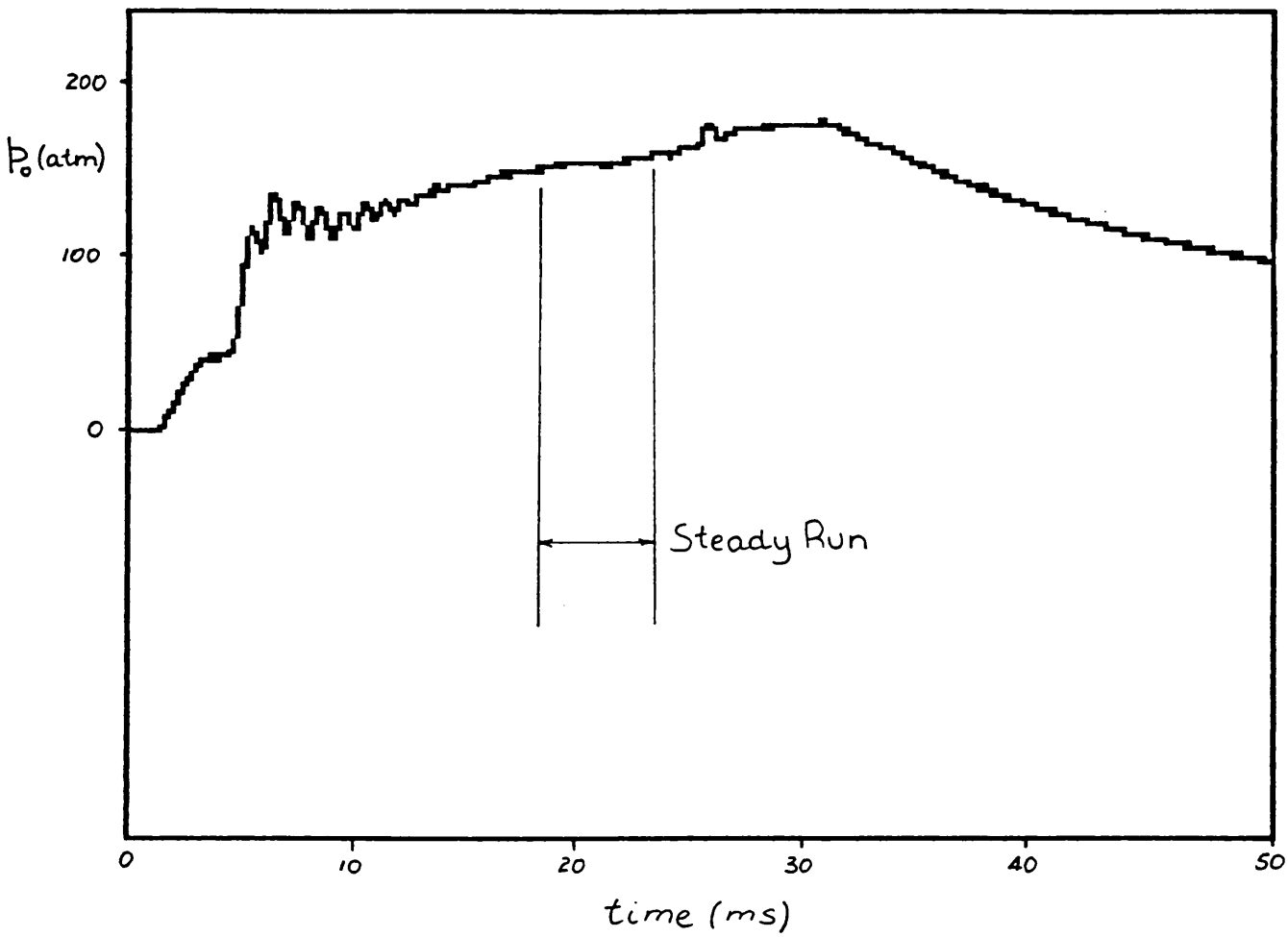

Fig.11 Typical total pressure trace

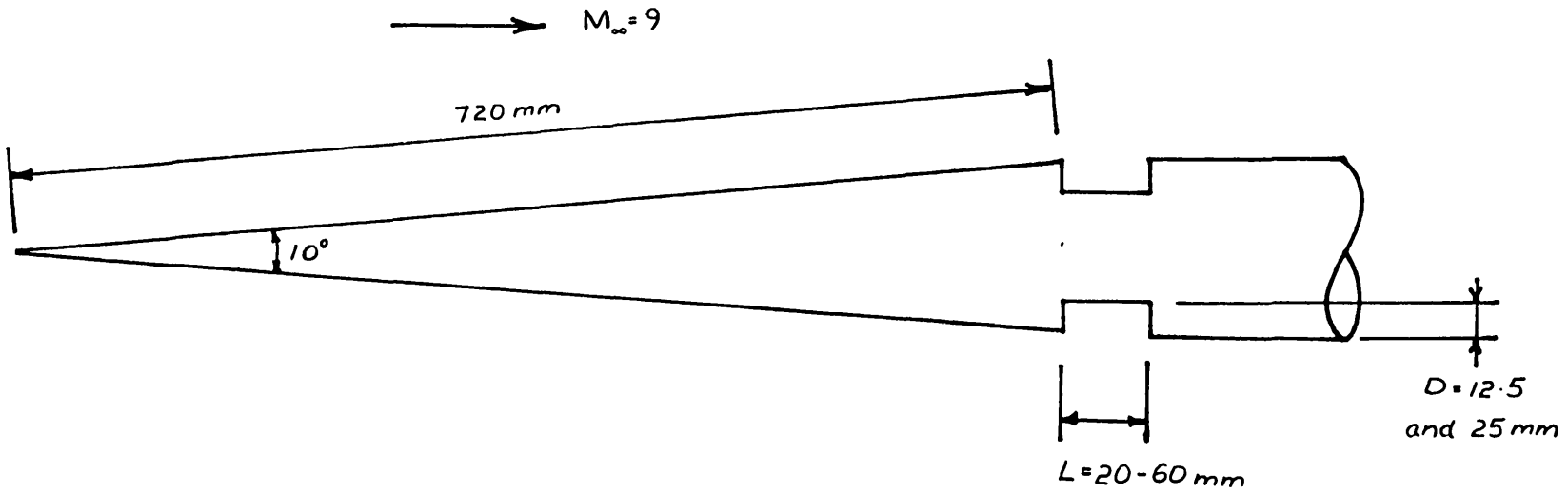

Fig.12 Schematic of model

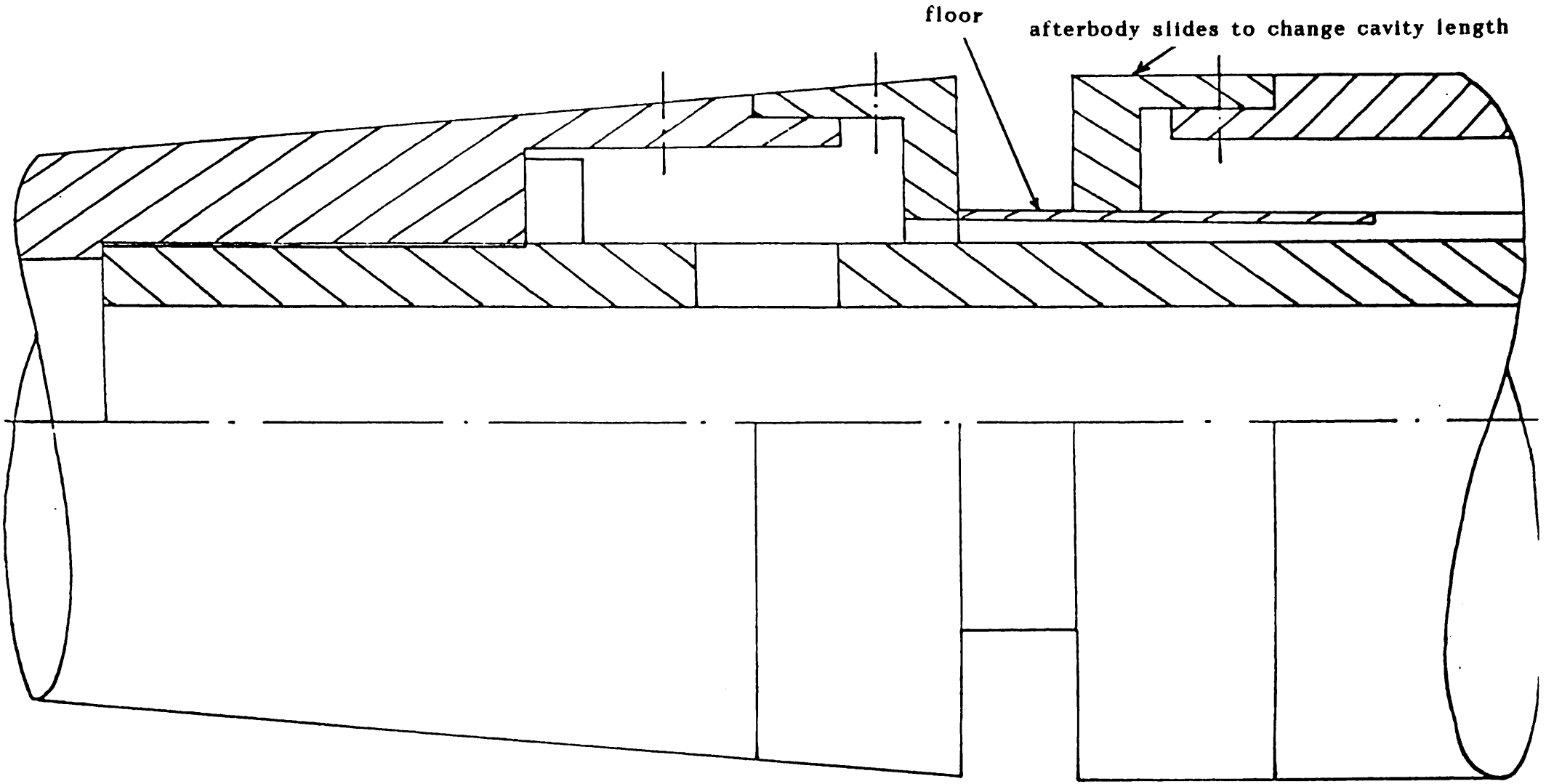

Fig.13 Cavity section of model

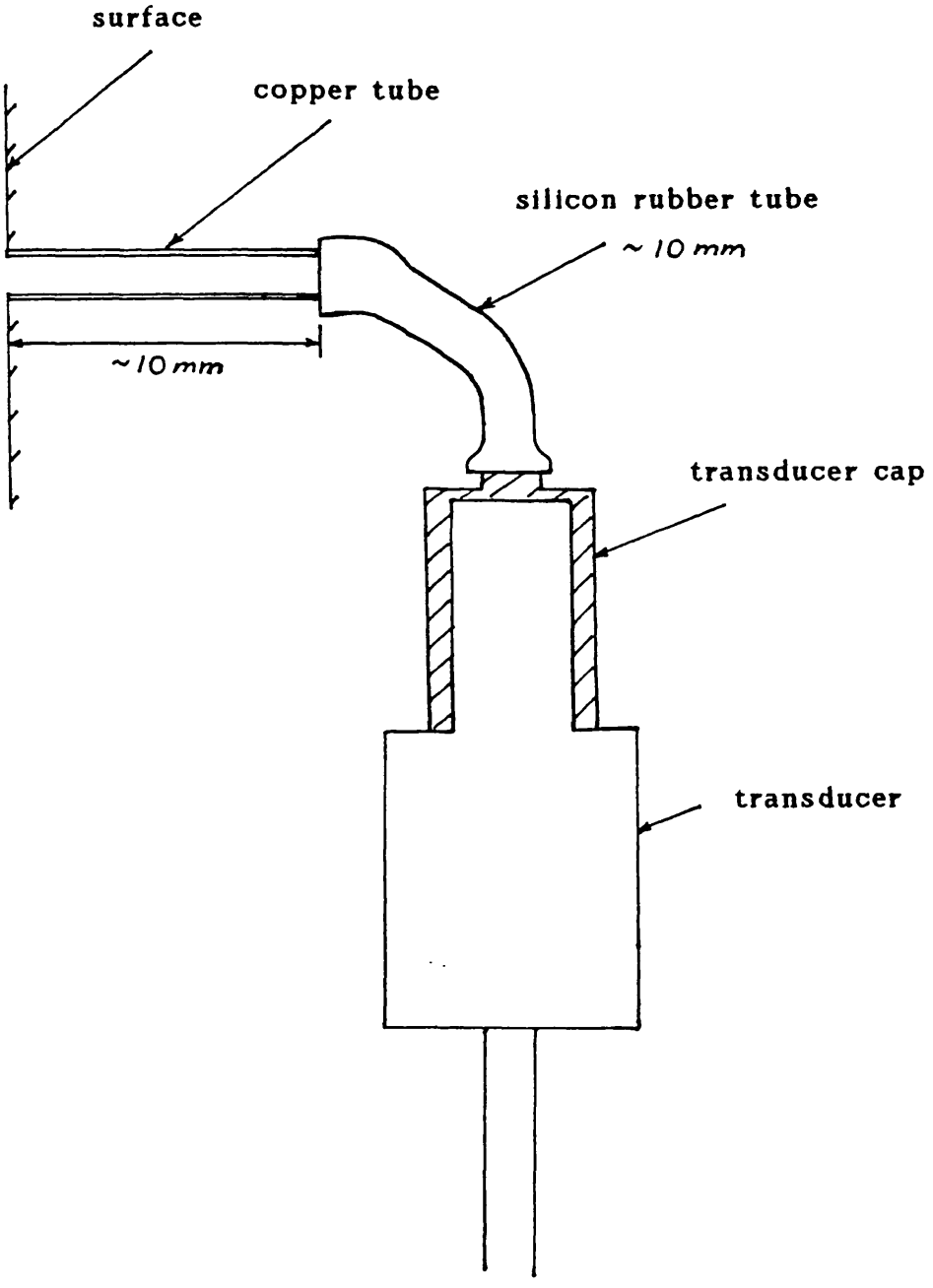

Fig.14 Static pressure instrumentation

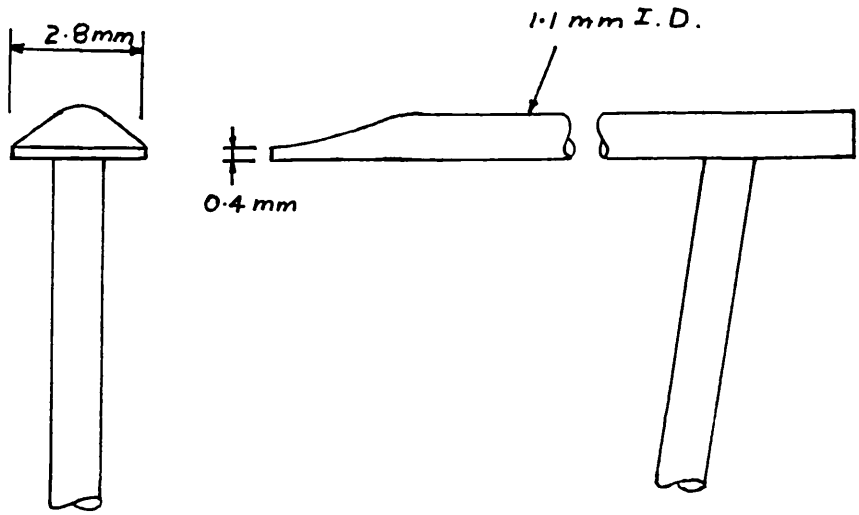

Fig.15 Pitot tube

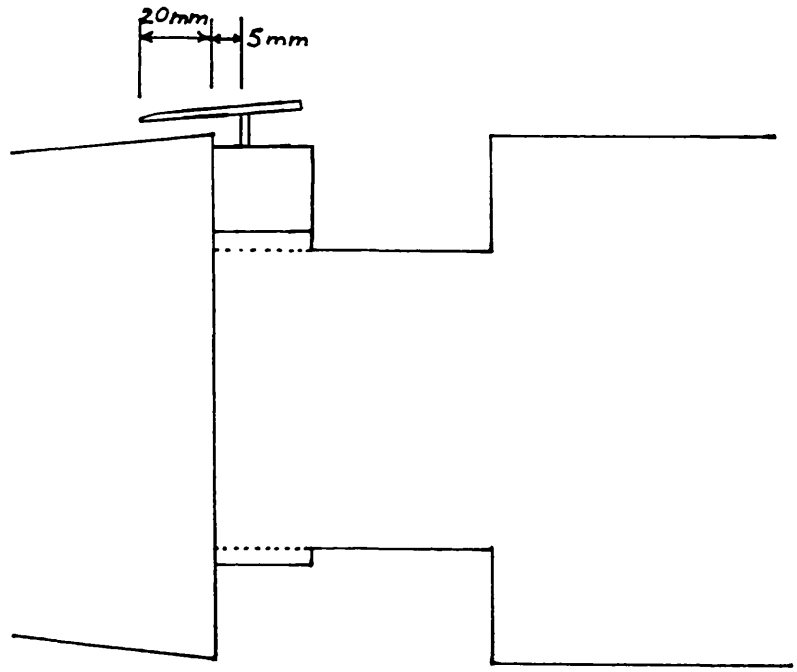

Fig.16 Pitot clamp arrangement

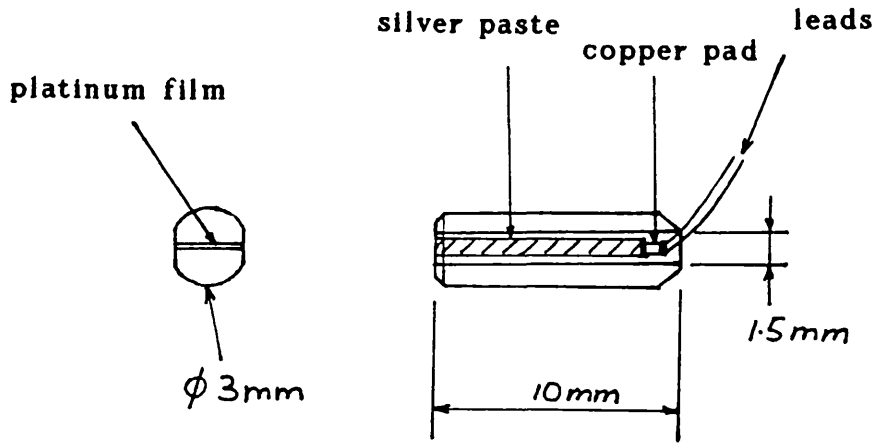

Fig.17 Heat transfer button gauges

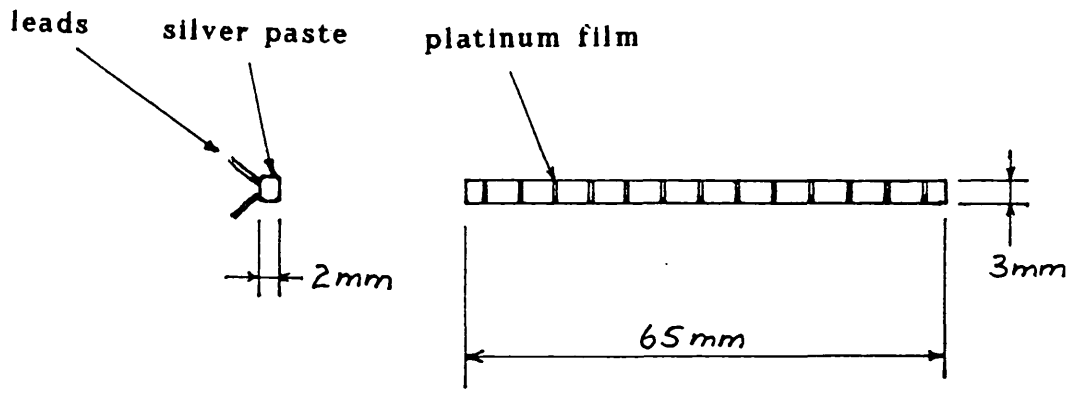

Fig.18 Heat transfer strip gauges

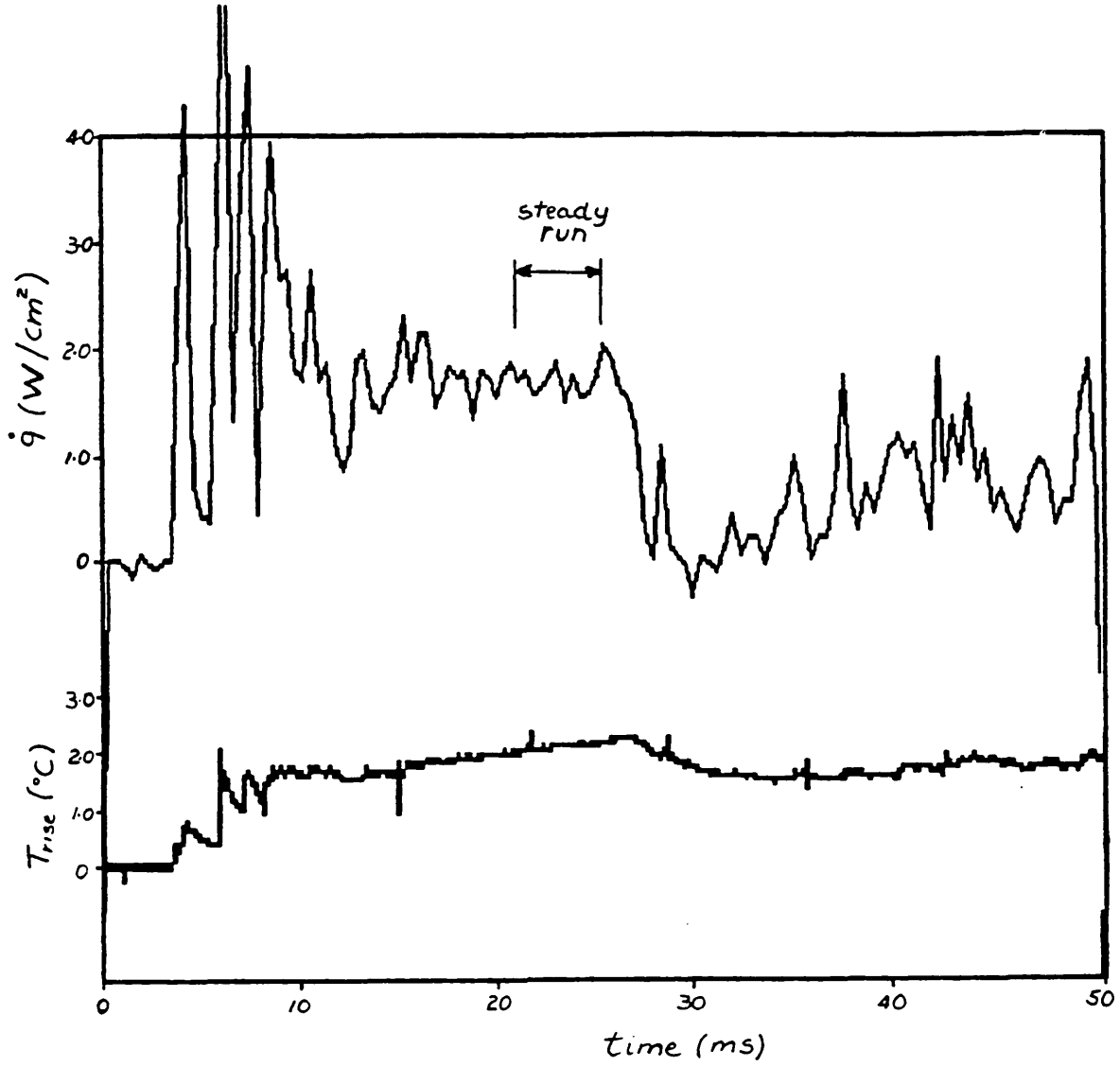

Fig.19 Surface temperature and corresponding heat transfer traces

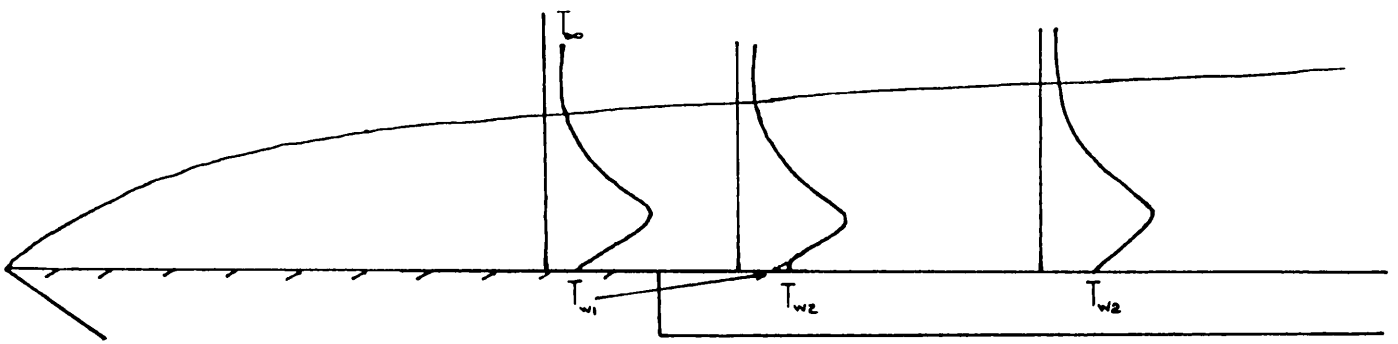

Fig.20 Effect of surface temperature discontinuity on thermal boundary layer

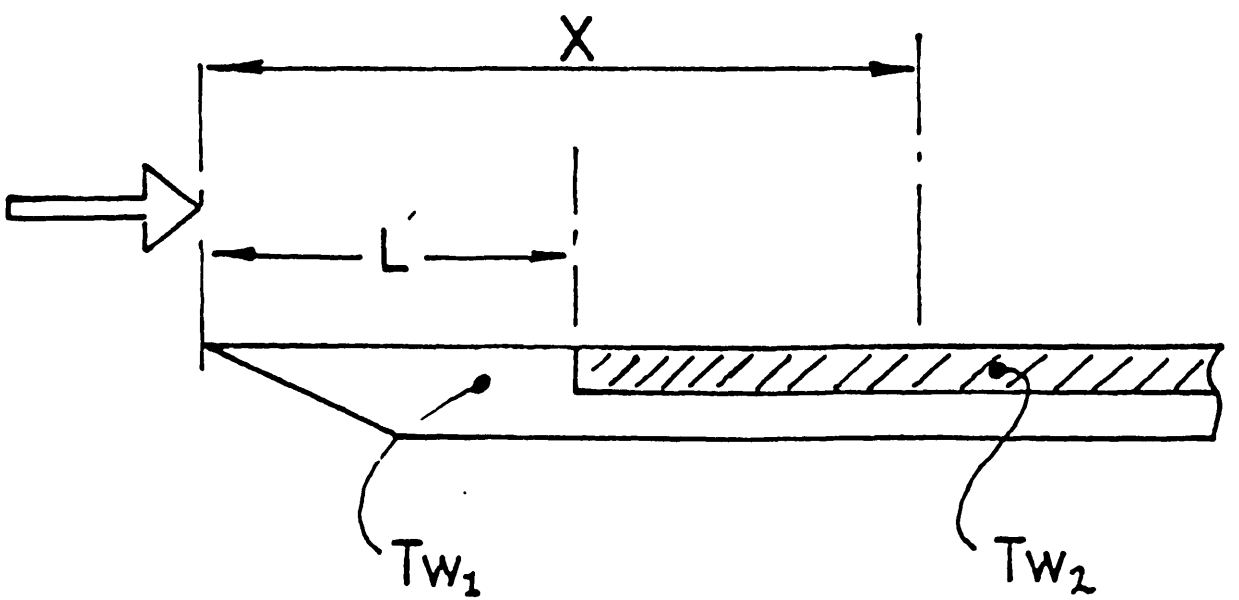

Fig.21 Co-ordinates for surface temperature discontinuity analysis

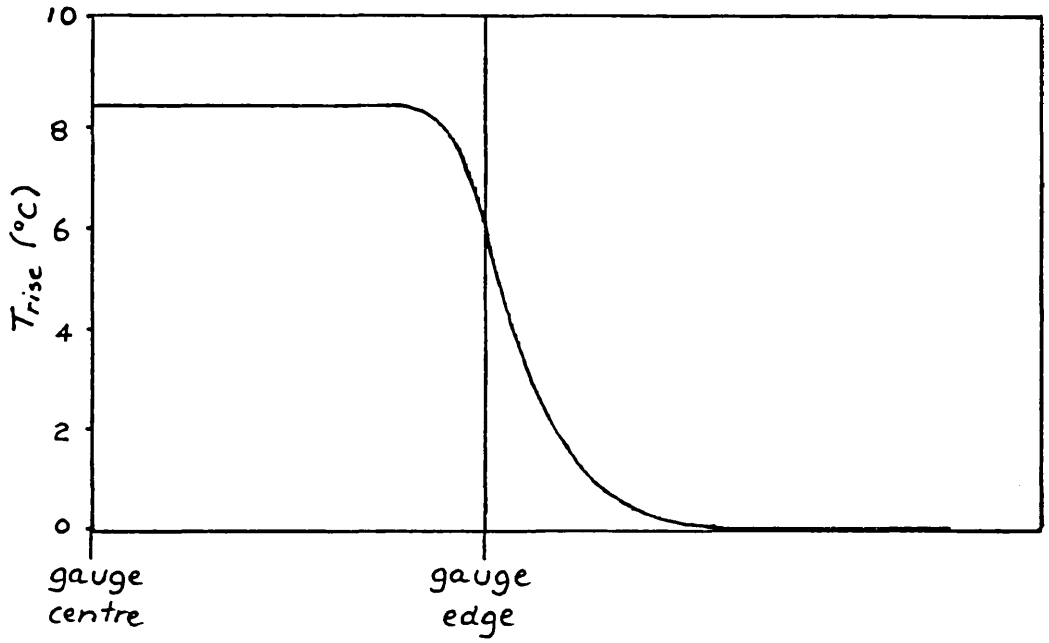

Fig.22 Heat leakage from gauge edge

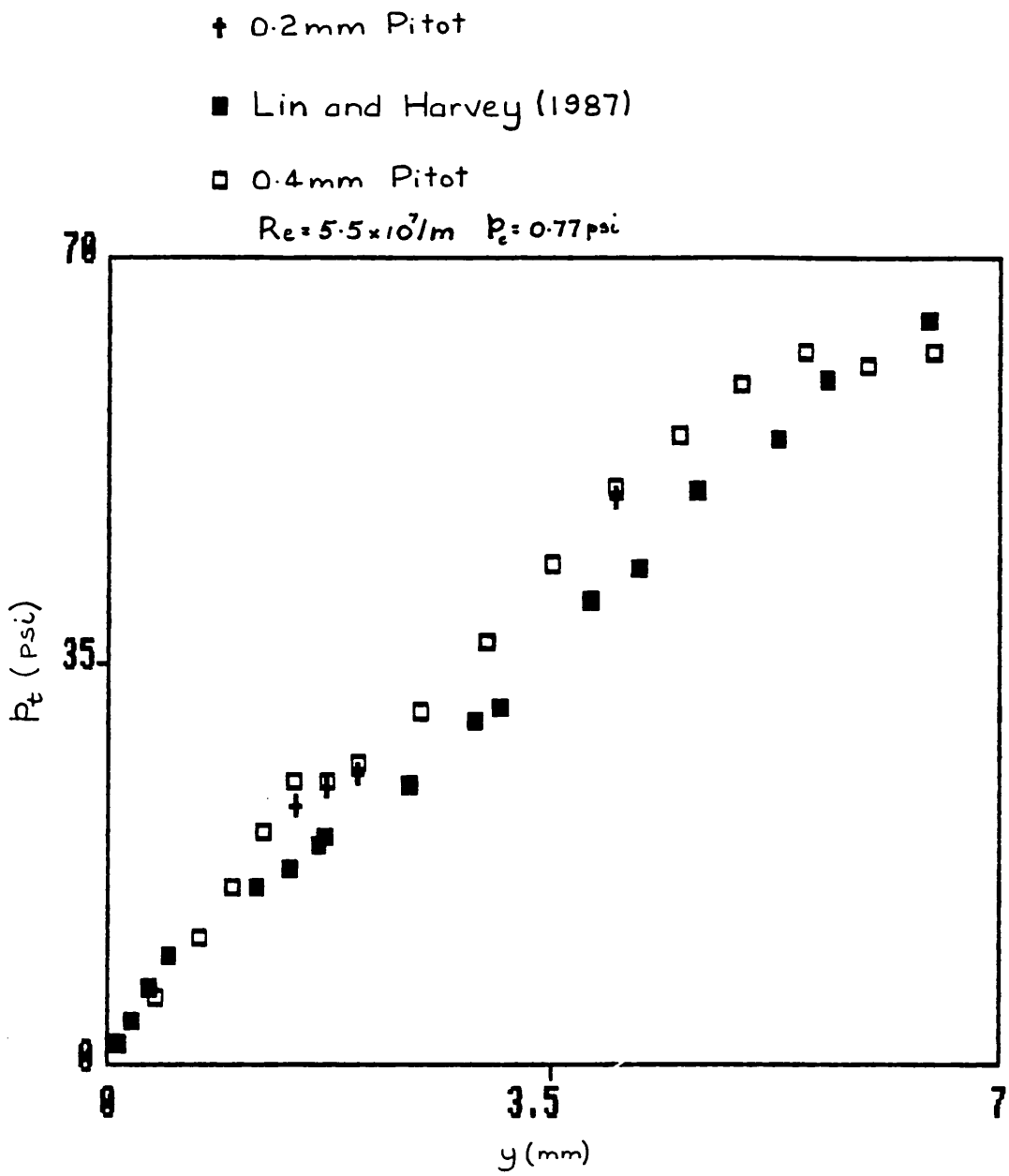

Fig.23 Pitot pressure vs height for upstream boundary layer

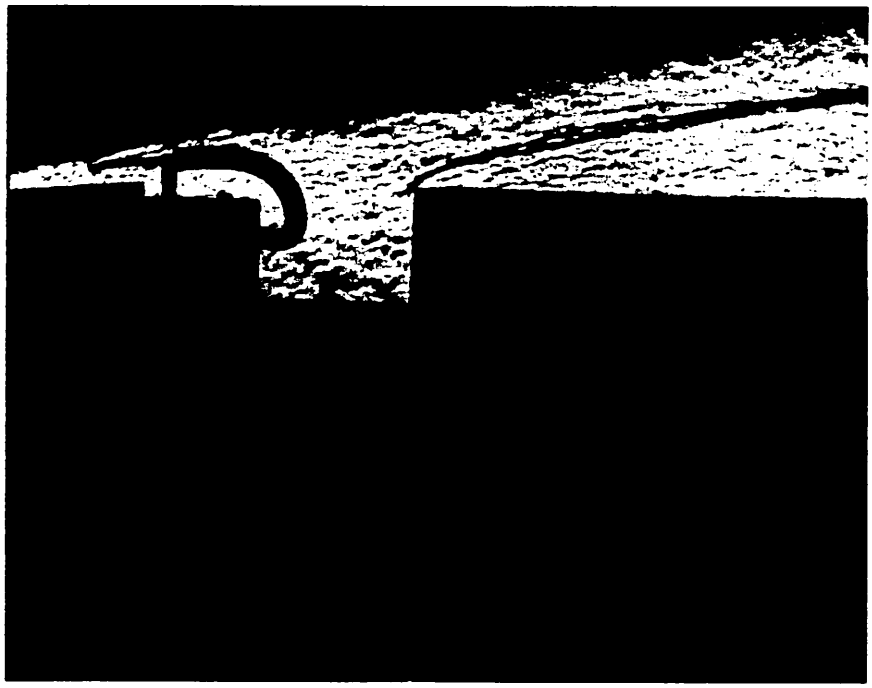

Fig.24 Schlieren photograph of pitot tube

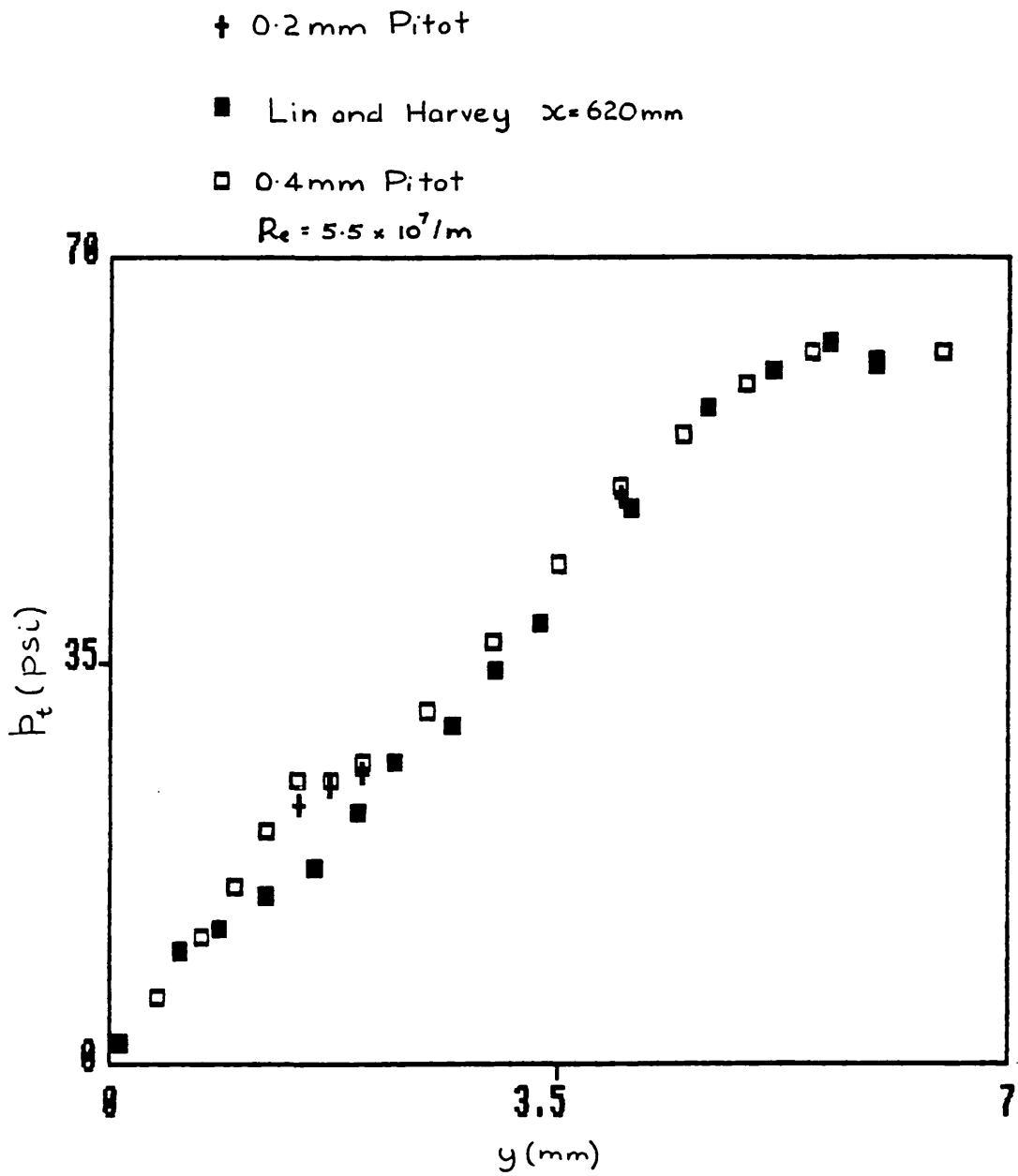

Fig.25 Pitot pressure vs height for upstream boundary layer

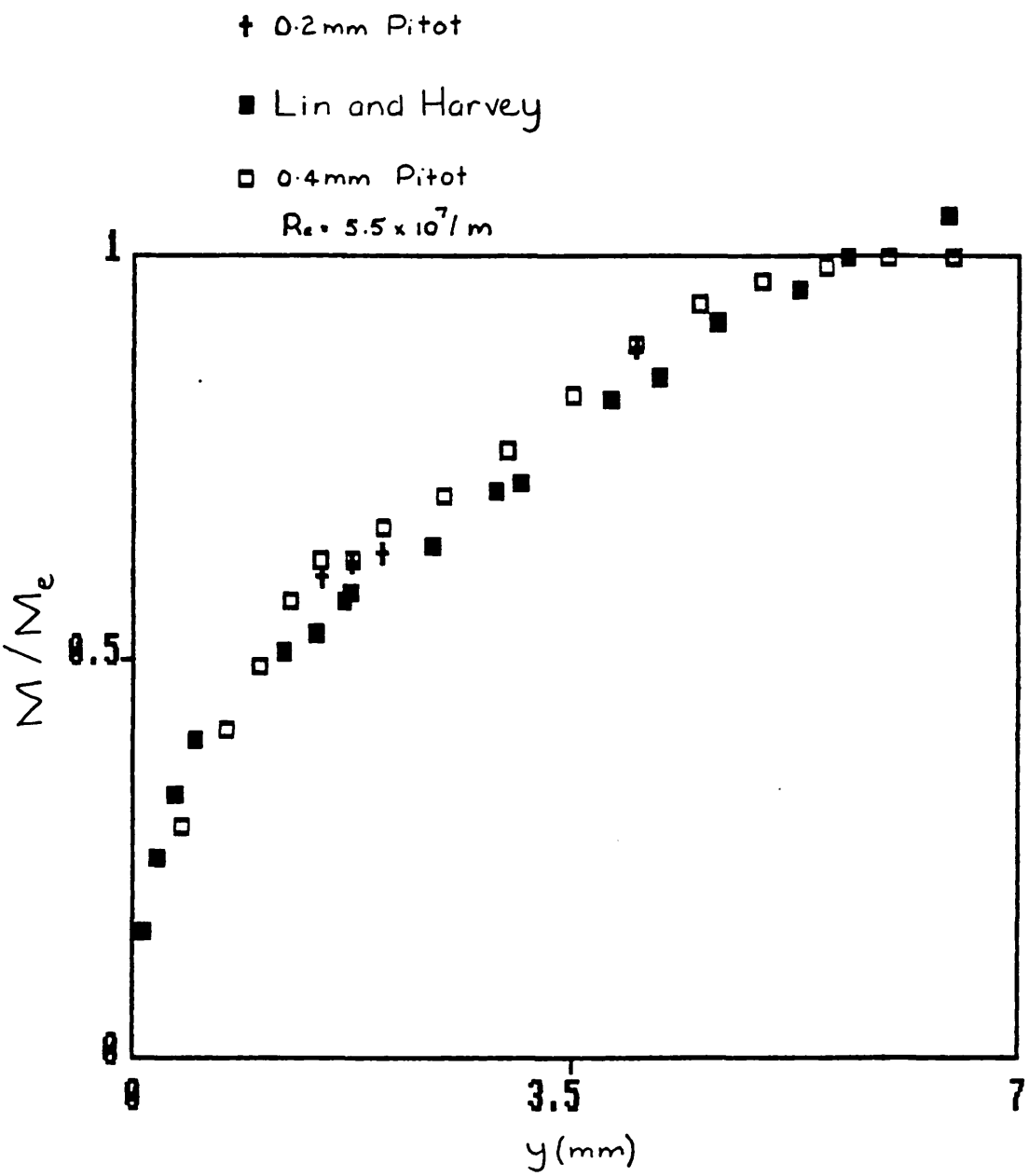

Fig.26 Mach number vs height for upstream boundary layer

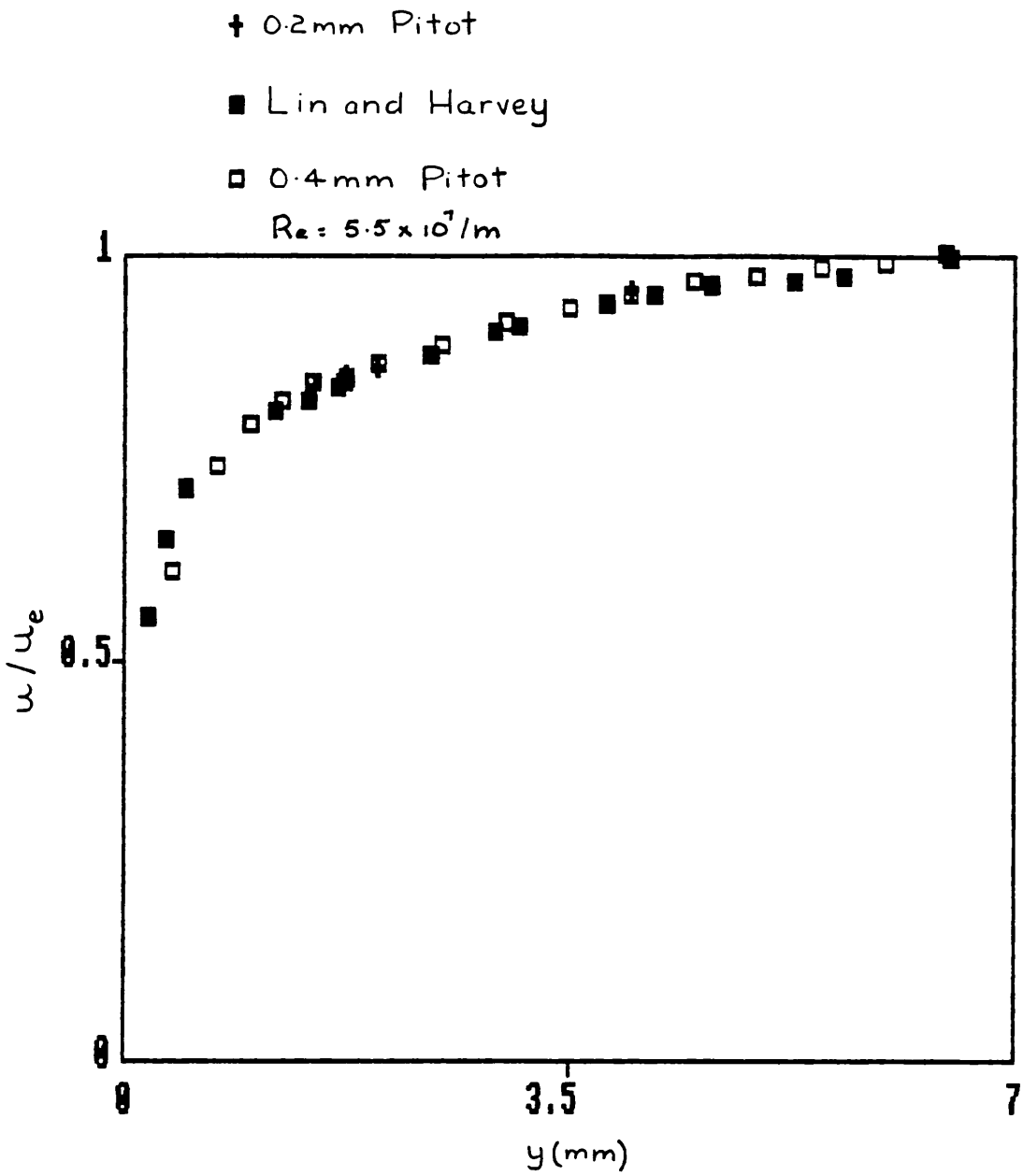

Fig.27 Velocity vs height for upstream boundary layer

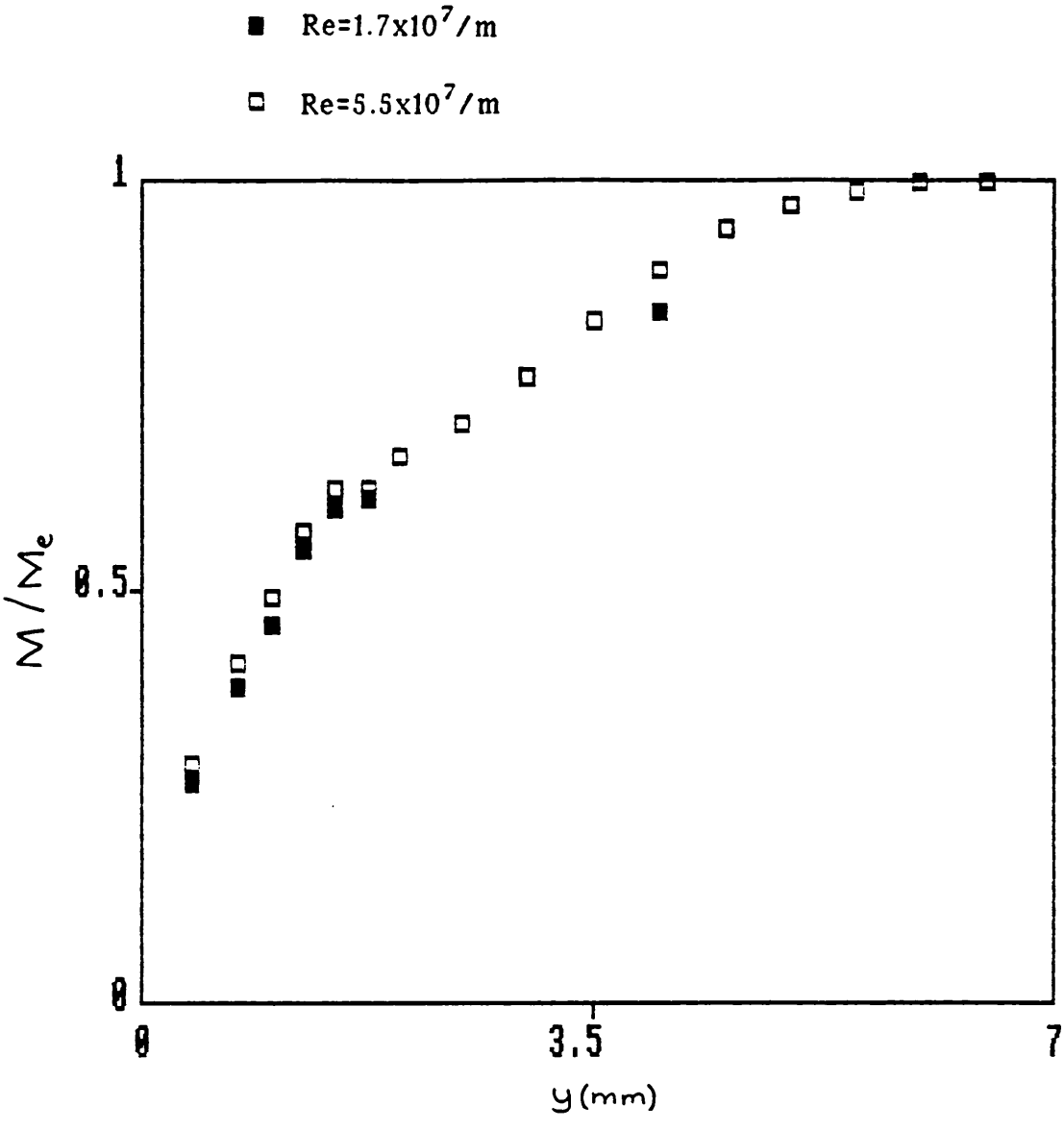

Fig.28 Mach number vs height in boundary layer for two Reynolds numbers

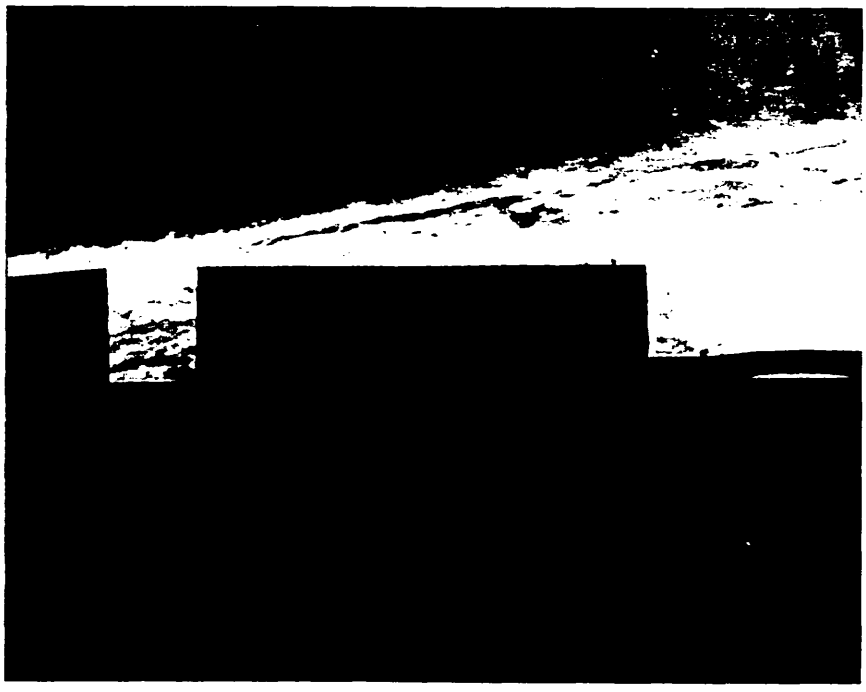

Fig.29 Schlieren photograph for L/D=0.8 cavity

Fig.30 Schlieren photograph for L/D=1.6 cavity

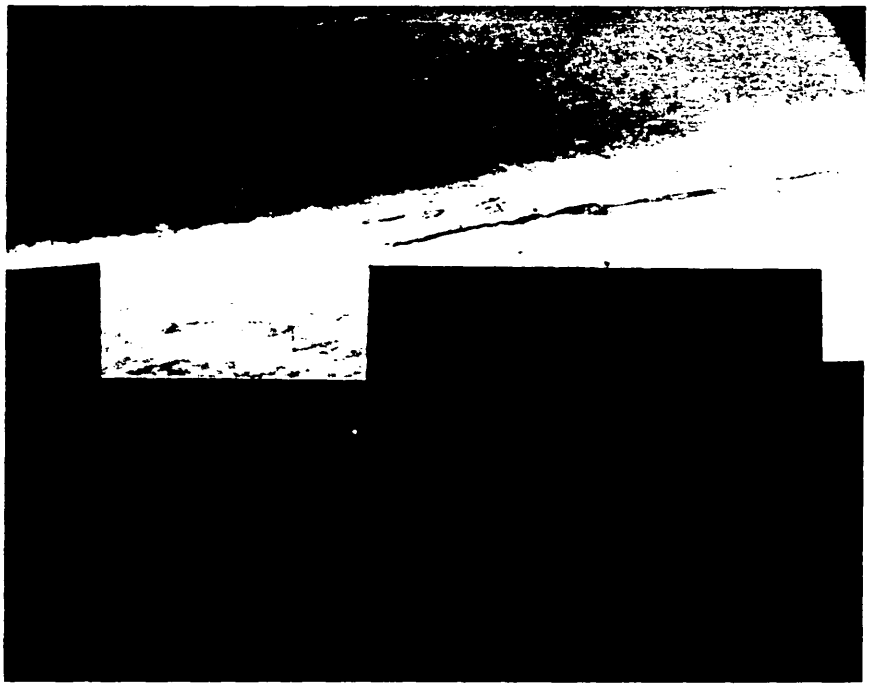

Fig.31 Schlieren photograph for L/D=2.4 cavity

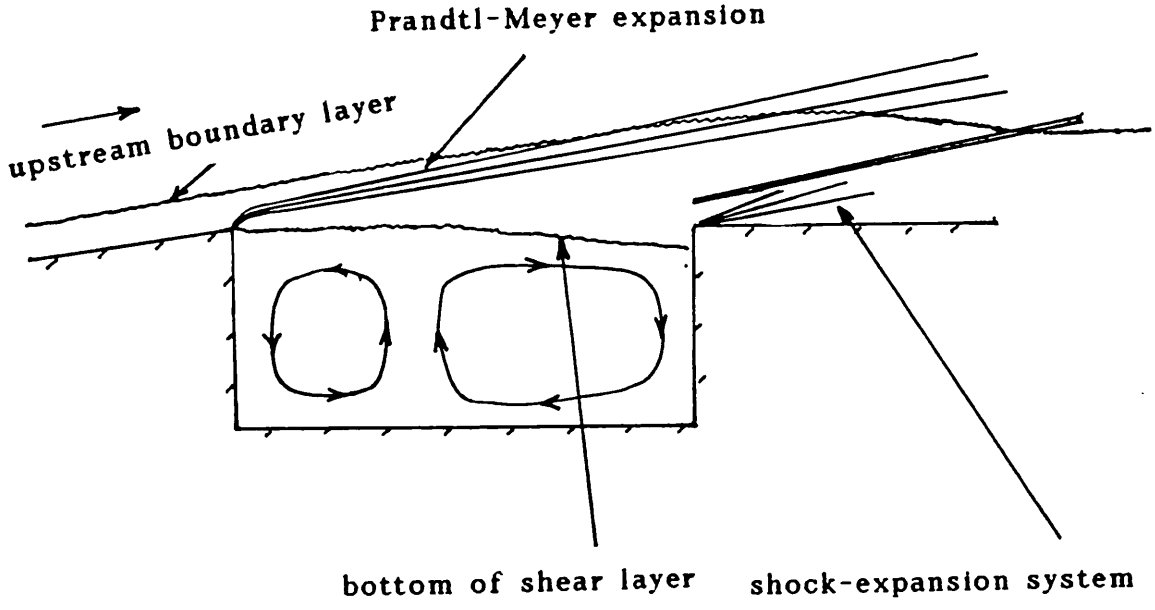

Fig.32 Schematic of cavity flowfield

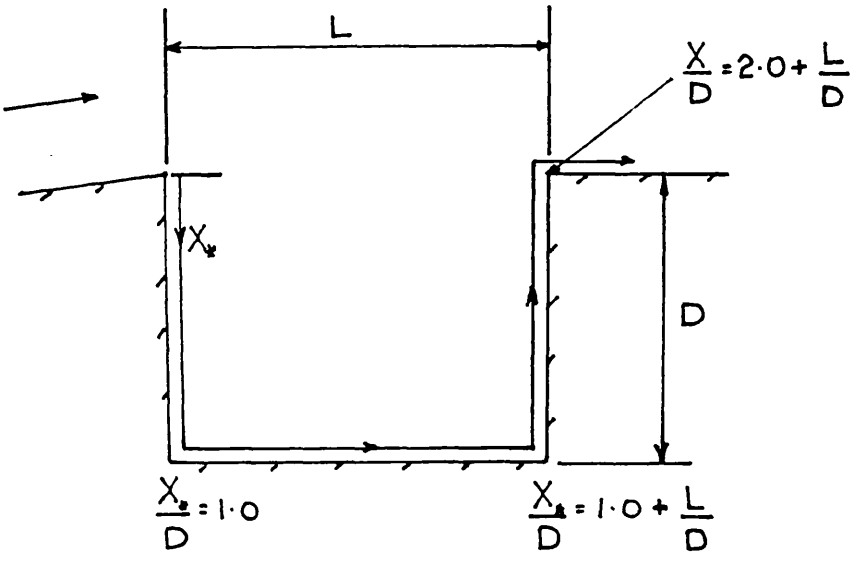

Fig.33 Cavity co-ordinate X_*

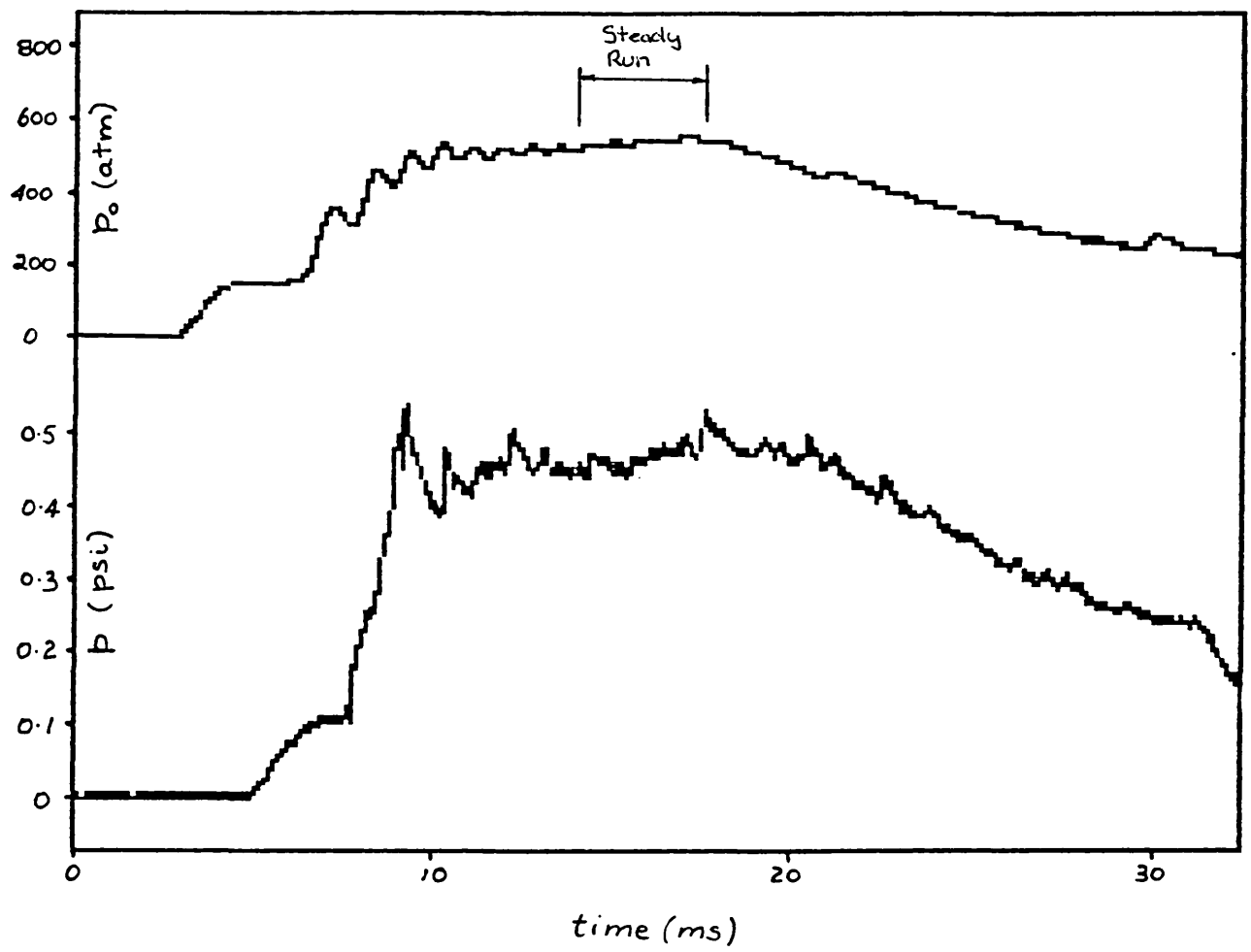

Fig.34 Typical pressure-time trace

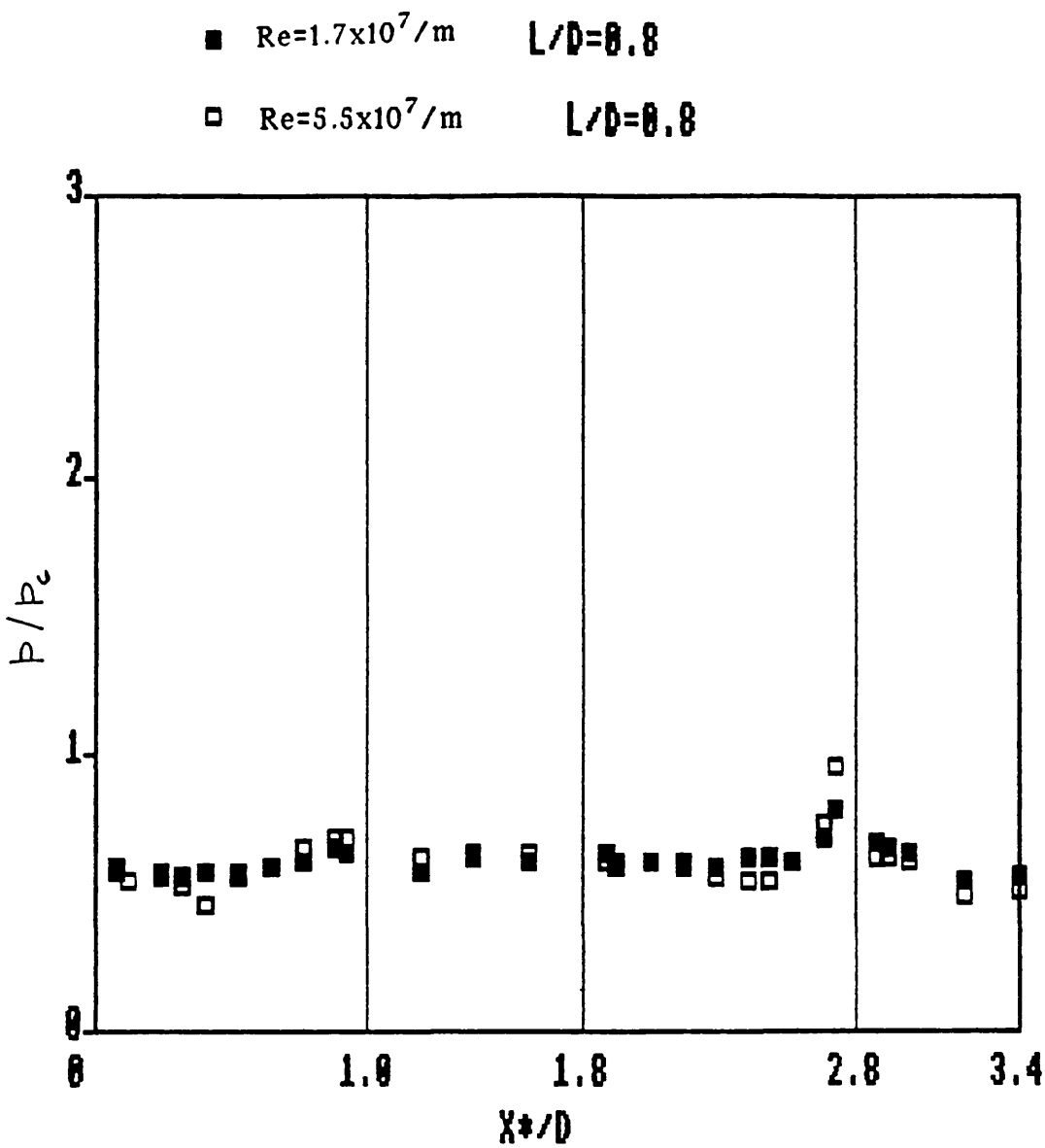

Fig.35 Surface pressure distribution-L/D=0.8 cavity

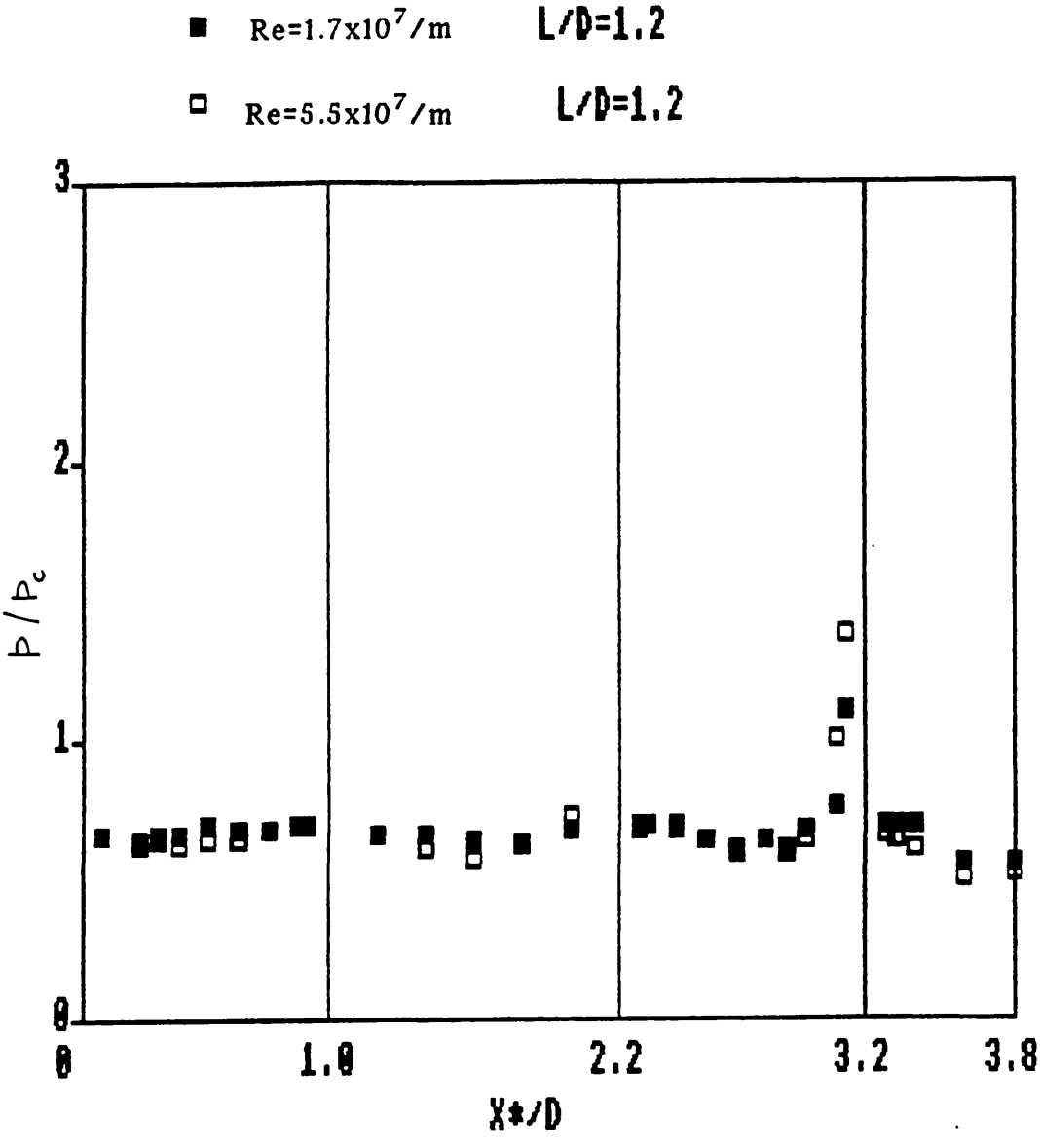

Fig.36 Surface pressure distribution-L/D=1.2 cavity

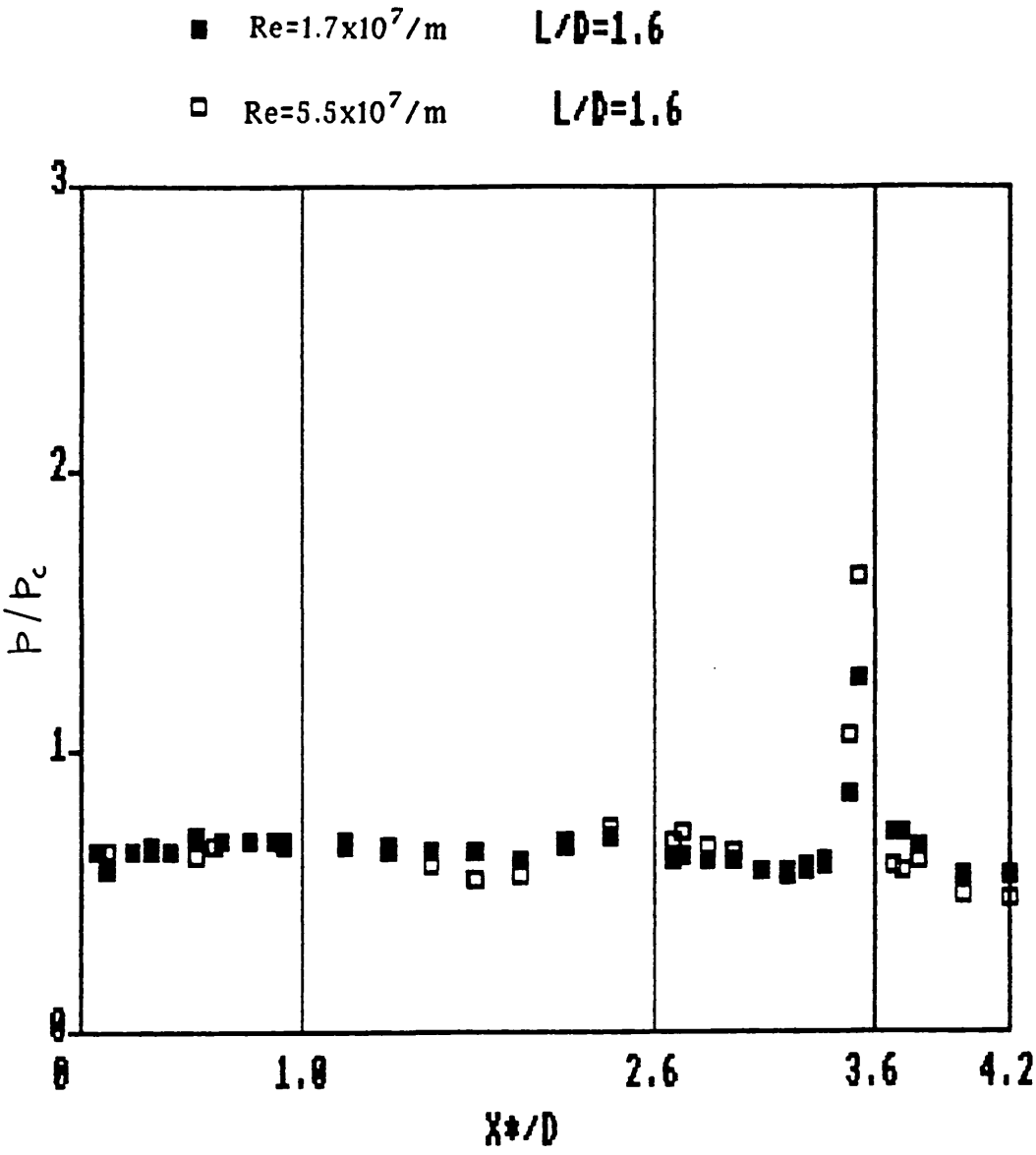

Fig.37 Surface pressure distribution-L/D=1.6 cavity

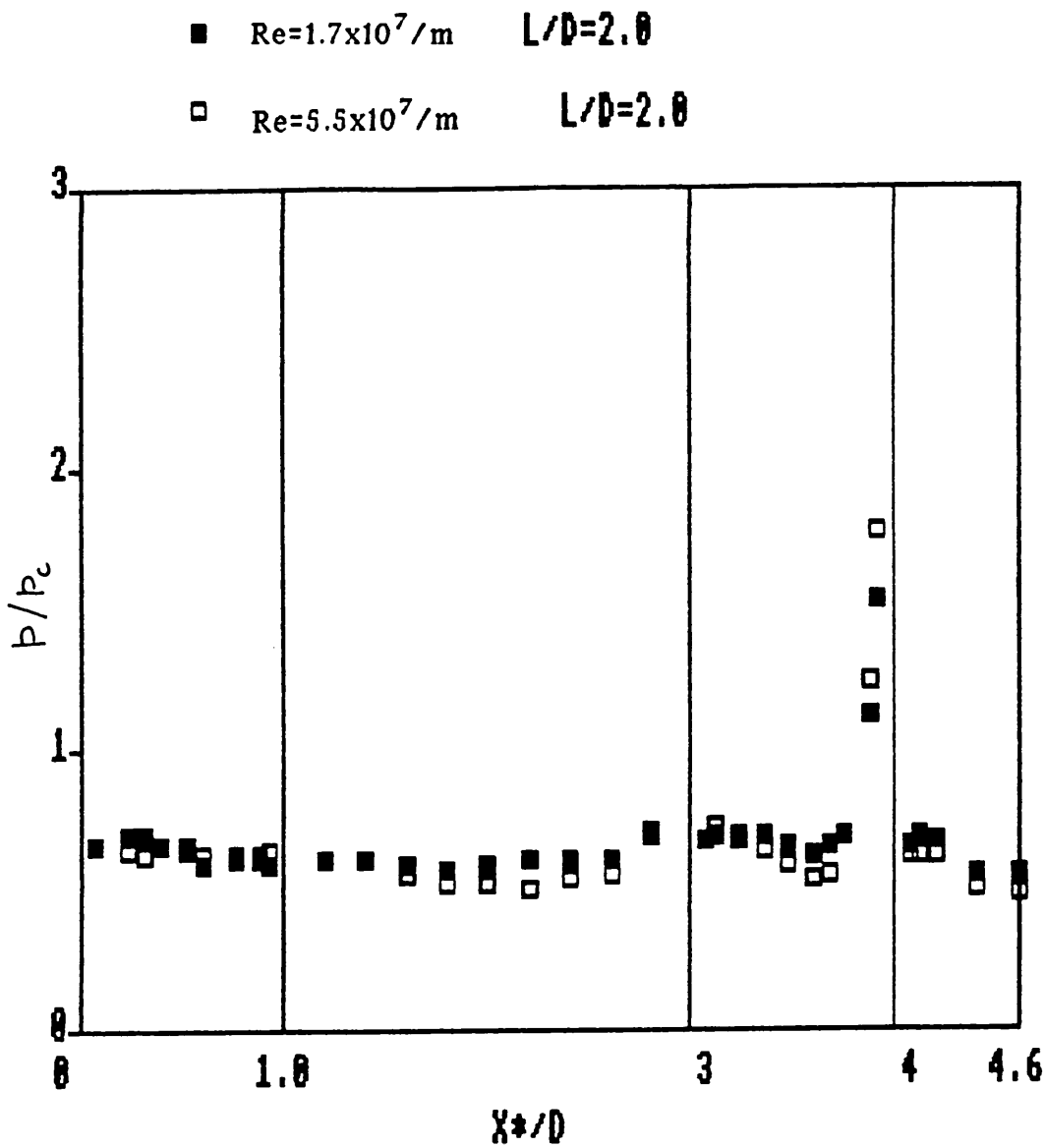

Fig.38 Surface pressure distribution-L/D=2.0 cavity

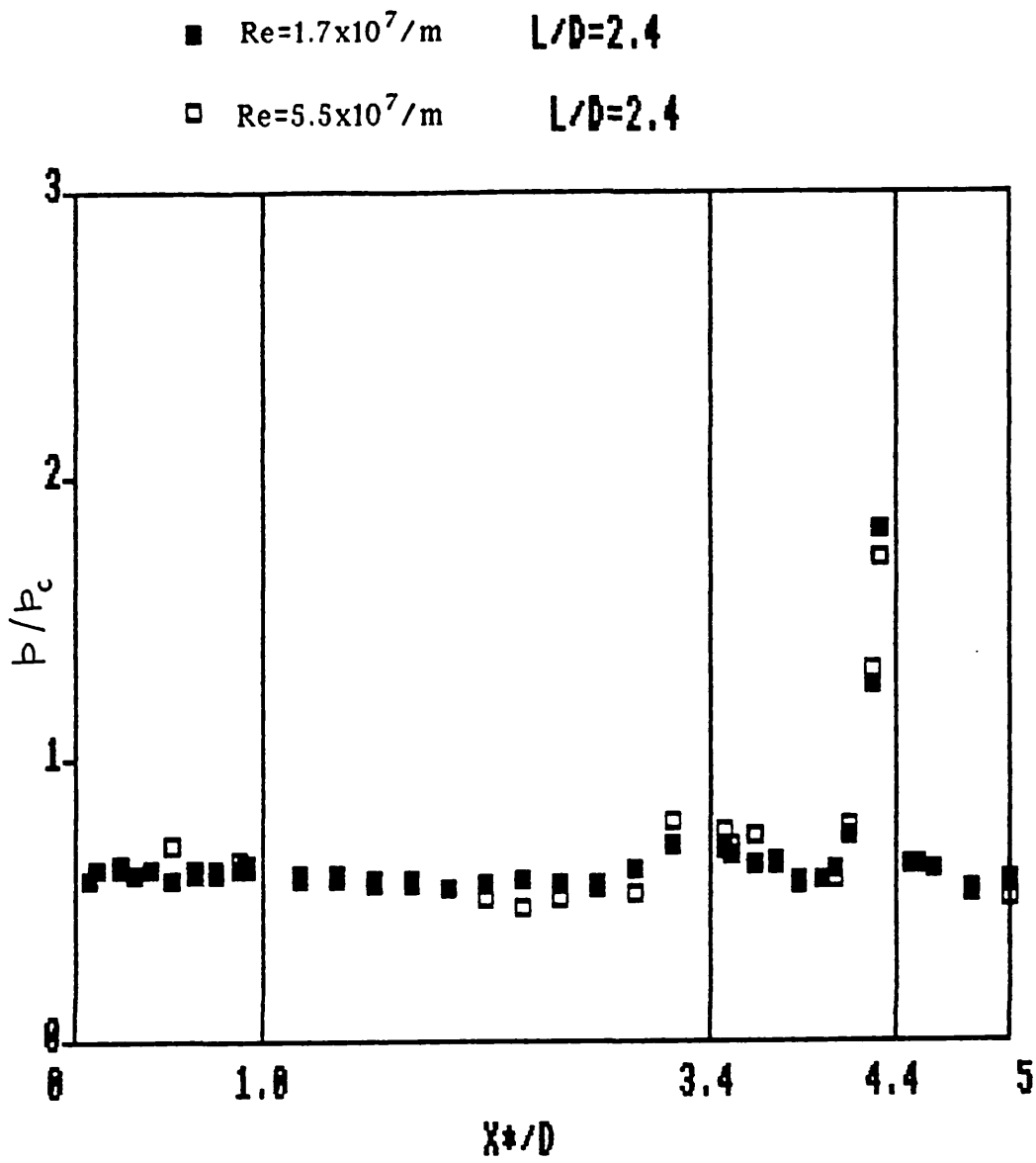

Fig.39 Surface pressure distribution-L/D=2.4 cavity

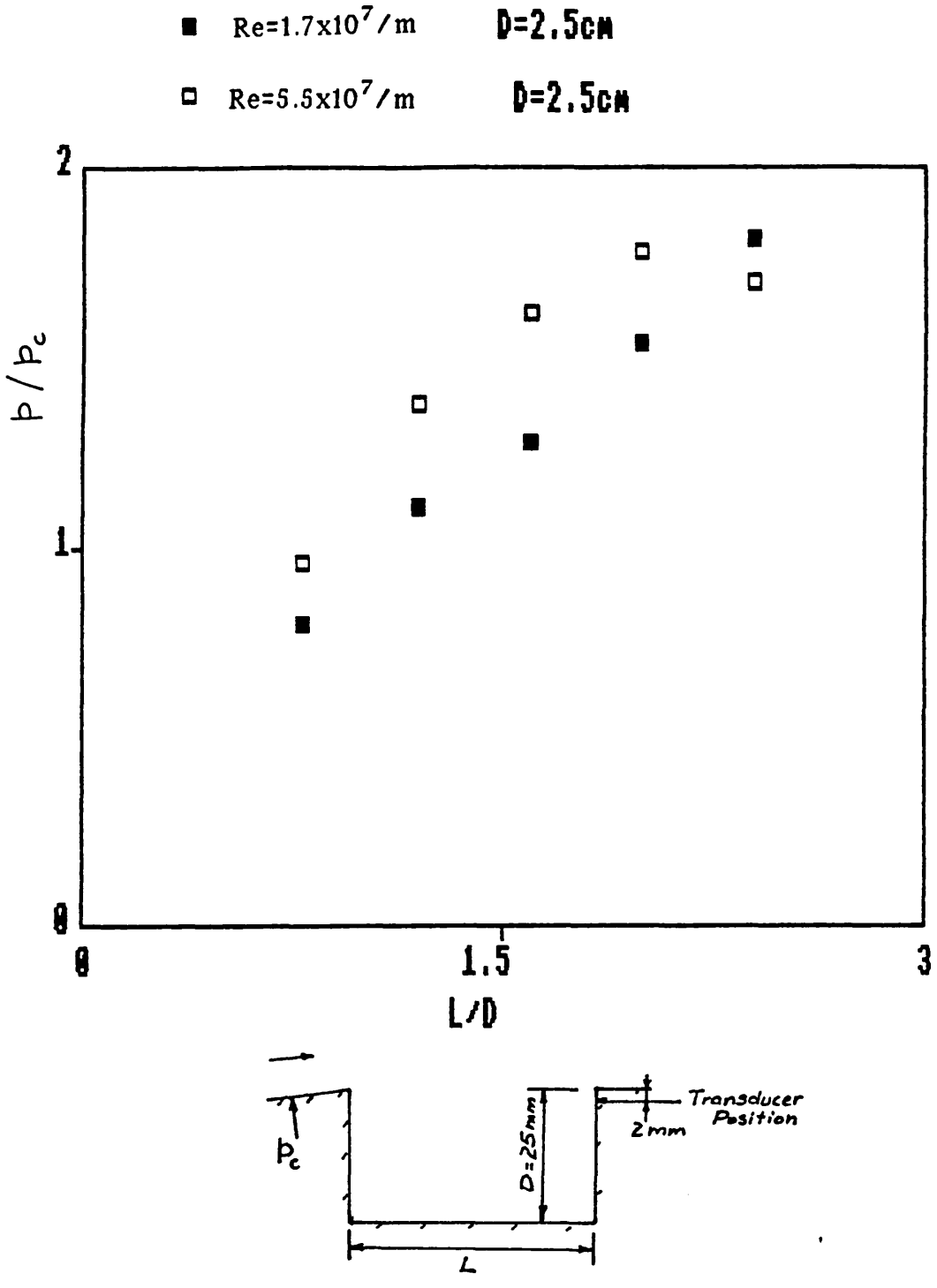

Fig.40 Peak reattachment pressure vs L/D

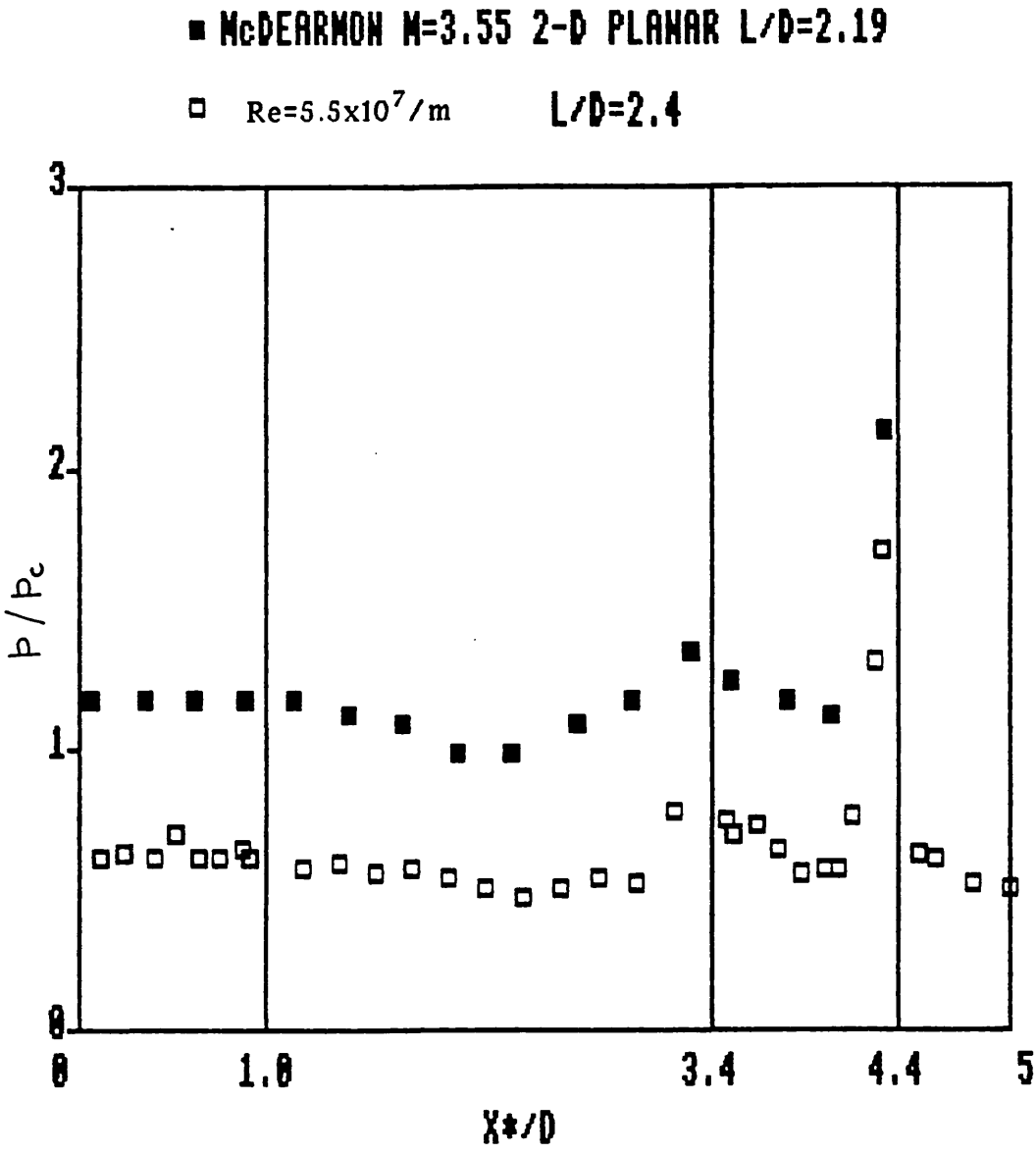

Fig.41 Comparison of L/D=2.4 results with McDearmon(1960)

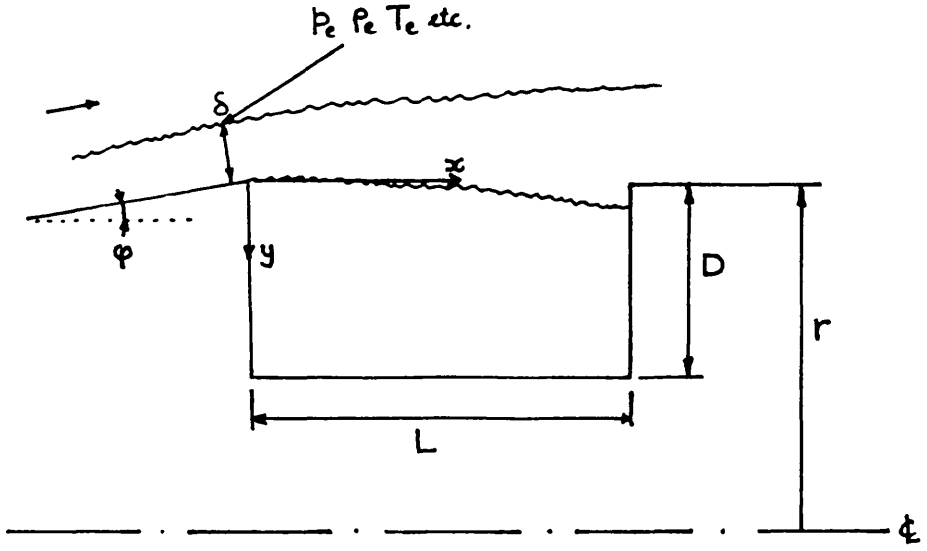

Fig.42 Variables for dimensional analysis

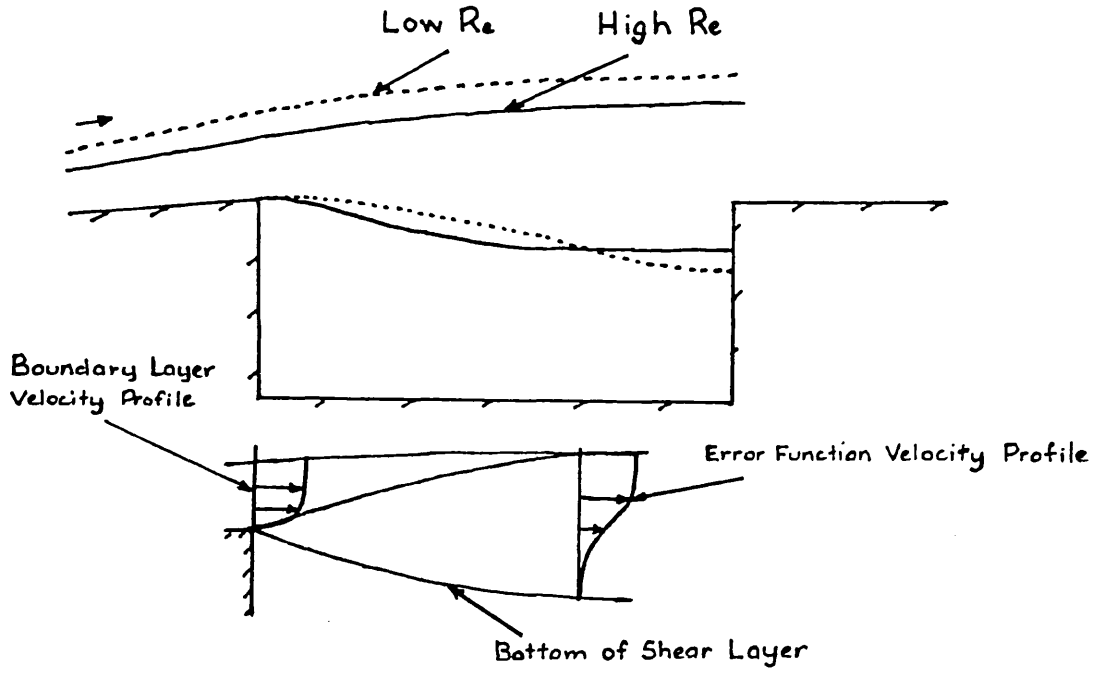

Fig.43 Shear layer spreading for different Reynolds numbers

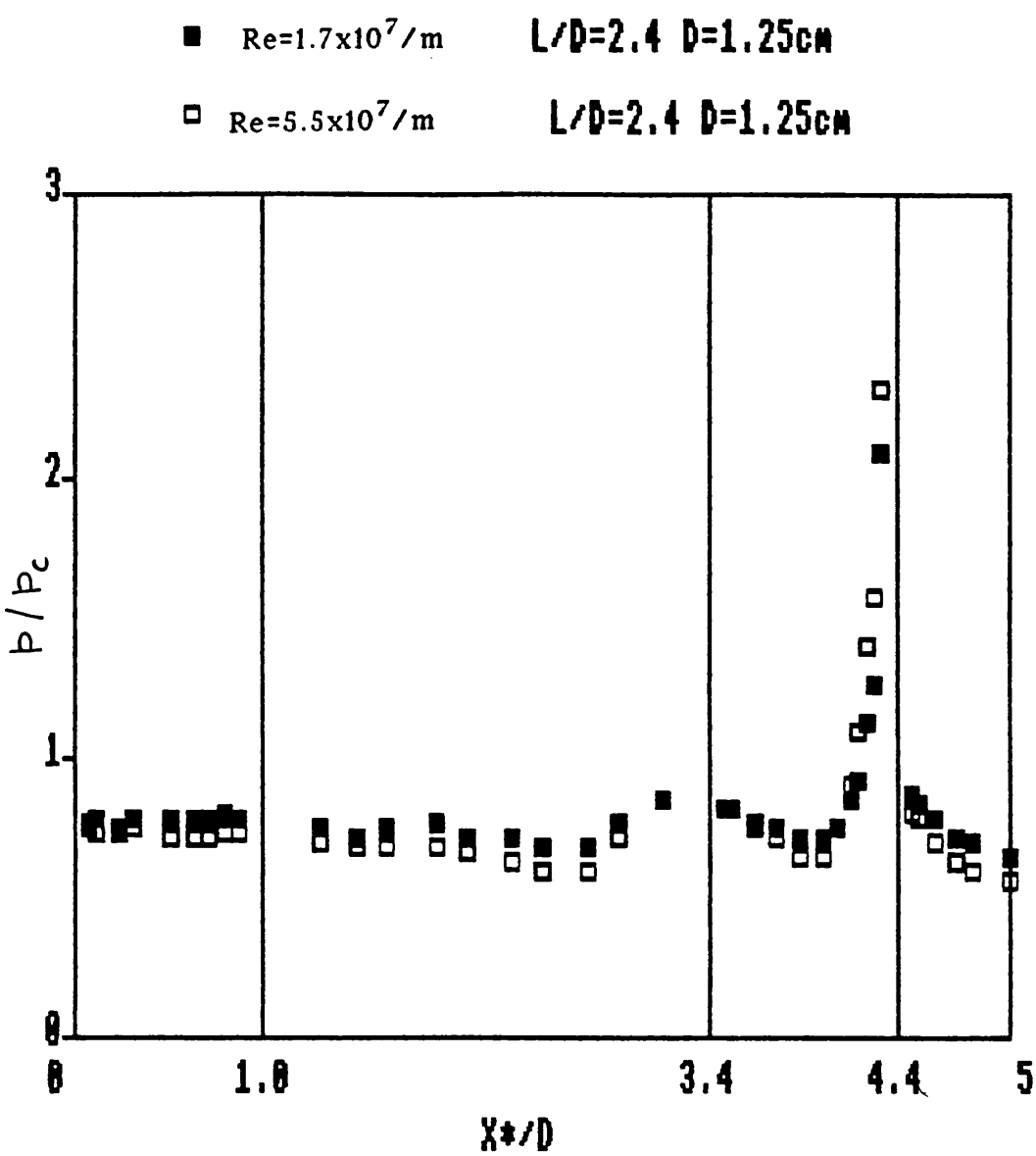

Fig.44 Surface pressure distribution-L/D=2.4 D=1.25cm cavity

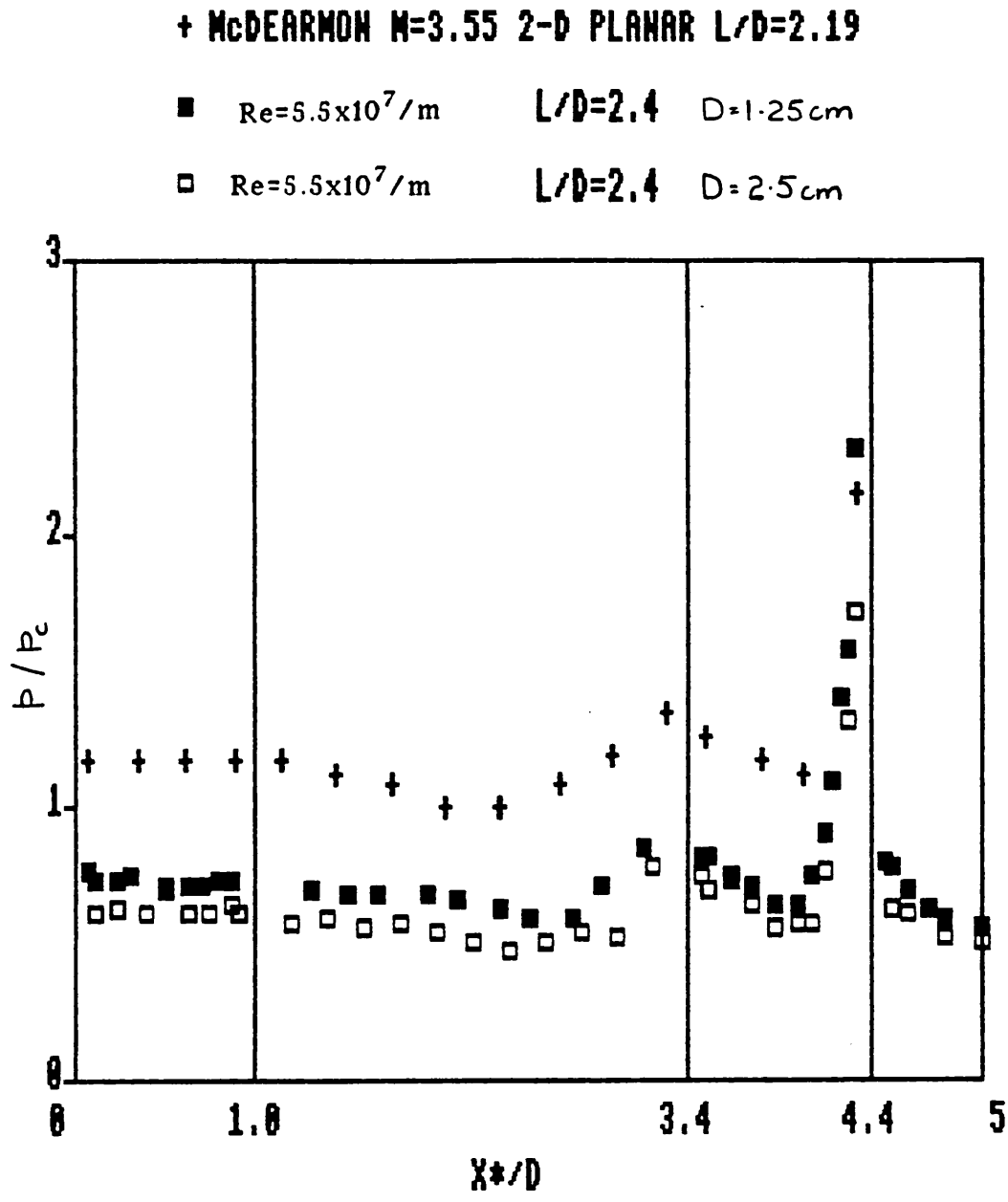

Fig.45 Comparison of surface pressure for different cavity depths

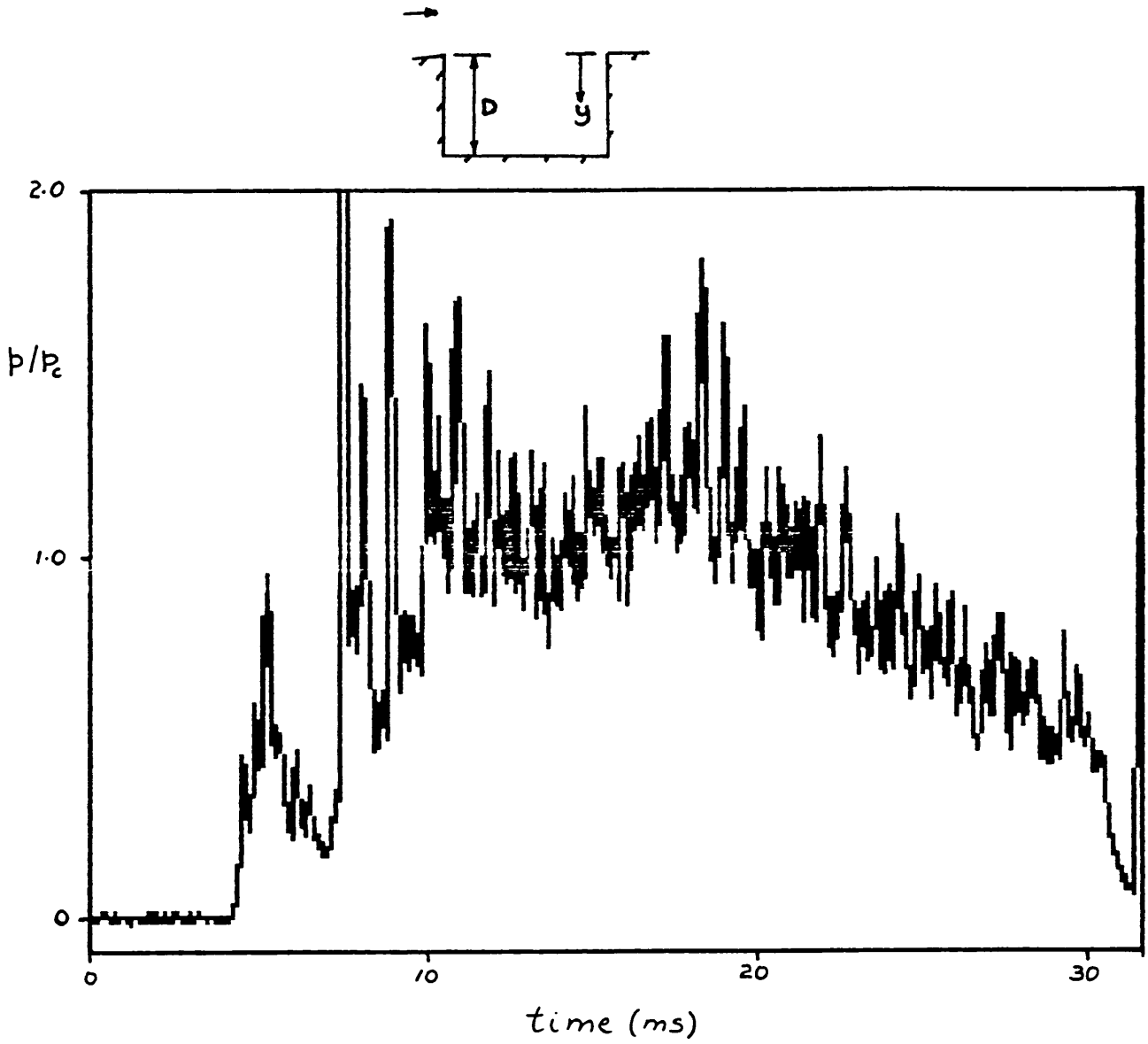

Fig.46 Pressure trace on rear face at y/D=0.25

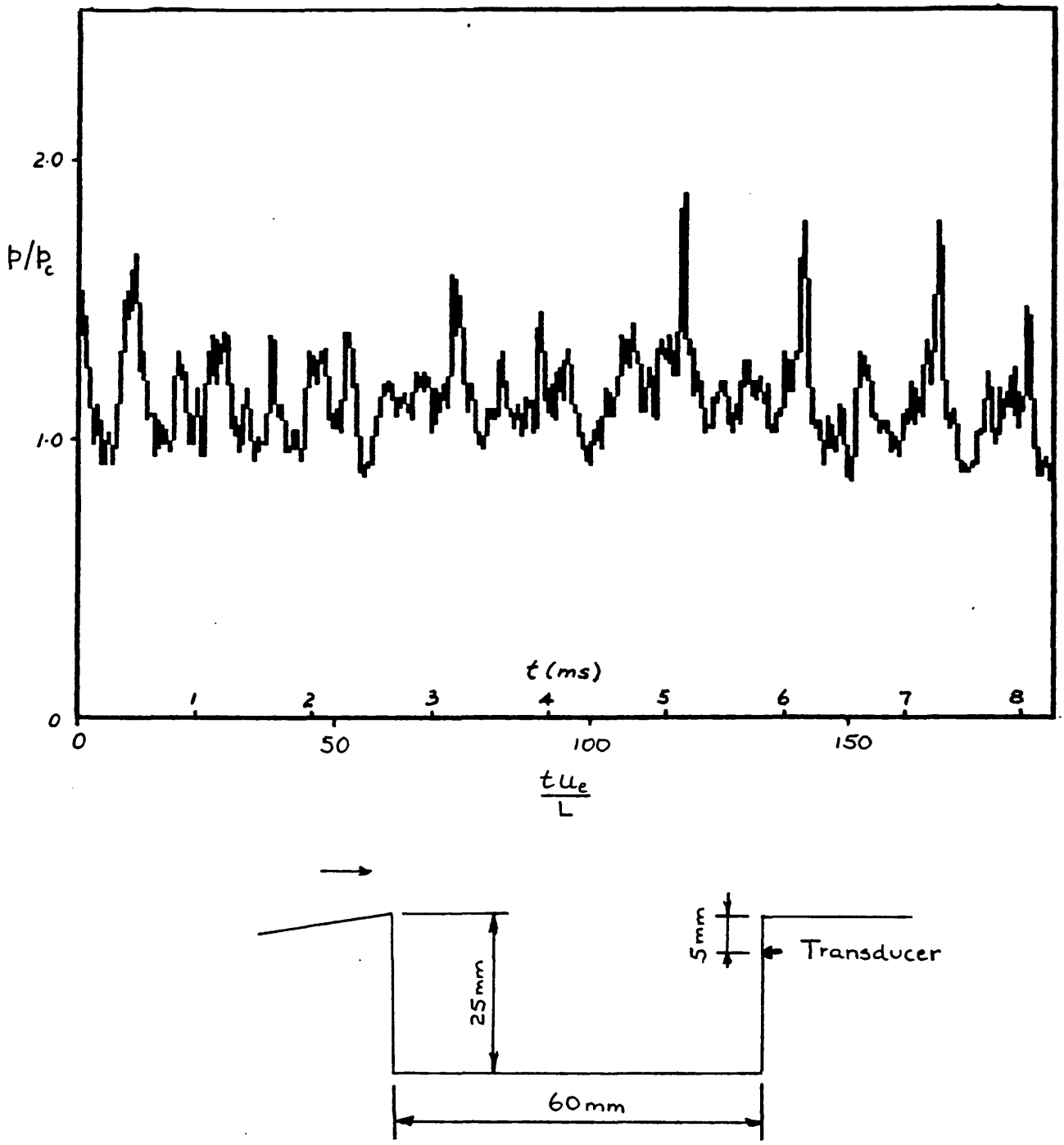

Fig.47 Pressure trace on rear face over steady run time at y/D=0.25

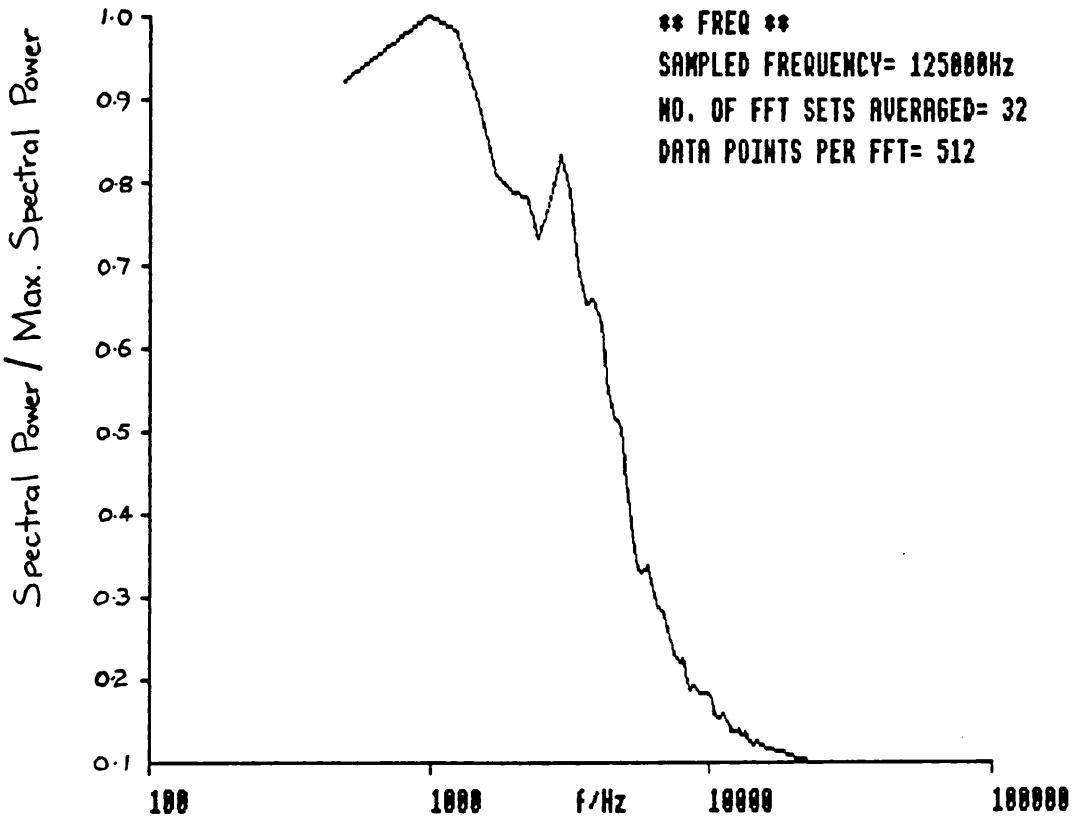

Fig.48 Result of Fast Fourier Transform analysis

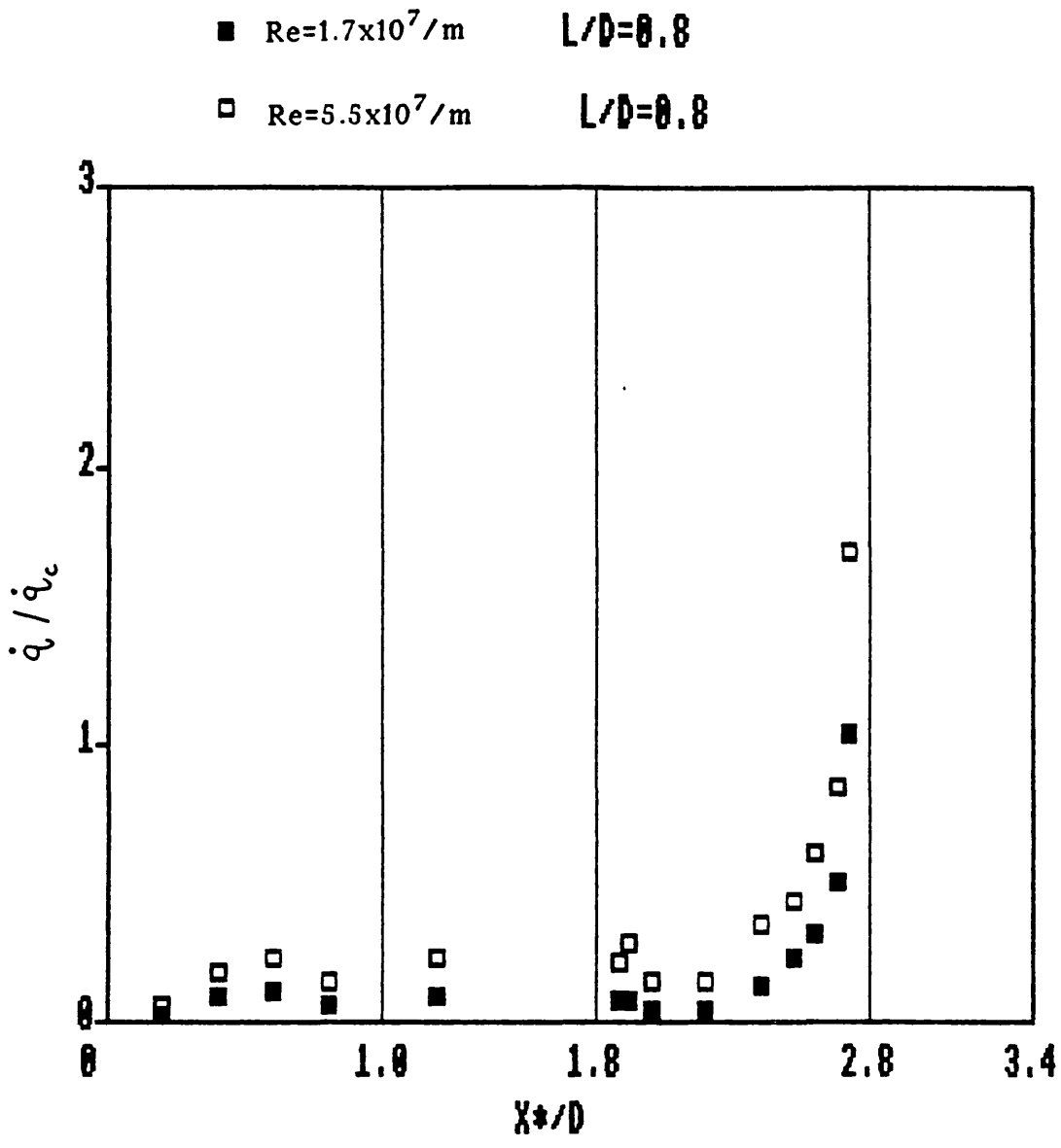

Fig.49 Cavity heat transfer rates-L/D=0.8

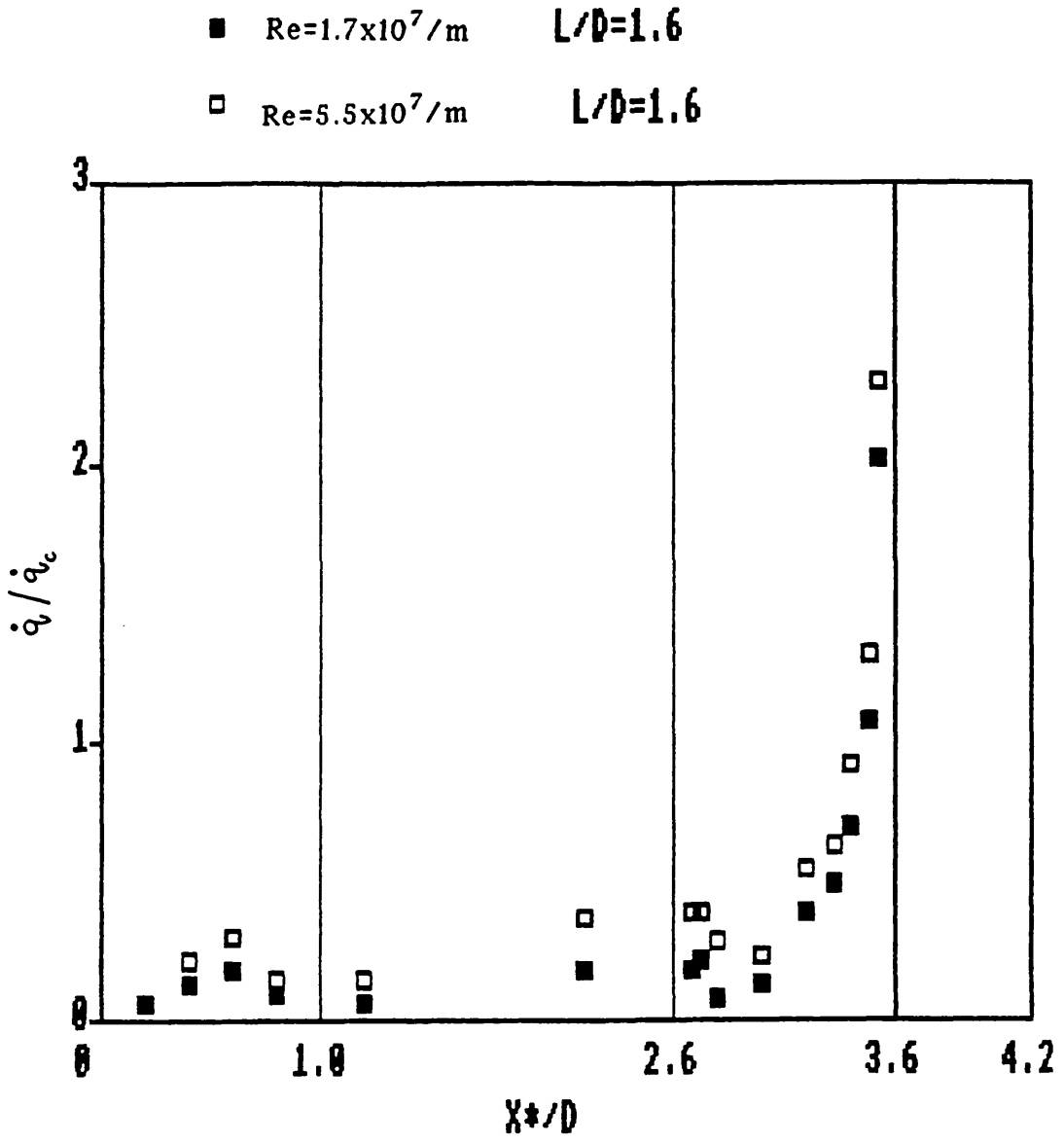

Fig.50 Cavity heat transfer rates-L/D=1.6

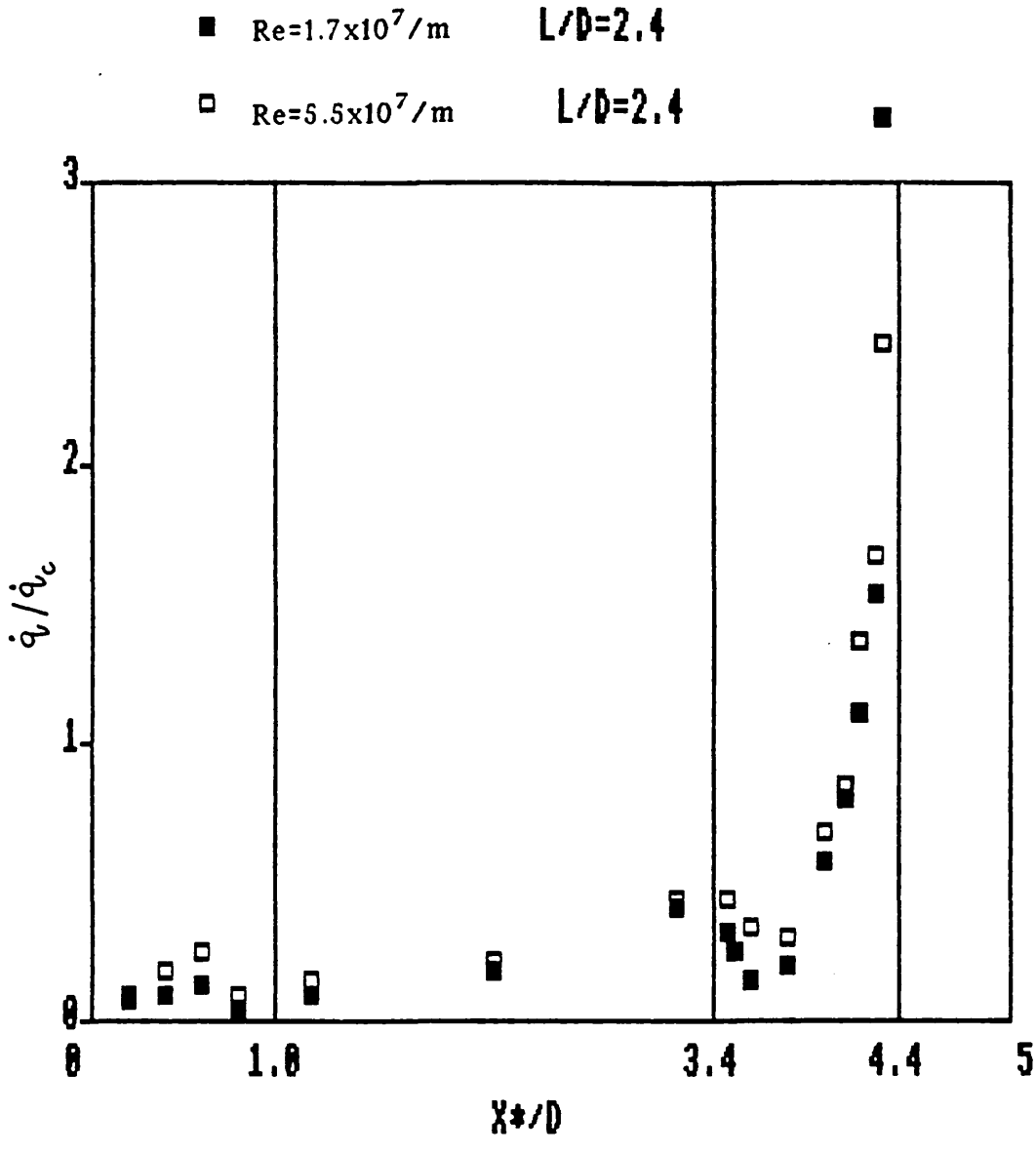

Fig.51 Cavity heat transfer rates-L/D=2.4

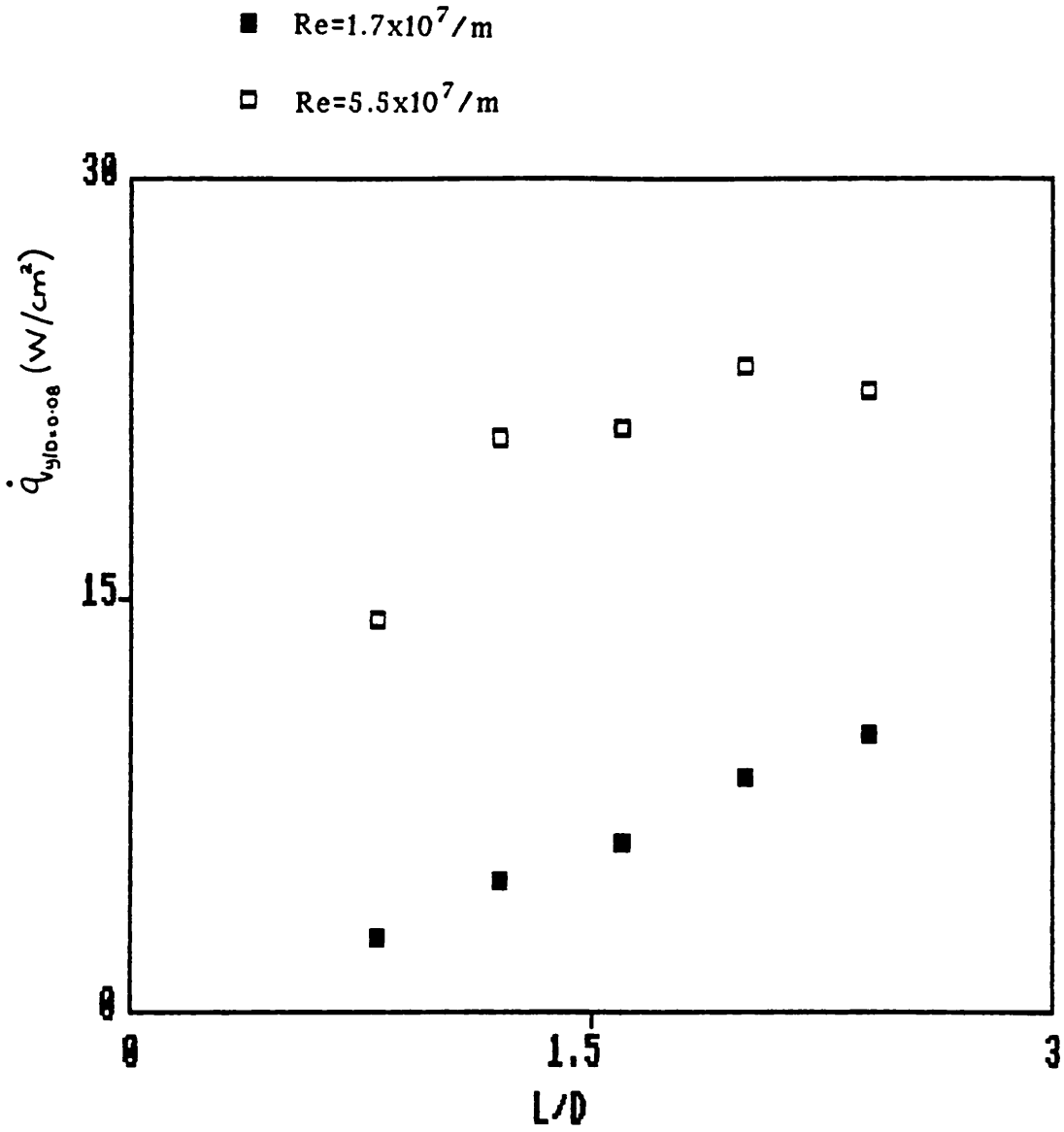

Fig.52 Peak reattachment heat transfer rate vs L/D

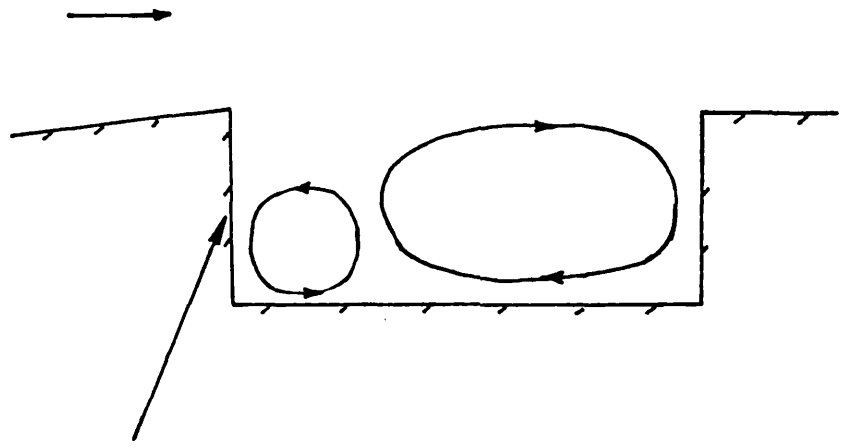

Fig.53 Possible position of cavity vortices

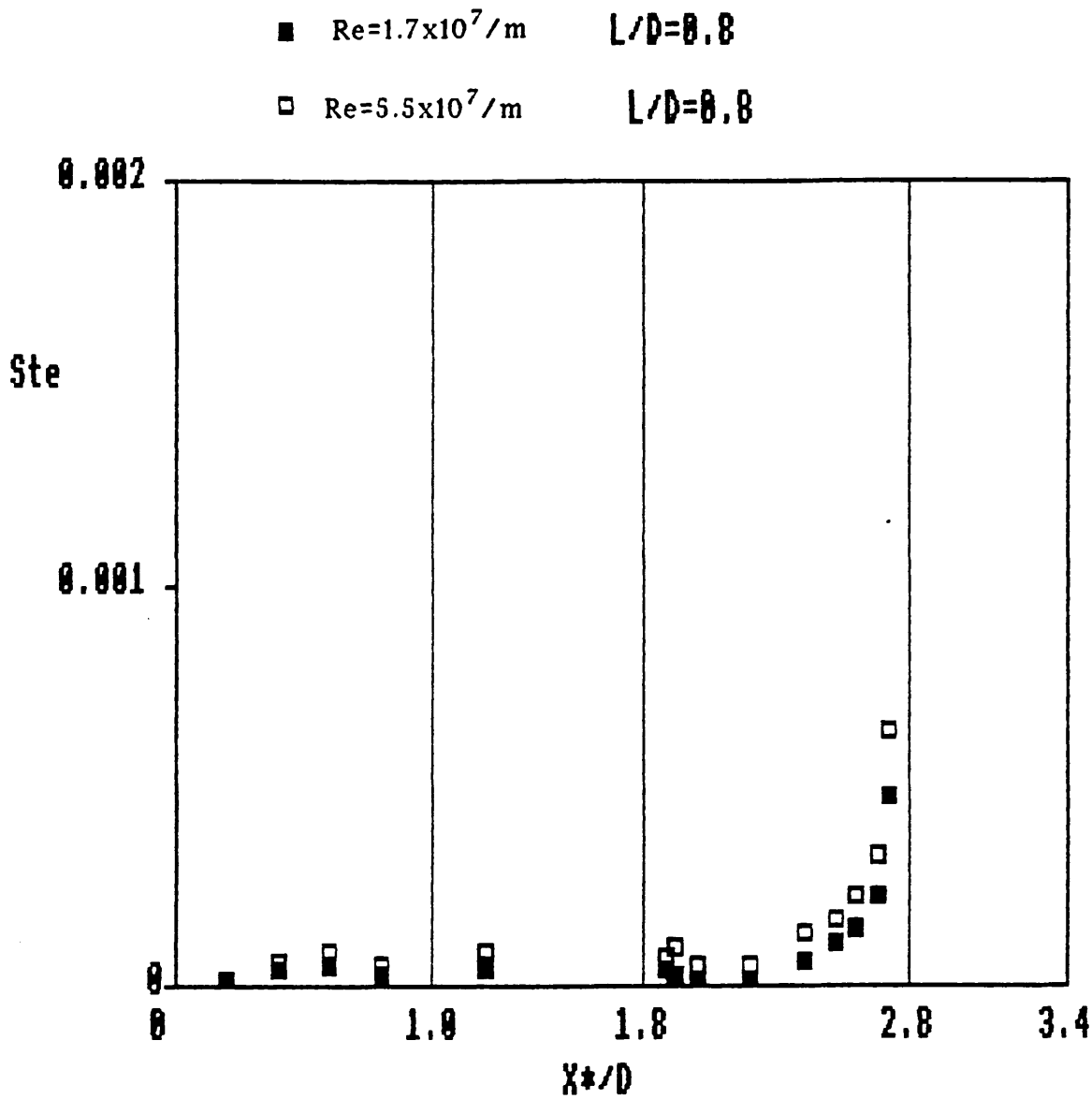

Fig.54 Cavity Stanton numbers-L/D=0.8

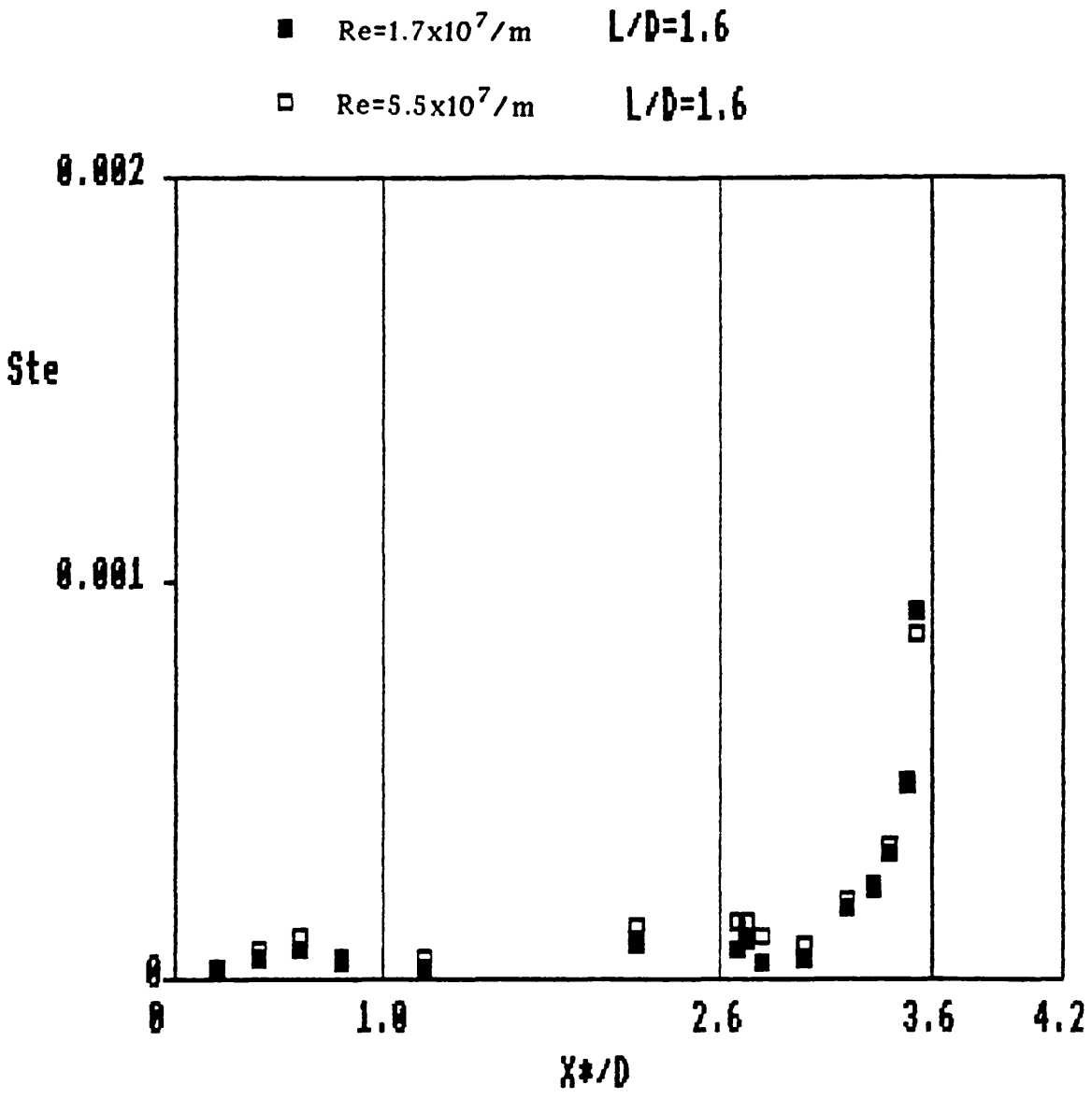

Fig.55 Cavity Stanton numbers-L/D=1.6

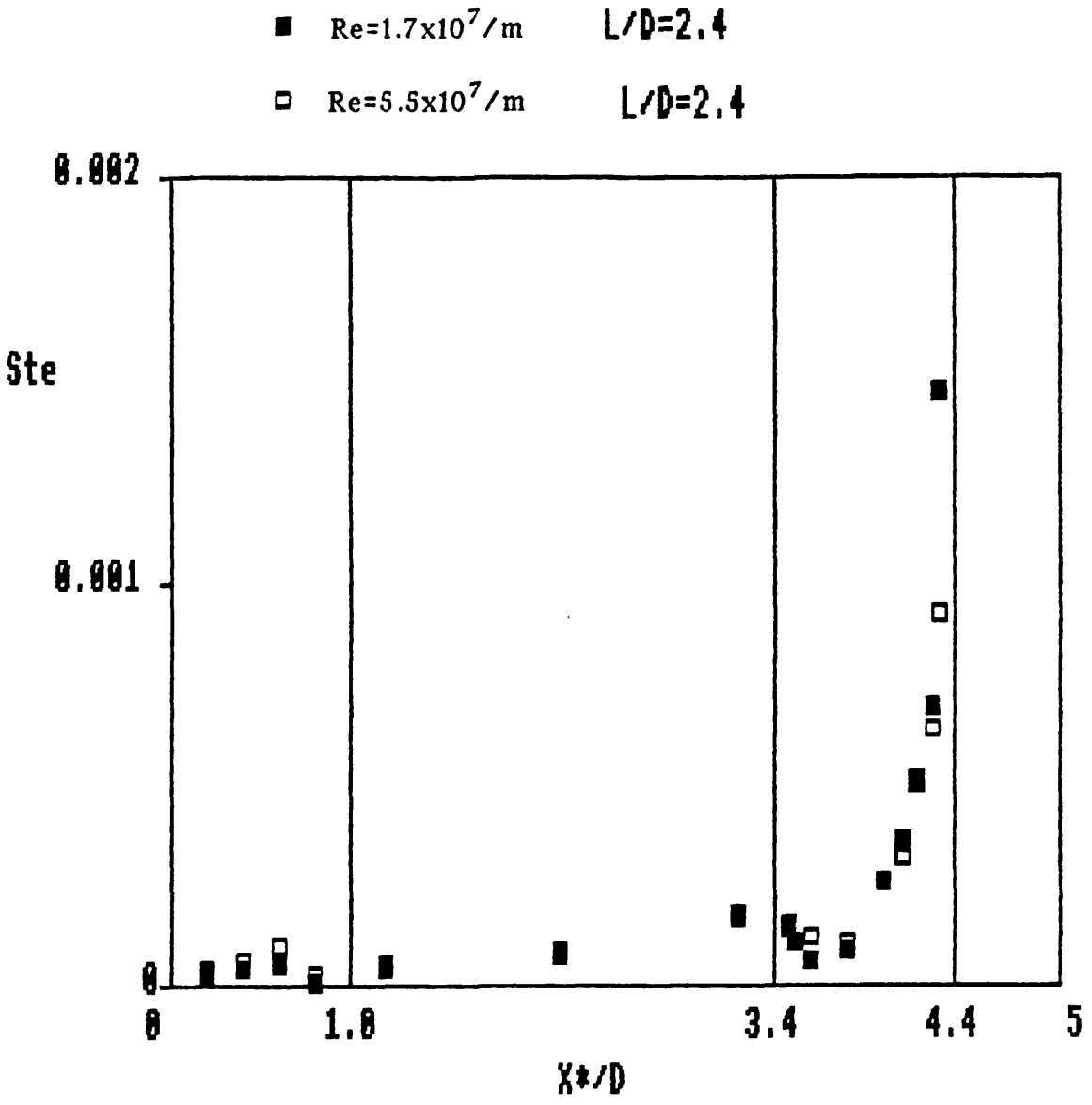

Fig.56 Cavity Stanton numbers-L/D=2.4

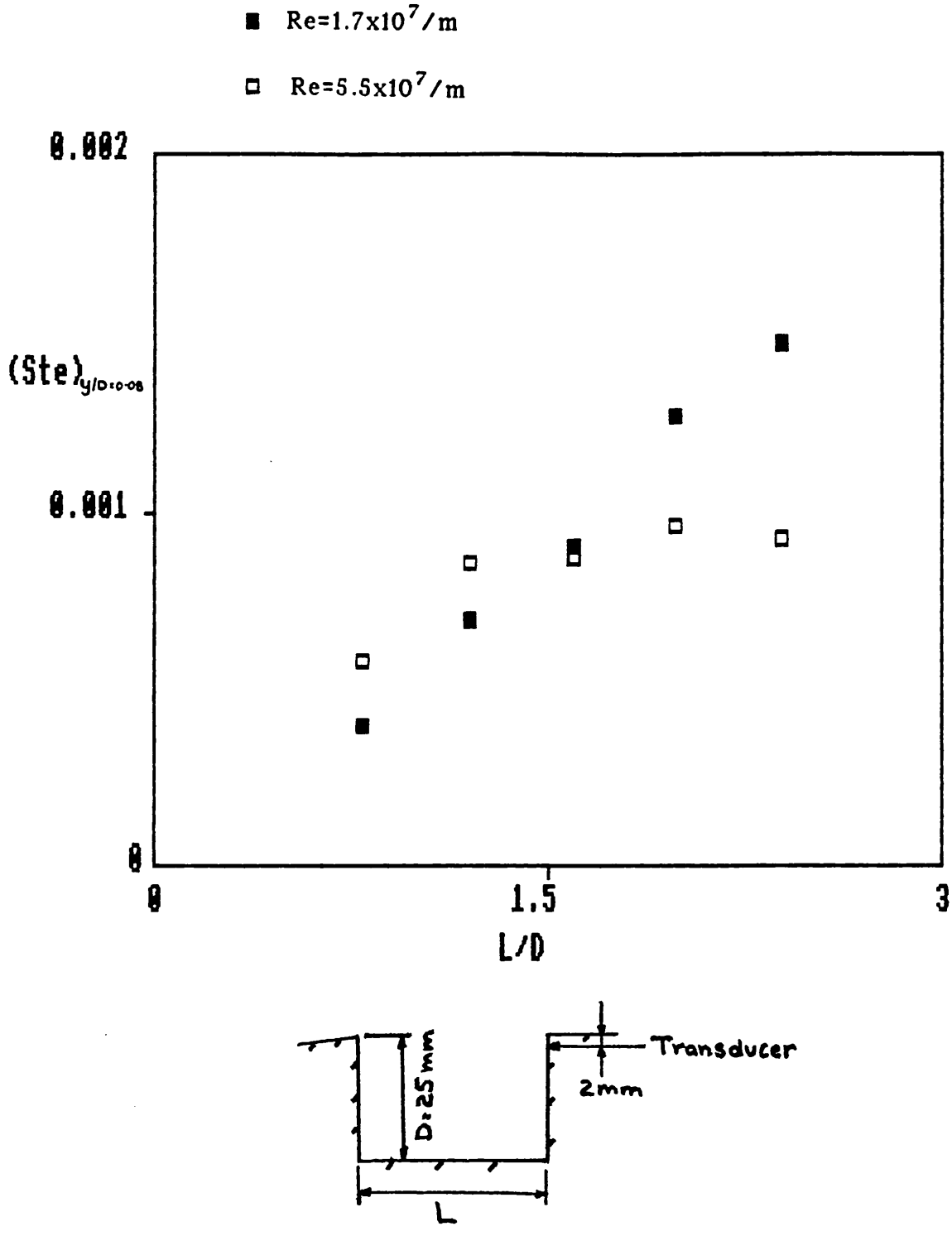

Fig.57 Peak Stanton number vs L/D

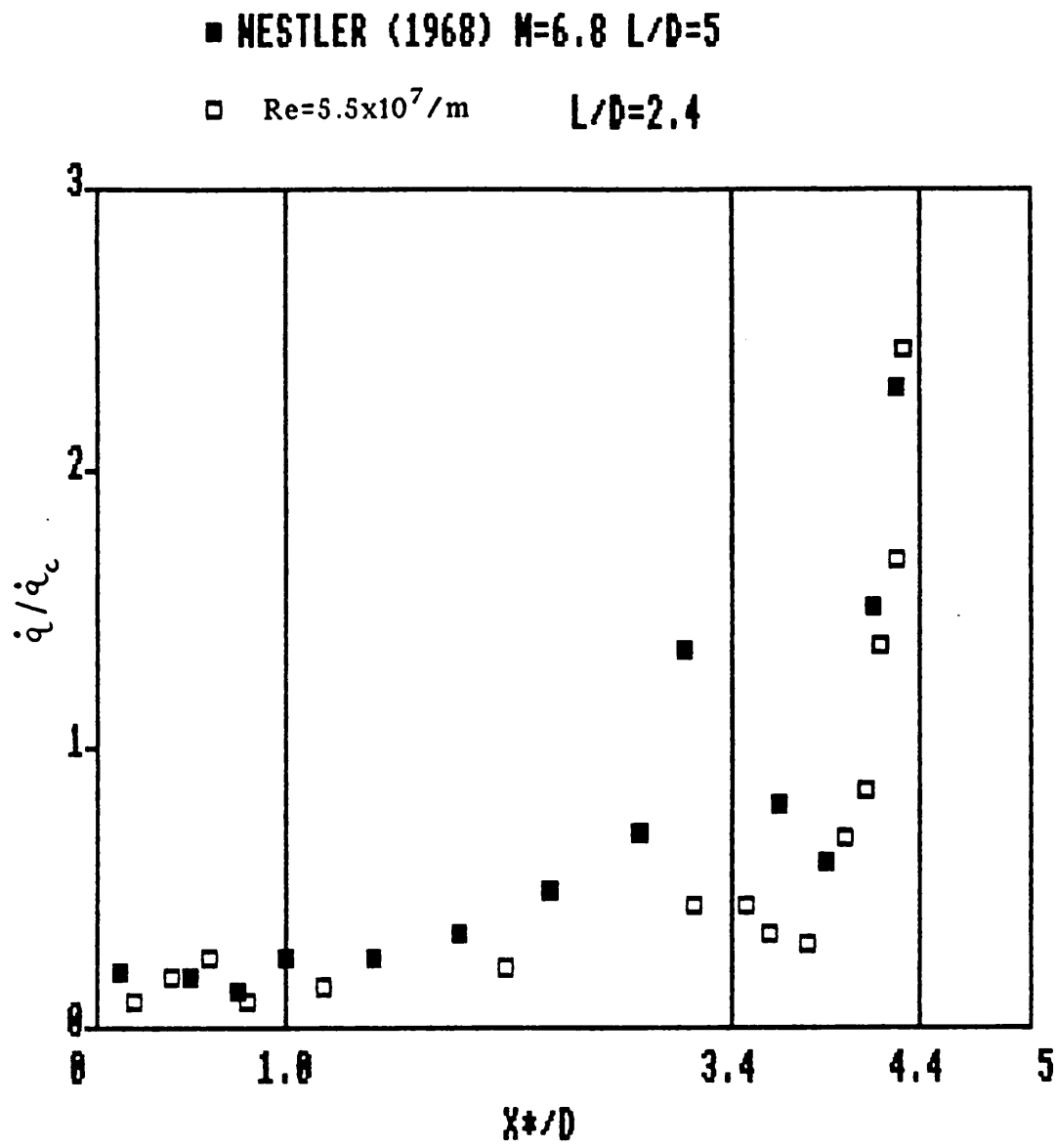

Fig.58 Comparison of heat transfer results with Nestler(1968)

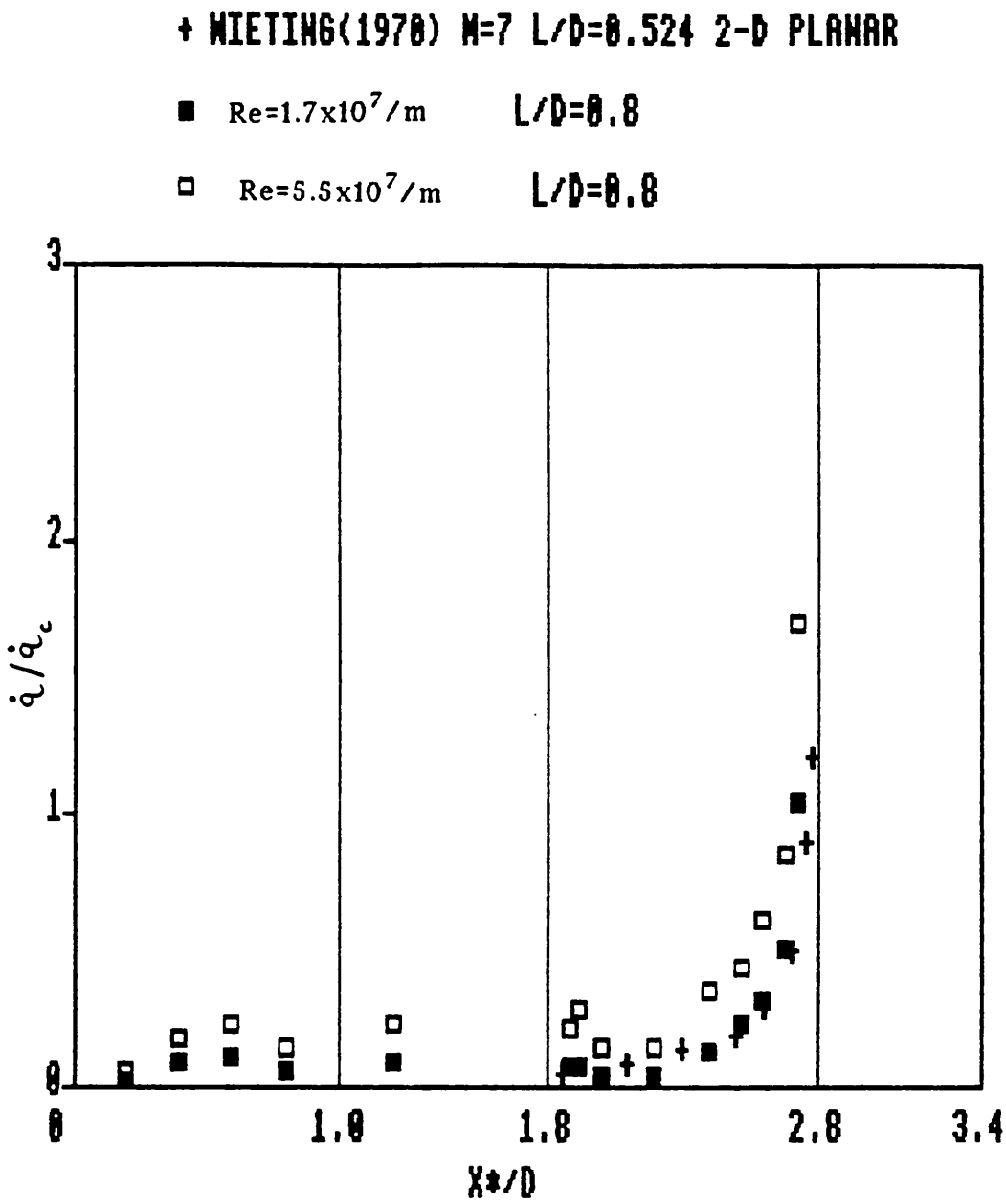

Fig.59 Comparison of heat transfer results with Wieting(1970)

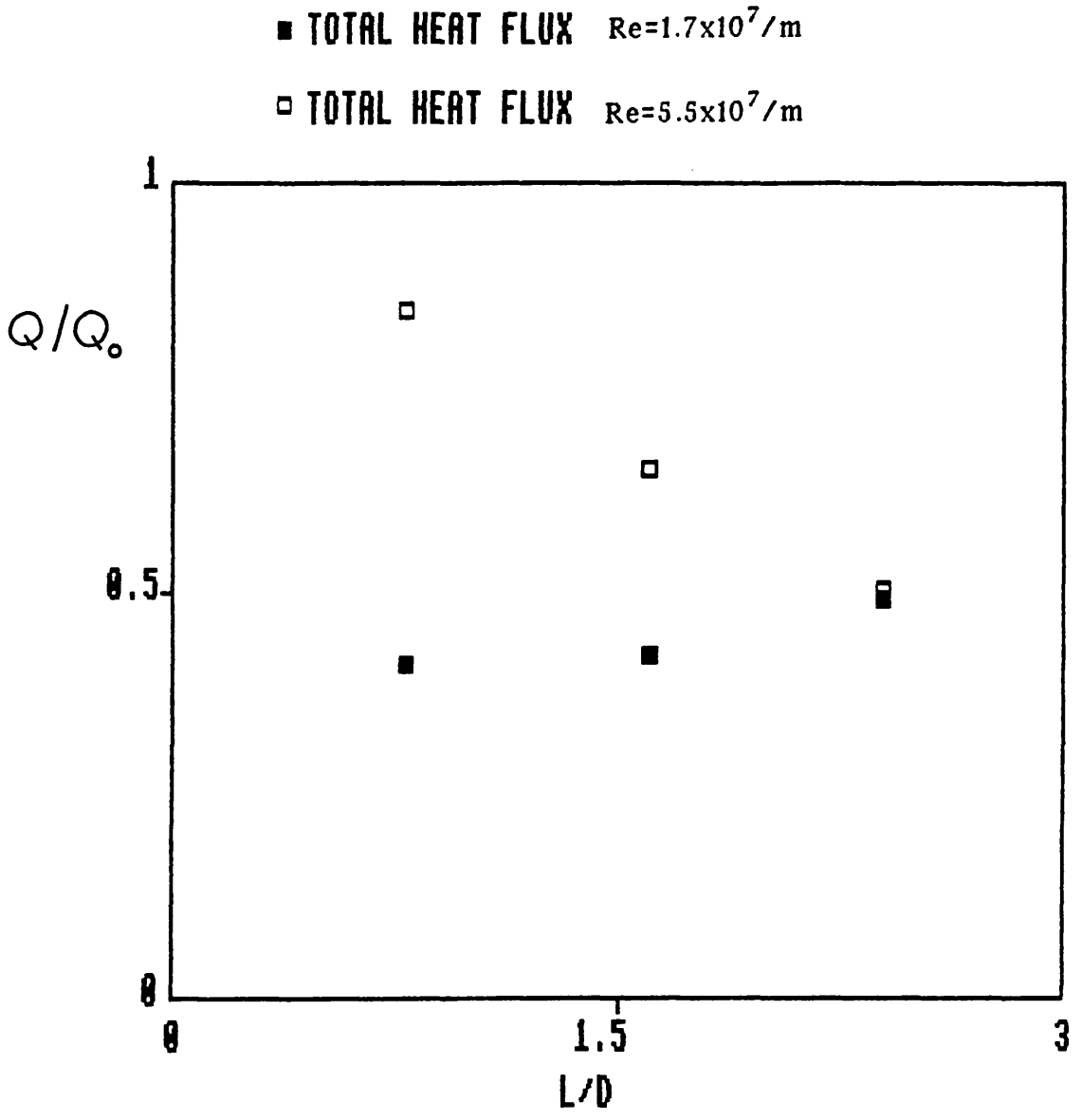

Fig.60 Total heat flux vs L/D

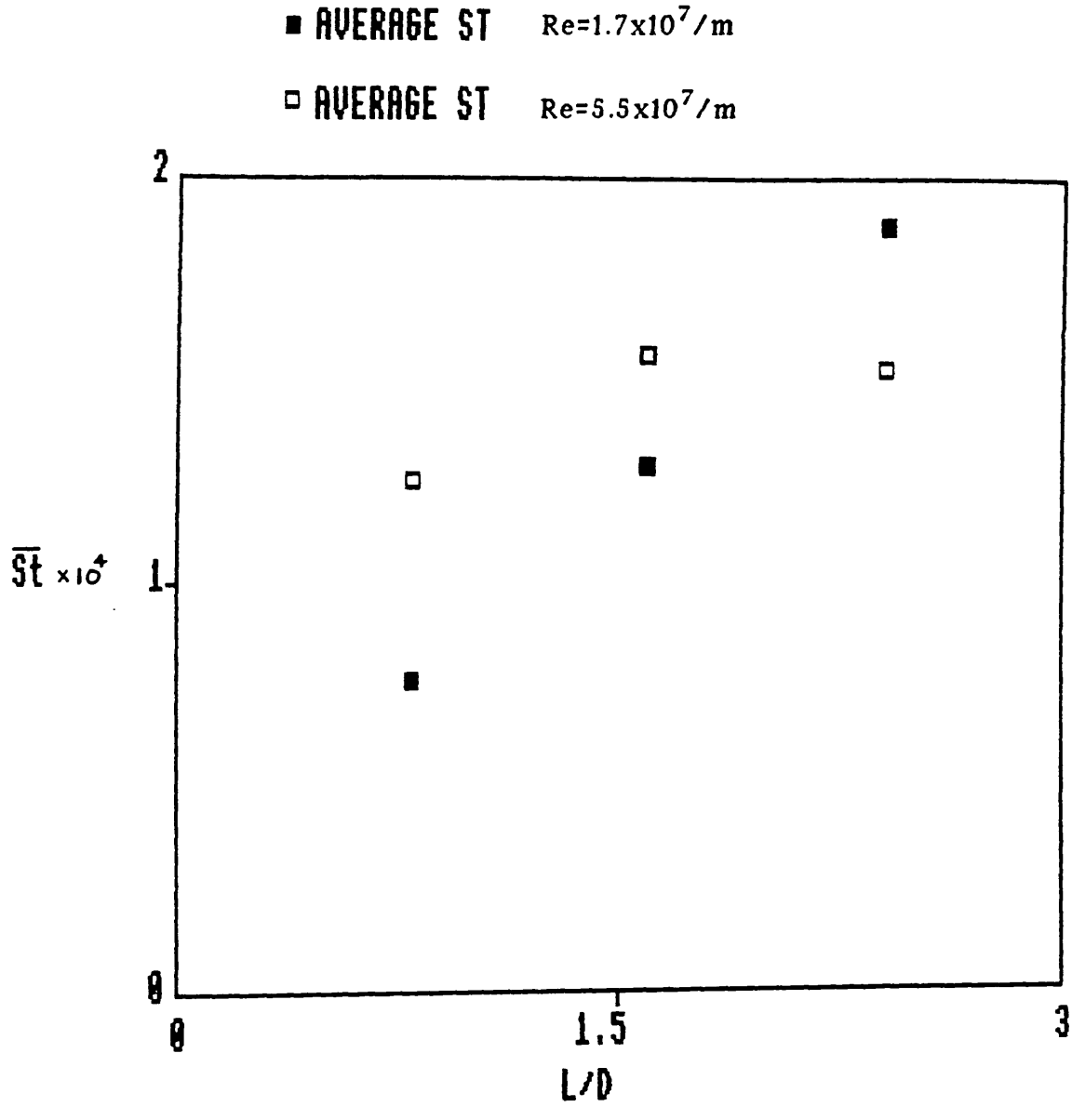

Fig.61 Average cavity Stanton number vs L/D

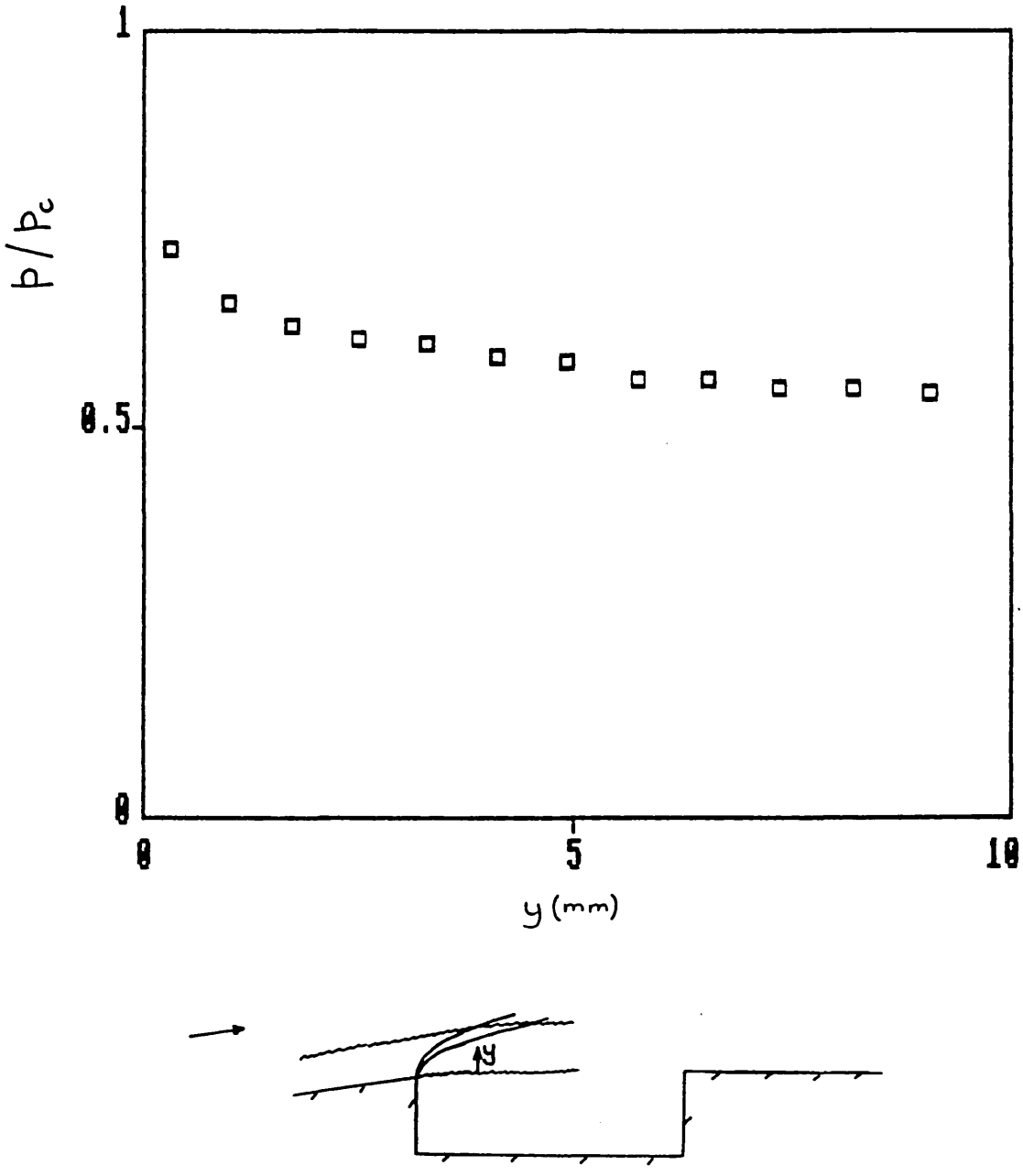

Fig.62 Shear layer pressure profile after expansion

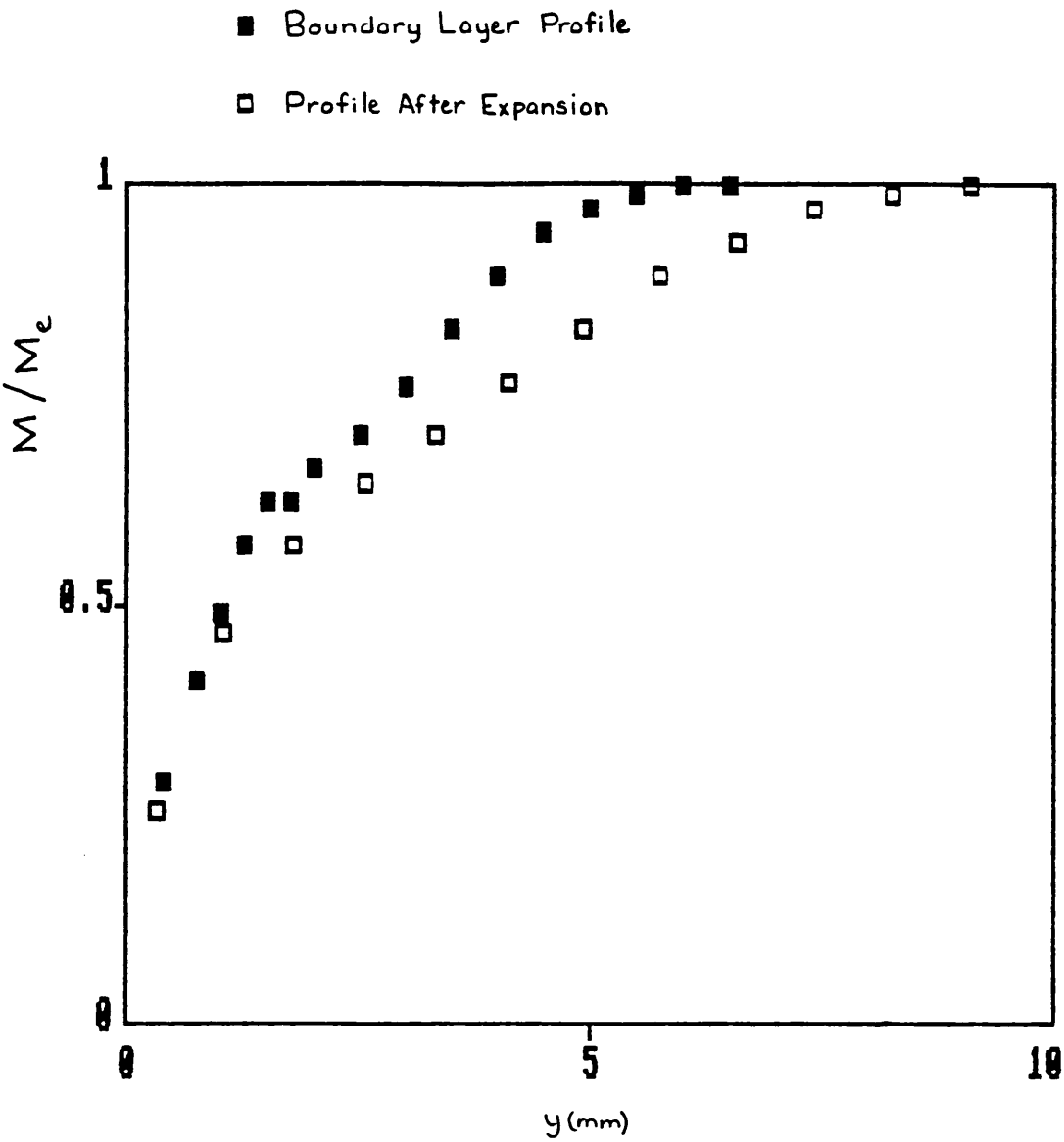

Fig.63 Shear layer Mach number profile after expansion

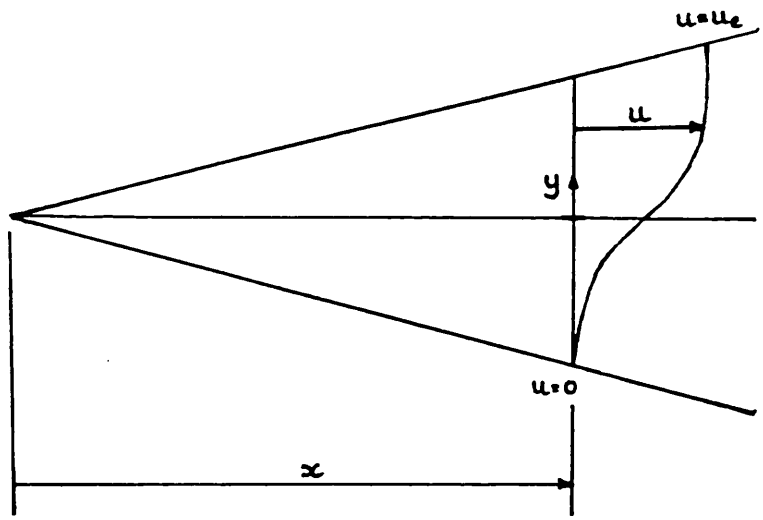

Fig.64 Co-ordinates for shear layer spreading calculation

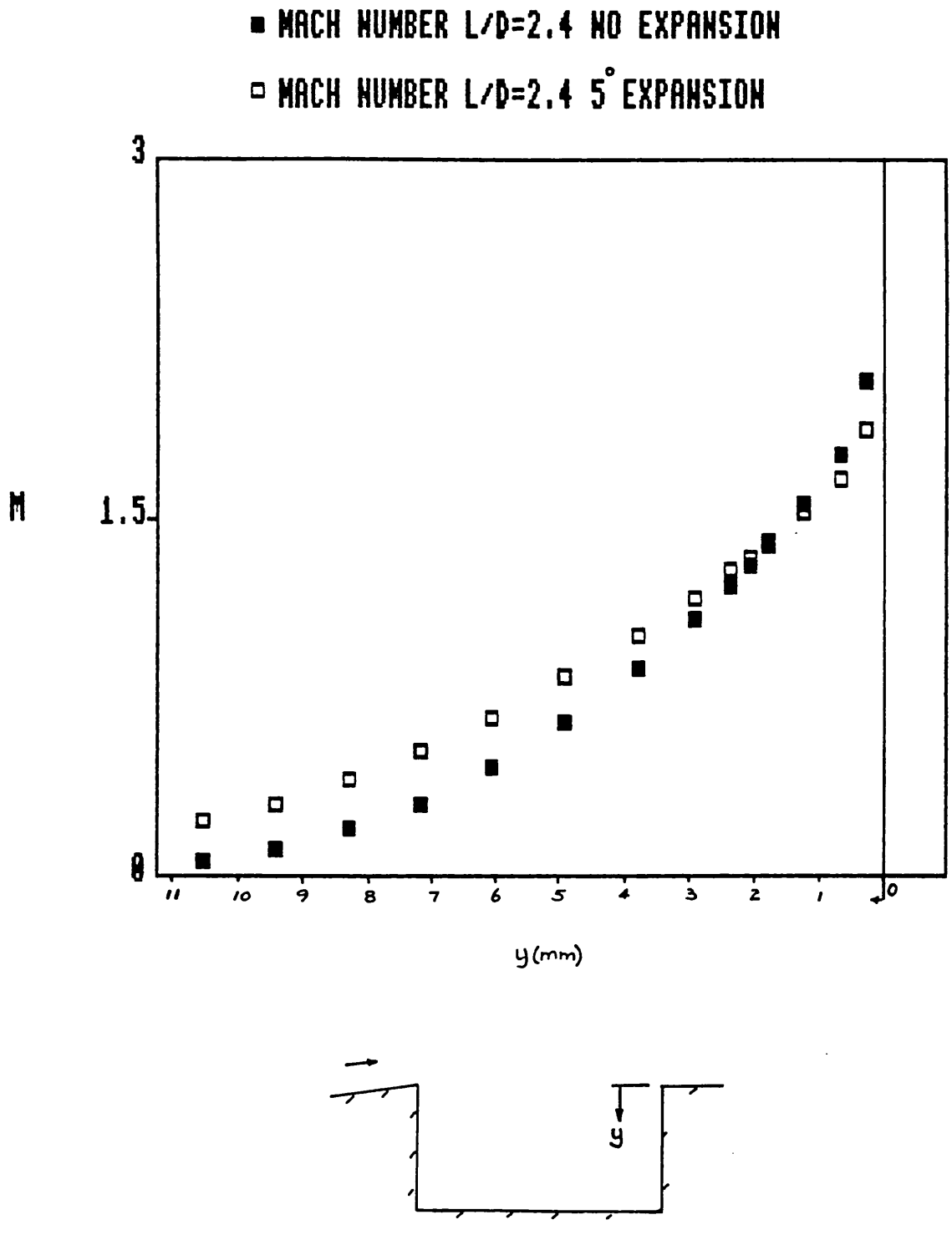

Fig.65 Calculated Mach number profile at reattachment (L=6cm)

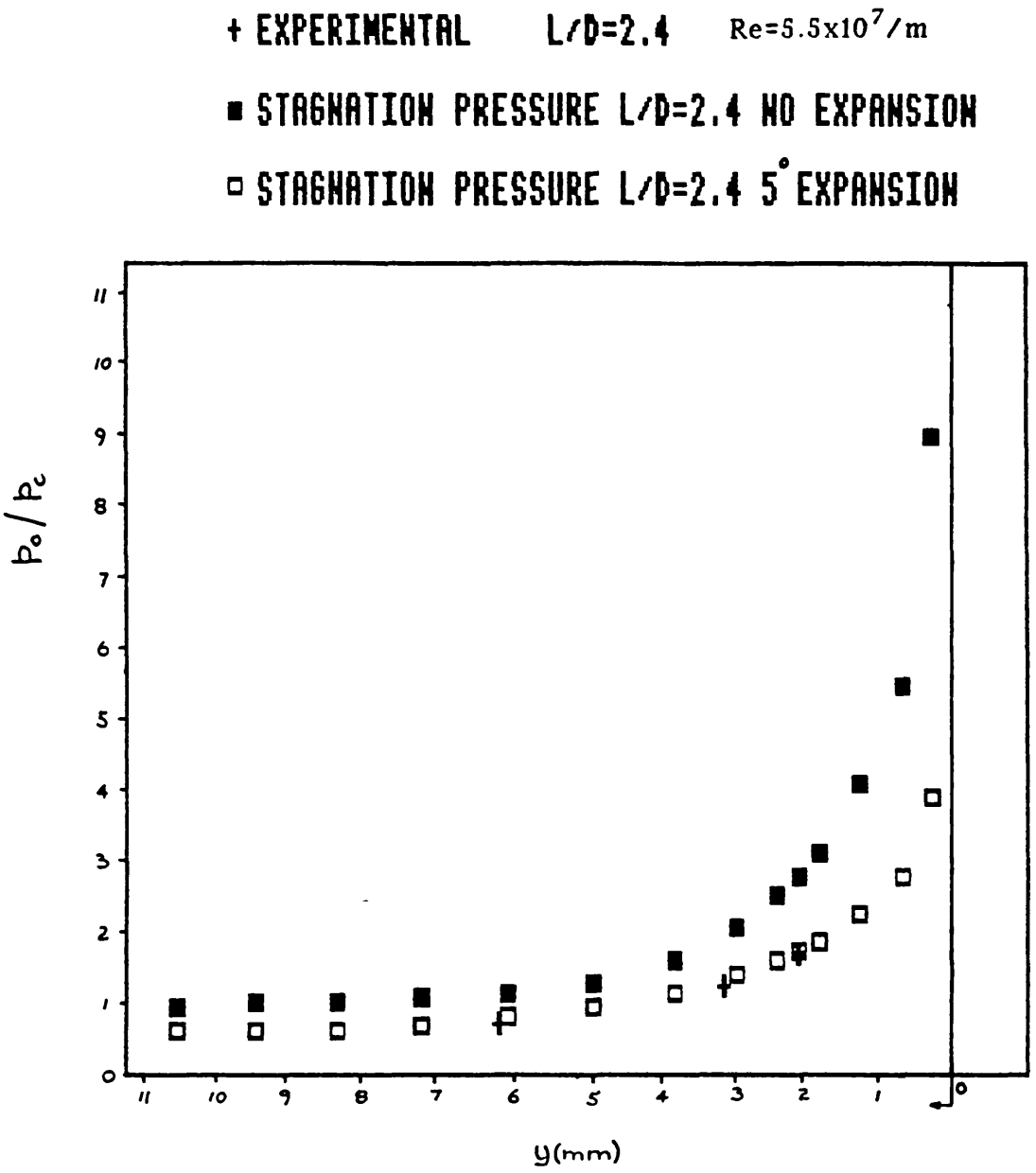

Fig.66 Calculated reattachment pressures (L=6cm)

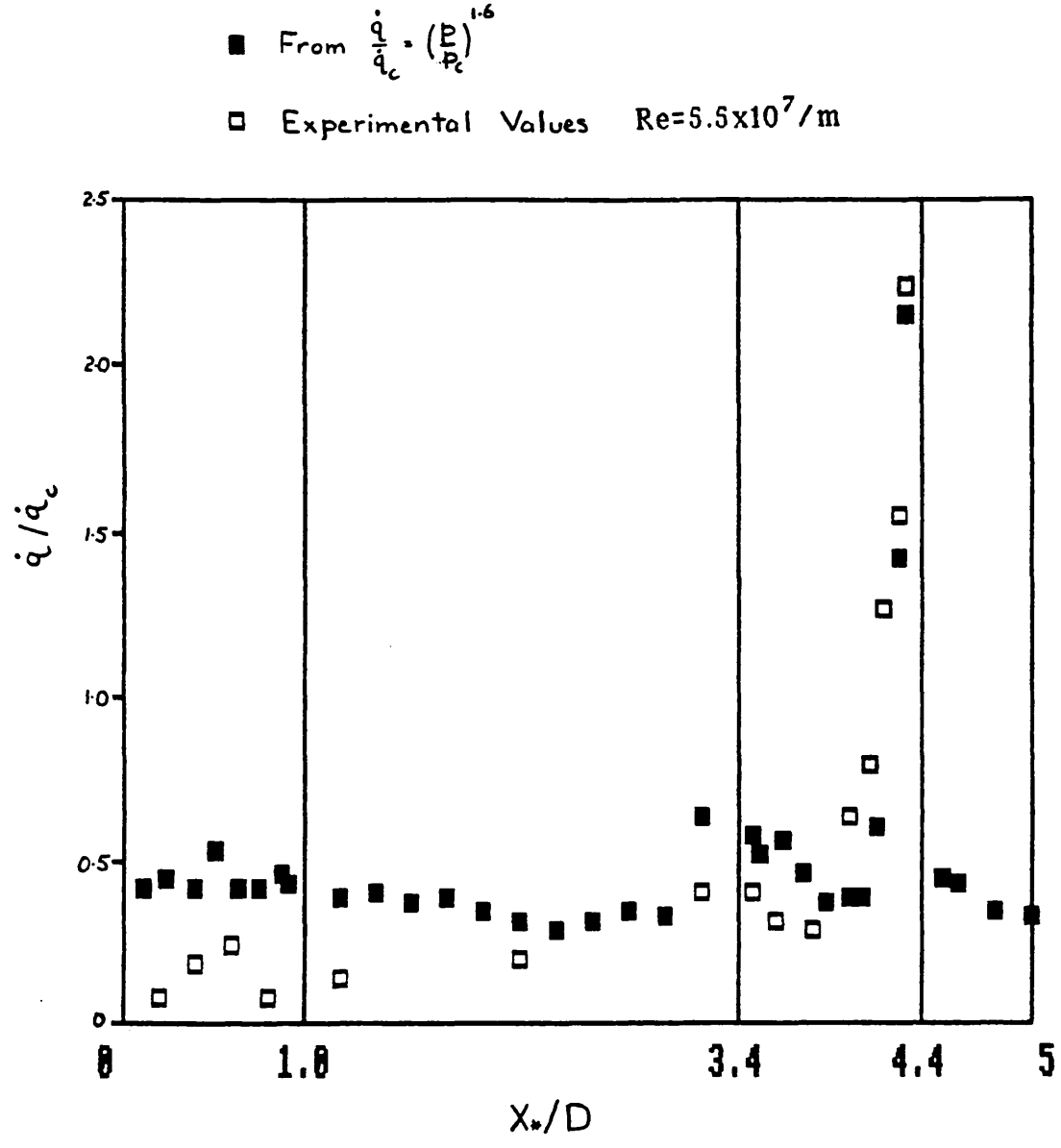

Fig.67 Heat transfer rates calculated from pressure measurements

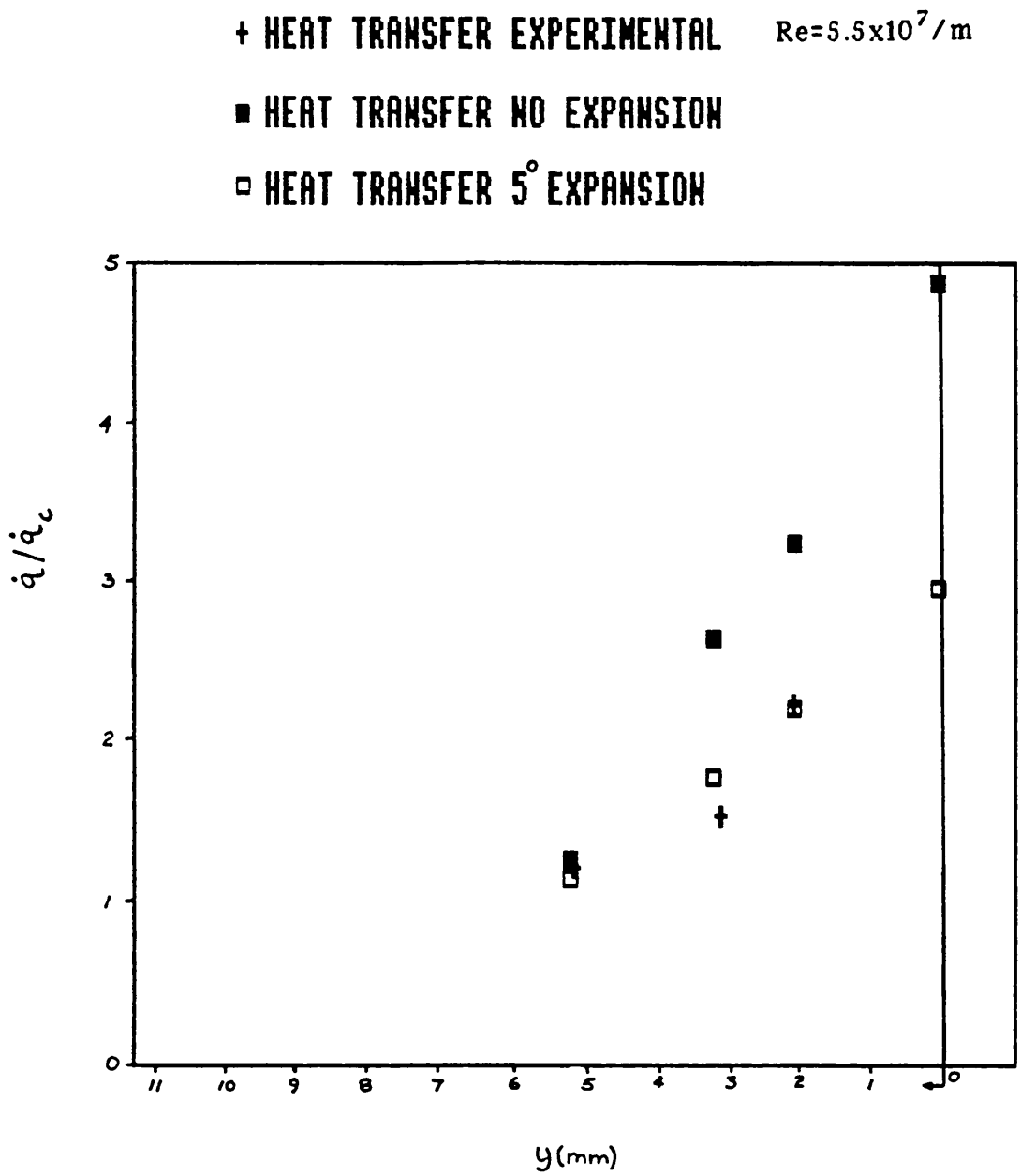

Fig.68 Calculated reattachment heat transfer rates from eqn.1

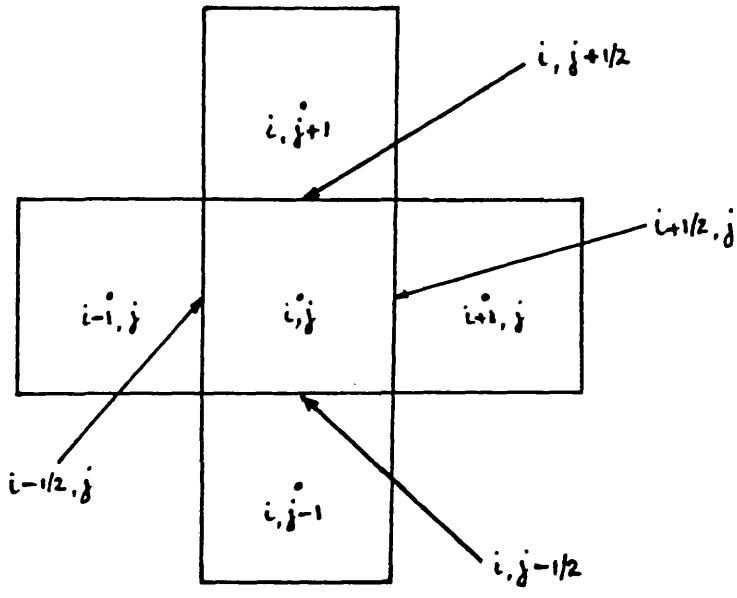

Fig.69 Computational cells

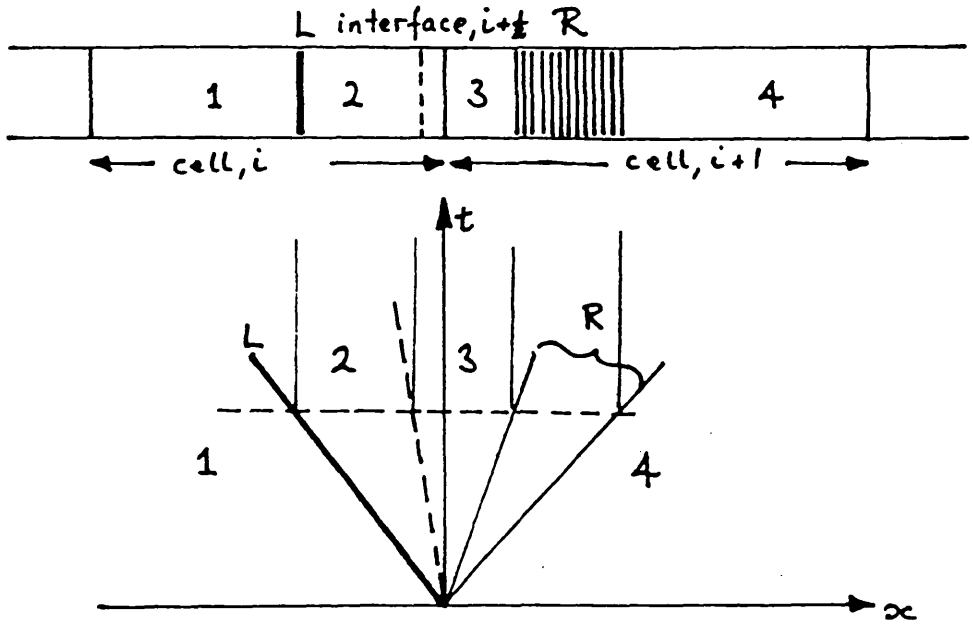

Fig.70 One dimensional Riemann problem

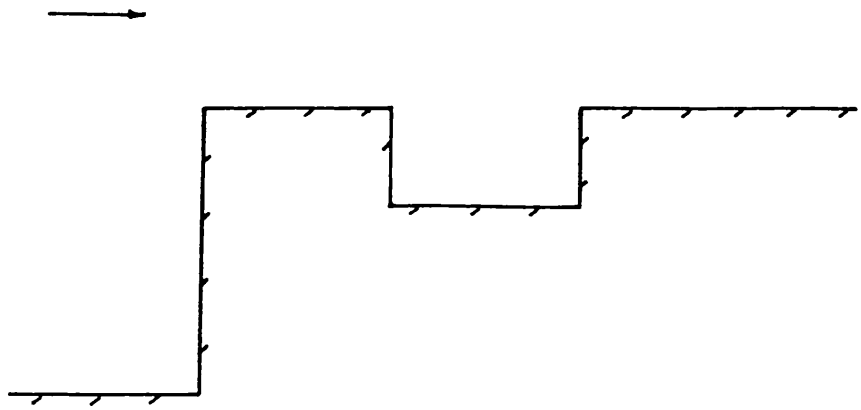

Fig.71a Blunt nosed body with cavity

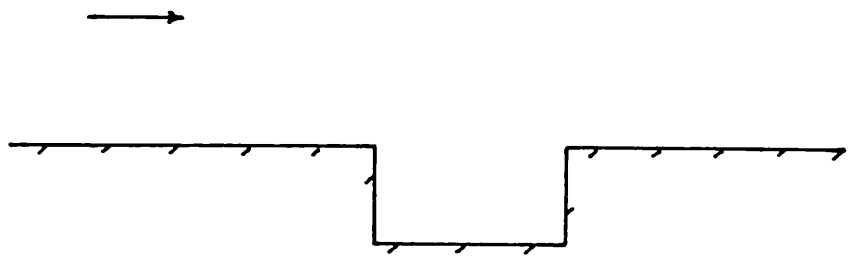

Fig.71b Flat plate with cavity

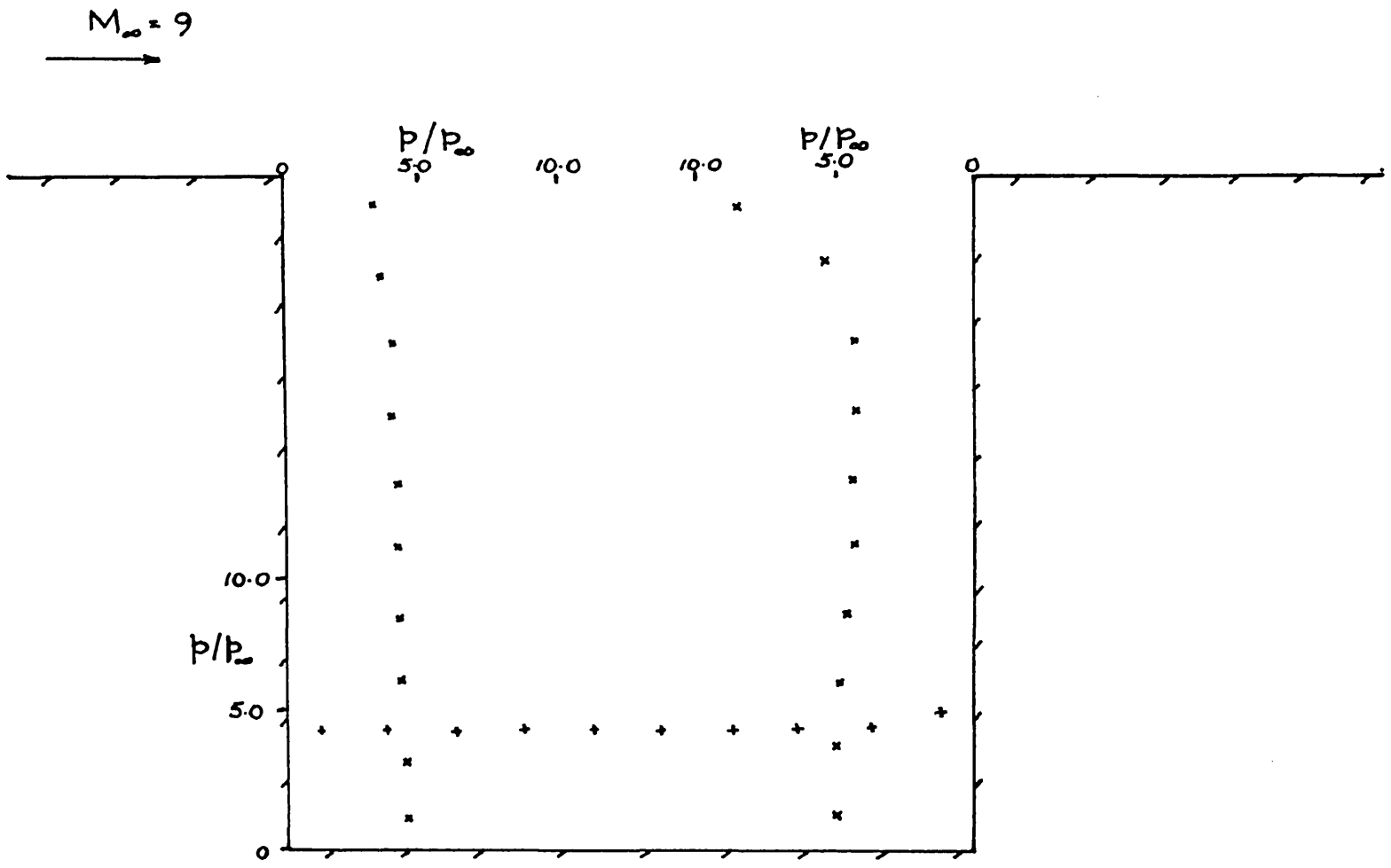

Fig.72 Inviscid cavity pressures for M=9

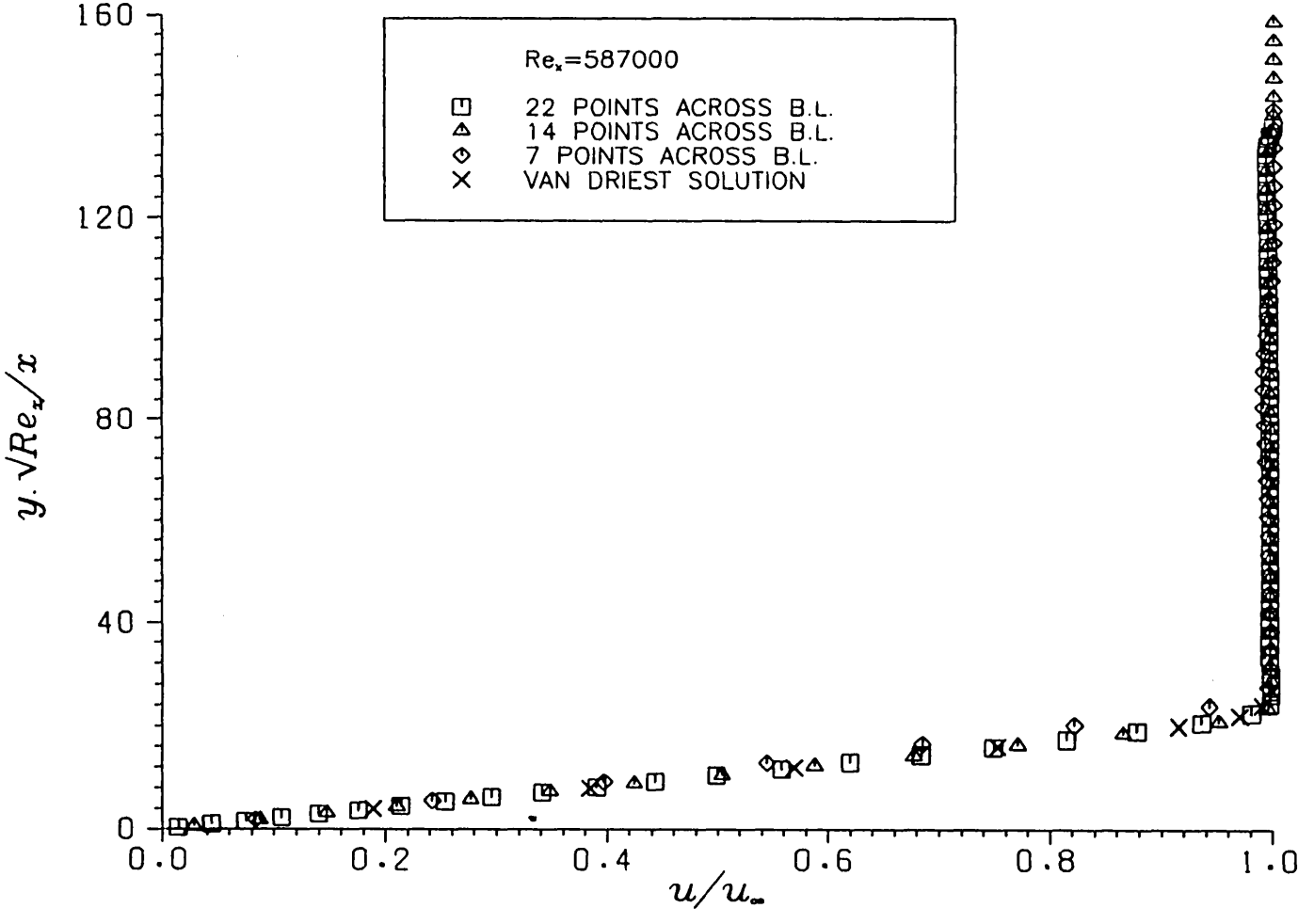

Fig.73 Velocity profiles for Mach 8 adiabatic wall flat plate boundary layer at Re_x=587 000

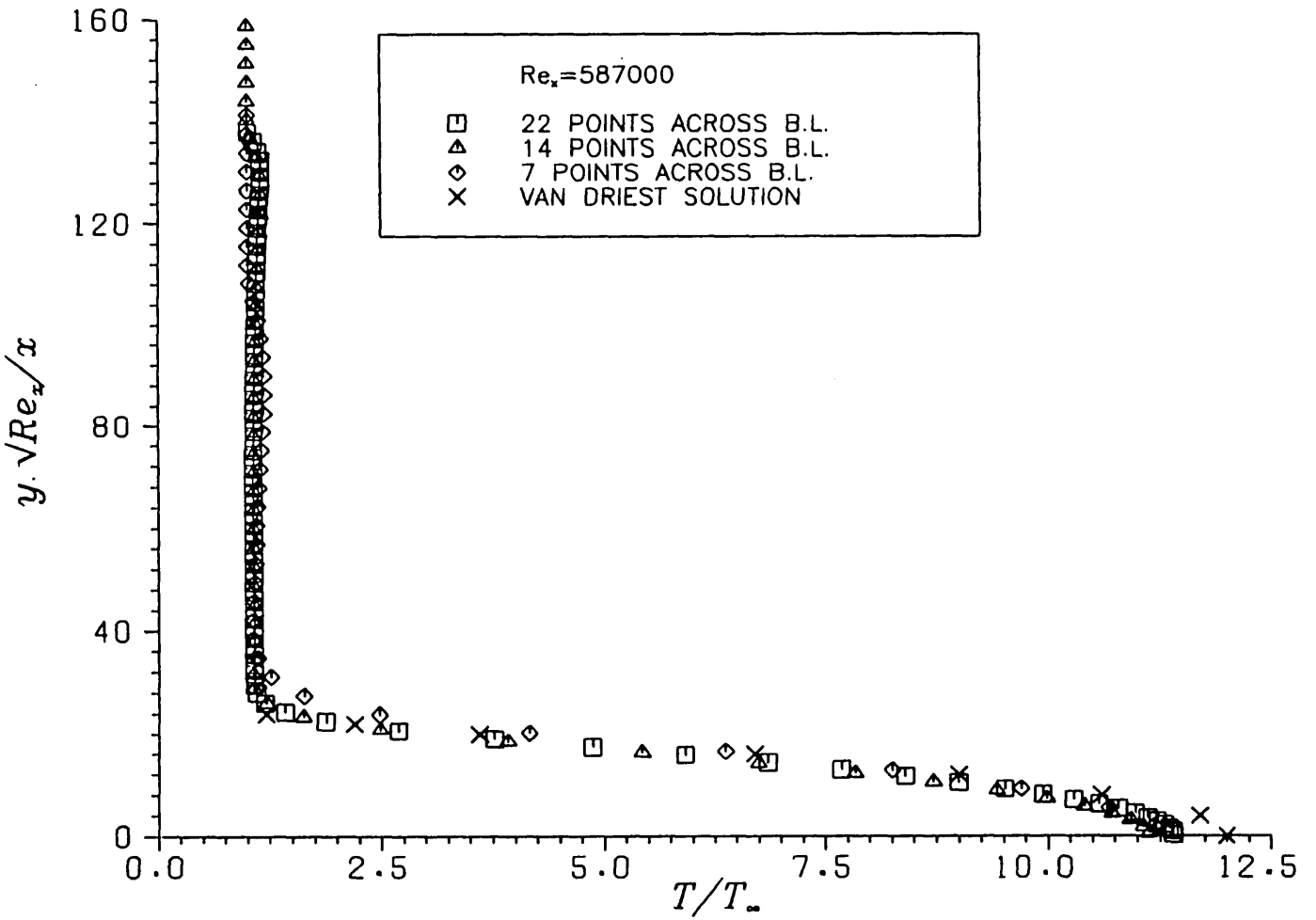

Fig.74 Temperature profiles for Mach 8 adiabatic wall flat plate boundary layer at Re_x=587 000

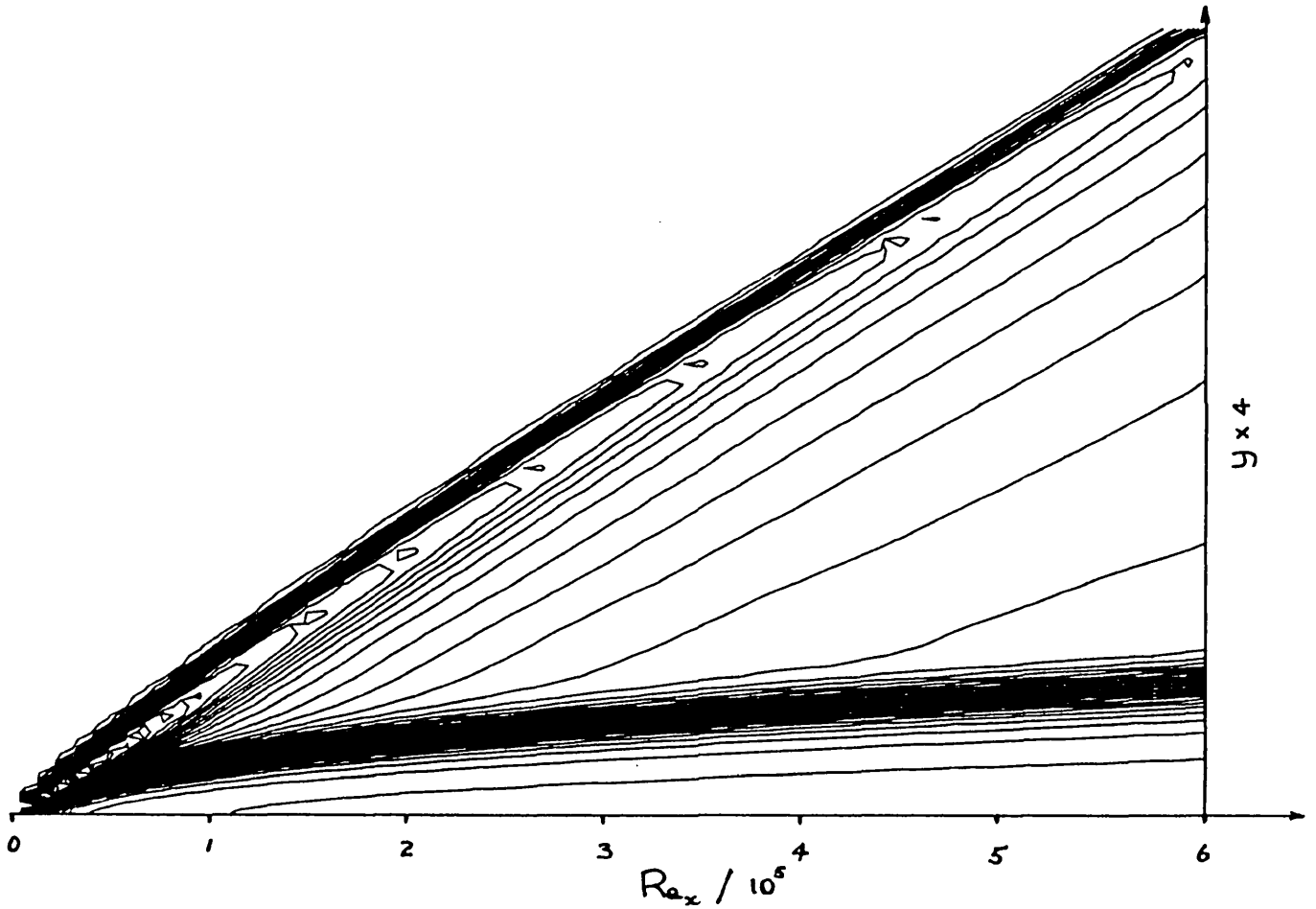

Fig.75 Density contours for Mach 8 adiabatic wall flat plate boundary layer with 22 points across the boundary layer at the downstream end

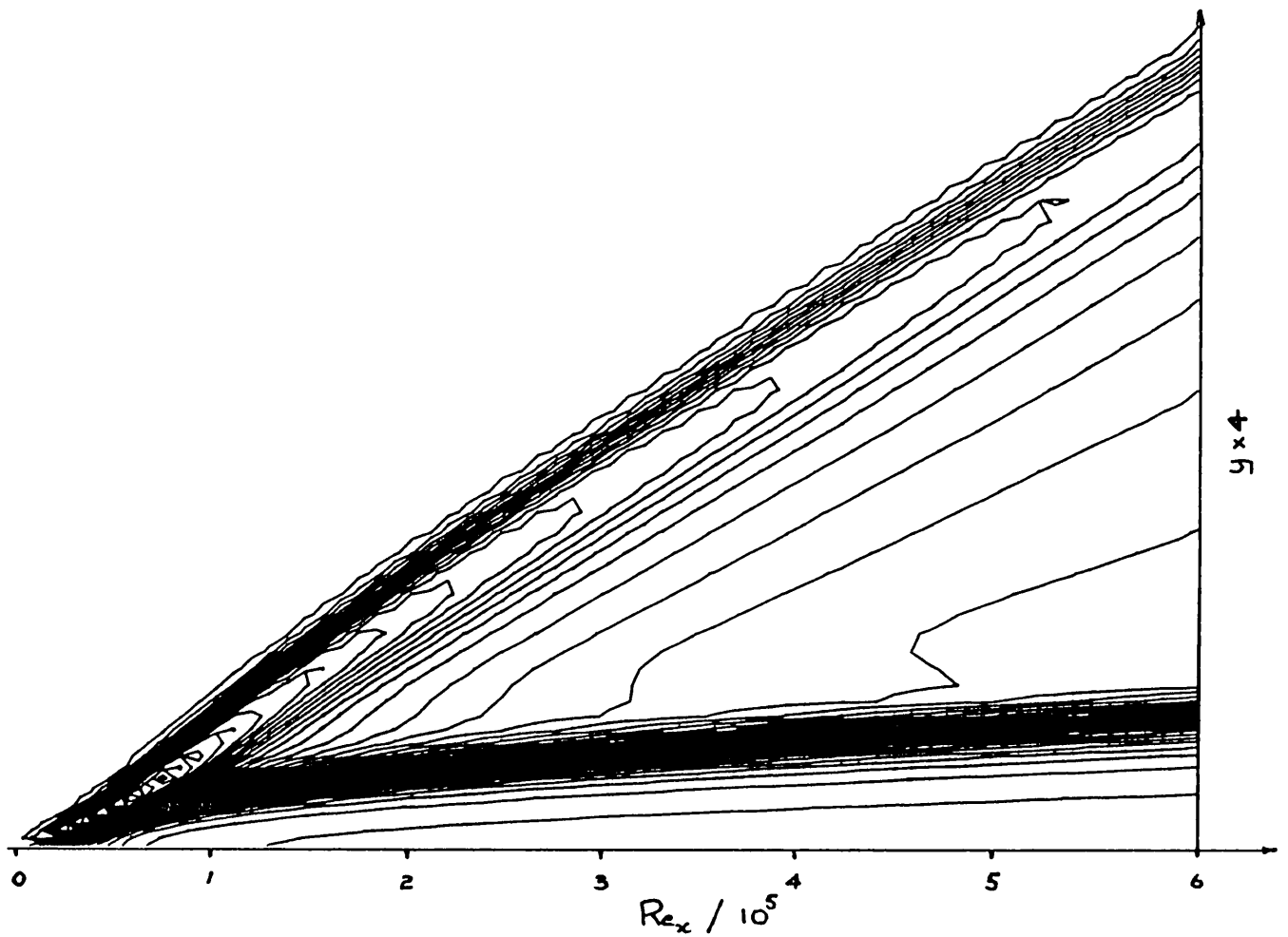

Fig.76 Density contours for Mach 8 adiabatic wall flat plate boundary layer with 14 points across the boundary layer at the downstream end

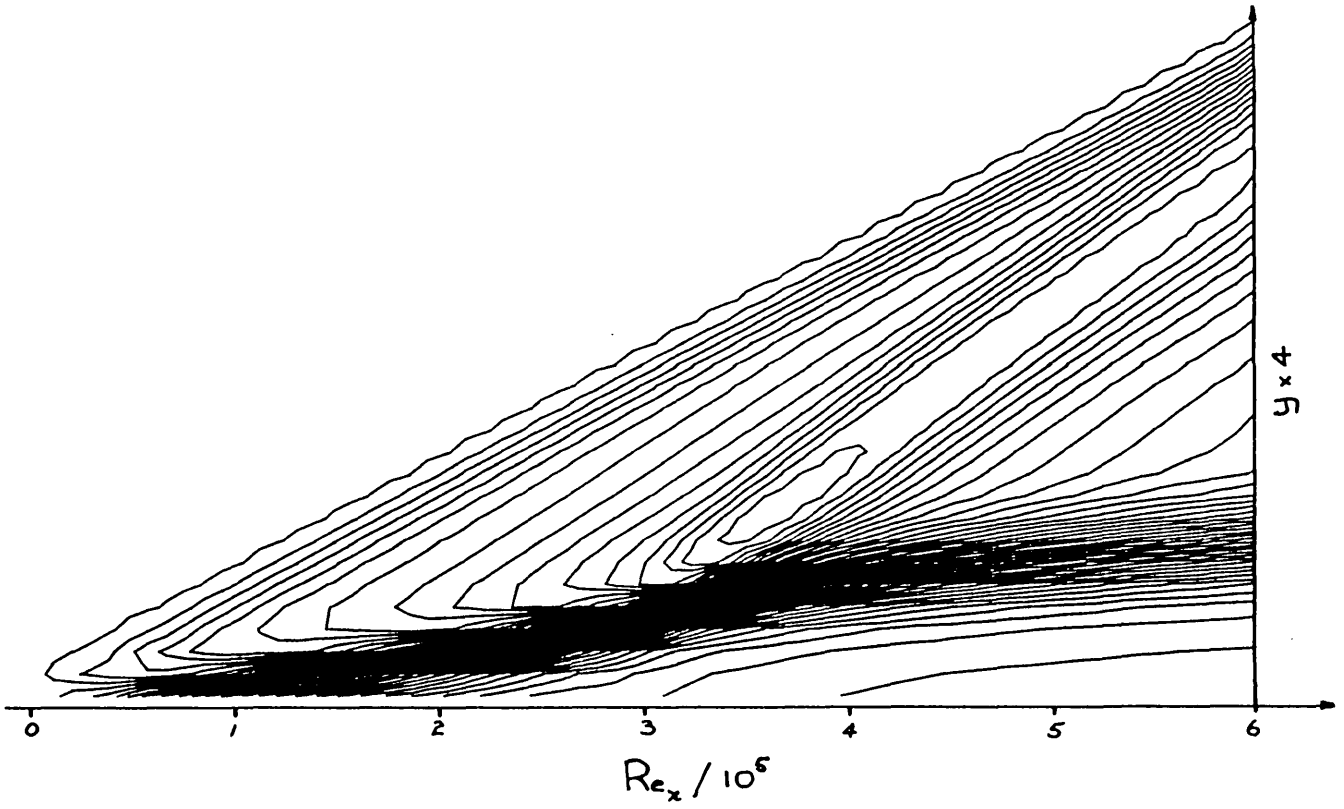

Fig.77 Density contours for Mach 8 adiabatic wall flat plate boundary layer with 7 points across the boundary layer at the downstream end

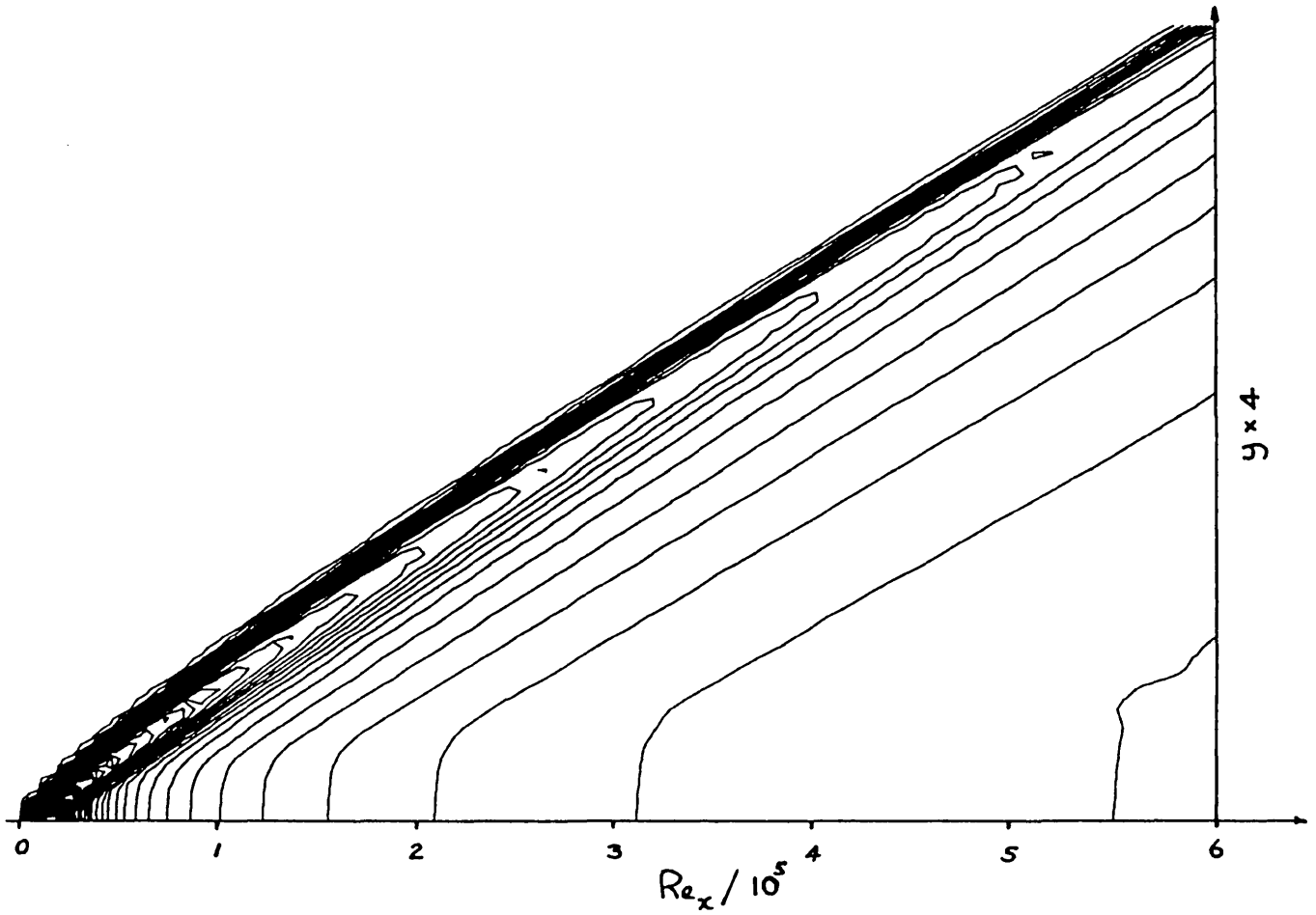

Fig.78 Pressure contours for Mach 8 adiabatic wall flat plate boundary layer with 22 points across the boundary layer at the downstream end

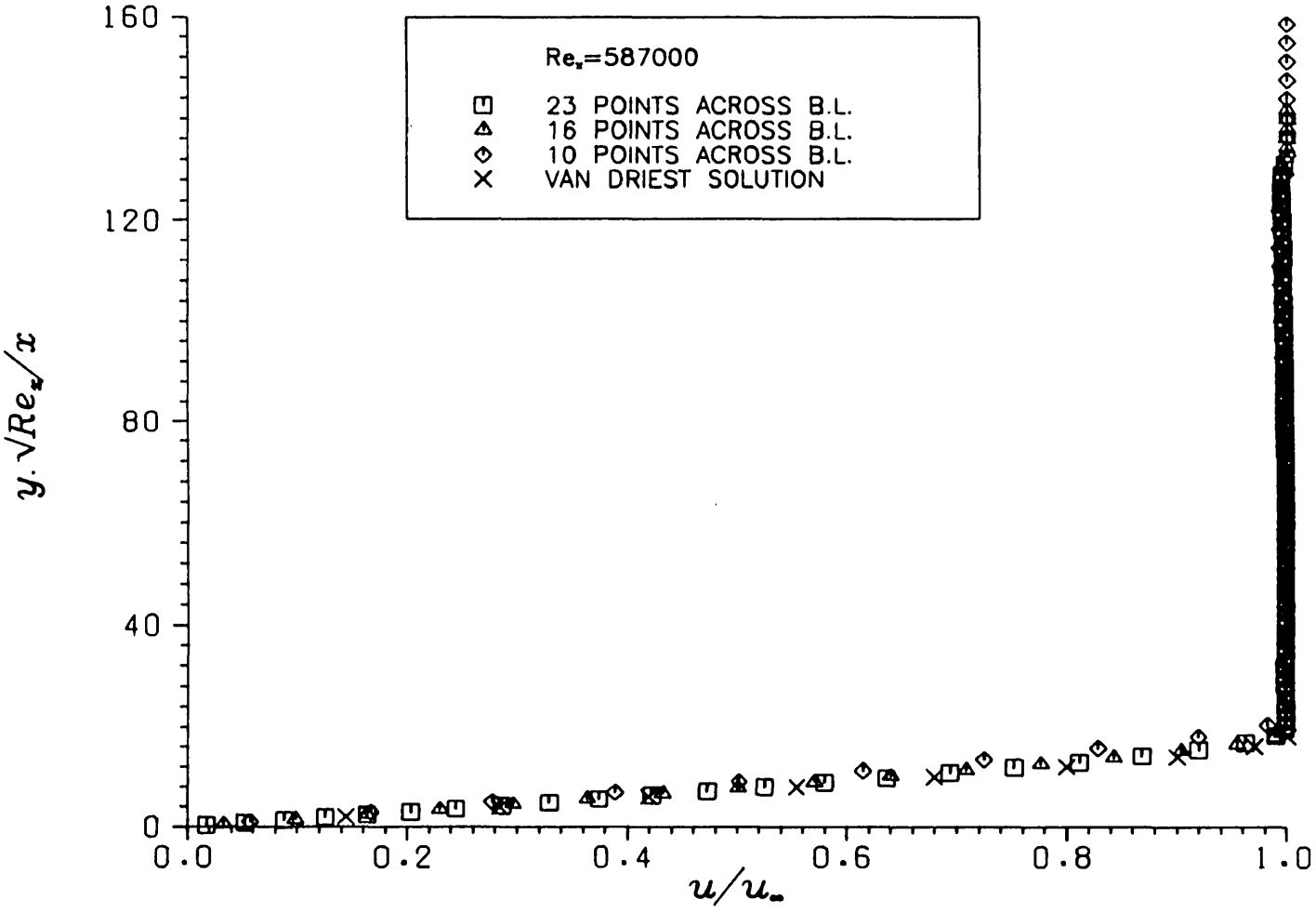

Fig.79 Velocity profiles for Mach 8 isothermal wall (T_w/T_∞=6) flat plate boundary layer at Re_x=587 000

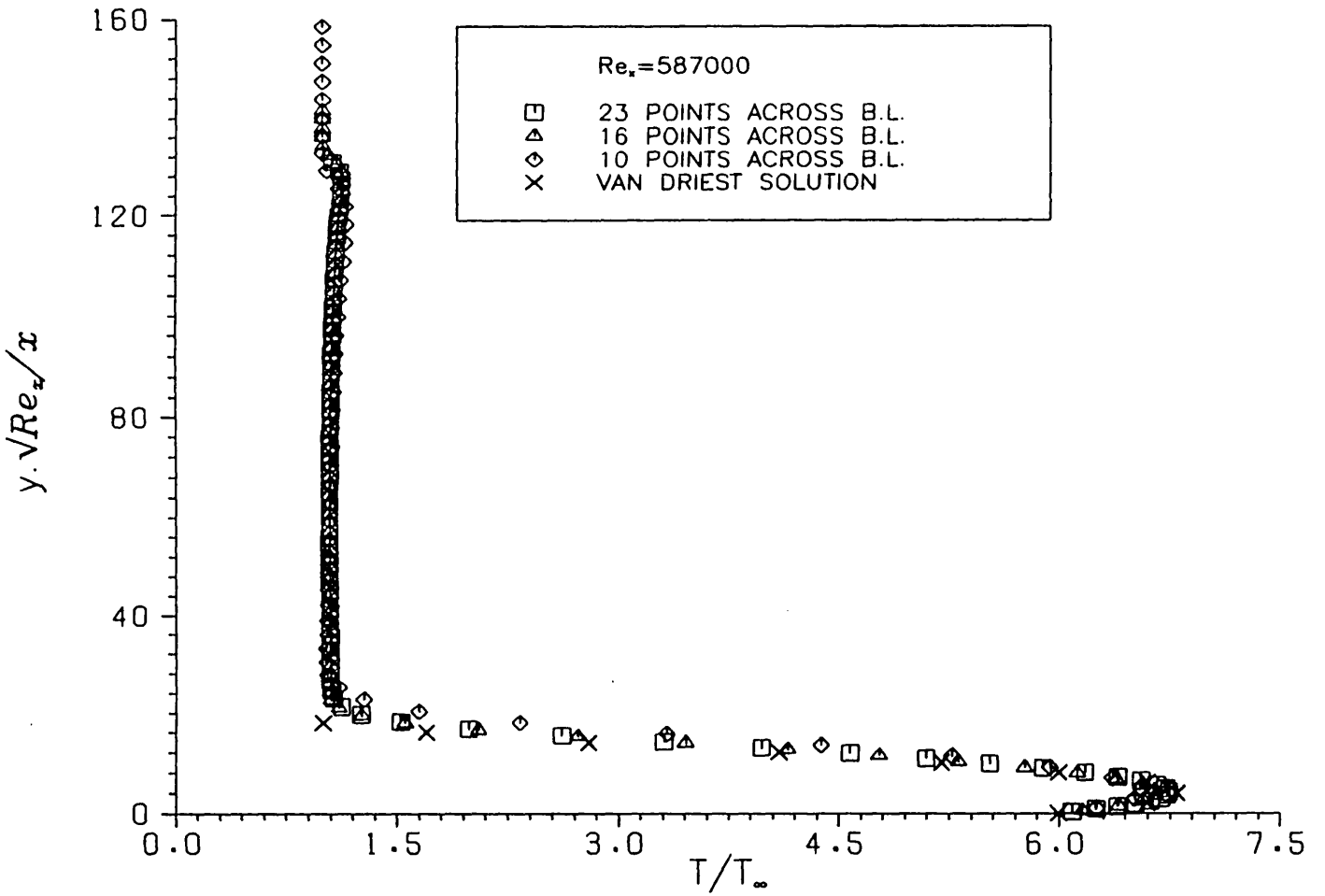

Fig.80 Temperature profiles for Mach 8 isothermal wall (T_w/T_∞=6) flat plate boundary layer at Re_x=587 000

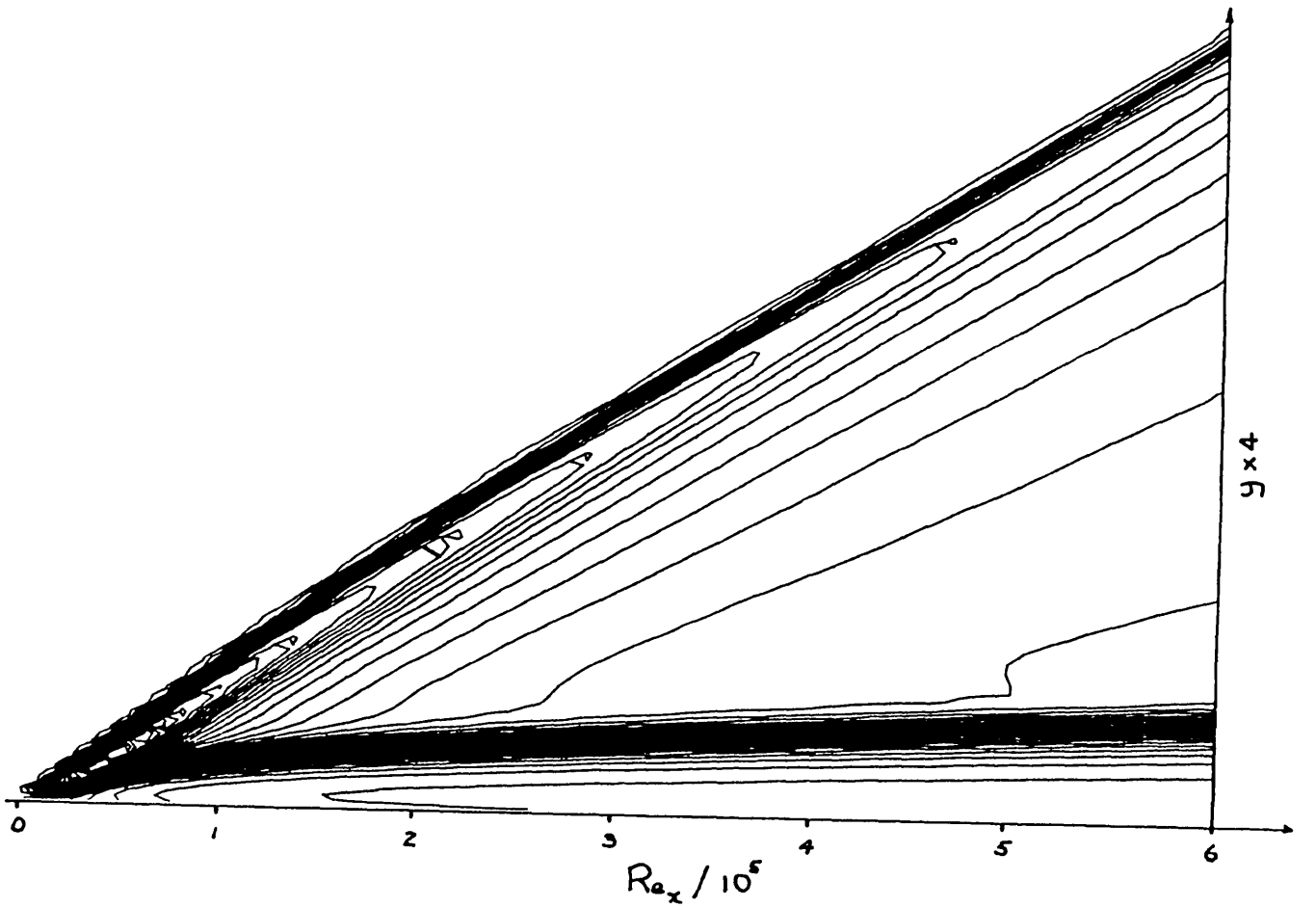

Fig.81 Density contours for Mach 8 isothermal wall (T_w/T_∞=6) flat plate boundary layer with 23 points across the boundary layer at the downstream end

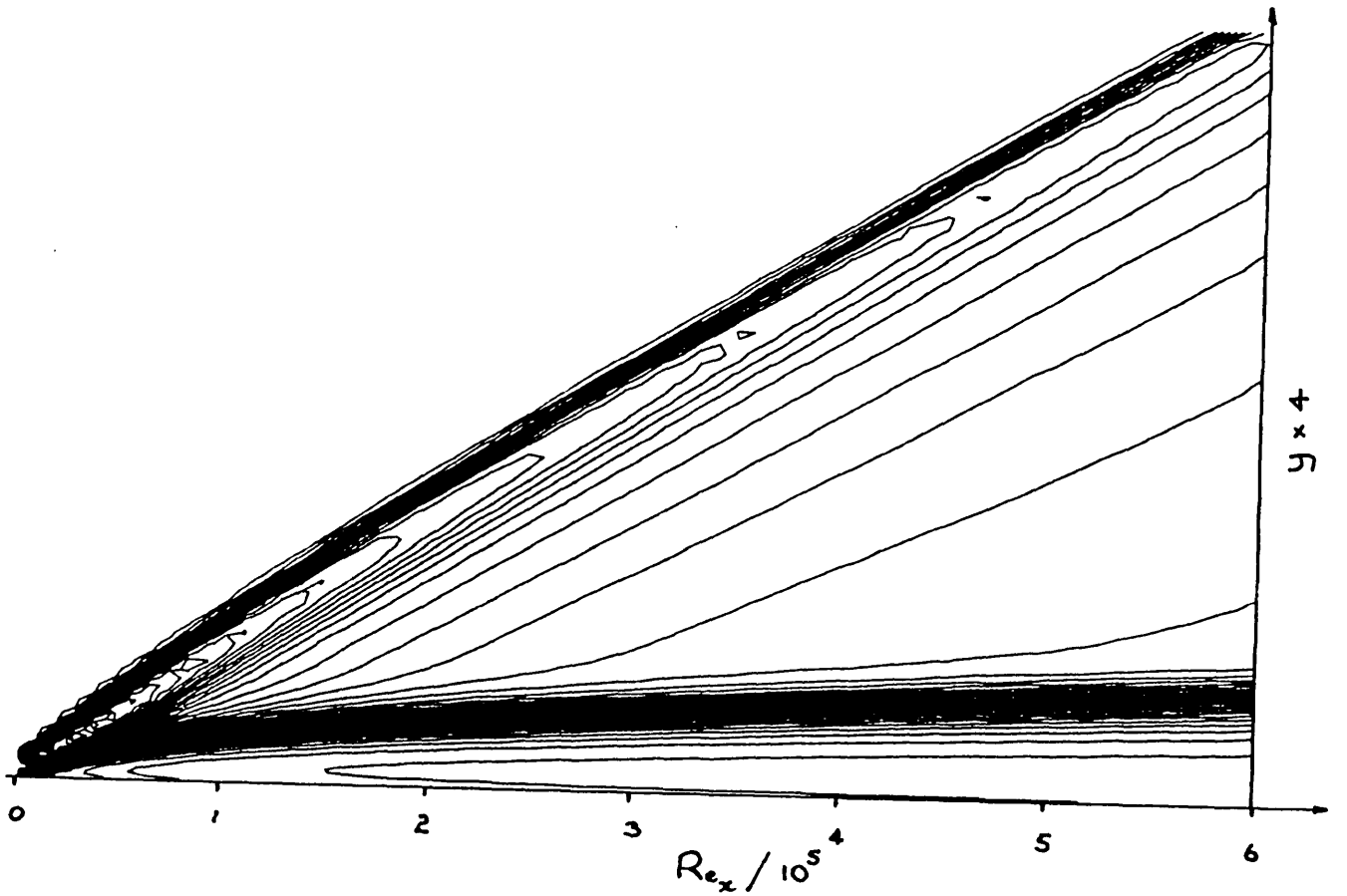

Fig.82 Density contours for Mach 8 isothermal wall (T_w/T_∞=6) flat plate boundary layer with 16 points across the boundary layer at the downstream end

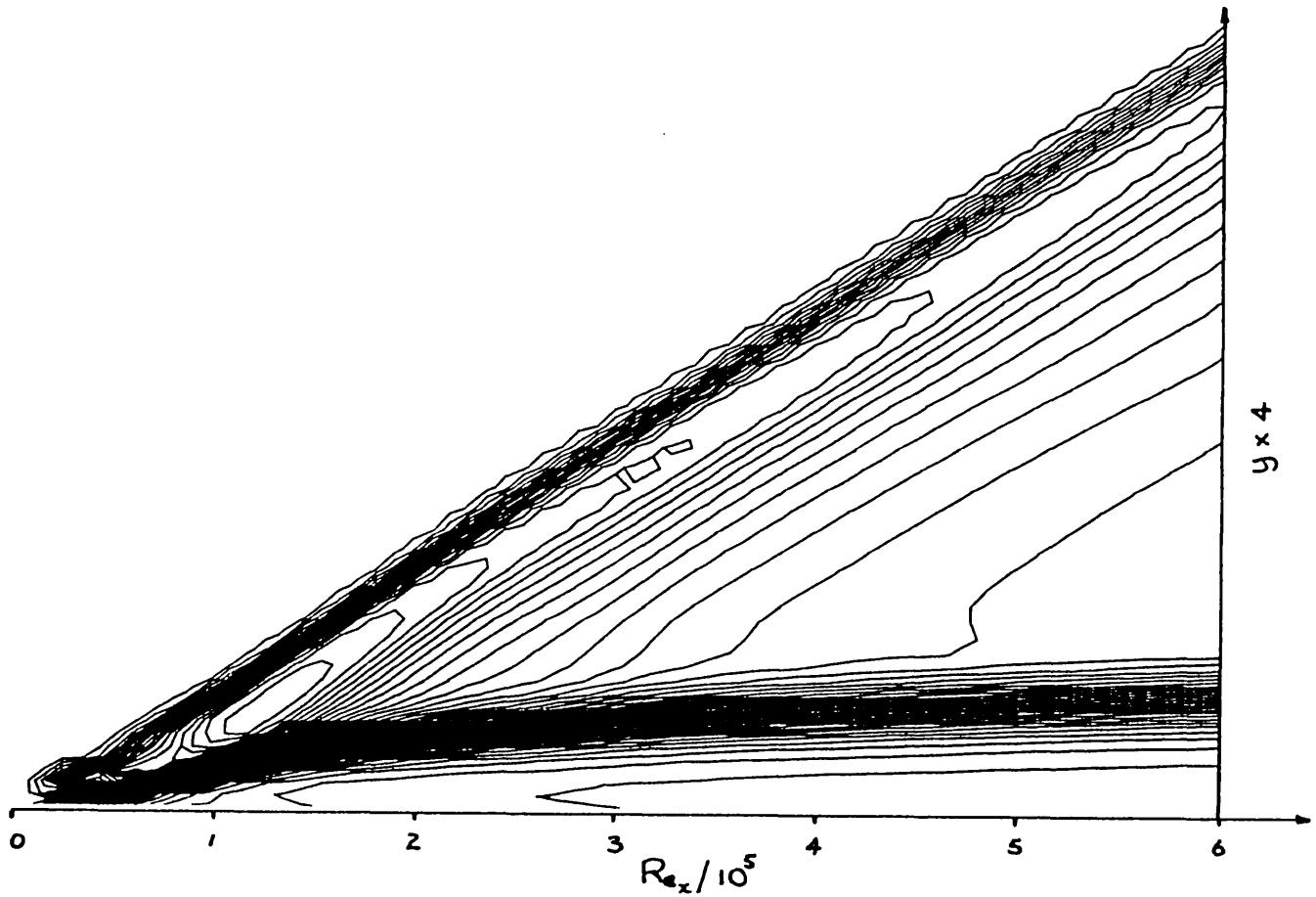

Fig.83 Density contours for Mach 8 isothermal wall (T_w/T_∞=6) flat plate boundary layer with 10 points across the boundary layer at the downstream end

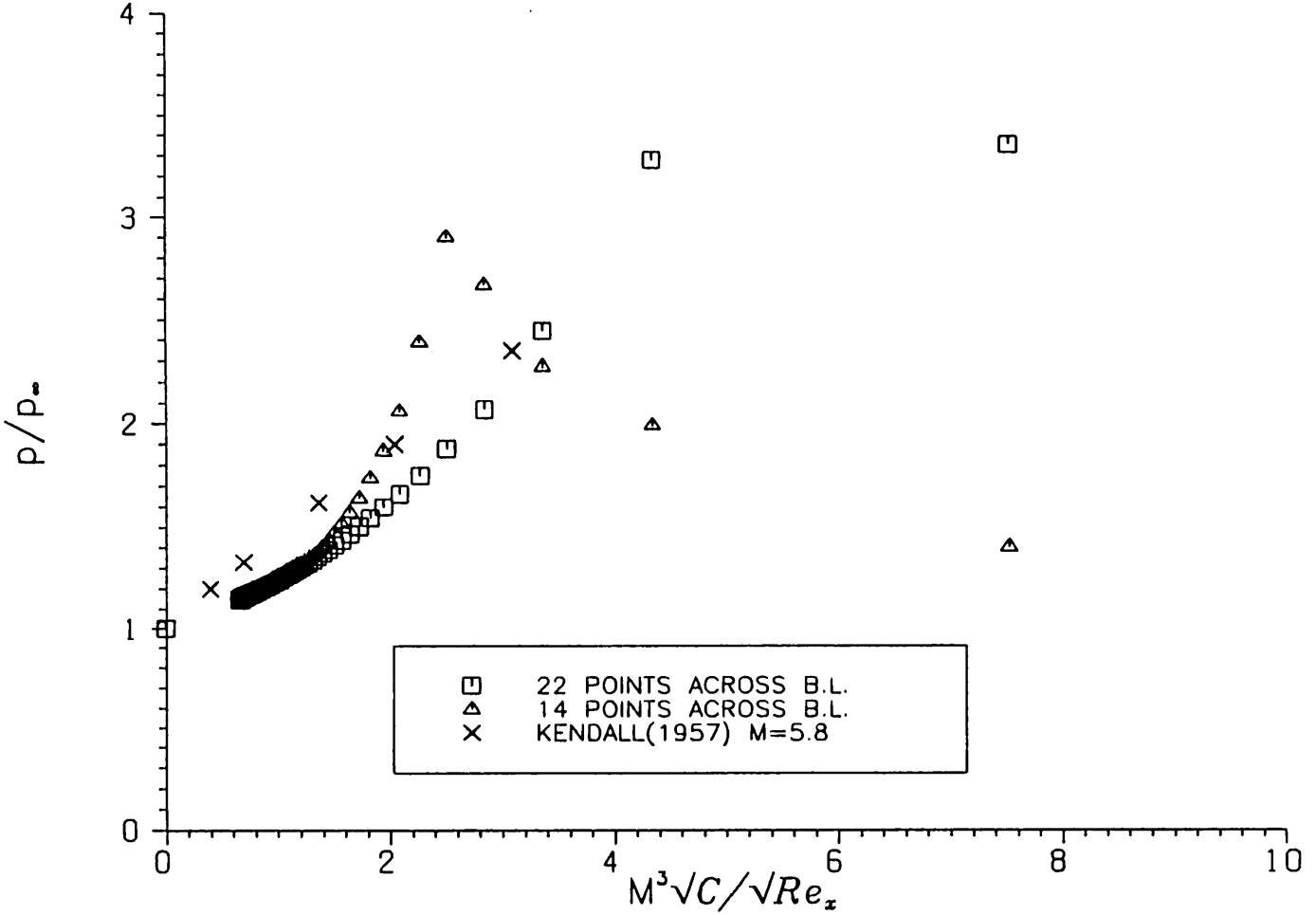

Fig.84 Surface pressure vs leading edge interaction parameter

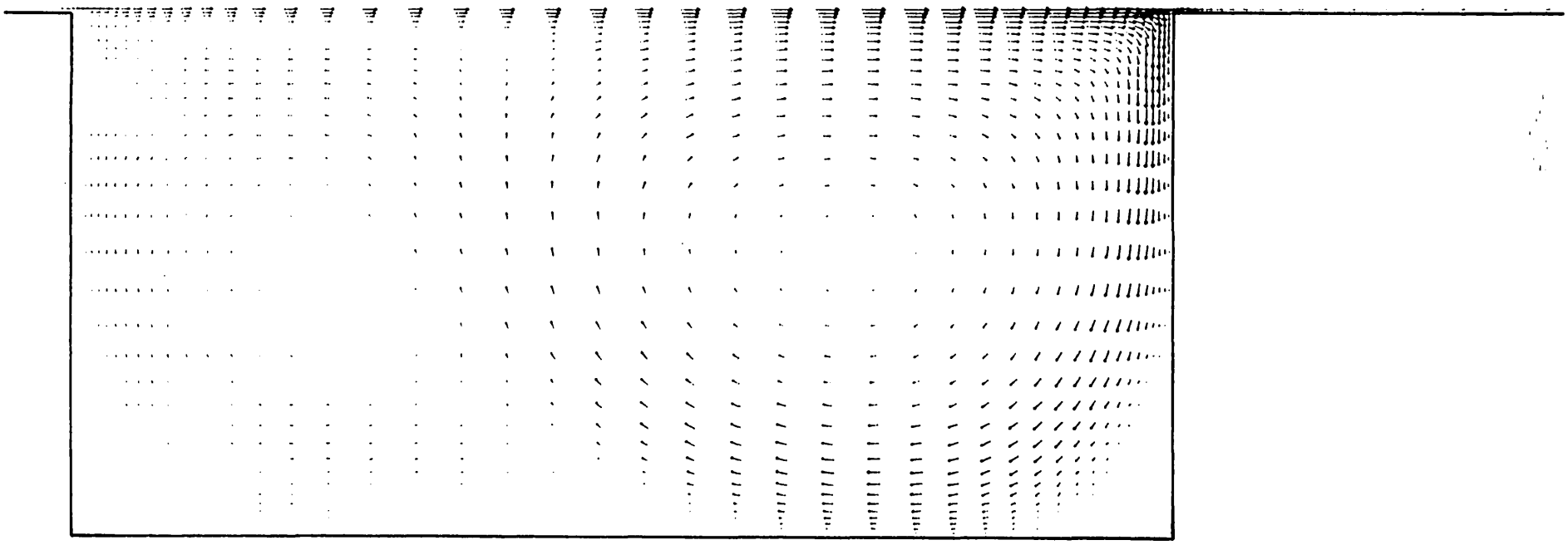

Fig.85 Mach 8 L/D=2.0 laminar cavity flowfield-vector length directly proportional to velocity

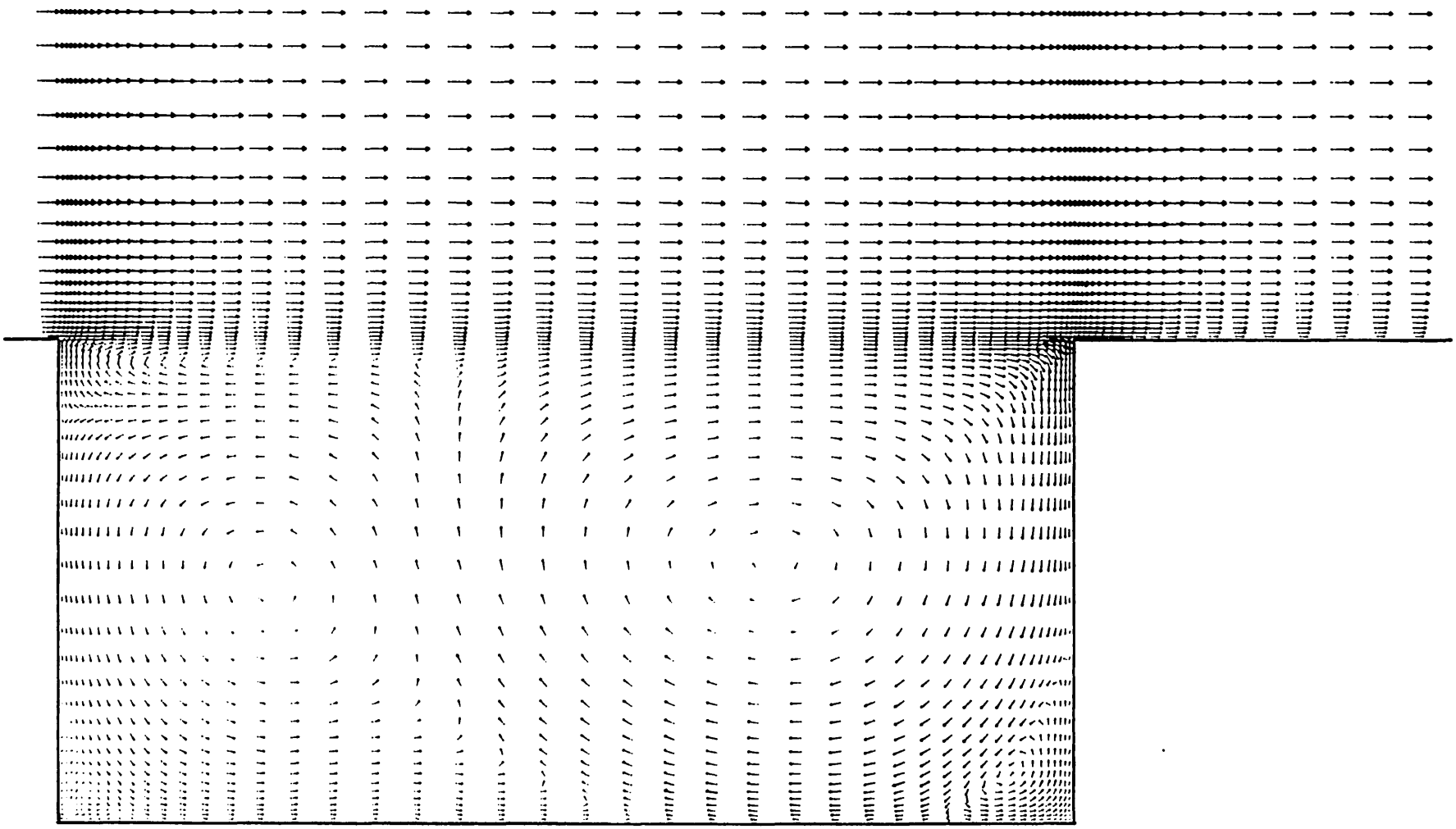

Fig.86 Mach 8 L/D=2.0 laminar cavity flowfield-vector length proportional to velocity to the power of 0.25

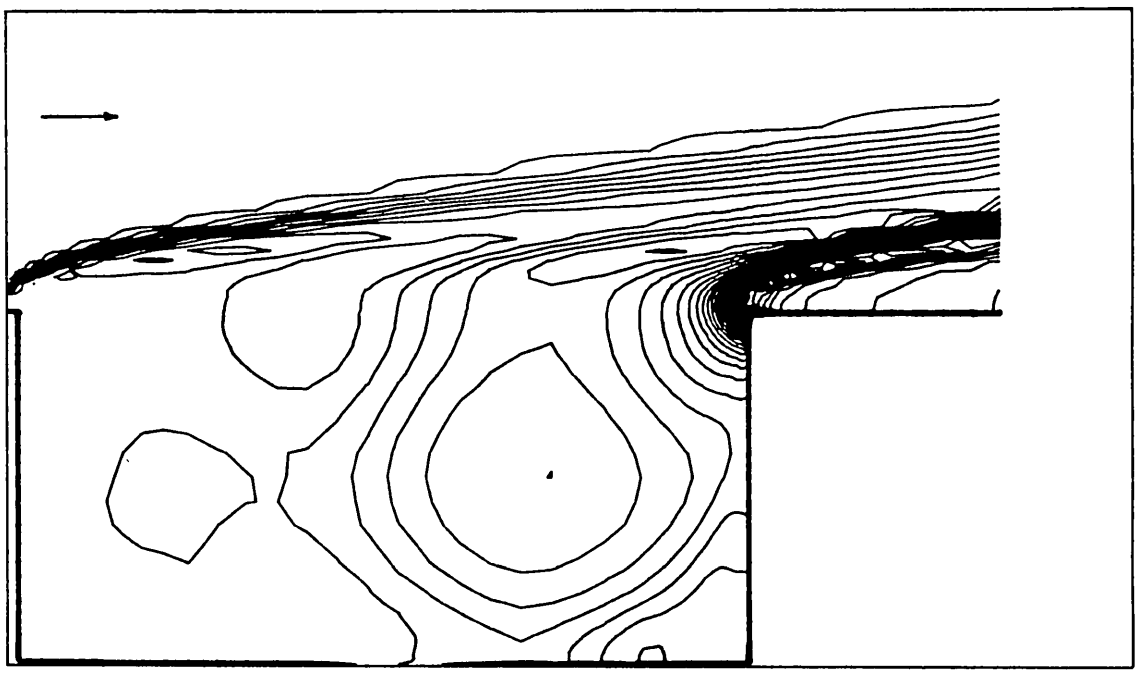

PRESSURE

CONTOUR DATA

NO. OF CONTOURS	=	40
MIN. CONTOUR LEVEL	=	0.8851
MAX. CONTOUR LEVEL	=	1.1450
CONTOUR INCREMENT	=	0.0067

Normalised by
free stream values

Fig.87 Pressure contours for Mach 8 L/D=2.0 laminar cavity flow

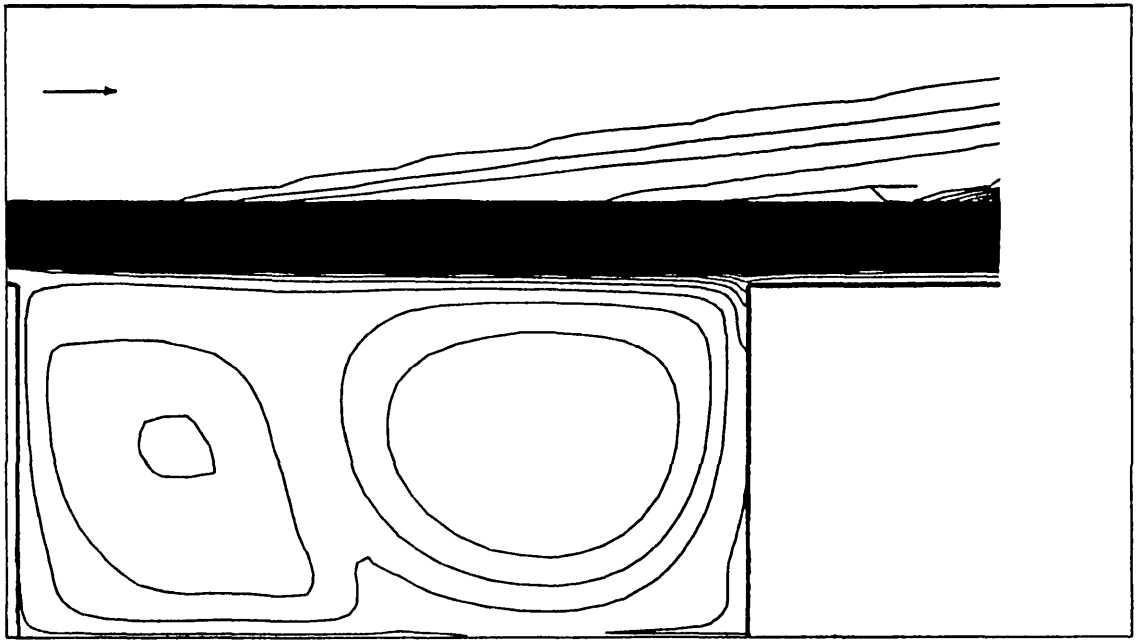

DENSITY

CONTOUR DATA

NO. OF CONTOURS	=	80
MIN. CONTOUR LEVEL	=	0.0974
MAX. CONTOUR LEVEL	=	1.0204
CONTOUR INCREMENT	=	0.0117

Normalised by
free stream values

Fig.88 Density contours for Mach 8 L/D=2.0 laminar cavity flow

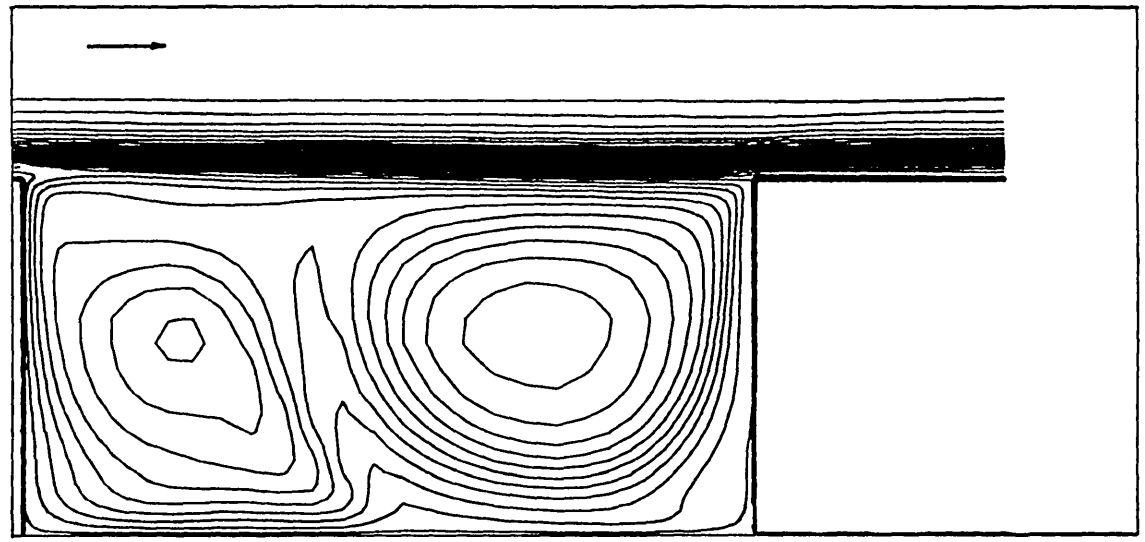

TEMPERATURE

CONTOUR DATA

NO. OF CONTOURS	=	40
MIN. CONTOUR LEVEL	=	1.0923
MAX. CONTOUR LEVEL	=	9.8869
CONTOUR INCREMENT	=	0.2255

Normalised by
free stream values

Fig.89 Temperature contours for Mach 8 L/D=2.0 laminar cavity flow

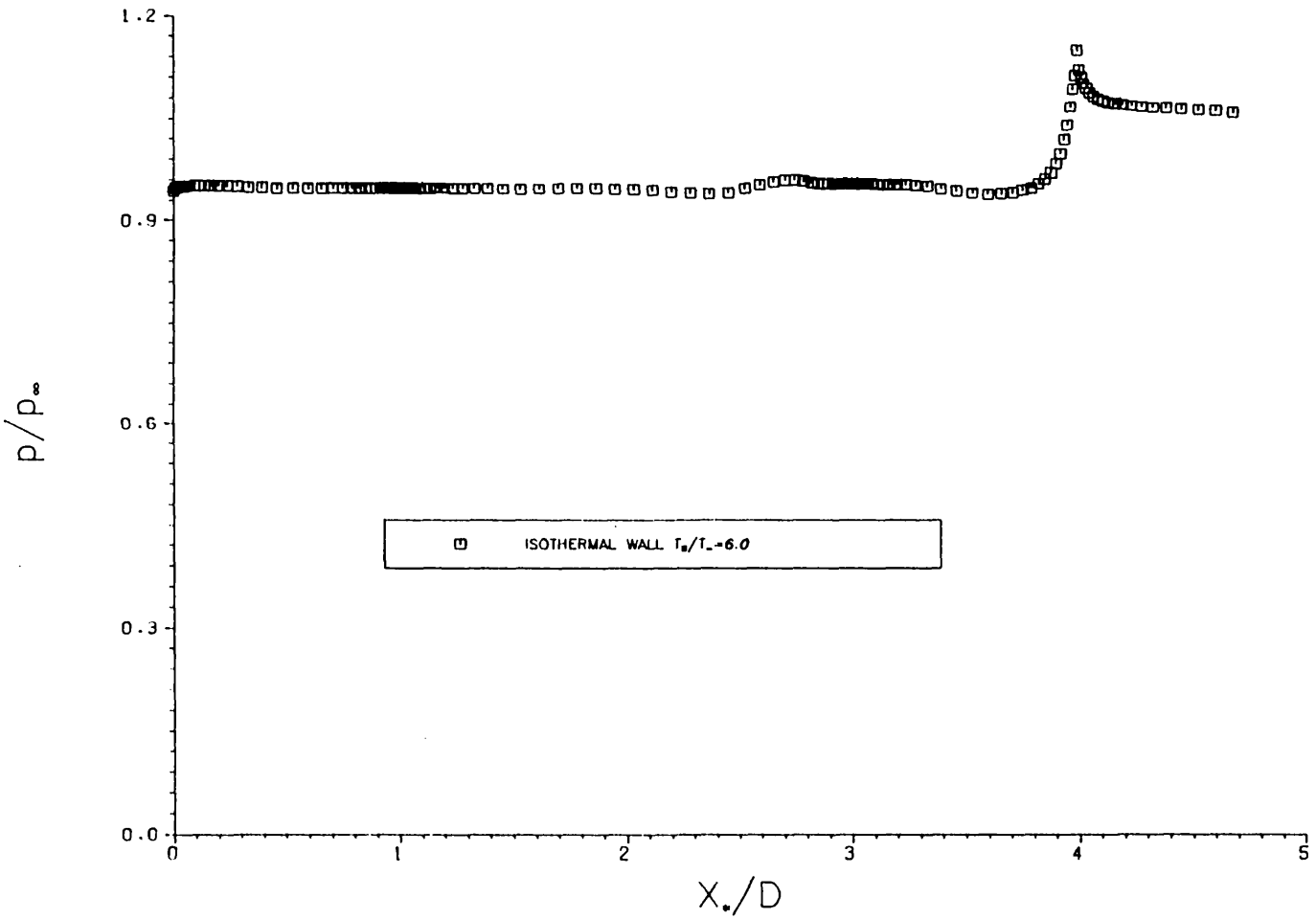

Fig.90 Surface pressure in computational cavity

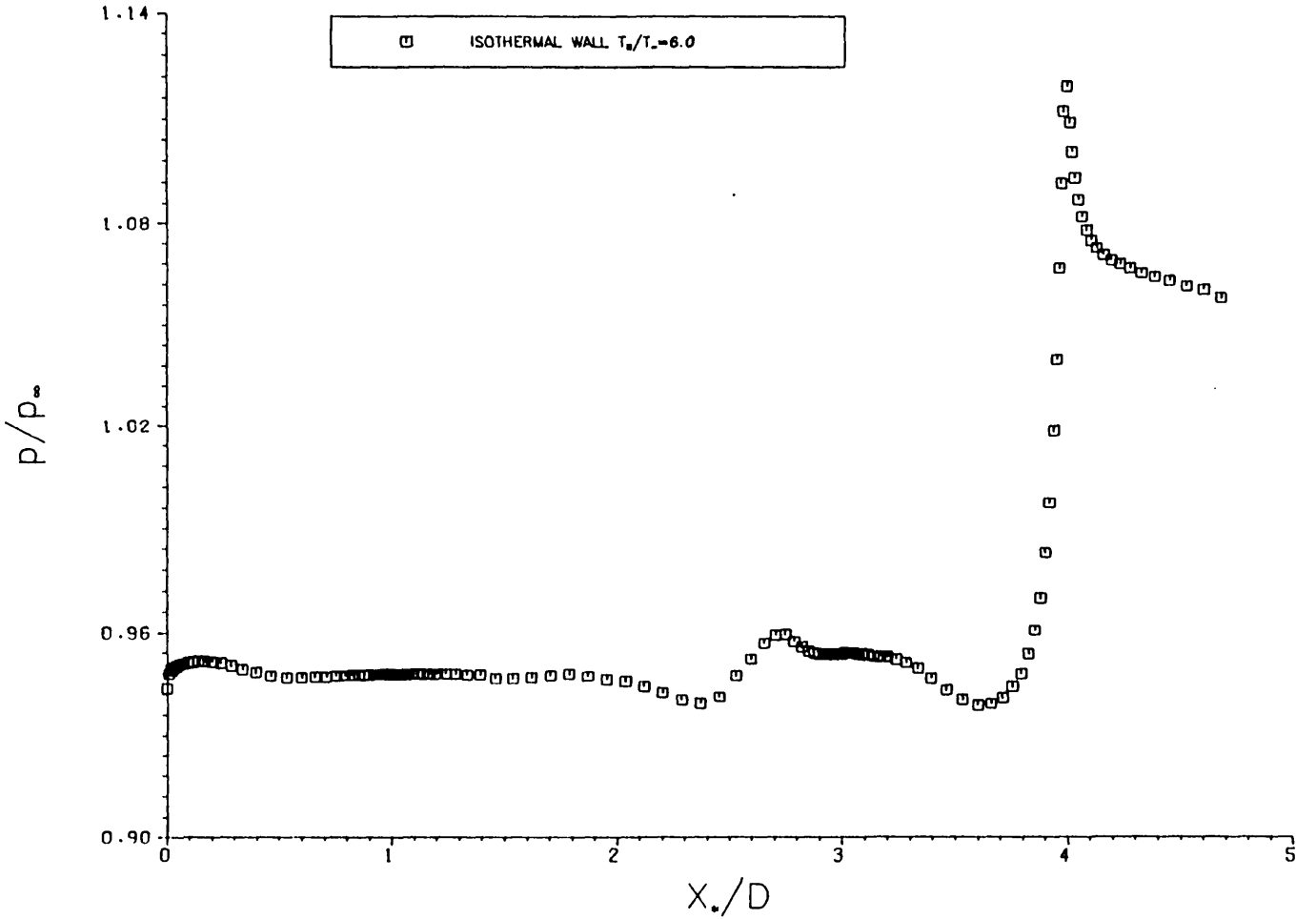

Fig.91 Surface pressure in computational cavity-expanded scale

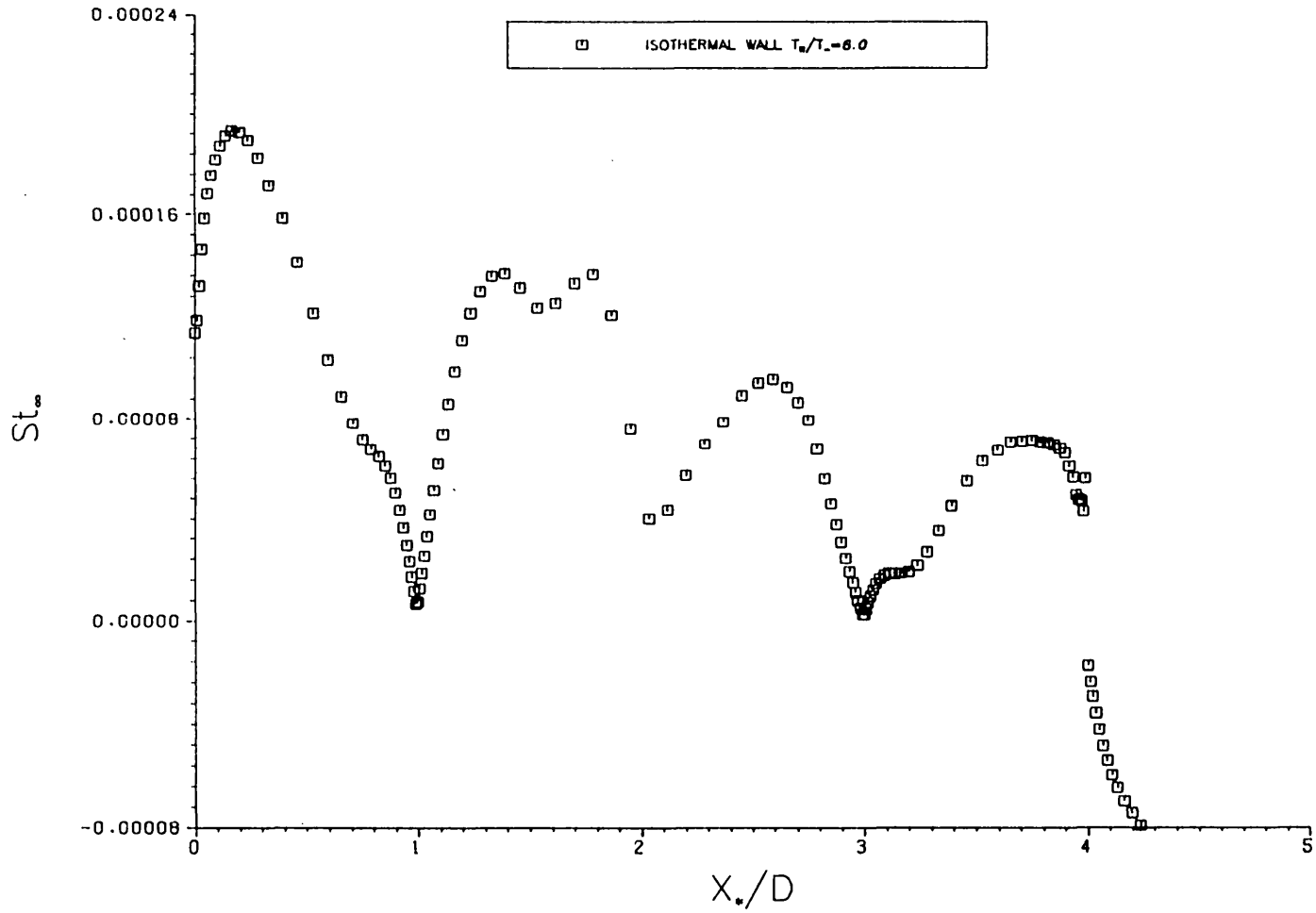

Fig.92 Stanton number distribution in computational cavity

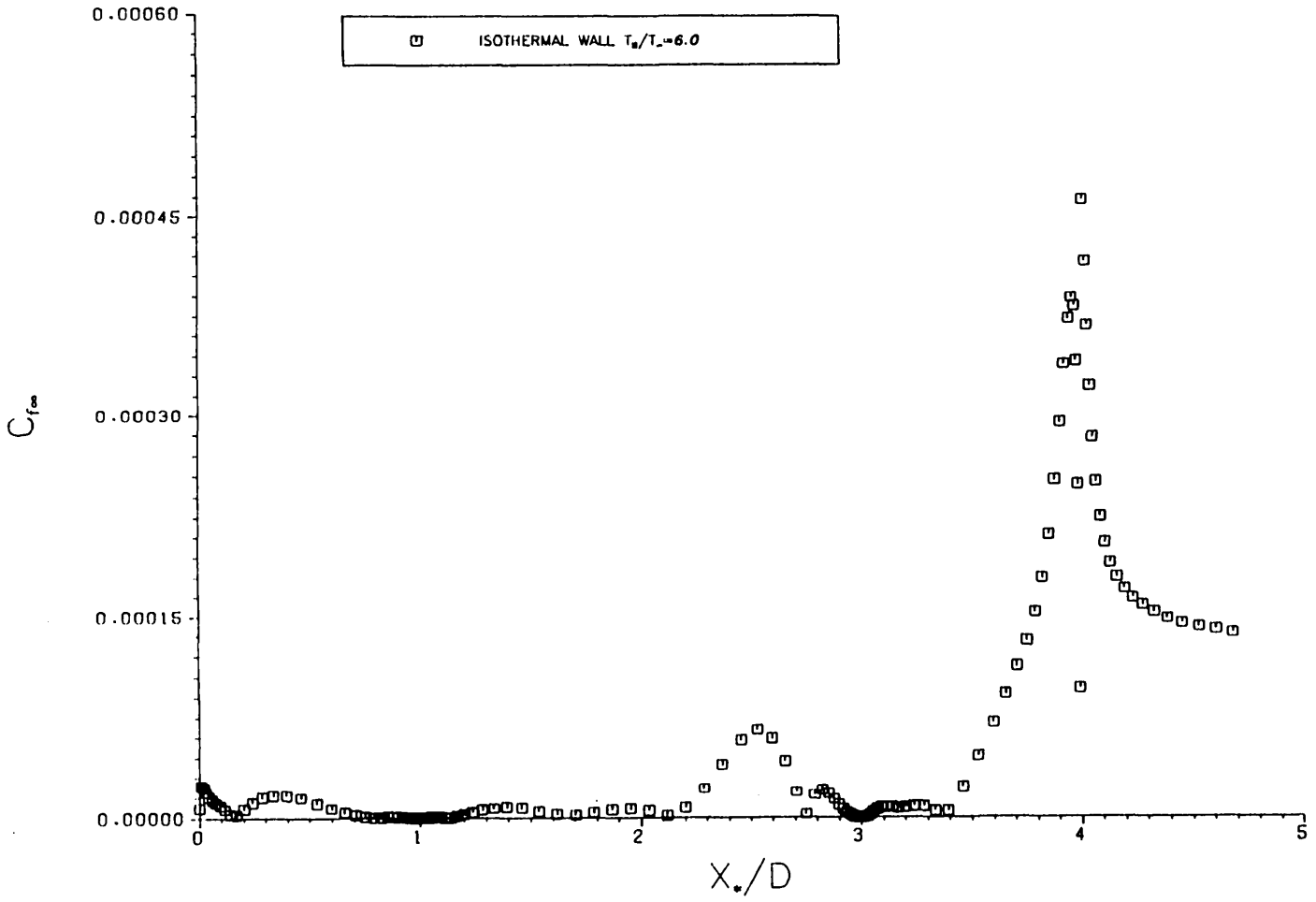

Fig.93 Skin friction distribution in computational cavity

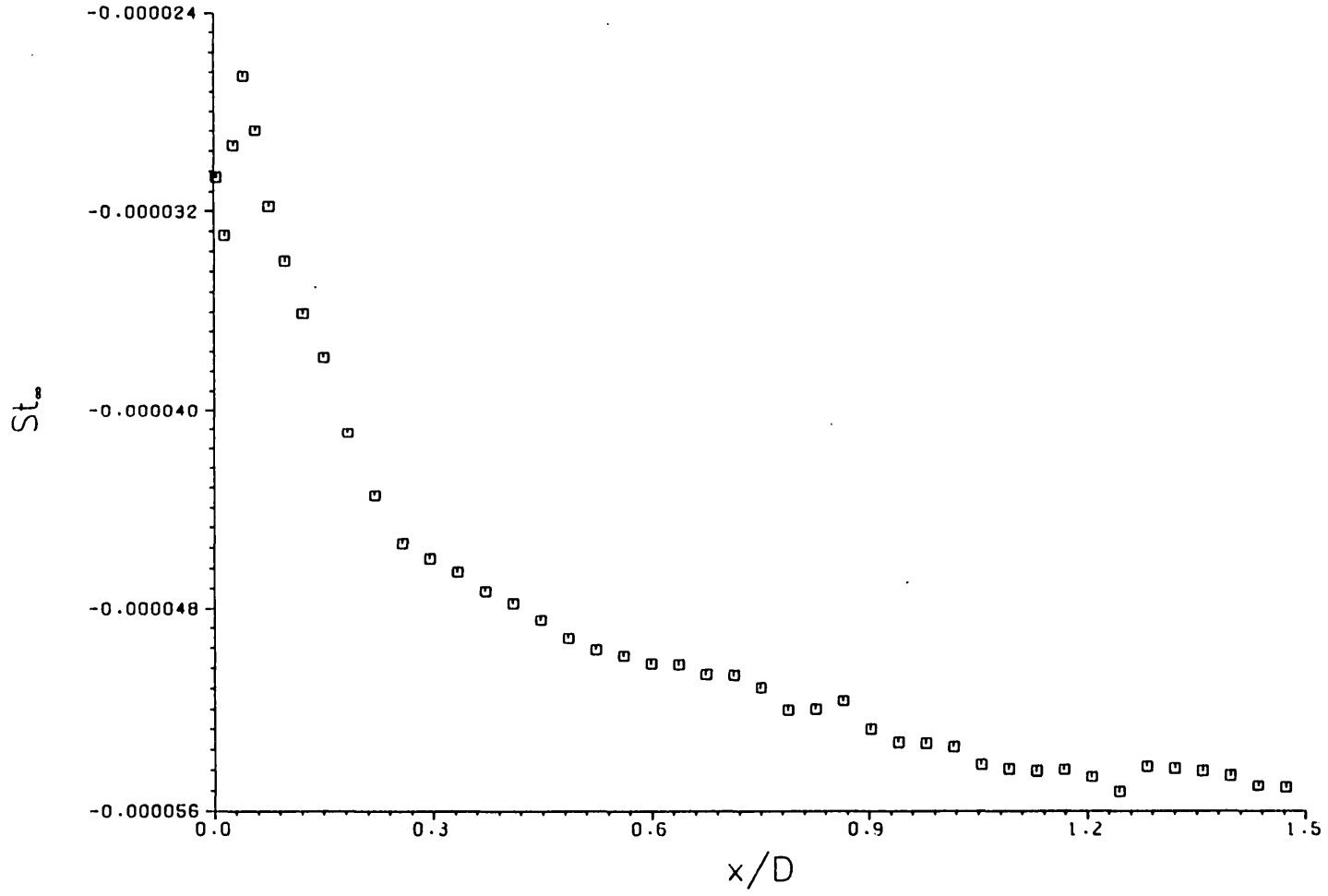

Fig.94 Stanton number distribution on afterbody

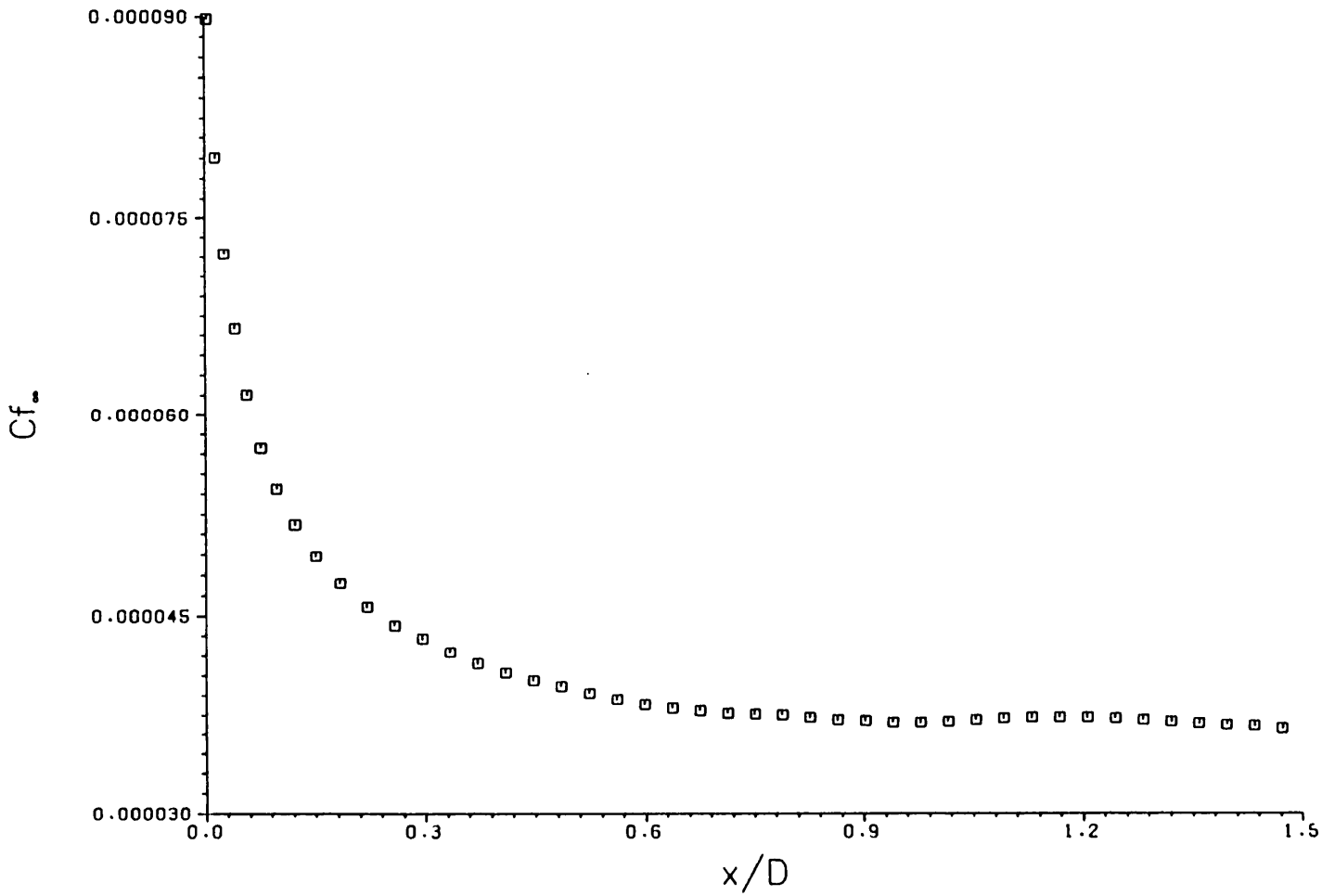

Fig.95 Skin friction distribution on afterbody

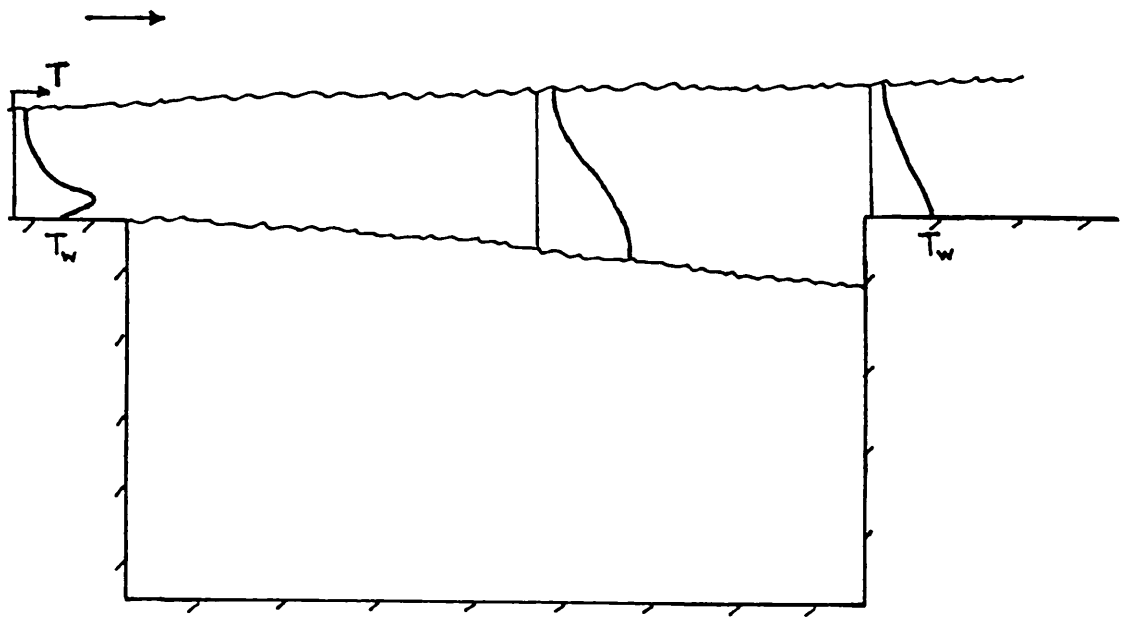

Fig.96 Schematic of temperature profile at reattachment

Appendix 1 Experimental Results

BOUNDARY LAYER DATA

HIGH REYNOLDS NUMBER

WIDE NOSED PITOT

y (mm)	P_p (psi)
0.400	5.800
0.750	11.000
1.000	15.650
1.250	20.200
1.500	24.600
1.750	24.600
2.000	26.510
2.500	30.600
3.000	36.610
3.500	43.550
4.000	50.500
4.500	54.900
5.000	59.330
5.500	61.860
6.000	60.600
6.500	61.850

LOW REYNOLDS NUMBER

y (mm)	P_p (psi)
0.400	1.390
0.750	2.650
1.000	3.820
1.250	5.430
1.500	6.440
1.750	6.690
4.000	12.620

NARROW NOSED PITOT

y (mm)	P_p (psi)
1.500	22.700
1.750	24.000
2.000	25.200
4.000	49.200

PRESSURE RESULTS - HIGH REYNOLDS NUMBER - D=2.5cm

L=6cm

X_*	P/P_c
0.120	0.612
0.240	0.640
0.400	0.609
0.520	0.709
0.640	0.612
0.760	0.612
0.880	0.643
0.920	0.623
1.200	0.588
1.400	0.592
1.600	0.568
1.800	0.588
2.000	0.547
2.200	0.509
2.400	0.475
2.600	0.509
2.800	0.544
3.000	0.530
3.200	0.795
3.480	0.746
3.520	0.698
3.640	0.736
3.760	0.643
3.880	0.571
4.000	0.581
4.080	0.578
4.160	0.767
4.280	1.314
4.320	1.706
4.520	0.640
4.600	0.623
4.800	0.537
5.000	0.519

L=4cm

X_*	P/P_c
3.360	0.612
3.280	0.595
3.200	0.564
3.480	1.060
3.080	0.574
2.720	0.722
2.840	0.664
2.960	0.657
2.680	0.685
3.520	1.627
2.200	0.664
2.400	0.736
1.200	0.664
1.400	0.643
1.600	0.595
1.800	0.547
2.000	0.571
0.080	0.647
0.120	0.643
0.240	0.650
0.400	0.647
0.320	0.643
0.760	0.678
0.920	0.678
0.600	0.674
0.880	0.688
0.520	0.633
4.200	0.482
3.720	0.581
3.800	0.616
4.000	0.499
3.680	0.605

P_c= 0.77psi (average)

PRESSURE RESULTS - HIGH REYNOLDS NUMBER - D=2.5cm

L=5cm

X_*	P/P_c
1.200	0.619
1.600	0.571
1.800	0.537
1.400	0.612
2.000	0.526
2.400	0.554
2.600	0.564
2.200	0.516
2.800	0.712
0.520	0.671
0.920	0.647
0.600	0.633
0.880	0.633
0.760	0.640
0.400	0.664
0.080	0.664
0.320	0.633
0.240	0.647
3.920	1.785
3.600	0.547
3.120	0.733
3.880	1.259
3.360	0.657
3.680	0.571
3.480	0.592
3.080	0.685
3.760	0.705
3.240	0.681
4.600	0.499
4.120	0.640
4.200	0.633
4.400	0.516
4.080	0.630

L=3cm

X_*	P/P_c
1.600	0.585
1.800	0.636
1.400	0.616
2.000	0.736
1.200	0.674
0.920	0.695
0.640	0.657
0.880	0.702
0.760	0.691
0.400	0.633
0.080	0.660
0.240	0.650
0.320	0.647
0.520	0.643
3.080	1.004
2.560	0.657
2.880	0.599
2.680	0.602
2.280	0.709
2.960	0.657
2.440	0.695
3.120	1.383
3.800	0.526
3.320	0.654
3.280	0.660
3.600	0.513
3.400	0.623

PRESSURE RESULTS - HIGH REYNOLDS NUMBER - D=2.5cm

L=2cm

X_*	P/P_c
2.720	0.963
2.680	0.757
2.560	0.619
2.480	0.550
2.280	0.568
2.400	0.544
2.160	0.602
1.880	0.619
1.920	0.595
2.040	0.623
0.320	0.537
1.400	0.647
1.200	0.640
1.600	0.643
0.120	0.550
0.080	0.602
0.640	0.592
0.920	0.698
0.400	0.461
0.520	0.588
0.240	0.581
0.760	0.671
0.880	0.695
3.400	0.509
2.920	0.640
3.000	0.612
3.200	0.506
2.880	0.630

PRESSURE RESULTS - LOW REYNOLDS NUMBER - D=2.5cm

L=6cm

X_*	P/P_c
4.320	1.569
4.080	0.616
3.520	0.664
3.480	0.688
4.280	1.273
4.000	0.585
3.760	0.630
3.640	0.636
3.880	0.578
4.160	0.740
3.200	0.702
2.800	0.568
2.600	0.564
2.400	0.574
2.200	0.564
2.000	0.547
1.800	0.568
1.600	0.581
1.400	0.585
1.200	0.595
3.000	0.619
0.240	0.616
0.120	0.619
0.520	0.585
0.400	0.623
0.640	0.605
0.920	0.626
0.320	0.605
0.760	0.599
0.880	0.616
0.080	0.585
5.000	0.574
4.520	0.633
4.600	0.619
4.800	0.550
4.480	0.633

L=5cm

X_*	P/P_c
1.200	0.612
1.600	0.595
1.800	0.574
1.400	0.612
2.000	0.595
2.200	0.609
2.400	0.612
2.600	0.612
2.800	0.698
0.520	0.643
0.920	0.599
0.600	0.602
0.880	0.616
0.760	0.616
0.400	0.674
0.080	0.671
0.320	0.695
0.240	0.698
3.120	0.702
3.600	0.640
3.920	1.545
3.880	1.128
3.360	0.702
3.680	0.674
3.480	0.664
3.080	0.691
3.760	0.695
3.240	0.695
4.600	0.561
4.120	0.709
4.200	0.688
4.400	0.561
4.080	0.674

p_c= 0.22psi (average)

PRESSURE RESULTS - LOW REYNOLDS NUMBER - D=2.5cm

L=4cm

X_*	P/P_c
3.360	0.595
3.280	0.585
3.200	0.588
3.480	0.853
3.080	0.585
2.720	0.626
2.840	0.616
2.960	0.623
2.680	0.612
3.520	1.276
2.200	0.685
2.400	0.709
1.200	0.685
1.600	0.643
2.000	0.619
1.400	0.674
1.800	0.647
0.080	0.647
0.120	0.588
0.240	0.643
0.400	0.657
0.320	0.664
0.760	0.685
0.920	0.674
0.640	0.688
0.880	0.685
0.520	0.698
4.200	0.568
3.720	0.716
3.800	0.671
4.000	0.557
3.680	0.719

L=3cm

X_*	P/P_c
1.600	0.643
1.800	0.626
1.400	0.660
1.000	0.678
1.200	0.674
0.920	0.695
0.640	0.688
0.880	0.709
0.760	0.678
0.400	0.660
0.080	0.674
0.320	0.671
0.240	0.630
0.520	0.702
2.320	0.705
2.800	0.643
3.080	0.771
2.560	0.643
2.880	0.619
2.680	0.619
2.280	0.688
2.960	0.688
2.440	0.685
3.120	1.111
3.320	0.702
3.400	0.705
3.600	0.571
3.280	0.702
3.800	0.568

PRESSURE RESULTS - LOW REYNOLDS NUMBER - D=2.5cm

L=2cm

X_*	P/P_c
0.880	0.667
0.240	0.557
0.320	0.561
0.760	0.609
0.400	0.588
0.640	0.595
0.520	0.571
0.080	0.581
1.200	0.585
1.600	0.609
1.400	0.636
2.400	0.626
2.680	0.709
2.040	0.616
2.160	0.616
2.720	0.798
2.560	0.612
1.920	0.616
1.880	0.643
2.480	0.640
2.280	0.602
3.400	0.561
2.920	0.674
3.000	0.643
3.200	0.544
2.880	0.688
2.880	0.688

PRESSURE RESULTS - D=1.25cm L=3cm

HIGH REYNOLDS NUMBER

X_*	P/P_c
4.320	2.305
4.280	1.572
4.240	1.404
4.200	1.101
4.160	0.912
4.080	0.750
4.000	0.657
3.880	0.643
3.760	0.716
3.640	0.757
3.520	0.819
3.480	0.822
4.480	0.805
4.520	0.791
4.600	0.695
4.720	0.636
4.800	0.602
5.000	0.571
3.160	0.853
2.360	0.636
2.120	0.667
2.520	0.595
2.760	0.599
2.920	0.722
1.960	0.678
1.320	0.702
1.520	0.688
1.680	0.691
0.080	0.764
0.120	0.729
0.240	0.729
0.320	0.746
0.520	0.712
0.640	0.712
0.720	0.722
0.800	0.736
0.880	0.743

LOW REYNOLDS NUMBER

X_*	P/P_c
4.320	2.085
4.280	1.273
4.240	1.132
4.200	0.929
4.160	0.850
4.080	0.757
4.000	0.722
3.880	0.726
3.760	0.757
3.640	0.774
3.520	0.815
3.480	0.822
4.480	0.877
4.520	0.839
4.600	0.781
4.720	0.722
4.800	0.698
5.000	0.654
3.160	0.850
2.360	0.719
2.120	0.726
2.520	0.688
2.760	0.685
2.920	0.774
1.960	0.767
1.320	0.746
1.520	0.722
1.680	0.746
0.080	0.760
0.120	0.781
0.240	0.753
0.320	0.791
0.520	0.781
0.640	0.781
0.720	0.784
0.800	0.805
0.880	0.795

HEAT TRANSFER RESULTS - HIGH REYNOLDS NUMBER - D=2.5cm

L=6cm

X_*	$\dot{q}(W/cm^2)$
4.320	22.360
4.280	15.460
4.200	12.560
4.120	7.860
4.000	6.280
3.800	2.800
3.600	3.120
3.480	4.020
3.200	4.060
2.200	2.000
1.200	1.360
0.800	0.920
0.600	2.360
0.400	1.800
0.200	0.920

L=4cm

X_*	$\dot{q}(W/cm^2)$
3.520	21.020
3.480	12.120
3.400	8.440
3.320	5.860
3.200	5.020
3.000	2.200
2.800	2.720
2.720	3.560
2.680	3.560
1.200	1.480
2.200	3.400
0.800	1.400
0.600	2.880
0.400	2.000
0.200	0.640

L=2cm

X_*	$\dot{q}(W/cm^2)$
2.720	15.520
2.680	7.920
2.600	5.680
2.520	4.120
2.400	3.340
2.200	1.360
2.000	1.380
1.920	2.600
1.880	2.060
1.200	2.180
0.800	1.460
0.600	2.260
0.400	1.800
0.200	0.560

L/D	$\dot{q}_{y/D=0.08}(W/cm^2)$
2.400	22.378
1.600	21.022
0.800	14.267
2.000	23.244
1.200	20.756

HEAT TRANSFER RESULTS - LOW REYNOLDS NUMBER - D=2.5cm

L=6cm

X	$\dot{q}$ (W/cm²)
4.320	10.060
4.280	4.760
4.200	3.440
4.120	2.520
4.000	1.800
3.800	0.660
3.600	0.480
3.520	0.800
3.480	1.000
3.200	1.280
2.200	0.600
1.200	0.340
0.800	0.080
0.600	0.420
0.400	0.340
0.200	0.280

L=4cm

X	$\dot{q}$ (W/cm²)
3.520	6.280
3.480	3.360
3.400	2.160
3.320	1.560
3.200	1.240
3.000	0.400
2.800	0.280
2.720	0.680
2.680	0.580
1.200	0.220
2.200	0.600
0.800	0.340
0.600	0.560
0.400	0.400
0.200	0.200

L=2cm

X	$\dot{q}$ (W/cm²)
2.720	3.260
2.680	1.580
2.600	1.000
2.520	0.760
2.400	0.440
2.200	0.160
2.000	0.140
1.920	0.240
1.880	0.280
1.200	0.340
0.800	0.200
0.600	0.380
0.400	0.300
0.200	0.120

L/D	$\dot{q}_{y/D=0.08}$ (W/cm²)
2.400	10.067
1.600	6.133
0.800	2.733
2.000	8.622
1.200	4.733